Stars Eating Planets

John Wimarsson

Lund Observatory
Lund University

2020-EXA171

Degree project of 60 higher education credits (for a degree of Master)
December 2020

Supervisor: Alexander Mustill

Lund Observatory
Box 43
SE-221 00 Lund
Sweden

Abstract

In a phase of instability during the dynamical evolution of some multiple exoplanetary systems, exchange of angular momentum and/or energy through gravitational interactions between planets will lead to alterations of their orbital properties. In some cases, planetary orbits end up crossing, which leads to close encounters between two planets. In turn, they undergo a planet–planet scattering event, where a large exchange of angular momentum and energy leads to a significant change in trajectories and thereby their orbits. The distribution of eccentricity for observed giant planets provides strong evidence for past planet–planet scattering events in many exoplanetary systems. One particular outcome of such an event is when one of the planets ends up on a highly eccentric orbit, which leads to a planet–star collision, also referred to as *planet consumption*. When a planet is consumed, it can transfer physical quantities such as angular momentum, energy and heavy elements to the host star, altering its properties. Due to the transfer of said quantities, a planet consumption event can have observational consequences for the host star that are detectable by astronomical instruments.

In this thesis, I first employ a semi-analytical two-body model to constrain which type of orbital configuration in a planetary system with a single star will facilitate planet consumption. I then use the constrained parameter space to formulate a fiducial planetary configuration. The dynamical evolution of said system is then modelled using 100 numerical N-body integrations, which allows me to further determine for which type of systems that planet consumption by planet–planet scattering is possible. Moreover, I tie the results of the semi-analytical and numerical analysis to a literature study in order to constrain which type of observational consequence will dominate for consumption of planets on highly eccentric orbits.

From the two-body analysis, I conclude that planet consumption is more probable for scattering events where: the planetary mass ratio is extreme, where the inner planet is less massive than the outer; the planets are orbiting a host star with low density; at least one of the orbits is highly eccentric, preferably that of the least massive planet; the event occurs at small separations from the host star. Based on these results, I also formulate the fiducial planetary system, which is a Solar System analogue with two Earth-mass planets inside of 1 AU and three initially unstable Jupiter-mass planets beyond 5 AU. From the numerical N-body integrations I find that hierarchical systems with low-mass planets and at least two unstable giant planets will consistently induce consumption of planets of 30 Earth masses and less. When the system has three giant planets, around 10% of the integrations lead to the consumption of a giant planet. Such an event can produce an observational consequence where a single giant planet ends up on a very distant orbit with arbitrary eccentricity. The integration results also show that there are three extreme pathways to planet consumption: *diffusive planet consumption*, where the eccentricity of a planet increases diffusively over a large number of scattering events; *strong planet consumption*, where the eccentricity is boosted up quickly over a small number of scatterings and *Lidov–Kozai planet consumption*, where the eccentricity increases through the Lidov–Kozai

mechanism which excludes planet–planet scattering.

In the literature study I determine that the dominant observational consequence highly depends on stellar properties such as age, metallicity, mass and radius, as well as planetary mass, radius and composition. Moreover, the minimum separation between the planet and the host star during an orbit determines the strength of detectable signatures. A majority of the observational consequences are difficult to directly tie to planet consumptions, meaning that detections of such events are good targets for future multi-waveband astronomy missions. From the results of the numerical integrations performed, I estimate that the dominant observational consequence from planet consumption in the Milky Way is metallicity enhancement by consumption of super-Earths. Outside the Galaxy, the dominant observational consequence is planet merger transients caused by the consumption of a giant planet, which induces an increase of stellar luminosity in the optical/infrared wavebands followed by a radio afterglow that lasts for a few thousand years.

Acknowledgements

First of all, I want to thank Alexander Mustill for stepping in to guide my work when I was left without a supervisor with only two months left before my deadline. Second, I want to express my deepest gratitude to Colin Carlile for thoroughly proofreading my thesis and Beibei Liu for providing useful comments. Lastly, I want to thank my siblings, Rož Ali, Alise Krūmiņa, Maja Jansson and Jesper Nielsen for their support and encouragement.

Popular science summary

Astronomers make for excellent investigators and the Milky Way provides an exciting crime scene full of clues and evidence of remarkable events in the past. Stars have collided with one another. Stars have been swallowed by black holes. Stars have exploded in supernovae, leaving black holes or neutron stars behind. Our galaxy has had a violent past, to say the least. But how do we know? Well, compared to detectives investigating criminal cases back on Earth, astronomers have a significant advantage. They can look back in time. The light shining down on us from countless of stars on the night sky during an evening stroll holds many secrets. Not only can the light tell us about stellar ages, masses, sizes and compositions, it can also provide us with clues about destructive events that have occurred in their past. For exoplanetary scientists, there is one mysterious case in particular that needs solving: Where have all the planets gone?

Observations of exoplanetary systems indicate that the Solar System is special. The large number of single planet systems and the lack of planets on short-period orbits near the Sun or highly elliptical orbits are all observational signatures that thicken the plot. Moreover, according to planet formation theory, planets are likely to be born on circular orbits in systems with more than one planet. In turn, there must be some mechanism that eliminates planets from the systems between their birth and the time of observation, while putting remaining planets on short-period and/or elliptical orbits. The clue that blows the case wide open is the fact that observed planetary systems with multiple planets have large average separations, meaning that there is a lack of systems where the planets are tightly packed together. Computer simulations of the evolution of planetary systems where the planets have small initial separations show that they are highly unstable. This instability often resolves in a violent celestial dance where the planets gravitationally interact and alter each other's orbits. This is called *planet–planet scattering*.

One particular outcome of this chaotic dance is that a planet can end up colliding with its host star in an event referred to as *planet consumption*. Depending on when and where the planet hits the host star and its impact velocity, it can alter different properties of the host star. A faster rotational velocity around its axis than predicted by theoretical models, a notable increase in metals within a star's atmosphere or a brief increase in its brightness are all smoking guns that point towards a past planet consumption event.

In this thesis, I have used an analytical model and computer simulations to investigate which type of planetary system architectures that consistently produce planet consumption events by planet–planet scattering and what kind of planet is more likely to end up being eaten. I have then performed a literature study of observational consequences induced by planet–star collisions to couple my simulation results to detectable signatures in the properties of a host star. I found that planets with thirty times the mass of the Earth and less consistently get eaten when they are in the same system as at least two giant planets of a third of Jupiter's mass or more. The low-mass planets are likely to create signatures in the light from the culprit star showing an increase in Lithium and heavy

metals. A giant planet can also get eaten in 10% of the systems if they are born with at least three giants. This can produce a large variety of observational signatures that can be seen millions of light-years away in neighbouring galaxies such as Andromeda. I found a previously unexplored observational consequence where the consumption of a giant planet can lead to the existence of systems where a single giant planet orbits the host star at large distances. The existence of such systems is poorly explained by planetary formation theory.

While the signatures caused by planet consumption generally are weak, the next generation of astronomical instruments such as the Square Kilometre Array and the Vera Rubin Observatory will most probably be able to consistently detect such events. In turn, exoplanetary scientists will develop their understanding of the early evolution of planetary systems and obtain a major piece of evidence regarding the mysterious uniqueness of the Solar System.

Contents

List of Figures

List of Tables

Chapter 1

Introduction

Ever since the first confirmed discovery of an exoplanet orbiting a Main Sequence (MS) star in 1995, when Mayor & Queloz detected 51 Pegasi, the field of planetary science and exoplanet observations has seen a monumental surge in activity and interest. At the time of writing, only 25 years later, there are 4277 confirmed exoplanets in the NASA exoplanetary archive (Akeson et al., 2013). From observations of planetary systems with NASA's Kepler Space Telescope mission ('Kepler', Borucki et al., 2010) and theoretical models of planet formation (Johansen & Lambrechts, 2017), it is clear that the architecture of the planets in the Solar System is by no means typical. A significant fraction of the observed exoplanetary systems host Jupiter-mass planets that orbit their star at small separations $\lesssim$ 0.2 AU. These planets are referred to as *hot Jupiters*[1]. The existence of hot Jupiters cannot be explained by planet formation theory alone and thereby hints at a history of rich dynamical evolution between multiple planets in the planetary systems hosting the hot Jupiters (Naoz, 2016). During a phase of instability, the intrinsic planet population within these systems exchange angular momentum and/or energy, which can significantly alter the properties of their orbits around the host star (Davies et al., 2014). In some cases, the exchange of angular momentum and/or energy leads to the crossing of two orbits and close encounters between planets where they gravitationally perturb the orbits of one another. The subsequent exchange of angular momentum and energy during such encounters that leads to alterations of their trajectories is known as a *planet–planet scattering*. Planet–planet scattering events have three distinct outcomes that lead to the disruption of an orbit, which are believed to be more frequent than the creation of hot Jupiters (Ford & Rasio, 2008):

1. ***ejection:*** A planet gets completely unbound from the planetary system.
2. ***planet–planet merger:*** The two planets merge, leaving a single more massive planet behind.

[1]Terms in italics throughout the thesis are explained in the glossary on page 155.

3. ***planet consumption:*** A planet on a highly elliptical orbit collides with its host star and gets consumed.

Planet–planet scattering has been studied extensively since the increase in popularity of planetary science from 1995 and the fractional rate of these three outcomes have been constrained using numerical integration (see Davies et al., 2014, and references therein). In turn, planet consumption has been widely regarded as an uncommon occurrence in planetary systems. However, in a recent paper, Carrera, Raymond, & Davies (2019) argued that many previous studies on planet–planet scattering have preemptively removed planets on highly elliptical orbits from their integrations, leading to an underestimation of the number of planet consumptions in their studies. In turn, said outcome may be more common than previously believed.

A key feature of planet consumption events is that the disrupted planet will transfer physical quantities to the host star, altering its properties. Depending on the intrinsic physical properties of the two bodies, as well as the nature of their close encounter, there will be a dominant exchange of either angular momentum, energy or heavy elements. Each type of dominant exchange leads to a different observational consequence for the host star that can be detectable with the use of astronomical instruments. For example, exchange of angular momentum can lead to spin-up of the host star's rotation (Qureshi, Naoz, & Shkolnik, 2018). While a majority of studies investigating the effect of planet–star collisions have investigated observational consequences for planets on orbits near their host star that decay over time (e.g. Laughlin & Adams, 1997; Sandquist et al., 1998, 2002; Li et al., 2008; Metzger et al., 2012), more recent studies show that planets on highly elliptical orbits colliding with their host star will induce different observational signatures (Yamazaki et al., 2017; Church et al., 2020; Stephan et al., 2020).

In this thesis, I have carried out semi-analytical and numerical studies of planet–planet scattering in single star planetary systems to develop a better understanding of how often and for which type of configurations planet–planet scattering leads to planet consumption. Further, I have performed a literature study followed up with toy–model calculations to constrain which type of observational consequence is most detectable for planet consumption of planets on highly elliptical orbits.

The thesis is structured as follows:

- **Chapter 2:** I lay out the fundamentals of planetary orbits and properties used to quantify their position relative to their host star.
- **Chapter 3:** I present the current picture of planetary multiplicity, mass distribution, orbital properties, as well as host star properties of exoplanetary systems according to observations and planet formation theory.
- **Chapter 4:** I explain how long-term dynamical interactions between planets lead to instabilities in their planetary systems, ultimately producing planet–planet scattering events.

- **Chapter 5:** I investigate planet–planet scattering using a toy–model two-dimensional and isolated two-body model, where the orbits of two planets are crossing. In section 5.1, I derive the analytical solutions for the problem. In section 5.4, I use the model to constrain the parameter space for planetary and stellar properties that will enhance the probability of having planet consumption events.
- **Chapter 6:** I numerically integrate the three-dimensional dynamical evolution of potentially planet-consuming systems to better constrain how often planet–planet scattering leads to ejection, merger and planet consumption. I go through the details of the numerical setup in section 6.1, present the fiducial choice of orbital configuration of planets in section 6.2 and the resulting planetary systems are discussed in section 6.3.
- **Chapter 7:** I perform a literature study of planet consumption events and introduce the various observational consequences that they can induce. By performing toy–model calculations of the effects planet consumption has on the host star, I further tie the results of my numerical integrations to observational consequences.
- **Chapter 8:** I discuss the results of my investigation of planet consumption by planet–planet scattering with respect to shortcomings of the theoretical models used, planet formation theory and detectability of observational consequences. Finally, I present possible future improvements that can be made to expand the study.
- **Chapter 9:** I briefly summarise the work done in the thesis and present the major conclusions drawn from my results.

The major conclusions from chapters 5 through 8 are found in sections 5.5, 6.7, 7.8 and 8.3.5, respectively. Furthermore, a list of symbols that are commonly used throughout the thesis are found on page 151. For all symbols, the subscript p ($\star$) indicates that the quantity is a property of a planet (host star). For a list of acronyms and the glossary explaining words and terms in italics, see pages 154 and 155, respectively.

Chapter 2

Properties of planetary orbits

In order to properly discuss the behaviour of planets as they undergo dynamical evolution in planetary systems, it is necessary to lay out the basics of their orbits. I use this chapter to present the key features of a planetary orbit according to Kepler's laws of planetary motion.

2.1 Planetary orbits are elliptical

According to Kepler's first law, a planetary orbit is an ellipse with a star at one of its foci. The semi-major axis of the ellipse is denoted by a and the distance from the centre of the ellipse, C, to the focus where the star is positioned is c. These planetary orbit components are shown in figure 2.1. The eccentricity of an orbit is defined as

$$e = \frac{c}{a} \tag{2.1}$$

and is a measure of its ellipticity, i.e. how flattened the ellipse is. Increasing the eccentricity of an orbit in turn increases its ellipticity. There are three limiting cases that we consider

1. $e = 0$: The orbit is circular.
2. $e = 1$: The orbit becomes parabolic and unbound from the system.
3. $e > 1$: The orbit becomes hyperbolic and unbound from the system.

The effect of altering the eccentricity of an orbit is illustrated in figure 2.2.

Since an ellipse is a conic section, I can use polar coordinates to express the distance between any point on the ellipse and the star as

$$r_{\mathrm{p}} = \frac{\ell}{1 + e\cos(\theta)}, \tag{2.2}$$

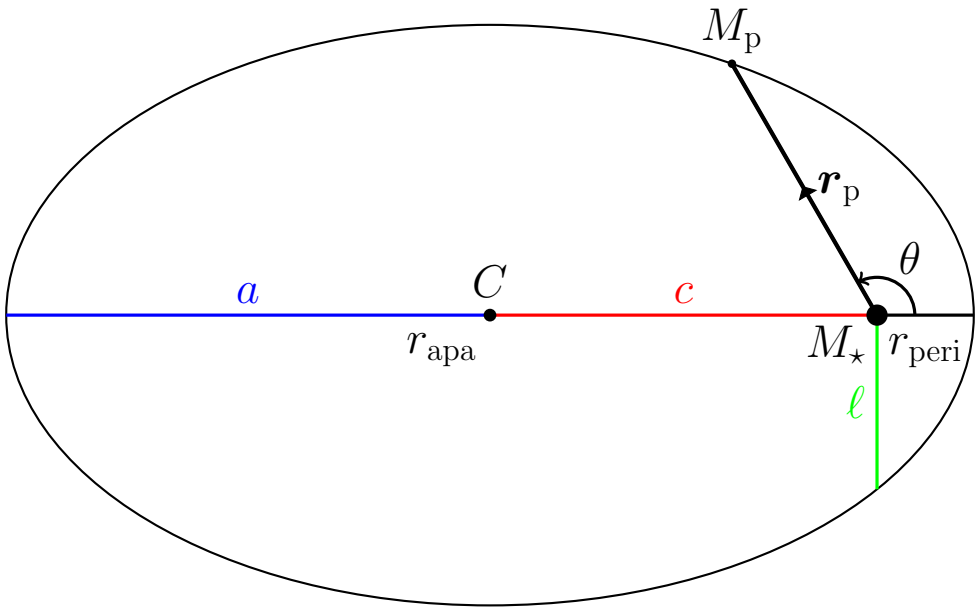

Figure 2.1: A schematic showing the geometry of a Keplerian orbit with an eccentricity of $e = 0.8$, as seen face-on. The different components are indicated by their respective variable names at the midway point of their length.

where θ is the angular coordinate to this point measured from the semi-major axis, pointing away from C, and ℓ is the semi-latus rectum. The semi-latus rectum is defined as half the distance of a line passing through one of the foci of the ellipsis orthogonal to the semi-major axis. Furthermore, I show the periastron and apastron distances in figure 2.1, r_peri and r_apa, which are the closest and the farthest separations between the host star and the planet on its orbit, respectively. From the geometry of the orbit it is straightforward to find that

$$r_\mathrm{peri} + r_\mathrm{apa} = 2a. \tag{2.3}$$

Next, I can use equation (2.2) to express these two distances as

$$r_\mathrm{peri} = \frac{\ell}{1+e}, \text{ and } r_\mathrm{apa} = \frac{\ell}{1-e}, \tag{2.4}$$

where I have used the fact that the periastron has a true anomaly of $\theta = 0$ and the apastron has a true anomaly of $\theta = \pi$. Combining these two expressions with equation (2.3) and solving for a, I find that for an ellipsis the semi-latus rectum can be written as

$$\ell = a(1 - e^2). \tag{2.5}$$

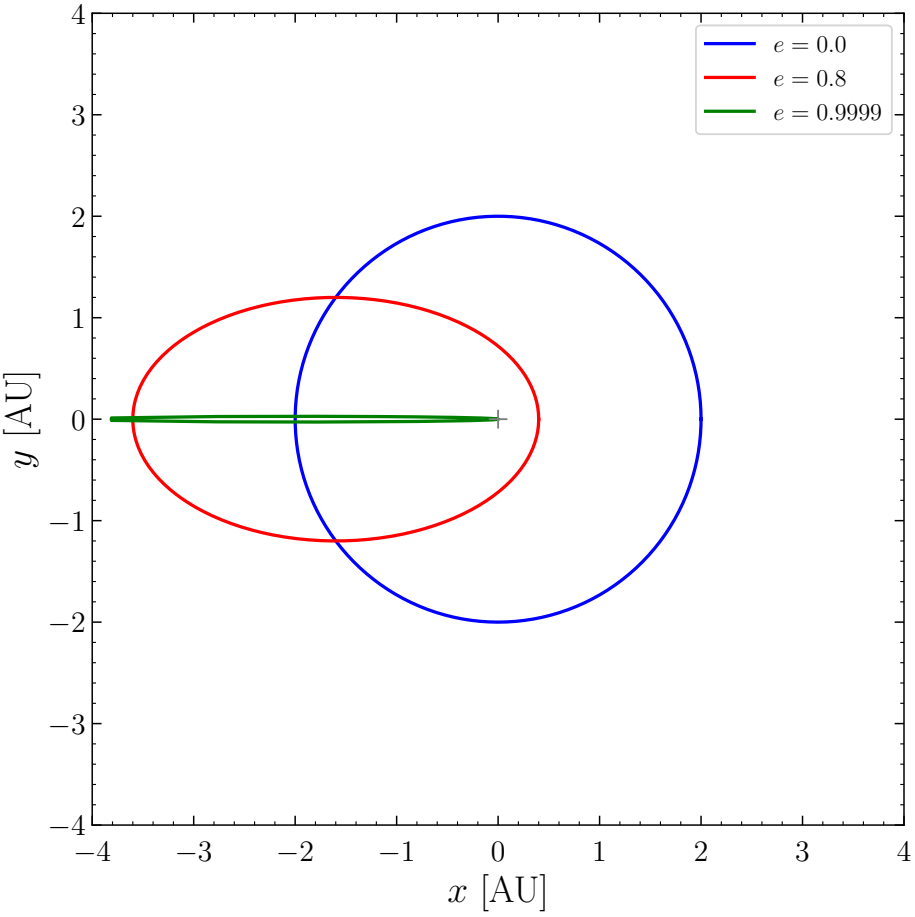

Figure 2.2: Illustration of the effect of varying the eccentricity of a planetary orbit with a static semi-major axis a. In blue is a circular orbit with $e = 0$, in red an eccentric orbit with $e = 0.8$ and in green a highly eccentric orbit with $e \lesssim 1$. The grey plus sign indicates the position of the host star.

Now combining (2.5) with (2.2), I can obtain the more useful expression for r that is valid for elliptical orbits

$$r_{\mathrm{p}} = \frac{a(1 - e^2)}{1 + e\cos(\theta)}. \tag{2.6}$$

2.2 Orbital elements

In the instance of a planetary system containing more than one planet, it is useful to identify them and compare their relative positions using a reference system that is based on more than their eccentricity and semi-major axes. While it is possible to use a Cartesian

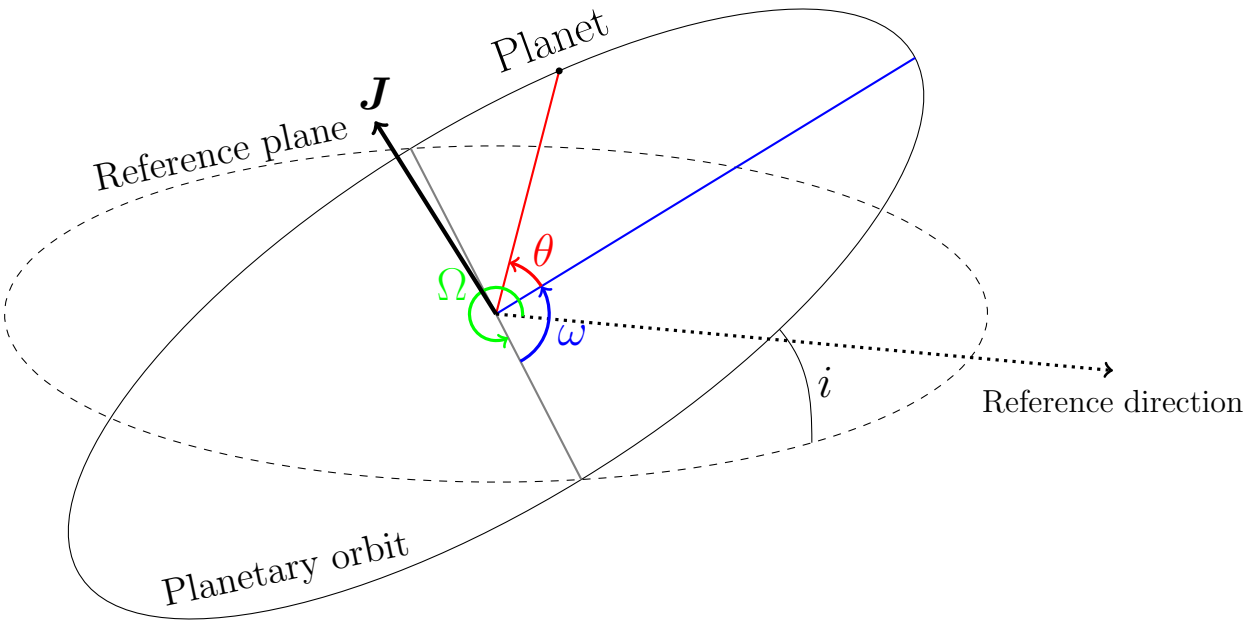

Figure 2.3: A Keplerian orbit, shown in a frame defined by the plane of reference and a reference direction. The diagram displays four of the six orbital elements of a Keplerian orbit: the inclination i; the argument of the periastron ω; the longitude of the ascending node and the true anomaly θ. The angular momentum vector $\boldsymbol{J}$, which is orthogonal to the plane of rotation, is also shown.

coordinate system, it is common practice to use the so-called Keplerian elements. In total, a Keplerian orbit can be uniquely identified using six elements which are defined relative to a reference direction and a reference plane. I have already introduced the semi-major axis, a, and eccentricity, e, which provide a measure of the shape of the ellipsis. The remaining four orbital elements displayed in figure 2.3, which determine the orientation of the orbit relative to the reference system, are defined as follows:

- **Orbital inclination i:** The vertical tilt between the orbital plane and the reference plane measured at the intersection of the two planes, which is referred to as the ascending node.
- **Longitude of the ascending node Ω:** The angle between the reference direction and the ascending node in the reference plane.
- **Argument of the periastron ω:** Measure of the angle between the ascending node of the orbit and its periastron.
- **True anomaly θ:** The angle between the periastron and the current position of the orbiting body.

Figure 2.3 also displays the angular momentum vector $\boldsymbol{J}$, which is orthogonal to the orbital plane and is given by

$$\boldsymbol{J} = \boldsymbol{r}_{\mathrm{p}} \times M\boldsymbol{v}_{\mathrm{p}}, \tag{2.7}$$

where M is the mass of the object and $\boldsymbol{v}_{\mathrm{p}}$ is the velocity vector. An important property of the angular momentum vector is that it is effectively constant for a given orbit and only changes due to external forces, such as gravitational interaction with other bodies in a planetary system. Moreover, it is highly related to the eccentricity of a planet since a circular orbit will have maximal angular momentum for a given semi-major axis. If the planet loses angular momentum to another body in the system, its orbit will become more eccentric. Hence, the fact that it is a conserved quantity during planet–planet and planet–star interactions is key for understanding planetary dynamics, which is discussed in detail in chapter 4. Another useful quantity is the specific angular momentum vector, $\boldsymbol{h}$, which simply is given by

$$\boldsymbol{h} = \boldsymbol{r}_{\mathrm{p}} \times \boldsymbol{v}_{\mathrm{p}}. \tag{2.8}$$

The *mutual inclination*, i_{m}, for two orbits, which represents the angle between the two angular momentum vectors can be computed using the law of cosines (Muterspaugh et al., 2006):

$$\cos(i_{\mathrm{m}}) = \cos(i_1)\cos(i_2) + \sin(i_1)\sin(i_2)\cos(\Omega_1 - \Omega_2). \tag{2.9}$$

The mutual inclination value can be interpreted using the following reference values:

- $i_{\mathrm{m}} = 0°$: The angular momentum vectors are parallel.
- $i_{\mathrm{m}} = 90°$: The angular momentum vectors are perpendicular.
- $90° < i_{\mathrm{m}} < 180°$: One orbit is retrograde with respect to the other.
- $i_{\mathrm{m}} = 180°$: The angular momentum vectors are anti-parallel.

Note that all orbital elements will be static for a single planet except for θ, which will change as the planet travels along its orbit. The remaining five elements can only be altered by external perturbations from other forces, such as gravitational interaction with another planet or a passing star.

2.3 Motion of a planet on an elliptical orbit

I now consider a two-body system of the kind displayed in figure 2.1, where a solitary planet orbits a star positioned at the origin of the coordinate system. The position of the

planet is given by the vector $\boldsymbol{r}_\mathrm{p}$ and it has a velocity of $\boldsymbol{v}_\mathrm{p}$. As indicated in figure 2.4, the velocity vector can be divided into two components, the radial velocity v_r and the tangential velocity v_θ, which means that the velocity can be written as

$$\boldsymbol{v}_\mathrm{p} = v_r\hat{\boldsymbol{r}} + v_\theta\hat{\boldsymbol{\theta}} \tag{2.10}$$

$$= \dot{r}_\mathrm{p}\hat{\boldsymbol{r}} + r_\mathrm{p}\dot{\theta}\hat{\boldsymbol{\theta}} \tag{2.11}$$

where e.g. $\dot{\theta}$ is the time-derivative of θ[1]. Let the angle in between $\boldsymbol{v}_\mathrm{p}$ and v_r be denoted α. Using the definition of the cross product, I can write the magnitude of the specific angular momentum vector from equation (2.8), $h = |\boldsymbol{h}|$, as

$$h = |\boldsymbol{r}_\mathrm{p} \times \boldsymbol{v}_\mathrm{p}| = r_\mathrm{p} v_\mathrm{p} \sin(\alpha), \tag{2.12}$$

where $v = |\boldsymbol{v}|$. From the geometry in figure 2.4 I then work out that

$$\sin(\alpha) = \frac{v_\theta}{v_\mathrm{p}} \iff v_\mathrm{p}\sin(\alpha) = v_\theta. \tag{2.13}$$

In combination with equation (2.12), I end up with the useful relation

$$h = r_\mathrm{p} v_\theta = r_\mathrm{p}^2\dot{\theta}. \tag{2.14}$$

Since my system is isolated, the only force acting on each body is the gravitational force exerted by the companion body. An expression for the relative motion of such a system that can be derived from Newton's laws (De Pater & Lissauer, 2015) is given by

$$\boldsymbol{F}_g = \mu_r \frac{\mathrm{d}^2\boldsymbol{r}_\mathrm{p}}{\mathrm{d}t^2} = -\frac{G\mu_r M_\mathrm{tot}}{r_\mathrm{p}^2}\hat{\boldsymbol{r}}, \tag{2.15}$$

where μ_r is the reduced mass of the system

$$\mu_r = \frac{M_\mathrm{p} M_\star}{M_\mathrm{p} + M_\star} \tag{2.16}$$

and $M_\mathrm{tot} = M_\mathrm{p} + M_\star$ is the total mass of the system. Moreover, I consider the centripetal force required to keep an object of mass μ_r in a circular orbit of radius r around an object of mass $M_\star$

$$\boldsymbol{F}_c = \frac{\mu_r v_\theta^2}{r}\hat{\boldsymbol{r}} = r\dot{\theta}^2\hat{\boldsymbol{r}}. \tag{2.17}$$

[1]Note that $\dot{r}_\mathrm{p}$ is the radial velocity component and not $|\dot{\boldsymbol{r}}_\mathrm{p}|$

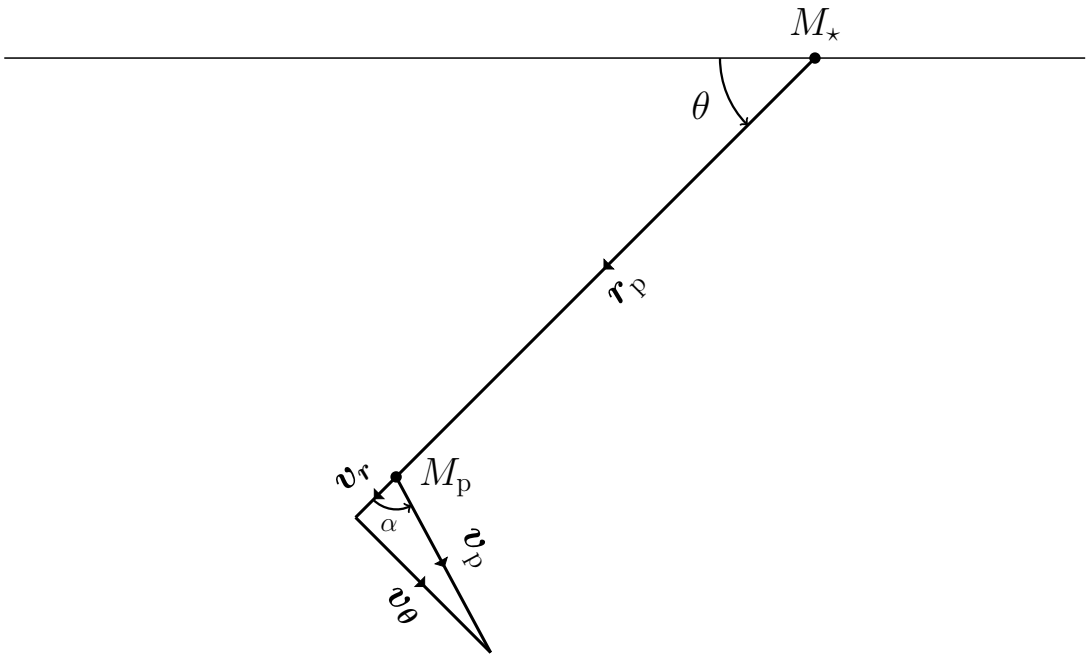

Figure 2.4: Simple schematic of the two-body problem in figure 2.1, where I consider the components of the velocity vector that indicate the motion of the planet due to its gravitational interaction with the host star.

Using that $\boldsymbol{F}_g - \boldsymbol{F_c} = 0$ for this circular orbit, I obtain that

$$v_c = \sqrt{\frac{GM_\mathrm{tot}}{r}}. \tag{2.18}$$

However, it would be much more useful to rewrite this velocity in terms of the orbital elements for an elliptical orbit. Furthermore, I need to find an expression for $\dot{\theta}$. In order to achieve this, I recognise that the acceleration in the radial direction for a body on an orbit more generally can be described as the sum of two terms, the time derivative of the radial velocity and the centripetal acceleration. Setting the sum of these two components equal to the gravitational acceleration, I obtain the radial equation of motion

$$\ddot{r}_\mathrm{p} - r_\mathrm{p}\dot{\theta}^2 = -\frac{GM_\mathrm{tot}}{r_\mathrm{p}^2}. \tag{2.19}$$

The standard solution for this differential equation is found in Szebehely (1989)

$$r_{\mathrm{p}} = \frac{h^2/GM_{\mathrm{tot}}}{1 + (Ah^2/GM_{\mathrm{tot}})\cos(\theta)}, \tag{2.20}$$

where A is a constant of integration. This is another form of the expression for the distance between the focus and a point on a conic section, in my case an ellipse, which is given in equation (2.2). Comparing the two relations, I find that

$$\ell = \frac{h^2}{GM_{\mathrm{tot}}}. \tag{2.21}$$

Now I have two independent expressions that contains the magnitude of the specific angular momentum, h, in equations (2.14) and (2.21). Equating them, I arrive at another useful expression

$$r_{\mathrm{p}}^2\dot{\theta} = \sqrt{GM_{\mathrm{tot}}\ell}. \tag{2.22}$$

I am now fully equipped to express the components of the orbital velocity $\boldsymbol{v}$ in terms of orbital elements. Using the chain rule and employing equations (2.2) and (2.22), I find that

$$\dot{r}_{\mathrm{p}} = \frac{\mathrm{d}r_{\mathrm{p}}}{\mathrm{d}\theta}\dot{\theta} = \frac{\ell e\sin(\theta)}{(1+e\cos(\theta))^2}\left(\frac{(1+e\cos(\theta))}{\ell}\right)^2\sqrt{GM_{\mathrm{tot}}\ell} \tag{2.23}$$

$$= e\sin(\theta)\sqrt{\frac{GM_{\mathrm{tot}}}{\ell}} \tag{2.24}$$

Finally, using that $\ell = a(1-e^2)$ from equation (2.5) I obtain an expression for the radial velocity

$$v_r = \left(\frac{GM_{\mathrm{tot}}}{a(1-e^2)}\right)^{1/2} e\sin(\theta). \tag{2.25}$$

The tangential velocity component is found by dividing equation (2.22) by r_{p} and again inserting equation (2.5), which yields

$$v_\theta = \left(\frac{GM_{\mathrm{tot}}}{a(1-e^2)}\right)^{1/2}(1+e\cos(\theta)). \tag{2.26}$$

These expressions can easily be verified by considering the case of a circular orbit with $e = 0$, as this yields $v_\theta = v_c$ and $v_r = 0$.

2.4 Orbital energy

Another important quantity of an elliptical orbit is orbital binding energy. Given a set configuration with a host star of mass $M_\star$ and a planet of mass M_p, the orbital energy solely depends on the semi-major axis of the orbit. Hence, the orbital binding energy is useful when quantifying how bound a planet is to the system.

The total energy of the bound system in the rest frame of the host star is the sum of the kinetic energy and potential energy of the body, which can also be written in terms of the semi-major axis

$$E = \frac{1}{2}\mu_r v_\mathrm{p}^2 - \frac{GM_\mathrm{tot}\mu_r}{r_\mathrm{p}} = -\frac{GM_\mathrm{tot}\mu_r}{2a}. \tag{2.27}$$

From this equation, it is clear that the planet is bound when its potential energy is larger than its kinetic energy. Moreover, the energy goes to zero as $a \to \infty$. Therefore, a planet that has an energy of $E < 0$ is considered bound to the system, while a planet with an energy of $E \geq 0$ can be considered unbound and ejected from the system.

Chapter 3

Observed exoplanetary systems

In this chapter, I lay out the current understanding of exoplanet occurrence and architecture based on the data of detected exoplanets, which serves as a basis for the potentially planet-consuming planetary systems I have investigated in this thesis.

Detecting an exoplanet orbiting one or more host stars is no simple feat due to the large mass differences between star and planet and a lack of intrinsic luminosity of the planet itself. Instead, one has to opt for indirect methods of detection. 76.1% of the current 4277 confirmed detections in NASA's exoplanetary archive (Akeson et al., 2013) have been made with the transit method, where an instrument measures reductions in the light flux from the host star which occurs when a planet passes the star along the line of sight of the observer. 19.2% of the detections are from the radial velocity method, which measures the Doppler shift in spectral lines of the host star induced by variations in the radial motion due to gravitational interaction with a planet in orbit around it. There exists a number of additional methods including astrometry, gravitational microlensing and direct imaging that accounts for the remaining detections. Nevertheless, are not discussed in this thesis. For an extensive review of exoplanetary detection methods, see Wright & Gaudi (2013).

Another difficulty for exoplanet detection apart from the requirement of indirect methods is that the presence of a planet orbiting a host star cannot be confirmed by one method alone. Hence, to fully confirm the observation of an exoplanet additional follow-up measurements and validations are needed. The most common practice is to combine the physical properties found through the radial and transit methods, which complement each other. The radial velocity exoplanet detection method provides a minimum limit for the mass of the planet and its orbital distance. The reason why the exact mass cannot be estimated is because it only provides the minimum mass of the planet $M_{\mathrm{p}} \sin(i)$, where i is the inclination of the planet's orbit. This parameter cannot be inferred from the radial velocity method alone. Instead, the inclination has to be provided by the transit method, which also provides the planetary radius. Hence, by combining the two, the density of the planet

can be found. Knowing the density of the object, it is possible to deduce if the detection is in fact an exoplanet or a false positive (De Pater & Lissauer, 2015).

The majority of the detected exoplanets have been found by 'Kepler' which used the transit method. Hence, most of the conclusions drawn regarding occurrence and architecture of exoplanetary systems are largely based on a single mission. Furthermore, it is necessary to take into account the fact that it is easier to detect more massive planets since they will yield a larger perturbation on the host star, both in terms of radial velocity and light flux in case of a transit event. This leads to a lack of data for planets of Earth-mass and below. In turn, there is a possibility that the current perception of exoplanetary system occurrence and architecture may suffer from heavy bias. For example, Zink, Christiansen, & Hansen (2019) found that the detection efficiency of the 'Kepler' pipeline drops after the first detection of an exoplanet, which may introduce a bias towards mis-identifying multiple systems as single-planet systems. Previous studies have found that there appears to be a strong indication that 'Kepler' system planets have similar properties to other planets present in the system (e.g. Millholland et al., 2017; Weiss et al., 2018). As a response, another source of bias was pointed out by Zhu (2020), where the varying transit signal-to-noise ratio detection thresholds could favour detection of planets of a given size around a host star of a specific mass. The claims by Zink, Christiansen, & Hansen and Zhu have triggered an ongoing debate regarding the validity of some of the conclusions drawn from the 'Kepler' sample (Sandford et al., 2019; Weiss & Petigura, 2020; Murchikova & Tremaine, 2020; Gilbert & Fabrycky, 2020). While taking a stance in this debate is beyond the scope of this thesis, I proceed by noting the potential biases in the 'Kepler' sample and discuss any possible implications that they could have on the results from this work in chapter 8. The gap in information due to the lack of detected planets below the mass of Neptune, M_{Nep}, is likely to be filled by next generation exoplanetary surveys such as NASA's Transiting Exoplanet Survey Satellite (TESS), which is expected to detect over $\sim$ 10 000 exoplanets, among which about 1000 will be of terrestrial mass (Ricker et al., 2015). Another ongoing mission is ESA's CHaracterising ExOPlanet Satellite (CHEOPS), which is set to provide first estimates or improvements of planatary radii using the transit method (Benz et al., 2020).

In order to investigate the properties of observed and confirmed exoplanets, I have opted to use a parameter-limited sample in which all planets have estimates for their mass and radius, henceforth referred to as the MR-sample. This yields a data set consisting of 550 planets (NASA Exoplanet Archive, 2020). Since the mass and radius of a planet requires detection through at least different two detection methods, there will be a bias towards planets that can be detected with the radial velocity method. Since detection depends on a sufficiently strong gravitational interaction between planet and host star (Wright & Gaudi, 2013), the sample thereby mainly consists of giant planets, i.e. planets with masses larger than 0.3 Jupiter masses, M_J. Looking at the distribution of masses and semi-major axes for the planets in the sample in figure 3.1, there evidently is a surplus of massive planets

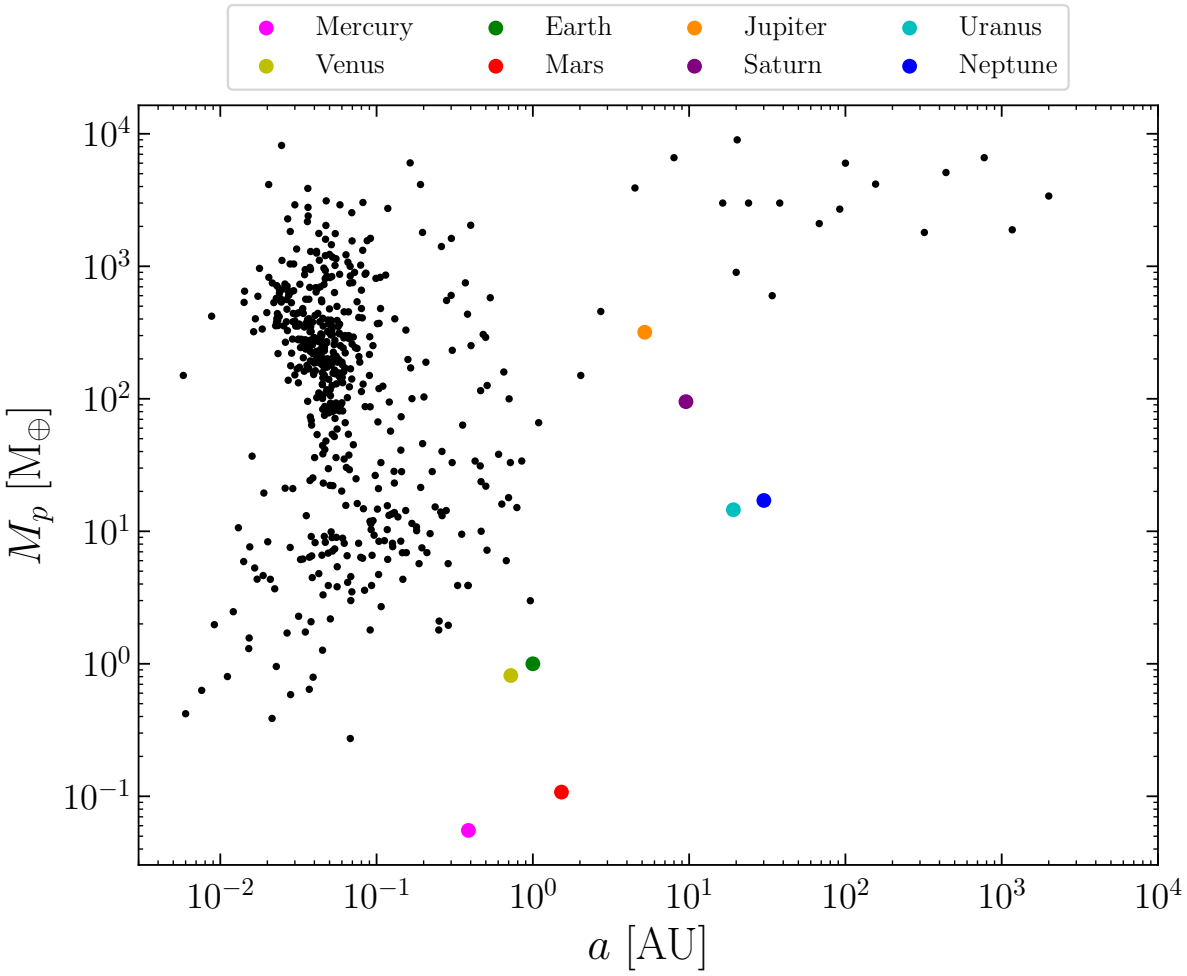

Figure 3.1: The mass as a function of semi-major axis for confirmed exoplanets from the NASA exoplanet archive, as well as the Solar System planets. Note that this distribution is strongly biased towards giant planets that are easy to detect.

orbiting their stars on short-period orbits[1]. The incompleteness is further confirmed by including the masses and semi-major axes of the Solar System planets, showing a lack of terrestrial planets, ice giants such as Uranus and Neptune and Jupiter analogues. Data on the properties of the Solar System planets for this and future plots in this chapter have been taken from Williams (2019).

The reason why I still opted to use this sample as a reference for the properties of exoplanetary system will become more evident further on, e.g. in sections 5.1.3 and 5.4.1. To summarise the reasoning briefly, a planetary system with multiple planets is more likely to have planet-consuming events if it has planets with extreme mass ratios $M_{\mathrm{p},1}/M_{\mathrm{p},2}$,

[1] *Short-period orbits* have small semi-major axes, putting the planets near their host star, while *wide orbits* have large semi-major axes.

which speaks to planet consumption being more common in exoplanetary systems with e.g. a giant planet and a terrestrial planet or super-Earth, which are planets with masses $M_\oplus < M_p < M_{Nep}$. Hence, the systems of main interest will have at least one giant planet present. Since the short-period orbits of the giants may be a consequence of dynamical evolution (Dawson & Johnson, 2018), which I discuss more in detail in section 3.6, it is not certain that this distribution accurately represents the initial semi-major axes for these planets after the depletion of the protoplanetary disk that they formed in. What is important however, is that the systems in which these giants have been observed are in fact able to produce massive planets. I further discuss the occurrence of giant planets in the upcoming section. Systems with *cold Jupiters*, which are giants with $a \gtrsim 1$ AU seem to often host super-Earths as well (Zhu & Wu, 2018; Bryan et al., 2019). Hence, such systems are likely to host planets with extreme mass ratios. One explanation for this is that massive enough planets migrating through protoplanetary disks can open up a gap in the disk, effectively quenching the flow of pebbles inwards towards the host star which can limit the mass growth of inner planets (Lambrechts, Johansen, & Morbidelli, 2014). Given that I mainly considered the orbital elements of the planets at the onset of dynamical evolution, I had no idea of the initial configurations of the systems that are planet-consuming and if they in the end would produce systems with giants on short-period orbits. Hence, the systems in the data set of choice still provide key information about the properties of the relevant planets and the stars that are able to host giants.

3.1 Multiplicity of planets in exoplanetary systems

Modern surveys using the most common methods for detecting planets indicate that the probability of a random star within the mass range $0.5\ M_\odot \leq M_\star \leq 1.2\ M_\odot$ to host at least one planet is ~ 1 (Winn & Fabrycky, 2015). However, due to most of the planet detection techniques being biased towards planets of masses larger than M_{Nep}, there is a lack of information regarding the average number of planets within exoplanetary systems (Winn & Fabrycky, 2015). Nevertheless, as seen in figure 3.2, a significant fraction of the systems within the MR-sample host more than one planets. While a majority of the 'Kepler' systems found through the transit method appear to host a single planet, biases inherent in the observational technique (Kipping & Sandford, 2016) and treatment of data in the pipeline that disfavours multiple detections (Zink, Christiansen, & Hansen, 2019) indicate that the multiplicity in many systems has been underestimated. This apparent existence of two populations of planets within observed exoplanets, where one consists of systems with lower mass multiple planets of low mutual inclination and the other of systems with a single planet or multiple high mutual inclination planets of varying masses, is known as the *'Kepler' dichotomy* (Johansen et al., 2012).

For a sample consisting of the planetary systems of 1537 host stars of spectral classes F, G and K from the 'Kepler' mission, Sandford, Kipping, & Collins (2019) used a statistical approach to infer that 50% of the systems they investigated most likely has one or more

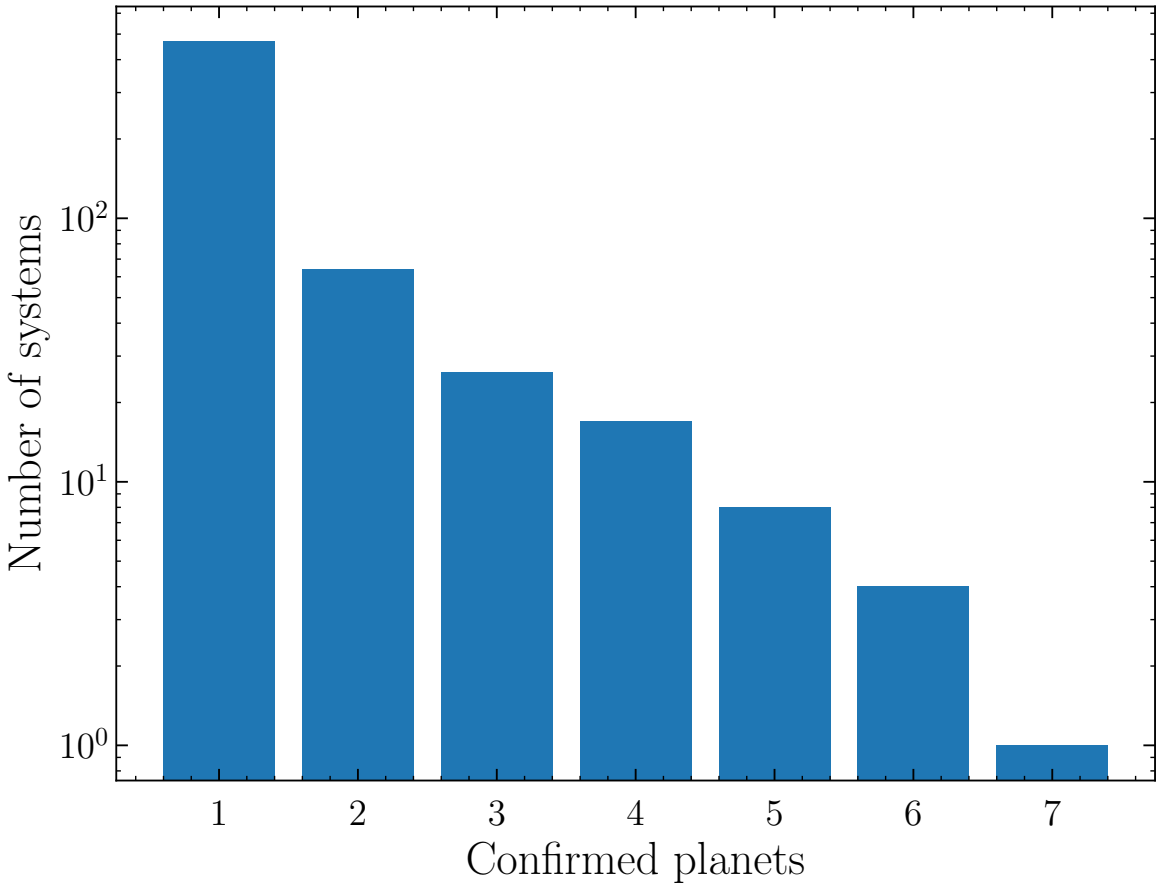

Figure 3.2: Plot showing the multiplicity of the observed and confirmed exoplanetary systems in the parameter-limited MR-sample. There is a clear trend where single planet systems are dominant, but this effect can be a product of observational bias in the 'Kepler' systems (Zink, Christiansen, & Hansen, 2019).

additional undetected planet(s). Hence, a surplus of single planet exoplanetary systems discovered by 'Kepler' probably host multiple planets. Since chaotic dynamical evolution within a planetary system will lead to the loss of planets, the initial number of planets created in a system may be even larger. Moreover, multiple planets and clustering is favoured over single planet systems given the 'Kepler' data (He, Ford, & Ragozzine, 2019).

3.1.1 Giant planet occurrence

When it comes to giant planets, they seem to be more common around stars of high mass (Johnson et al., 2010) with high metallicity (Sousa et al., 2011). Nevertheless, about $\sim 10-15\%$ of Solar-type stars have gas giants with $M_{\rm p} \gtrsim 50-100$ $\rm M_{\oplus}$ and despite the large proportion of short-period orbits in the MR-sample, a majority of discovered giant planets orbit at distances $a_{\rm p} \gtrsim 1$ AU (Cumming et al., 2008; Mayor et al., 2011; Fernandes

et al., 2019). Additionally, $\sim 25 - 30\%$ of exoplanetary systems that contain a gas giant will host additional giant planet companions (Wright et al., 2009; Wittenmyer et al., 2020). Among these systems, a surplus of the host stars have super-Solar metallicities (Buchhave et al., 2018). Furthermore, the cold Jupiters orbiting these high metallicity stars have a broader distribution of eccentricities (Winn & Fabrycky, 2015). Hence, chaotic dynamical evolution could be more common in super-Solar metallicity stars. As for the initial orbital configuration of giant planets, there is still much to be learned from the limited understanding regarding the formation history of distant giant planets since they undergo substantial migration through the protoplanetary disk (Johansen & Lambrechts, 2017). Nevertheless, massive protoplanetary disks with a high flux of pebbles can consistently produce multiple cold Jupiters, which is also consistent with the production of lower mass planets interior to their orbits due to pebble flux quenching (Lambrechts et al., 2019; Bitsch et al., 2019; Wimarsson et al., 2020).

3.2 Orbital elements of observed planetary systems indicate scattering events

Exoplanets observed through the radial velocity method show a rich distribution of eccentricities. Merely looking at the distribution of eccentricities and semi-major axes for the planets in the MR-sample in figure 3.3, a large fraction of the population has orbital eccentricities larger than zero and a few planets with $a_{\mathrm{p}} > 0.2$ AU have extreme eccentricities between 0.8 and 0.9. There is an indication that the eccentricity increases with orbital distance from the host star as well, which can be attributed to *tidal circularisation*, where a planet on an eccentric and/or wide orbit loses angular momentum and energy through tidal interactions with the host star, putting it on a more circular and shorter period orbit (Winn & Fabrycky, 2015). This effect becomes relevant for orbits with $a_{\mathrm{p}} < 0.2$ AU, which explains the lack of highly eccentric orbits with small semi-major axes. Since planets form in protoplanetary disks that effectively dampen eccentricities (Nelson et al., 2000), keeping the orbit circular, some mechanism is needed that can explain the large eccentricities of some planets that reach values up to 0.8 and 0.9 after depletion of the protoplanetary disk.

An important feature of the distribution of eccentricity is that it seems to be heavily coupled to the multiplicity of the planets in the system both according to analysis of observational (Wright et al., 2009) and synthetic (He et al., 2020) data. Planets within planetary systems with multiple planets have lower eccentricities and mutual inclinations (Tremaine & Dong, 2012; Johansen et al., 2012) while planets within systems where only one planet has been confirmed are more often highly eccentric and inclined to the rotational plane of the host star. Given that a large fraction of the single planet systems are likely to host additional planets and that the rich eccentricity distribution can be modelled well through planet–planet interactions within multiple planetary systems (Davies et al., 2014), it seems that the distributions of orbital elements of planets are highly dependent on the dynamical

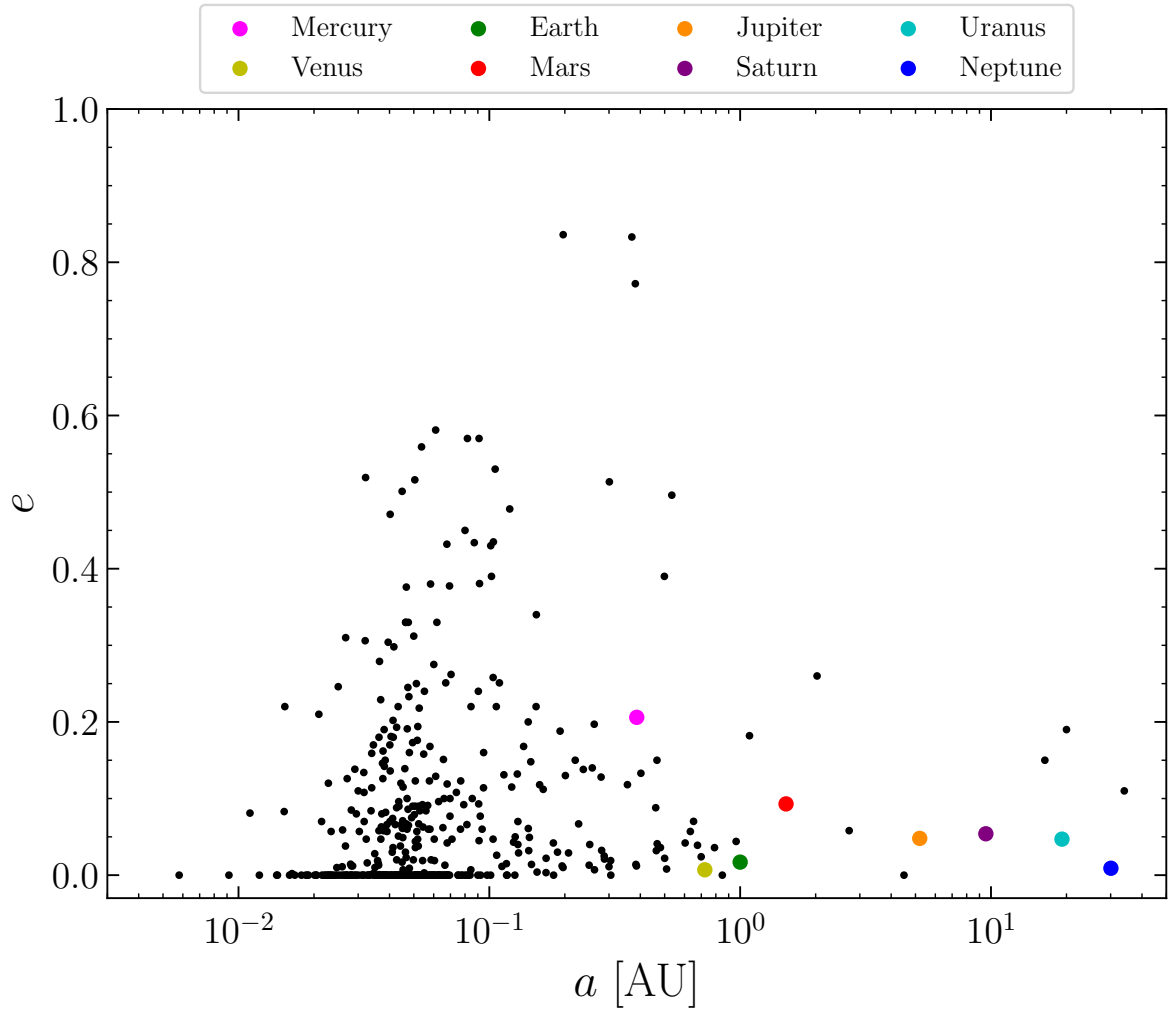

Figure 3.3: The eccentricity as a function of semi-major axis for confirmed exoplanets from the NASA exoplanet archive, as well as the Solar System planets. Note the difference in limits on the x-axis from figure 3.1, which is due to the lack of information of the eccentricity for wide orbit giant planets.

history of their system. Hence, one of the possible explanations for the 'Kepler' dichotomy is that the singles on eccentric and inclined orbits originally were formed in a multiple planetary system with several gas giants that dynamically evolved in a manner that led to excitation or disruption of orbits, making the observed planets appear as single in transit surveys (Pu & Wu, 2015; Mustill, Davies, & Johansen, 2017). Another hypothesis is that the dichotomy is created in the early stages of planet formation, where the formation of an outer giant planet suppresses the growth of detectable planets above terrestrial masses within its semi-major axis, creating inherent single planet systems (Johansen et al., 2012). This creates the hierarchical distribution of mass among the planets that we observe in the Solar System, where the low-mass rocky planets are situated closer to the star than the

giant planets. Recently, Bitsch, Trifonov, & Izidoro (2020) found that inefficient dampening of orbital eccentricities during the planet formation phase allows for early close encounters between planets, effectively reproducing the observed eccentricity distribution of massive giant planets. Their simulation results also indicate that highly eccentric massive giant planets above 5 M_J are less likely to host super-Earths interior to their orbits, while less massive giant planets on nearly circular orbits are more likely to harbour super-Earths. Furthermore, He et al. (2020) found that the 'Kepler' dichotomy in fact might be explained by a single population with a broad distribution of mutual inclinations. In agreement with Bitsch, Trifonov, & Izidoro, they concluded that planetary systems with more planets after the depletion of the protoplanetary disk will have lower median eccentricities and mutual inclinations.

In this thesis, I am interested in systems that are hierarchical in mass, undergoing rich dynamical evolution and thereby adopt the view that my systems of interest are created around FGK stars with multiple giant planets exterior to one or more terrestrial planets. Furthermore, I assume that the initial orbits are circular and of low mutual inclinations that proceed to evolve chaotically, leading to the loss of one or more planets.

3.3 Orbital spacing in multiple planetary systems

As I explain in more detail in chapter 4, the timescale for unstable dynamical evolution of a planetary system is highly dependent on the separation between planets (Chambers, Wetherill, & Boss, 1996). Studies of 'Kepler' systems with multiple planets indicate that planets have uniform spacing ratios in terms of their semi-major axes. Furthermore, this spacing is large enough for the planetary system to be considered dynamically stable (Weiss et al., 2018; Weiss & Petigura, 2020; Gilbert & Fabrycky, 2020; He et al., 2020). Nevertheless, this is one of the observational patterns for the 'Kepler' systems that are a source of controversy due to potential detection biases (Zhu, 2020; Murchikova & Tremaine, 2020).

As previously stated, I proceed by simply assuming that this is a real effect and will address the potential errors this could produce in my results at a later stage. The key consequence of this behaviour of exoplanets for the work in this thesis is that observation of multiple planetary systems with small separations between their planets is highly unlikely. This is due to the fact that planets with small separations evolve on very short timescales as their dynamical interactions lead to changes in orbital elements that grow with time. They are thus classified as dynamically unstable, as I discuss further in section 4.1.5. Since apparent single planet systems have on average more eccentric orbits that are more inclined with the respect to the rotational plane of their host star, there is an additional indication that these systems had a larger intrinsic number of planets that were closely spaced and thus evolved by exciting or disrupting several orbits. Due to the fact that this evolution occurs on a short timescale as compared to the lifetime of the planetary system (Davies et al., 2014), it is highly unlikely that any closely packed systems would be observed before they

have completed their dynamical evolution.

3.4 Exoplanet properties

To create a synthetic configuration of planets with given properties, I wanted to consistently be able to couple the mass of the planets to a given radius and density. This was easiest done by using an empirically and statistically derived Mass-Radius relation (MR-relation). Given the current lack of data for terrestrial planets and limited data for super-Earths and mini-Neptunes, as well as the diverse range of bulk compositions for planets below 30 $M_\oplus$ (Jontof-Hutter, 2019), it is challenging to develop a strong empirical relation for low-mass exoplanets. In this thesis, I have employed a semi-empirical formula from Zeng, Sasselov, & Jacobsen (2016). They made use of the fact that the most well-studied rocky planet in the Universe is the Earth, whose composition has been carefully modelled from seismic measurements, which resulted in the Preliminary Reference Earth Model (PREM: Dziewonski & Anderson, 1981). By extrapolating the PREM equations of state for the interior of the Earth, Zeng, Sasselov, & Jacobsen produced an MR-relation dependent on the Core Mass Fraction (CMF) of rocky exoplanets given by

$$\left(\frac{R_\mathrm{p}}{R_\oplus}\right) = (1.07 - 0.21 \times \mathrm{CMF}) \left(\frac{M_\mathrm{p}}{M_\oplus}\right)^{1/3.7}. \tag{3.1}$$

As for the CMF value, it can be directly computed from equation (3.1) for a planet with known M_p and R_p. For example, the Earth has a CMF of 0.33 according to the formula. To facilitate the modelling of exoplanets in this study, I have simply assumed that all planets below a limiting mass for rocky planets have a CMF equal to that of Earth.

To model the planets that are not rocky, I have made use of the log-quadratic empirical MR-relation for planets in the mass range 30 $M_\oplus \leq M_\mathrm{p} \leq$ 3000 $M_\oplus$ from Tremaine & Dong (2012)

$$\log\left(\frac{R_\mathrm{p}}{R_\mathrm{J}}\right) = 0.087 + 0.141 \log\left(\frac{M_\mathrm{p}}{\mathrm{M_J}}\right) - 0.171 \left(\frac{M_\mathrm{p}}{M_J}\right)^2. \tag{3.2}$$

I have plotted the resulting joint MR-relation in figure 3.4 along with the masses and radii for the population in the MR-sample, as well as the Solar System planets. I have chosen the transition mass of $M_\mathrm{p} = 2.62\ M_\oplus$, which is the mass value where these two relations intersect. While the joint MR-relation provides a good fit for the terrestrial planets below the intersection and for gaseous planets above this limiting mass, there is a lack of information regarding the apparent bimodal population of planets in the range $2.62\ M_\oplus < M_\mathrm{p} \lesssim 20\ M_\oplus$, showing the aforementioned compositional diversity of low-mass exoplanets.

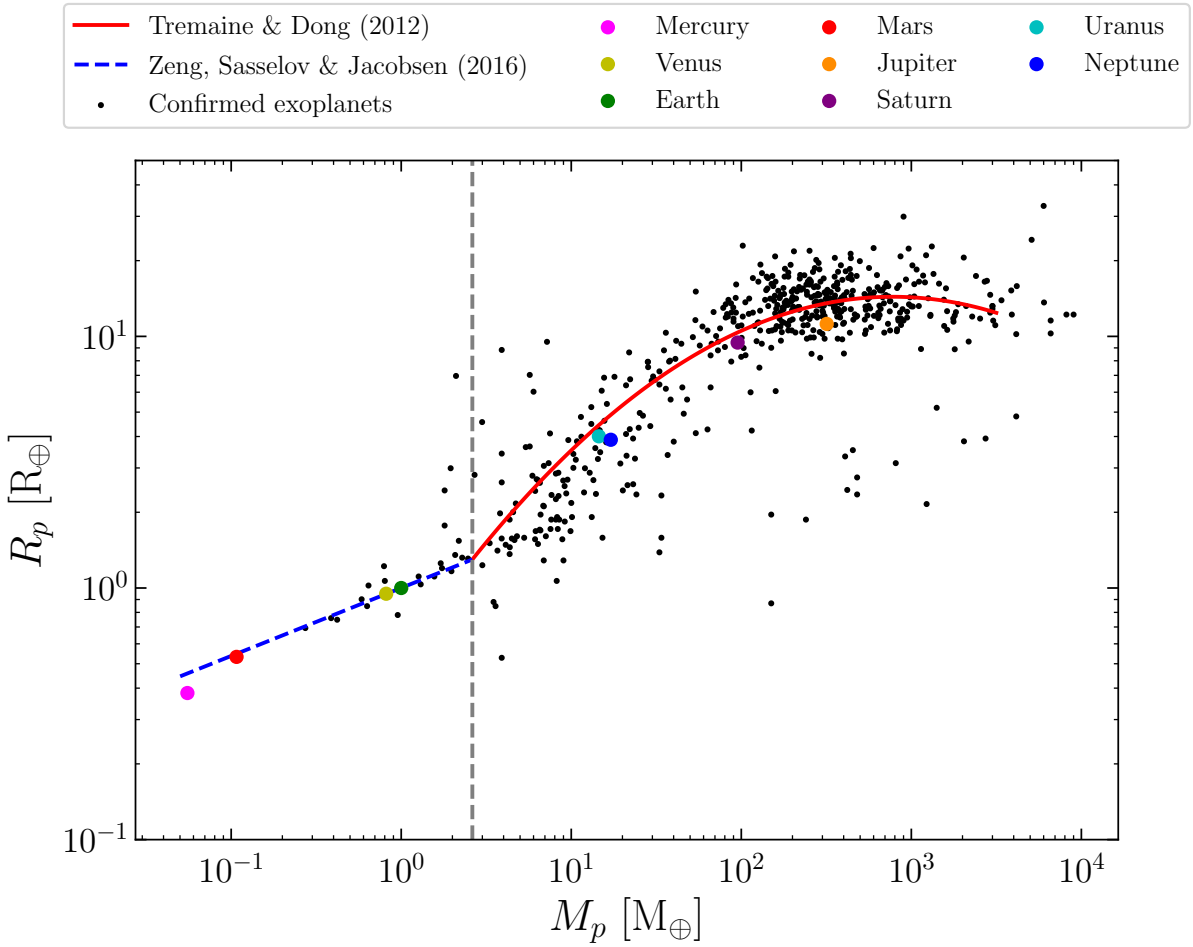

Figure 3.4: The mass as a function of radius for confirmed exoplanets from the NASA exoplanet archive, as well as the Solar System. I have also plotted the joint mass-radius relation I used in the project.

Hence, the use of this joint MR-relation introduces a strong assumption that all planets below 2.62 M$_\oplus$ are rocky, while all planets above said mass are gaseous, which is not the case (Jontof-Hutter, 2019). I note that this issue could be avoided by using the bimodal low-mass exoplanet MR-relation from Otegi, Bouchy, & Helled (2020), which became available late during the thesis work or the more complex joint MR-relations from Bashi et al. (2017) or Neil & Rogers (2020). Nevertheless, I chose to commit to my simplistic joint relation since it still provides a reasonable fit for the MR-sample. Any implications for the results are addressed in chapter 8.

3.4.1 Metal content of exoplanets

While giant planets are over ~ 100 times more massive than rocky exoplanets, the difference in planetary metallicity of these two planet types is not as significant. The low density

of giant planets, as inferred from the MR-relation from figure 3.4, hints at a significant compositional difference. Planet formation theory indicates that the most massive planets form by accreting a heavy gaseous envelope onto a rocky core that typically has a mass of at least ~ 10 $M_\oplus$ (Johansen & Lambrechts, 2017). By using the measured masses and radii of several giant exoplanets from transit and radial velocity observations and employing a thermal and structural evolution model, Thorngren et al. (2016) obtained an estimate of the heavy metal content of 47 giant planets at $a_p \gtrsim 0.1$ AU. Many of these specimens display a high metallicity, indicating that many of the giants have cores more massive than 10 $M_\oplus$. Ginzburg & Chiang (2020) further showed that this result is consistent with collisions and mergers of multiple cores before the onset of runaway gas accretion during the early planet formation stage. Moreover, results from Wimarsson, Liu, & Ogihara (2020) indicate that mergers of multiple cores migrating through the protoplanetary disk speed up the formation timescale of giant planets. Thorngren et al. (2016) also used their model to infer that Jupiter has a core mass of around 37 $M_\oplus$, meaning that the core of Jupiter also could have formed through the collision of multiple protoplanets during the early evolution of the Solar System. Given that the Jupiter-mass planets from the MR-relation in equation (3.2) are less dense than Jupiter, I assumed a more conservative heavy metal content of 20 $M_\oplus$ for giant planets considered in this thesis. Furthermore, I considered completely rocky planets, i.e. beneath 2.62 $M_\oplus$, to have a metallicity of $Z_p = 1$. As for the more massive cases of 3 $M_\oplus$, 10 $M_\oplus$ and 30 $M_\oplus$ which are assumed to have gaseous envelopes, I opted for a core mass of 2.5 $M_\oplus$. This was motivated by the core mass threshold for gas accretion in in-situ formation models for low-mass planets (Jontof-Hutter, 2019).

3.5 Properties of host stars

Given that the goal of this thesis is to couple the results from the dynamical modelling of chaotic planetary systems to the effect of planets being consumed by their host stars, it is also important to understand which type of stars will host giant planets. Hence, I used the properties of the host stars from the MR-sample. The NASA Exoplanet Archive assigns masses to the host stars using their Tycho catalogue B-V or V-K colours (Høg et al., 2000) in combination with the empirical mass-colour relationships from Gray (1992) and Henry & McCarthy (1993). It is noteworthy that these relationships assume Solar metallicities, so the masses for stars with higher or lower metallicities will be systematically shifted from their true values. As for the estimated stellar radii, the NASA Exoplanet Archive has computed them using the measured effective temperatures and luminosities of the stars in the expression

$$R_\star^2 = \frac{L_\star}{4\pi\sigma_{\rm SB} T_{\rm eff}^4}, \tag{3.3}$$

where $\sigma_{\rm SB}$ is the Stefan-Boltzmann constant. I only selected stars with relative fractional errors in the mass or radius that are less than 0.1.

The mass-radius relationship I employed to compute radii for synthetic stars in this work is valid for Zero Age Main Sequence (ZAMS) stars and is an empirically derived formula from Tout et al. (1996) that holds for metallicities $Z_\star = 0.0001$ to 0.03. The radius is given by

$$R_\star = \frac{\kappa_0 M_\star^{2.5} + \kappa_1 M_\star^{6.5} + \kappa_2 M_\star^{11} + \kappa_3 M_\star^{19} + \kappa_4 M_\star^{19.5}}{\kappa_5 + \kappa_6 M_\star^2 + \kappa_7 M_\star^{8.5} + M_\star^{18.5} + \kappa_8 M_\star^{19.5}}. \tag{3.4}$$

The values of the coefficients κ_k are dependent on the metallicity of the star and can be computed using the following relations

$$\kappa_k = c_0 + c_1 \log_{10}\left(\frac{Z_\star}{Z_\odot}\right) + c_2 \log_{10}\left(\frac{Z_\star}{Z_\odot}\right)^2 + c_3 \log_{10}\left(\frac{Z_\star}{Z_\odot}\right)^3 + c_4 \log_{10}\left(\frac{Z_\star}{Z_\odot}\right)^4, \tag{3.5}$$

where the values of the constants c_k can be found in table 2 of Tout et al. (1996).

The resulting MR-relation for host stars has been plotted together with the measured masses and estimated radii in figure 3.5. The colours of the data points indicates the host star metallicity. From the plot, there is an apparent discrepancy in the empirical ZAMS MR-relation and the measured MR data points, especially for the higher mass stars. This is due to the fact that many of the observed stars have already left the main sequence. Moreover, since the time spent on the main sequence is proportional to the mass of the star (Prialnik, 2000), the discrepancy will be more pronounced for higher mass stars. Nevertheless, the ZAMS approximation is still appropriate due to the fact that the timescale for the evolution ~ 10 Myr of the dynamically unstable planetary system is less than the time it takes for a star to leave the MS (Davies et al., 2014). Hence, I expected the unstable systems of interest in this thesis to finish dynamically evolving before entering their post-MS phases.

Due to the aforementioned study of Sousa et al. (2011) indicating that giant planets are more likely to orbit stars of higher metallicity, I expect the MR-sample to mainly contain super-Solar metallicity stars. Figure 3.6, depicting the measured metallicity of the host star as a function of its estimated mass, shows that this is indeed the case.

3.6 Hot Jupiters and their origin

From the distribution of masses and semi-major axes for the MR-sample, it is clear that many of the observed giant exoplanets in the mass range $0.25\ \mathrm{M_J} \leq M_\mathrm{p}\sin(i) \leq 20\ \mathrm{M_J}$ are on short-period orbits. This phenomenon has given rise to the term 'hot Jupiter', which refers to massive giants with an orbital period of 10 days or shorter ($a_\mathrm{p} \lesssim 0.1$ AU). While they are highly abundant in the MR-sample, only $\sim 1\%$ of Solar-type stars host a hot Jupiter (Johnson et al., 2010). Nevertheless, their existence poses a significant challenge

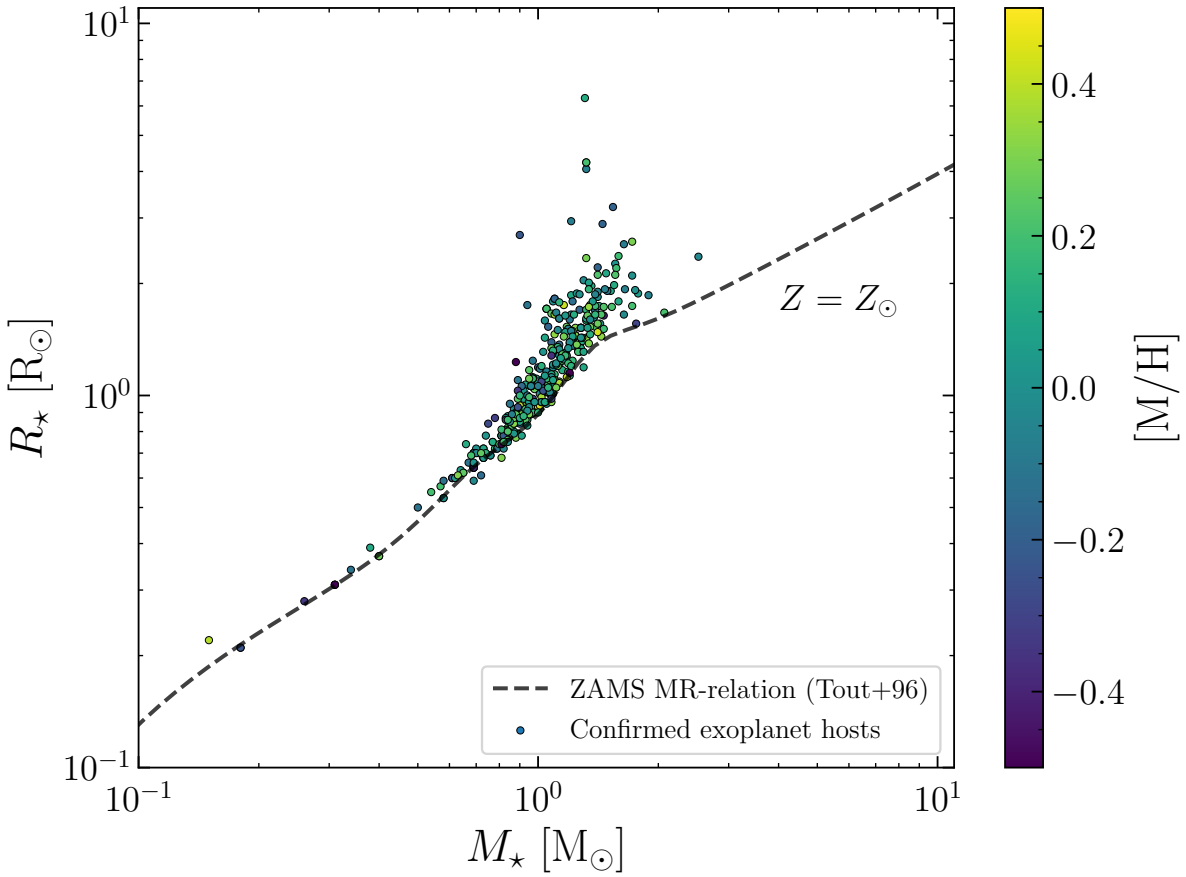

Figure 3.5: The stellar mass-radius relation from Tout et al. (1996) that I employed in the project plotted together with the masses and radii of the observed host stars for the exoplanets in figure 3.4. The colour gradient indicates the stellar metallicities.

for modelling the dynamical evolution of planetary systems. There are three main theories that could explain how hot Jupiters come to be (Dawson & Johnson, 2018)

1. **In-situ formation:** Hot Jupiters form at their present short-period orbits.
2. **Gas disk migration:** Some gas giants migrate through the protoplanetary disk due to the force exerted on them by torques from the gaseous disk component and end up at low semi-major axis orbits.
3. **Tidal circularisation:** Cold Jupiters on highly eccentric orbits tidally interact with the host star which circularises the orbit at a lower semi-major axis.

The current understanding of giant planet formation is that planetary embryos are formed far out in the protoplanetary disk when a planetesimal increases in mass through pebble accretion and/or collision, while it continuously migrates through the disk. If the embryo forms at too small a distance from the host star, it will not to reach its pebble isolation

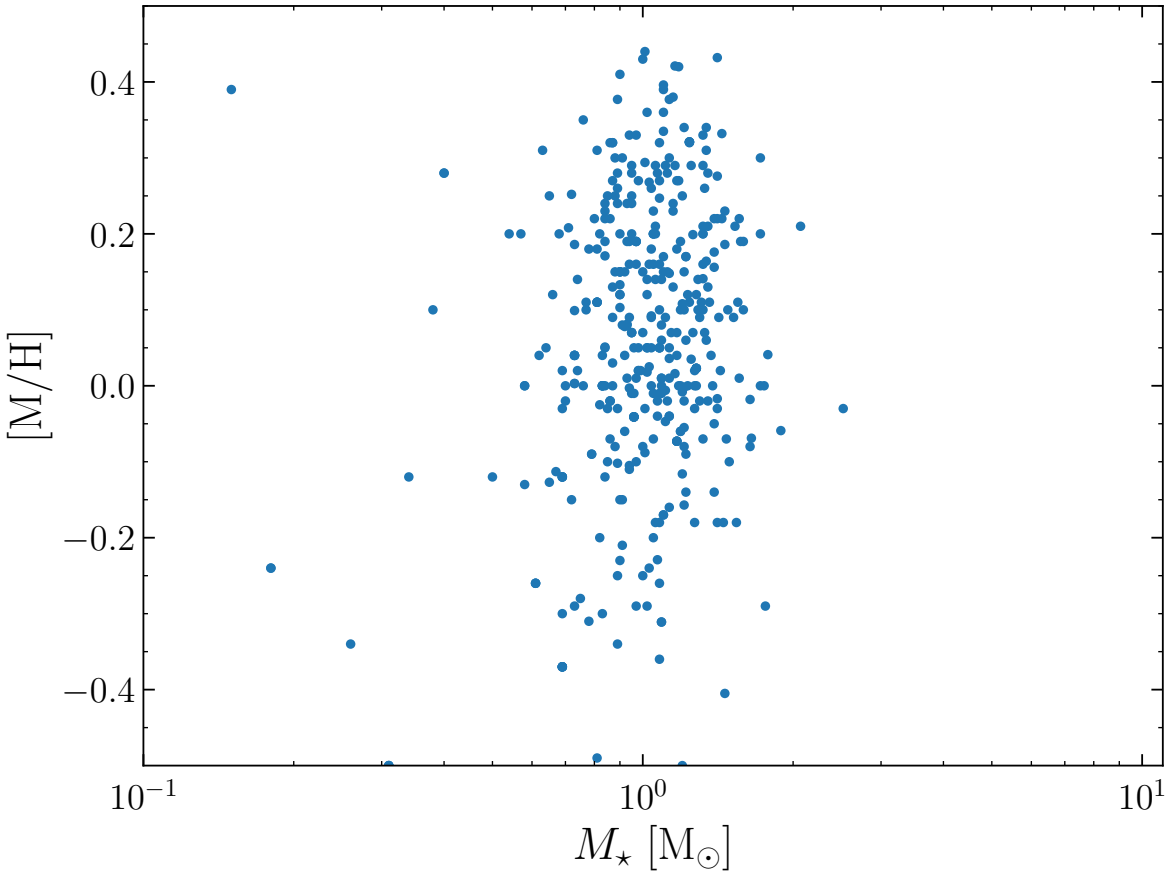

Figure 3.6: The stellar mass, as well as stellar metallicity for the host stars of the exoplanets in the mass-radius relation of figure 3.4.

mass at an early stage. Again, reaching pebble isolation mass will prevent pebbles from reaching the parts of the system interior to the orbit and triggers slow migration (Bitsch et al., 2015; Johansen & Lambrechts, 2017). Therefore, if it does not reach its isolation mass, the embryo will not be able to grow to its observed mass before reaching its final semi-major axis of $a_\mathrm{p} < 0.1$ AU. Hence, in situ formation is highly unlikely. Nevertheless, neither gas disk migration nor tidal circularisation can solely account for the population of giant planets, meaning that the full formation history of hot Jupiters is most probably given by a combination of the two (Dawson & Johnson, 2018).

As argued in the previous sections, the picture of intrinsic planetary systems I have adopted in this thesis is based on the assumption that my systems of interest initially consist of several cold Jupiters outside the orbits of one or more terrestrial planets. As discussed in the next chapter, such a configuration is likely to produce giants on highly eccentric orbits that could be tidally circularised and thus create a hot Jupiter.

Chapter 4

Dynamical evolution of multiple planetary systems

The apparent differences between the configurations of observed exoplanets and the planets in our very own Solar System hint at an underlying process that can significantly alter the architecture of planetary systems. Long-term gravitational interactions between planets in planetary systems after the conclusion of the planet formation stage have been made subject to a variety of studies in the past two decades and provide a plausible pathway to the diverse distribution of observed orbital eccentricities (e.g. Chatterjee et al., 2008; Ford & Rasio, 2008; Jurić & Tremaine, 2008; Raymond et al., 2010, 2011). In this chapter, I go through the fundamental mechanisms of planet–planet interactions and how they lead to the dynamical evolution of planetary systems that ultimately ends in excitation and/or disruption of planetary orbits.

4.1 The stability of planetary systems

Due to gravitational interactions between planets and matter in protoplanetary disks, orbits in multiple planetary systems are likely to initially be coplanar and nearly circular after the planetary formation stage has concluded and the disk has been depleted of material (Nelson et al., 2000). Hence, the driving process behind the observed excited orbits of exoplanets must have occurred sometime in between the culmination of the protoplanetary disk phase and today. Gravitational interactions between planets lead to the exchange of angular momentum and/or energy that can significantly alter orbital elements. The energy is inversely proportional to the semi-major axis while the angular momentum is directly proportional to the tangential velocity of the orbit. Hence, the angular momentum of an orbit is related to the eccentricity of an orbit. A completely circular orbit will have a maximal angular momentum for a given semi-major axis, while a highly eccentric orbit with $e \lesssim 1$ will have little to no angular momentum. Therefore, the removal of angular momentum from a planet will increase its eccentricity allowing it to move further outwards

or inwards in the system, given that the minimum and maximum distances from the host star is given by $r_{\rm min} = a(1-e)$ and $r_{\rm max} = a(1+e)$, respectively. Henceforth, I will refer to decreasing values of $r_{\rm min}$ as *radial incursions* and increasing values of $r_{\rm max}$ as *radial excursions*. When it comes to the exchange of energy between planets, gaining energy makes the planet less bound to the system, which follows from equation (2.27) where $E \to 0$ when $a \to \infty$.

An important property of the total angular momentum and energy in a planetary system in the rest frame of the host star is that it will be conserved among the bodies in the system, assuming that they do not undergo interactions with an external celestial object or dissipate energy in tides or collisions. Hence, any exchanges of angular momentum and energy will be restricted to occur between the planets unless they end up on very short-period or highly eccentric orbits that allow for strong gravitational interaction with the host star. Given the nature of gravitational forces, the strength of the interaction between two bodies is highly dependent on their separation. In turn, the strongest of gravitational interactions, and thereby exchanges of angular momentum and energy, occur when two planetary orbits are crossing. The separation between two planets in a planetary system is usually measured in terms of mutual Hill radii given by

$$R_{\rm Hill,m} = \left(\frac{M_k + M_{k+1}}{3M_\star} \right)^{1/3} \frac{a_k + a_{k+1}}{2}, \tag{4.1}$$

where M_k and a_k are the planetary mass and semi-major axis of its orbit, respectively. Two planets within one Hill radius of each other can undergo gravitational encounters that are strong enough to significantly alter the trajectory of one or both of the planets. When two planets are within such a distance of each other, it is known as a *close encounter*. As for the gravitational encounter that leads to a change in trajectories, I again refer to such an event as a *planet–planet scattering*.

The separation between two planets is thus a good measure of the stability of their system. If the orbits of two planets will never cross, they are referred to as *Hill stable*. Gladman (1993) showed analytically that a two-planet system with initially circular and coplanar orbits is Hill stable if

$$\Delta = \frac{(a_2 - a_1)}{R_{\rm Hill,m}} \gtrsim 2\sqrt{3}. \tag{4.2}$$

For systems with three or more planets there exists no such analytical criterion, but Hill stability is still commonly used as a reference for the stability of two adjacent planets. The timescale for stability is also highly related to the separation between the planets, as well as the mass ratio between the planet and the host star $q_\star \equiv M_{\rm p}/M_\star$. Chambers, Wetherill, & Boss (1996) found through numerical experiments that the time before the first close encounter, $t_{\rm CE}$, in a system of three equal-mass planets is well approximated by

$\log(t_{\rm CE}) = b\Delta + c$, where b and c are constants. Moreover, their investigation showed that such systems will almost always be unstable if the planets are separated such that $\Delta < 10$. For 'Kepler' systems, the spacing between planets has a lower limit of $\Delta \sim 10$ (Weiss et al., 2018).

4.1.1 Secular theory

For stable systems, there is also a continuous exchange of angular momentum and/or energy, but the magnitude of these exchanges are not large enough to induce a large change in orbital elements that could trigger further instability. By averaging the small changes in orbital elements due to gravitational interactions for a fixed Keplerian orbit over a long period of time, Lagrange and Laplace formulated the *secular theory* (Davies et al., 2014). This functions as a first order approximation for the evolution of orbits in multiple planetary systems, where the semi-major axes remain constant while the orbital eccentricities and inclinations oscillate with periods of $\sim 10^5$ yr. Since there are no long-term trends for this theory, the secular approximation easily breaks down when the interplanetary separations are smaller, allowing for an oscillation amplitude that grows over time.

4.1.2 Mean motion resonance

Another instance where the secular approximation breaks down is in the presence of Mean-Motion Resonance (MMR) (Davies et al., 2014). Said effect occurs when the orbital periods of two planets in a given system are a simple integer ratio of each other. For example, in a 2:1 MMR, the planet with the shorter period will complete two revolutions when the longer period planet has completed one revolution. The dynamical behaviour of a planetary system can change completely under the influence of MMRs, as they can become destabilised due to eccentricity and inclination oscillations increasing in amplitude over time. They can also become stabilised due to two planets on crossing orbits getting locked in an MMR where they will never undergo a close approach. Nevertheless, I did not include a discussion of MMRs in the analysis of dynamical evolution in this thesis due to time-restriction.

4.1.3 Angular momentum deficit

A more useful tool for quantification of instability within a planetary system with $N \geq 3$ bodies is the Angular Momentum Deficit (AMD) (Laskar, 1997, 2000), which is given by

$$\mathrm{AMD} = \sum_k \Lambda_k \left(1 - \cos(i_k)\sqrt{1 - e_k^2}\right), \tag{4.3}$$

where

$$\Lambda_k = \frac{M_k M_\star}{M_k + M_\star} \sqrt{G(M_k + M_\star) a_k} \tag{4.4}$$

is a constant for a planet k with mass M_k and an orbit with semi-major axis a_k, eccentricity e_k and inclination i_k around a host star with mass $M_\star$. The AMD gives insight in the total eccentricities and inclinations of the planetary orbits within a given system. As the name suggests, the AMD of a given planet provides a measure of its lack of angular momentum relative a reference plane in the planetary system. Therefore, being highly inclined to that plane can still yield a significant AMD for a completely circular orbit. Moreover, the AMD is a conserved quantity in the absence of MMRs and scattering, meaning that the total AMD available in a system can be interpreted as a dynamical temperature that will limit the possible outcomes for a system. Naturally, it can also be used to formulate a criterion for stability (Laskar & Petit, 2017). If the AMD is low enough in a system, there cannot be a rearrangement of AMD between the planets that yields orbit crossing and planet–planet scattering and the system can as a result be considered to be long-term stable.

4.1.4 Long-term stable planetary systems

A planetary system can be considered to be long-term stable if it has an instability timescale such that $t_{\mathrm{CE}} \sim \tau$, where τ is the lifetime of the system. In such a scenario, the Lagrange-Laplace secular approximation will hold. Nevertheless, it is difficult to assess whether or not a system will in fact remain stable for the entirety of its lifetime. For example, the Solar System is stable according to secular theory. However, for a full numerical integration of the dynamical evolution, there are cases where AMD can be transferred from the outer giant planets to the terrestrial subsystem, ultimately leading to large radial excursions and the crossing of orbits. I refer to long-distance exchange of AMD between planets as *action at a distance*. It is not possible to infer the exact evolution of a system using a numerical integration, but there still exists a small possibility that the Solar System could become unstable within a few Gyr (for a review see Davies et al., 2014, and references therein).

4.1.5 Evolution of Hill unstable planetary systems

In Hill unstable planetary systems, the small interplanetary separation allows for exchanges of angular momentum that grow in magnitude over time. Hence, the orbit of one planet will gradually become more eccentric, allowing for larger radial incursions and excursions in the system. In turn, the planet will have closer approaches with other bodies in the system, increasing the exchange of angular momentum and/or energy. Ultimately, the orbit will be eccentric enough to cause orbit crossing where planets can undergo close encounters. The number of orbits needed to trigger the first close encounter again depends strongly on the initial separation between the planets. For example, changing the separation between three

planets of $q_\star = 3 \times 10^{-5}$ from $\Delta = 4$ to $\Delta = 5$ will increase the number of periods to reach the first close encounter from $\sim 10^3$ to $\sim 10^6$ (Chambers, Wetherill, & Boss, 1996).

There are several possible origins for instability within a planetary system. The system can have an intrinsic instability after the depletion of the protoplanetary disk. However, even if the planets within a planetary system have large initial separations, there are external sources that can perturb their orbits, triggering instability. For example, such sources can be a passing star within a high number density stellar environment (Malmberg, Davies, & Heggie, 2011), passing through a molecular gas cloud (Kokaia & Davies, 2019) and scattering within minor body belts (e.g. Morbidelli et al., 2005; Tsiganis et al., 2005). Furthermore, the departure of a host star from the main sequence leads to mass loss from the stellar envelope that can destabilise a multiple planetary system (e.g. Debes & Sigurdsson, 2002; Veras et al., 2013; Voyatzis et al., 2013).

4.2 The Lidov–Kozai mechanism

An important dynamical mechanism is *Lidov–Kozai* oscillation which is an alternative way of putting planets on high-eccentricity orbits that does not require close encounters between planets. While the finding of this phenomenon is usually attributed to Lidov and Kozai, who discovered it separately in 1962, it was originally introduced by von Zeipel in 1910 (Ito & Ohtsuka, 2019). Nevertheless, I have opted to refer to the mechanism as Lidov–Kozai in this work. This mechanism involves a planet with a companion on a highly inclined orbit, either in the form of a star in a binary stellar system or another planet in a single star multiple planetary system. Since the scope of this work does not cover analysis of scattering in binary star systems, I only consider the Lidov–Kozai effect in the latter type of system. The highly inclined companion gravitationally perturbs the planetary orbit which induces large periodic changes in the orbital eccentricity and inclination due to exchange of angular momentum on a secular timescale. As a result, the Lidov–Kozai oscillations can put the perturbed planet onto a highly eccentric orbit, which in turn can induce orbit crossing and planet–planet scattering. Further, this mechanism provides another way of forming hot Jupiters as it can lead to tidal circularisation (Dawson & Johnson, 2018).

In a simple approximate solution, where I consider a test particle with negligible mass compared to a distant perturbing planet on orbits with a mutual inclination and low initial eccentricities that allow for Lidov–Kozai oscillations, the angular momentum will be constant

$$J = \sqrt{(1 - e^2)} \cos i_\mathrm{m} = \text{const.} \tag{4.5}$$

This relation shows that eccentricity can be exchanged for inclination as a conserved property during transfer of angular momentum between the two bodies. The critical inclination for Lidov–Kozai to be possible is given by the limit $\cos(i_\mathrm{crit}) > \sqrt{3/5}$, which yields solu-

tions of $i_{\rm crit} \approx 39.20°$ and $i_{\rm crit} \approx 140.77°$ providing a range within which such angular momentum exchange is possible (Naoz, 2016).

For non-negligible masses of the perturbed body, the above approximation will break down. These more complex scenarios are easiest modelled using numerical integration. Such studies have shown that the Lidov–Kozai mechanism can increase orbital inclinations above 90°, producing retrograde orbits (see Naoz, 2016, and references therein).

4.3 Outcomes of dynamical instability

After the onset of instability when two planetary orbits are crossing, the two planets will undergo planet–planet scattering events until the instability is resolved. During each encounter there will be an exchange of angular momentum and energy, altering the orbits of the two planets to some extent. The mechanisms that determine the strength of each scattering events are discussed in chapter 5. There are four main outcomes for a given planet that will conclude the phase of close encounters (Davies et al., 2014).

Assuming that the primary planet in the scattering survives, the single outcomes for the secondary planet[1] are:

1. Survival through scattering onto a non-crossing orbit.
2. Ejection from the planetary system.
3. Merger with another planet.
4. Collision with the host star.

I now go through each outcome in order.

Survival: While being scattered onto a non-crossing orbit means that the current planet–planet scattering phase has concluded, it does not guarantee that the planet survives the dynamical instability of the system. It may still reach a new crossing of orbits with one of the remaining planets in the system, or undergo changes in its orbit due to the Lidov–Kozai mechanism.

Ejection: A planet gains a significant amount of energy putting it on an orbit with $e \geq 1$ and $E \geq 0$, meaning it becomes unbound from the system.

Planet–planet merger: The two planets collide with each other and merge, leaving a more massive surviving planet behind. Commonly referred to as *merger* in this work.

Planet consumption: A planet with a large amount of AMD ends up on a highly eccentric orbit $e \lesssim 1$, putting it at a distance of $r_{\rm min} = a(1-e) \leq R_\star$. For $R_\star = {\rm R}_\odot$, a planet at 1

[1]Throughout this analysis of planet–planet scattering events, I refer to the most massive planet as primary and the least massive planet as secondary.

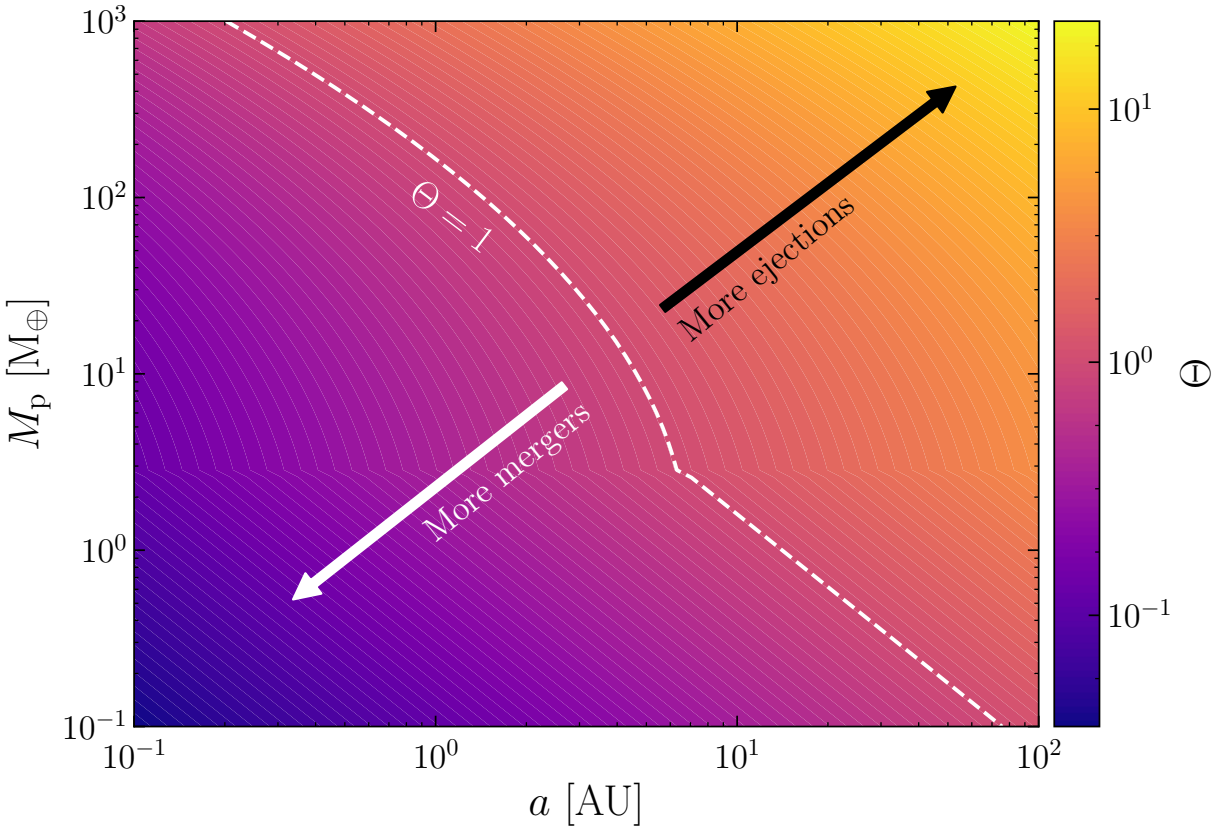

Figure 4.1: The Safronov number as a function of the planetary mass and the semi-major axis of its orbit. The dashed line indicates where in the system the surface and planetary system escape velocity are equal for various planetary masses.

AU needs an eccentricity of at least ~ 0.995 to be consumed by the host star. Henceforth, I will refer to an orbit with $r_\mathrm{min} \leq R_\star$ as a *planet-consuming orbit*.

4.3.1 The Safronov number

The outcome of a scattering event is partly governed by the location of the scattering event in the system and the relative masses and radii of the planets undergoing the encounter. A quantity that can be used to determine the favoured outcome is the Safronov number. This constant is a measure of the relative magnitude between the surface and planetary system escape velocities of the planet in the following formula

$$\Theta^2 = \left(\frac{M_\mathrm{p}}{M_\star}\right)\left(\frac{R_\mathrm{p}}{a_\mathrm{p}}\right)^{-1}. \tag{4.6}$$

If the Safronov number is larger than unity, the surface escape velocity is larger and the

scattering is thus more likely to resolve itself in an ejection. If instead the surface escape velocity is smaller than the system escape velocity, Θ will be less than unity and it will be more difficult to alter a planetary trajectory, which favours mergers (Ford & Rasio, 2008). Figure 4.1 shows a contour map of the Safronov number for a given combination of planetary mass, where the planetary radius is given by the MR-relation in section 3.4, and semi-major axis. For the combinations left of the dashed white line showing $\Theta = 1$, mergers are favoured while combinations to the left mainly lead to ejections. As can be interpreted from the map, ejection is highly favoured for massive low density planets while the high density low-mass planets most often will undergo mergers.

Chapter 5

Two-body analysis of planet–planet scattering

In order to gain a better understanding of the underlying physical processes in a scattering event between two planets in a multiple planetary system and in which scenarios I will get a planet–host star collision, I have used a simplified scattering scenario to semi-analytically evaluate the problem. In the system, there is a host star and two planets whose orbits are crossing. Due to the fact that it is not possible to solve a three-body scattering event analytically, I chose to isolate the scattering event by neglecting any gravitational interactions between the host star and the two planets. Hence, I only considered the exchange of energy and angular momentum that results from the work that the planets do on each other. Moreover, I further simplified the problem by ignoring any possible inclination of the orbits and focused on evaluating the two-body problem in two dimensions. These simplifications would only provide a fair approximation in real case physical scenarios when considering a coplanar two-planet system, where two planets undergo close encounters at a large distance from the host star. By equalising the forces exerted on the primary planet by the host star and the secondary planet using equation (2.15), I find that they will be equal when $\sqrt{M_{\rm p}/M_\star} = r_{\rm p}/d$, where d is the distance between the two planets. For a Jupiter-mass planet, this expression holds when $d \sim 0.03 r_{\rm p}$. Hence, for this model to be valid the planets would need to have separations of $R_{\rm p,1} + R_{\rm p,2} < d \ll 0.03 r_{\rm p}$.

Concerning the history of the system, I did not take into account how it has evolved prior to the scattering process. I have simply assumed that the system has become unstable and undergone dynamical evolution that has resulted in the current state of the system. In other words, the model omits any investigations of how a system evolves to a point where the orbits cross and focuses on the aftermaths of planet–planet scattering events.

5.1 Semi-analytical model of two-body scattering

Consider a planetary system where two planets of masses $M_{\mathrm{p},1}$ and $M_{\mathrm{p},2}$ orbit a star of mass $M_\star$. Invoking coplanarity of the two orbits, only working with a *flat system*, I can evaluate the problem in two dimensions, which greatly simplifies calculations. Hence, using a polar coordinate system where the host star is positioned at the origin, I can express the position of a planet in the system using the coordinate vector $\boldsymbol{r}_\mathrm{p} = (r_\mathrm{p}, \theta_\mathrm{p})$ (see figure 2.1). Using the θ coordinate for each planet, I can express the angle between the two major axes of the separate orbits as

$$\phi = \theta_1 - \theta_2. \tag{5.1}$$

As derived in section 2.1 in equation (2.6), the distance from the star to a planet on an elliptical orbit can be expressed as a function of θ

$$r_\mathrm{p} = \frac{a(1-e^2)}{1 + e\cos(\theta)}.$$

The mechanism that induces planet–star collision investigated in this work requires close encounters between two planets. Therefore, I am interested in planetary systems where the two orbits cross at some point, i.e. when $r_1(\theta_1) = r_2(\theta_2)$. Hence, I want to find the corresponding coordinates for each planet at this crossing point, given two pre-defined orbits with orbital parameters (a_1, e_1) and (a_2, e_2). In order to find analytical expressions for the crossing point coordinates, it is useful to relate the two azimuthal coordinates of the planetary orbits to each other and thereby reduce the number of variables in the problem. This is easily done by rewriting the azimuthal coordinate θ_1 as a function of θ_2 and ϕ using equation (5.1), which allows me to refer to the crossing point as $r_\mathrm{p}(\theta_1) = r_\mathrm{p}(\theta_1 - \phi)$. The value of ϕ, which is a constant, can be defined when setting up the problem. Since I already have expressions for the distances $r_1(\theta_1)$ and $r_2(\theta_1 - \phi)$ from equation (2.6), I can obtain the following expression

$$\frac{a_1(1-e_1^2)}{1 + e_1\cos(\theta_1)} = \frac{a_2(1-e_2^2)}{1 + e_2\cos(\theta_1 - \phi)}. \tag{5.2}$$

The value of θ_1 for which this expression holds, given a set of orbital parameters (a_1, e_1) and (a_2, e_2), corresponds to the azimuthal coordinate at the orbital crossing. I choose to denote these unique solutions to the analytical problem $\theta_{\mathrm{cross},1}$ and $\theta_{\mathrm{cross},2} = \theta_{\mathrm{cross},1} - \phi$. Unfortunately, equation (5.2) cannot be solved analytically and requires a numerical approach. I expand on the method used to obtain the solutions in section 5.2.

With the values of $\theta_{\mathrm{cross},1}$ and $\theta_{\mathrm{cross},2}$ at hand, I can obtain the initial velocity of the two planets on their orbits at the crossing point before any of their trajectories have been altered. This is done by utilising the expressions for the tangential and radial velocities

of a planet on an elliptical orbit found in equations (2.26) and (2.25), respectively. In the next section I go into the details of the interactions between the two planets during a close encounter and how they lead to new velocities, as well as new orbital parameters.

5.1.1 Close encounters

When two planetary orbits cross and the planets are within one $R_{\mathrm{Hill,m}}$ (see equation (4.1)) of each other, I classify the event as a close encounter. In such a scenario, the planets are close enough to undergo a planet–planet scattering event and exchange large quantities of energy and angular momentum. During the isolated encounter, the force exerted on each of the two bodies is given by

$$F_{\mathrm{pp}} = G\frac{M_{\mathrm{p},1}M_{\mathrm{p},2}}{d^2}, \tag{5.3}$$

where d is the separation between the two planets. There are scenarios in which this force will be strong enough to alter the trajectory and in turn the orbital properties (a, e) for one or both of the planets. This effect is referred to as *deflection*. A strong scattering signifies a strong deflection and a large change in the orbital properties. The strength of the scattering and its outcome depend on several physical properties of the system

1. The relative velocity between the two planets on their unperturbed orbits at the point where their orbits cross

$$\boldsymbol{v}_\infty = \boldsymbol{v}_1(\theta_{\mathrm{cross},1}) - \boldsymbol{v}_2(\theta_{\mathrm{cross},2}). \tag{5.4}$$

2. The mass ratio between the two planets, $q_{\mathrm{p}} = M_{\mathrm{p},2}/M_{\mathrm{p},1}$.
3. The distance from the host star, r_{cross}.
4. The mass of the host star, $M_\star$.
5. The *impact parameter*, b, which is the distance between the planets on their unperturbed orbits.

Since the properties in 1. to 4. all depend on inherent physical quantities for a given two-planet system, the impact parameter, b, is arguably the most important property of a scattering event. It determines the separation between the planets, $\boldsymbol{d}$, and in turn the angle between a planet's velocity prior the scattering, $\boldsymbol{v}$, and its new velocity after the scattering[1], $\tilde{\boldsymbol{v}}$. I denote this angle δ. Hence, there exists a wide range of impact parameters for each two-body problem and each value will result in a given solution for δ. If the impact parameter is too large, the deflection will be weak and will not lead to a significant change in velocity. If it is too small, i.e. $|b| \leq R_{\mathrm{p},1} + R_{\mathrm{p},2}$, the scattering will result in a head-on collision between the planets. Furthermore, due to deflection there are scenarios where

[1] A $\sim$ symbol above a given quantity will hereafter indicate its new value after a scattering event.

$|b| > R_{\mathrm{p},1} + R_{\mathrm{p},2}$ and the scattering leads to a collision as well. The type of deflection that enhances the chances for planet–planet collision is called *gravitational focusing*. Another important property of the impact parameter is that it can be both positive and negative. The sign determines the localised position of the planets relative to the host star at the point of orbit crossing. If the impact parameter is positive, the planet with the larger semi-major axis will be the planet farthest away from the host star and if the impact parameter is negative, the same planet will be closest to the host star.

Knowing that each value for the impact parameter will yield new velocities $\tilde{v}$, it is clear that the scattering will lead to a new set of values for the energy and angular momentum of each planet. In turn, since the energy and angular momentum of a planet can be directly related to the semi-major axis and eccentricity of its orbit, each b will yield a new set of orbital parameters $(\tilde{a}, \tilde{e})$. The properties of the new planetary orbit will in turn determine if the planet will merge with the other planet, get ejected from the system, be consumed by the host star or if the system will remain intact. In the remainder of this section, I show how these new orbital parameter values can be derived for planet–planet scattering within a given two-planet system.

5.1.2 The deflection angle

I now set out to derive an analytical solution for the deflection angle δ, guided by Spitzer (1987). To this end, I make use of figure 5.1 where I show a scattering event in the rest frame of the primary planet with mass $M_{\mathrm{p},1}$. Here, the impact parameter is small enough to result in a strong scattering and large enough to not result in a collision between the planets. The dashed lines represent the asymptotic relative trajectory of the secondary planet with mass $M_{\mathrm{p},2}$. There are two other angles except for δ that must be considered, as indicated in the diagram: φ, which is the angle measured from the point of closest separation during the encounter and ψ. In order to derive δ using the other two angles of importance, I have to find an expression for the distance between the planets during the scattering event. Using the fact that the trajectory of the secondary planet can be considered a conic section of eccentricity e_{sc} with its focus at the position of the primary planet in the current frame of reference, I can combine equations (2.2) and (2.21), which yields

$$d = \frac{h^2}{G(M_{\mathrm{p},1} + M_{\mathrm{p},2})} \frac{1}{1 + e_{\mathrm{sc}} \cos(\varphi)}. \tag{5.5}$$

Remembering that h is the specific angular momentum of the two-body problem from equation (2.12), I use the fact that the total angular momentum of the two bodies in this frame of reference is given by the angular momentum of the secondary planet. Due to the assumption that the angular momentum is conserved among the planets in this isolated close encounter, I can compute the specific angular momentum at any point. Assuming that the impact parameter is known, I directly obtain h for the secondary planet on its

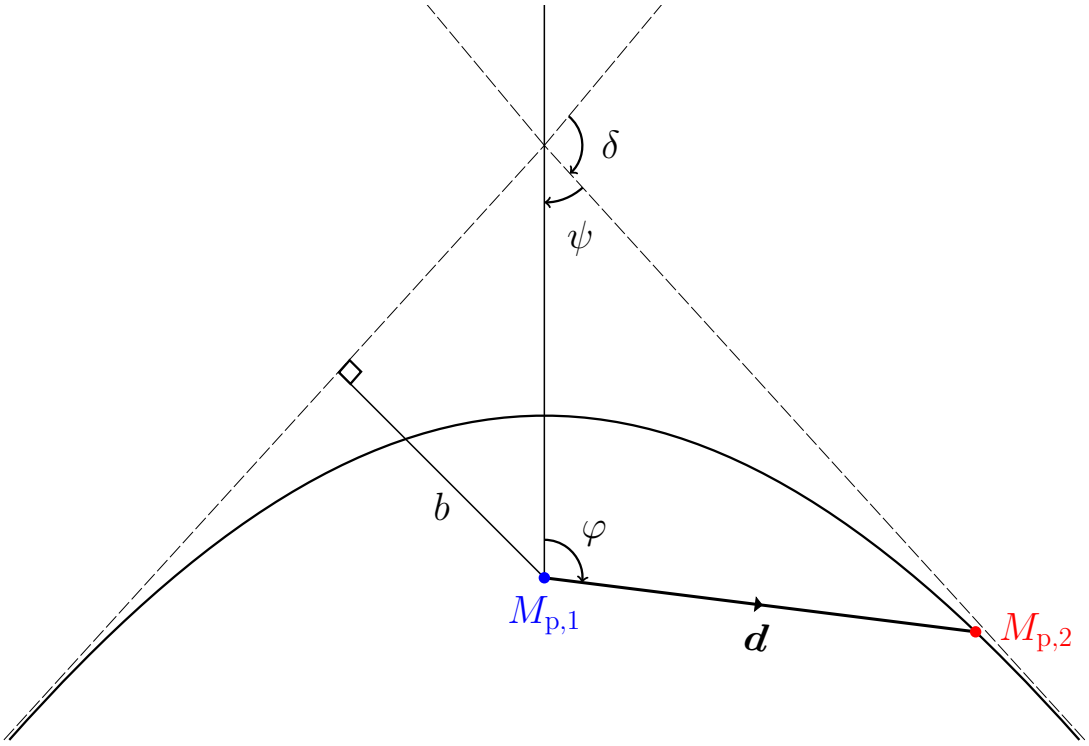

Figure 5.1: Diagram of the trajectory of the secondary planet (red) in the rest frame of the first planet (blue) during a scattering event. The impact parameter is indicated by b and the distance between the planets during the encounter is indicated by the vector $\boldsymbol{r}$. The angle δ is the deflection angle, φ is the angle from the point of closest separation and ψ is the angle between the orbits at infinite separation.

unperturbed orbit. The velocity of the secondary planet at that point is simply v_∞, which is the magnitude of $\boldsymbol{v}_\infty$ from equation (5.4). The angle between $\boldsymbol{v}_2$ and $\boldsymbol{d}$ at the point where $d = b$ on the unperturbed orbit is simply $\alpha = \pi/2$, meaning that

$$h = bv_\infty. \tag{5.6}$$

Inserting the new expression for h, valid during the scattering, into equation (5.5), I get

$$d = \frac{b^2 v_\infty^2}{G(M_{\mathrm{p},1} + M_{\mathrm{p},2})} \frac{1}{1 + e_{\mathrm{sc}} \cos(\varphi)}. \tag{5.7}$$

Since I can consider this a bound system, the total energy is given by equation (2.27). Dividing by the reduced mass and multiplying by a factor 2, I get the following expres-

sion

$$2\epsilon = v_{\mathrm{p}}^2 - \frac{2G(M_{\mathrm{p},1} + M_{\mathrm{p},2})}{d}, \tag{5.8}$$

where ϵ is the specific energy. The velocity is given by $v_{\mathrm{p}}^2 = v_{\mathrm{d}}^2 + v_{\varphi}^2$, which can be rewritten as $v^2 = v_d^2 + h^2/d^2$ with equation (2.12). Using said expression for the velocity, the above relation becomes

$$2\epsilon = \left(\frac{\mathrm{d}d}{\mathrm{d}t}\right)^2 + \frac{h^2}{d^2} - \frac{G(M_{\mathrm{p},1} + M_{\mathrm{p},2})}{d}. \tag{5.9}$$

Again making use of the conservation of quantities within this isolated system, I can find ϵ by computing it at any point of the scattering event. Hence, the total energy will be equal to the kinetic energy of the secondary planet at infinite separation, i.e. $\epsilon = v_\infty^2/2$. When it comes to $\mathrm{d}d/\,\mathrm{d}t$, I can use the chain rule and equation (2.14) to obtain

$$v_\infty^2 = \left(\frac{\mathrm{d}d}{\mathrm{d}\varphi}\frac{bv_\infty}{d^2}\right)^2 + \frac{b^2v_\infty^2}{d^2} - \frac{G(M_{\mathrm{p},1} + M_{\mathrm{p},2})}{d}. \tag{5.10}$$

From equation (5.7), I find the derivative to be

$$\frac{\mathrm{d}d}{\mathrm{d}\varphi} = \frac{h^2}{G(M_{\mathrm{p},1} + M_{\mathrm{p},2})}\frac{e_{\mathrm{sc}}\sin(\varphi)}{(1 + e_{\mathrm{sc}}\cos(\varphi))^2}. \tag{5.11}$$

The eccentricity of the conic section in figure 5.1 remains an unknown constant at this point. However, since I already have assumed that the impact parameter is known, I note that all other constants are known for a scattering event in a given two-planet system. Hence, I can calculate equation (5.10) at any value of φ to find an expression for e_{sc}. Therefore, I choose to evaluate the derivative at $\varphi = \pi/2$ and, after substituting h and d using equations (5.6) and (5.7), I simplify (5.10) to find the expression

$$e_{\mathrm{sc}}^2 = 1 + \frac{b^2v_\infty^4}{G^2(M_{\mathrm{p},1} + M_{\mathrm{p},2})^2}. \tag{5.12}$$

The importance of the angle ψ becomes clear when using figure 5.1 to determine that it is related to δ in the following manner

$$\delta = \pi - 2\psi. \tag{5.13}$$

Hence, if I know the value of ψ I can easily determine the deflection angle, which I need to calculate the new velocity vectors post-scattering. From the expression for d in equation

(5.5), the separation between the planets will go towards infinity when $1 + e_{\mathrm{sc}} \cos(\varphi) = 0$, which, according to figure 5.1, must occur at $\phi = \pi \pm \psi$. In turn, I deduce that $e_{\mathrm{sc}} = 1/\cos(\psi)$. Employing the relation $\tan^2(\psi) = 1/\cos^2(\psi) - 1$, I finally arrive at an expression for ψ from equation (5.12)

$$\tan(\psi) = \frac{b v_\infty^2}{G(M_{\mathrm{p},1} + M_{\mathrm{p},2})}. \tag{5.14}$$

Equations (5.13) and (5.14) clarify the importance of the impact parameter since it is the only varying parameter that determines the deflection angle for a close encounter within a given two-planet system.

5.1.3 Finding the new velocities

With the deflection angle at hand, one would think that it is straightforward to rotate the pre-scattering velocities and quickly find the new velocities $\tilde{\boldsymbol{v}}_1$ and $\tilde{\boldsymbol{v}}_2$. However, I still do not know the magnitudes of the new velocities. Furthermore, the entire idea behind this two-dimensional analysis is to gain a better understanding of the mechanisms that govern the outcome of planet–planet scattering and how this process can lead to planet consumption. Hence, I opt for a workaround that will facilitate both calculation and the visualisation of how deflection alters the velocities of the planets involved in the scattering.

The main idea behind this workaround is that the centre-of-mass velocity $\boldsymbol{v}_{\mathrm{cm}}$ for the isolated two-body system considered is a conserved quantity that is common to both planets. This velocity is weighted by the mass of the two planets such that

$$\boldsymbol{v}_{\mathrm{cm}} = \frac{M_{\mathrm{p},1}\boldsymbol{v}_1 + M_{\mathrm{p},2}\boldsymbol{v}_2}{M_{\mathrm{p},1} + M_{\mathrm{p},2}}. \tag{5.15}$$

Figure 5.2 shows the velocity vectors of two planets with crossing orbits prior to the scattering event in the centre-of-mass frame of reference. From the figure, it becomes clear that the initial velocities of each planet can be split up into two vector components, $\boldsymbol{v}_{\mathrm{cm}}$ and the planet's relative velocity to the centre-of-mass, denoted with a subscript b. As a result, the velocities can be written

$$\boldsymbol{v}_1 = \boldsymbol{v}_{\mathrm{cm}} + \boldsymbol{v}_{1,b} \tag{5.16}$$

$$\boldsymbol{v}_2 = \boldsymbol{v}_{\mathrm{cm}} + \boldsymbol{v}_{2,b}. \tag{5.17}$$

Since the radial and tangential components of the initial velocities can be computed using equations (2.25) and (2.26), calculating $\boldsymbol{v}_{\mathrm{cm}}$ is straightforward. Thus, the velocities $\boldsymbol{v}_{1,b}$ and

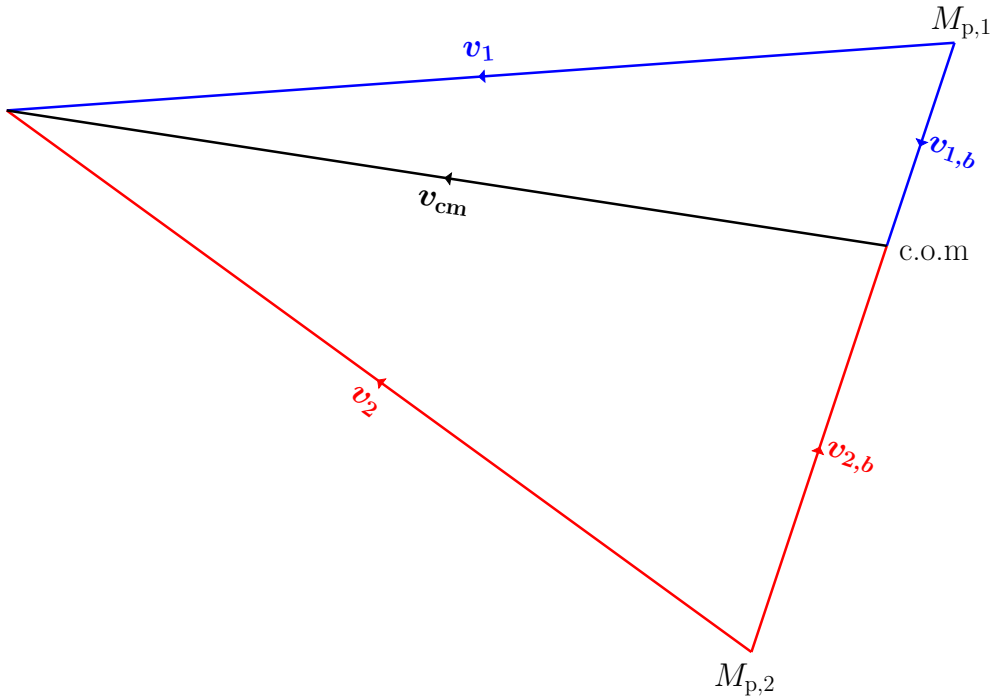

Figure 5.2: The velocity vectors of two planets with crossing orbits undergoing a close encounter in the centre-of-mass frame of reference. The centre-of-mass velocity is indicated by $\boldsymbol{v}_{\mathrm{cm}}$ and the planet velocities relative to the centre-of-mass is denoted $\boldsymbol{v}_{\mathrm{p},b}$.

$\boldsymbol{v}_{2,b}$ relative to the centre-of-mass can be directly found from equations (5.16) and (5.17), respectively. Due to the centre-of-mass velocity vector being conserved throughout the scattering event, the new velocities seem to only depend on $\boldsymbol{v}_{1,b}$ and $\boldsymbol{v}_{2,b}$. This is further illustrated in figure 5.3, where a deflection between a Jupiter-mass and an Earth-mass planet is shown in the centre-of-mass frame of reference. Note that the centre-of-mass in reality is much closer to the trajectory of the Jupiter-mass planet due to the small mass ratio $q_{\mathrm{p}} \sim 0.003$. Hence, the scaling has been exaggerated in order to facilitate visualisation. The same follows for the magnitudes of $\boldsymbol{v}_{1,b}$ and $\tilde{\boldsymbol{v}}_{1,b}$, which, due to the mass ratio, are merely ~ 0.003 of the corresponding magnitudes for the Earth-mass planet.

The Jupiter-mass planet is incoming from the left in the figure with an initial distance b from the Earth-mass planet which is incoming from the right. This distance is indicated with a dashed, dotted line in figure 5.3. As previously mentioned, the impact parameter can be negative as well. If I assume that a positive impact parameter in this scenario indicates that the Jupiter-mass planet is closest to the host star, this scattering would deflect the Earth-mass planet inwards into the system. A negative impact parameter would instead put the incoming Jupiter-mass planet on the top horizontal asymptote in this frame of reference, indicated by a dashed line, while the Earth-mass planet would be incoming on the bottom horizontal asymptote. Hence, the Earth-mass planet would be closest to the

host star and the deflection would instead be outwards, away from the system.

Given the small mass ratio, the velocity relative to the centre-of-mass of Jupiter is barely affected by the interaction with the Earth-mass planet, while the Earth-mass planet will be strongly gravitationally focused by the Jupiter-mass planet. During the scattering, the minimum separation between the two planets is $d_{\min}$, which is also indicated with a dashed, dotted line in the figure. Since it is clear from the figure that $d_{\min} \leq |b|$, a better definition for the occurrence of a planet–planet collision during a scattering event is when $d_{\min} \leq R_{\mathrm{p},1} + R_{\mathrm{p},2}$. In figure 5.1, d is equal to $d_{\min}$ for the case $\varphi = 0°$.

Due to the assumption that energy and angular momentum will be conserved within this isolated system, the magnitudes of these velocities relative to the centre-of-mass will be constant throughout the scattering, i.e. $|\boldsymbol{v}_{\mathrm{p},b}| = |\tilde{\boldsymbol{v}}_{\mathrm{p},b}|$. Using this fact, the new velocities of the two planets must simply be equal to

$$\tilde{\boldsymbol{v}}_1 = \boldsymbol{v}_{\mathrm{cm}} + \tilde{\boldsymbol{v}}_{1,b} \tag{5.18}$$

$$\tilde{\boldsymbol{v}}_2 = \boldsymbol{v}_{\mathrm{cm}} + \tilde{\boldsymbol{v}}_{2,b}. \tag{5.19}$$

Therefore, the only step left in the endeavour to find the new velocities $\tilde{\boldsymbol{v}}_1$ and $\tilde{\boldsymbol{v}}_2$ is to rotate the initial vectors $\boldsymbol{v}_{1,b}$ and $\boldsymbol{v}_{2,b}$ by the deflection angle δ, which yields $\tilde{\boldsymbol{v}}_{1,b}$ and $\tilde{\boldsymbol{v}}_{2,b}$.

5.1.4 New orbital parameters

Knowing the new velocities $\tilde{\boldsymbol{v}}$, I can now determine the parameters that I set out to find, $\tilde{a}$ and $\tilde{e}$. This comes from the fact that the new energy and angular momentum are directly related to the new velocities of the planets.

I combine the two equations I have previously used to describe the semi-latus rectum ℓ of the orbit, namely (2.5) and (2.21), which yields

$$\tilde{e}^2 = 1 - \frac{\tilde{h}^2}{GM_{\mathrm{tot}}\tilde{a}}. \tag{5.20}$$

This equation can be simplified by rewriting it in terms of J and E, which are easily computed with equations (2.12) and (2.27),

$$\tilde{e}^2 = 1 + \frac{2\tilde{E}\tilde{J}^2}{G^2\mu_r^3 M_{\mathrm{tot}}^2} \approx 1 + \frac{2\tilde{E}\tilde{J}^2}{G^2 M_{\mathrm{p}}^3 M_\star^2}. \tag{5.21}$$

Now I have everything I need in order to determine which outcome the two planets have suffered after their scattering. The validity of the equations derived in this section can

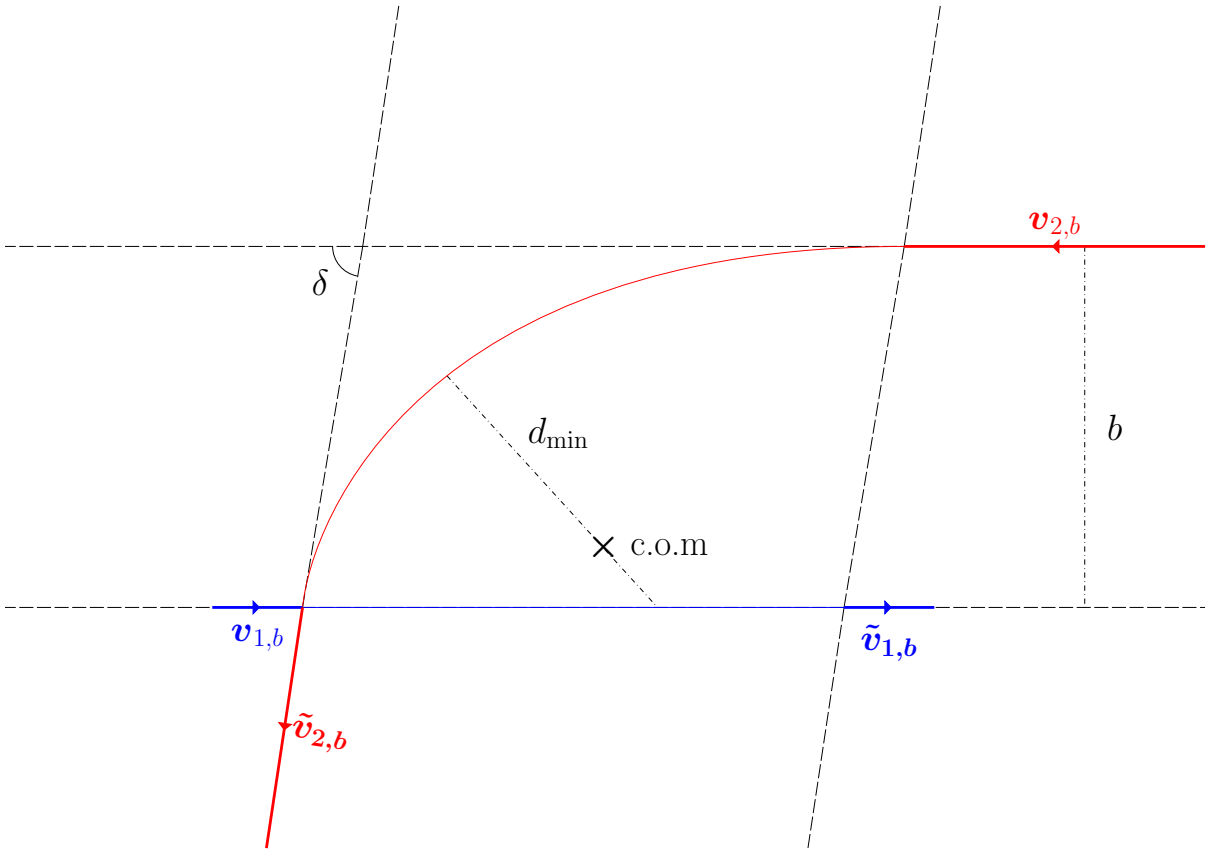

Figure 5.3: Deflection during a close encounter between a Jupiter-mass (blue) planet incoming from the left and an Earth-mass (red) planet incoming from the right in the centre-of-mass frame of reference. The planets are initially separated by the impact parameter b on their unperturbed orbits with centre-of-mass velocities $\boldsymbol{v}_{1,b}$ and $\boldsymbol{v}_{2,b}$. Their closest separation during the encounter is $d_{\min}$. After the encounter the Earth-mass planet will have been deflected by the angle δ and has a new velocity $\tilde{\boldsymbol{v}}_{2,b}$, while the Jupiter-mass planet velocity is nearly completely unperturbed with $\tilde{\boldsymbol{v}}_{1,b} \approx \boldsymbol{v}_{1,b}$. Note that the distance between the Jupiter-mass planet's trajectory and the centre-of-mass and the magnitudes of $\boldsymbol{v}_{1,b}$ and $\tilde{\boldsymbol{v}}_{1,b}$ have been greatly exaggerated.

easily be checked using the assumption that the total energy and angular momentum within this isolated two-planet system is conserved throughout the scattering, meaning that $E_1 + E_2 = \tilde{E}_1 + \tilde{E}_2$ and $J_1 + J_2 = \tilde{J}_1 + \tilde{J}_2$.

	a [AU]	e	$q_\star$	R_p [$\mathrm{R}_\oplus$]
Orbit 1	1.0	0.0	9×10^{-4}	13.44
Orbit 2	1.1	0.9	3×10^{-6}	1.00

Table 5.1: The physical properties of the primary example system we consider in this chapter with an Earth-mass and a Jupiter-mass planet orbiting a Solar-mass host star.

5.2 Implementation of the two-body model

In order to systematically be able to carry out simulations of planet–planet scatterings, I have implemented the equations derived in section 5.1 in a program. The program is called `Scattersim`[2] and is written in `Python3`. `Scattersim` consists of a class called `scatter` that is initiated using the following input

1. Initial semi-major axes and eccentricities for two orbits, $a_1,\ e_1,\ a_2,\ e_2$.
2. The masses of the two planets on said orbits, $M_{\mathrm{p},1},\ M_{\mathrm{p},2}$.
3. The angle between the major axes of the orbits, ϕ.
4. The mass of the host star, $M_\star$.

From the masses, the planetary radii and the stellar radius are directly computed using the relations in sections 3.4 and 3.5, respectively. Furthermore, a primary check for any orbit crossing points can be performed by simply checking if the periastron of the orbit with the largest semi-major axis is outside the apastron of the other orbit, i.e. if $a_{\max(a_1,a_2)}(1 - e_{\max(a_1,a_2)}) < a_{\min(a_1,a_2)}(1 + e_{\min(a_1,a_2)})$. If this is the case, the program will try to find the two points of intersection between the two orbits. I will refer to these as crossing points A and B. In figure 5.7 I show an example of two orbits crossing where the first orbit (blue) is circular with a Jupiter-mass planet and the second orbit (red) is highly eccentric with an Earth-mass planet. The orbital properties, as well as the mass ratio between the host star and the planet, $q_\star = M_\mathrm{p}/M_\star$, and the planetary radii are indicated in table 5.1.

The orbits will cross when $r_\mathrm{p}(\theta_1) = r_\mathrm{p}(\theta_1 - \phi)$. I have chosen to denote the corresponding angle $\theta_{\mathrm{cross},1}$ and $\theta_{\mathrm{cross},2} = \theta_{\mathrm{cross},1} - \phi$. Since there will be two points of crossing for this scenario, I also use a subscript to indicate which orbit crossing point I am referring to with A or B. These two angles are the solutions to equation (5.2) and can only be determined numerically. In order to achieve a satisfactory accuracy for the solutions, I used an approach based on linear extrapolation in the function `scatter.get_isec` which is structured as follows. First, I set up a range of equally spaced values for θ_1 with a step size of $\Delta\theta = 0.1°$. While it is unlikely that the solution will lie exactly on one of the values within said range, the step size is sufficiently small to catch sign changes in the difference between the distances to the host star, i.e. $\Delta r = r_1(\theta_1) - r_2(\theta_1 - \phi)$. This allows the program

[2]The main functions can be found in `scattersim.py` in the git repository https://github.com/Jooehn/Stars-Eating-Planets.git

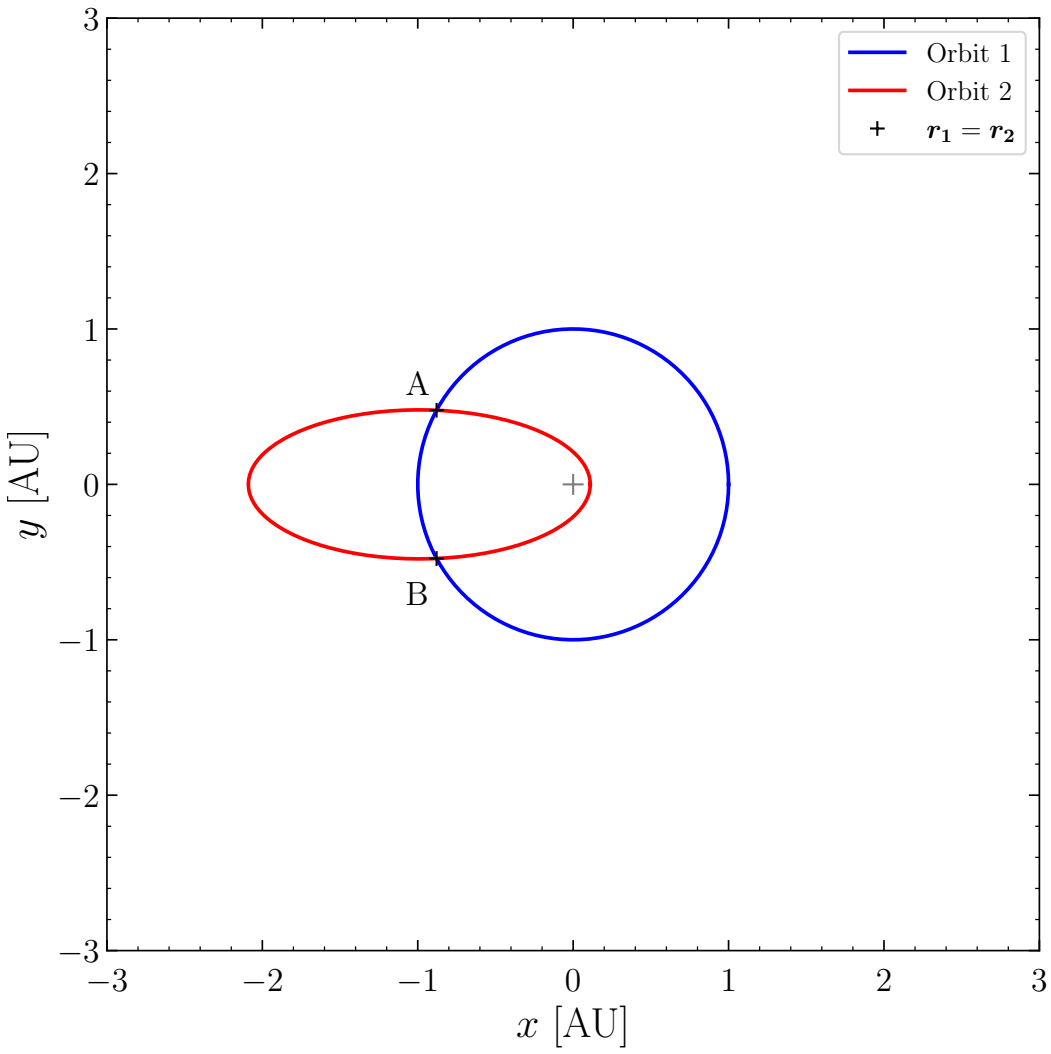

Figure 5.4: Example of a case where two orbits are crossing. The eccentric red orbit belongs to an Earth-mass planet, while the circular blue orbit belongs to a Jupiter-mass planet. The full properties of the system can be found in table 5.1. I have indicated the positions of the two different crossings A and B. The planets rotate clockwise in this face-on perspective.

to determine the two adjacent values $\theta_{1,k}$ and $\theta_{1,k+1}$ between which the sign of Δr will change. This will occur at two different points in the range of θ values considered. The exact azimuthal angle for the crossing points can then be computed using the following linear equations

$$r_1 = g_1\theta_1 + f_1 \tag{5.22}$$
$$r_2 = g_2\theta_1 + f_2, \tag{5.23}$$

where g and f are the first and zeroth order constants of the polynomial. The first order constant is easily determined from $g = \Delta r/\Delta\theta$ and the zeroth order constant can be determined by solving for f and computing r for a given θ with equation (2.6). The values of $\theta_{\mathrm{cross,1A}}$ and $\theta_{\mathrm{cross,1B}}$ are then found by letting $r_1 = r_2$ which from the linear equations above yields

$$\theta_{\mathrm{cross},1} = \frac{f_2 - f_1}{g_1 - g_2}. \tag{5.24}$$

While there exist two-planet systems where the orbital configuration is such that the above algorithm will only have one solution, they would be rare. Hence, I only chose to consider systems where the orbits cross at exactly two points as crossing.

With the crossing angles at hand, the program will proceed to compute the initial velocities of the planets on their unperturbed orbits. Knowing these velocities, there is no additional information needed to analytically compute the new orbital parameters using the equations derived in section 5.1. This is done in the function `scatter.scatter`, which takes one or a set of impact parameters as input. The new set of orbital parameters $(\tilde{a}, \tilde{e})$ for each planet can then be used to infer the outcome for each impact parameter value. The requirements for each outcome is as follows

- **Consumption:** A planet is consumed by the host star if the separation at nearest approach is less than the critical radius for consumption, $r_{\mathrm{peri}} = \tilde{a}(1 - \tilde{e}) \leq r_{\mathrm{crit}}$. In this thesis I use $r_{\mathrm{crit}} = R_\star$.
- **Planet–planet merger:** The planets will merge if their separation at nearest approach is less than their combined physical radii, $d_{\mathrm{min}} \leq R_{\mathrm{p},1} + R_{\mathrm{p},2}$.
- **Ejection:** A planet is ejected if its orbit becomes parabolic or hyperbolic, $\tilde{e} \geq 1$.
- **Survival:** There are less than two crossing angles.

In this thesis I refer to a planet that has suffered either consumption, merger or ejected as a Consumed, Merged or Ejected (CME)-type planet. Any planet left in the system after it has finished dynamical evolution is known as a 'survivor'.

Note that these definitions exclude the presence of tidal forces. The tidal forces between two planets are typically weak and will make a minor difference for the critical separation needed to induce mergers. However, such tidal forces can lead to the creation of planet–planet binary systems within planetary systems (Podsiadlowski et al., 2010; Ochiai et al., 2014). The tidal forces between the planet and the host star will be significantly stronger and could trigger tidal disruption of a planet at a separation larger than $R_\star$. Therefore, in a more physically accurate scenario $r_{\mathrm{crit}} > R_\star$. Hence, the fraction of new orbital parameter sets $(\tilde{a}, \tilde{e})$ that lead to planet consumption will be underestimated using this approach. Nevertheless, as previously stated the purpose of the two-body problem analysis

is to reach qualitative and not quantitative conclusions regarding the nature of planet-consuming scatterings. In turn, I choose to simply note these discrepancies from a more physical scenario and proceed without addressing the varying r_{crit} and d_{crit} and the possible creation of planet–planet binaries in my calculations.

The critical separation between the planet and the host star gives rise to a critical eccentricity for which the planet will be consumed. I recognise that the planet will be within the critical distance for interaction with the host star if $a(1-e) < r_{\text{crit}}$. In return, there must exist a critical eccentricity e_{crit} for a given semi-major axis where the periastron is equal to r_{crit}. Solving the previous inequality for e and equating the right and left hand sides give us said parameter

$$e_{\text{crit}} = 1 - \frac{r_{\text{crit}}}{a}. \tag{5.25}$$

5.2.1 The role of the impact parameter

As previously stated, the impact parameter plays an important role in the scattering event as it will directly determine the outcome for a close encounter within a given two-planet system. This is emphasised by the analysis in section 5.1. From figure 5.3 it becomes clear why the deflection of the Earth-mass planet will be insignificant if the impact parameter is too large despite the extreme mass ratio and that a collision will occur if the impact parameter is too small. In order not to oversample the impact parameter range and rely on an arbitrary process to find a good range, I introduce the parameter $b_{\max}$ which I now motivate.

First, it is important to understand how different values of the impact parameter will affect the outcome of the scattering process. The best way to think about this parameter is to recall the fact that every value corresponds to a given deflection angle. Of course, if $|b| > b_{\max}$, the angle will tend to $0°$ and for $b \to 0$, $\delta \to 180°$. This feature of the impact parameter is visualised in figure 5.5. Here I again consider the case of a scattering of a Jupiter-mass and an Earth-mass planet orbiting a Solar-mass star and focus on the change in the Earth-mass planet velocity. The physical properties of the system can be found in table 5.1 and they were chosen such that it would be potentially planet-consuming. The solid and dashed vectors represent $\boldsymbol{v}_2$ and $\boldsymbol{v}_{2,b}$, respectively. The velocity prior to the scattering is rendered in orange and the velocity after the scattering event is rendered in purple. The black vector represents the centre-of-mass velocity of the two-planet system. The most useful property of $\boldsymbol{v}_{2,b}$ is that its magnitude will be constant throughout a scattering event. This leads to the fact that all possible impact parameter values, and therefore all deflection angles, create a circle of possible $\tilde{\boldsymbol{v}}_{2,b}$ vectors in (v_r, v_θ)-space with a radius of $|\boldsymbol{v}_{2,b}|$. The size of this circle naturally changes with the mass ratio of the planets, as well as the properties of the initial orbit. For example, the corresponding velocity of the circle of the primary Jupiter-mass planet in this scattering event has a radius $|\tilde{\boldsymbol{v}}_{1,b}| \ll |\tilde{\boldsymbol{v}}_{2,b}|$. Since $\tilde{\boldsymbol{v}}_2 = \boldsymbol{v}_{\text{cm}} + \tilde{\boldsymbol{v}}_{2,b}$, the size of this circle also indicates the possible changes in the

magnitude of $\tilde{\boldsymbol{v}}_2$. The grey dashed line in figure 5.5 shows the position of $\boldsymbol{v}_{2,b}$ prior to the scattering event in order to facilitate the visualisation of the deflection angle. While the deflection angle is merely $\sim 35°$ in the example, the deflection still leads to a large change in the magnitude of the velocity. This leads to another noteworthy property of the scattering process. The maximum velocity does not occur for the largest deflection angle, but for the case when $\tilde{\boldsymbol{v}}_{2,b} || \boldsymbol{v}_{\text{cm}}$. Similarly, the minimum velocity occurs when the vectors are antiparallel. Hence, a smaller impact parameter will lead to a larger exchange of angular momentum and energy and in turn a larger change in the orbital parameters. However, due to the physical size of the planets, the impact parameters that would lead to the largest possible change in orbital parameters will instead induce a merger between the planets.

Further, the circle of $\boldsymbol{v}_{2,b}$ vectors has a green arc for which the planet has been put on a consuming orbit and from the figure it becomes clear that this is the case for the corresponding impact parameter. Said arc makes out a relatively small portion of the entire range of new velocities despite the fact that the mass ratio between the involved planets allows for extreme scattering events with large changes in the orbital parameters. This reinforces the idea that oversampling of the impact parameter could be harmful to the results of this analysis. If I probe too large a range in b, many of the values in the outer range will yield the same result, i.e a scattering with a deflection angle of $0°$. As a result, the fraction of impact parameters that yields a consuming orbit for a planet will be underestimated, especially if drawing random values from said range.

In order to find a satisfactory value of b_{max}, I first make use of the common definition that a close encounter occurs if the planets are within a distance of one mutual Hill radius. Hence, the maximum value of b_{max} should be $R_{\text{Hill,m}}$. However, recall that not only the mass ratio determines the strength of the scattering, but also the orbital configuration of the planets and the distance from the host star do. If planets are further out in the system, the planets will be less bound and the Safronov number in equation (4.6) indicates that the separation between the planets during the encounter can be larger and still induce a significant change in orbital parameters. With this in mind, it is clear that the value of b_{max} highly depends on the system at hand. Therefore, instead of simply letting $b_{\text{max}} = R_{\text{Hill,m}}$ I use a numerical approach to estimate the best value for this parameter.

1. I start off by assuming that $b_{\text{max}} = \beta R_{\text{Hill,m}}$, where $\beta \in [\beta_0, 1]$ and β_0 is the initial estimate of b_{max}.

2. I carry out N scatterings in the range $b \in [-b_{\text{max}}, b_{\text{max}}]$, where N typically is 1000. The impact parameter values will be equally spaced with a constant step of Δb such that $b_{\text{max}} = N\Delta b/2$. The motivation for using a uniform distribution of impact parameters can be found in appendix A.

3. I compute the eccentricity gradient at the edges of the impact parameter range and

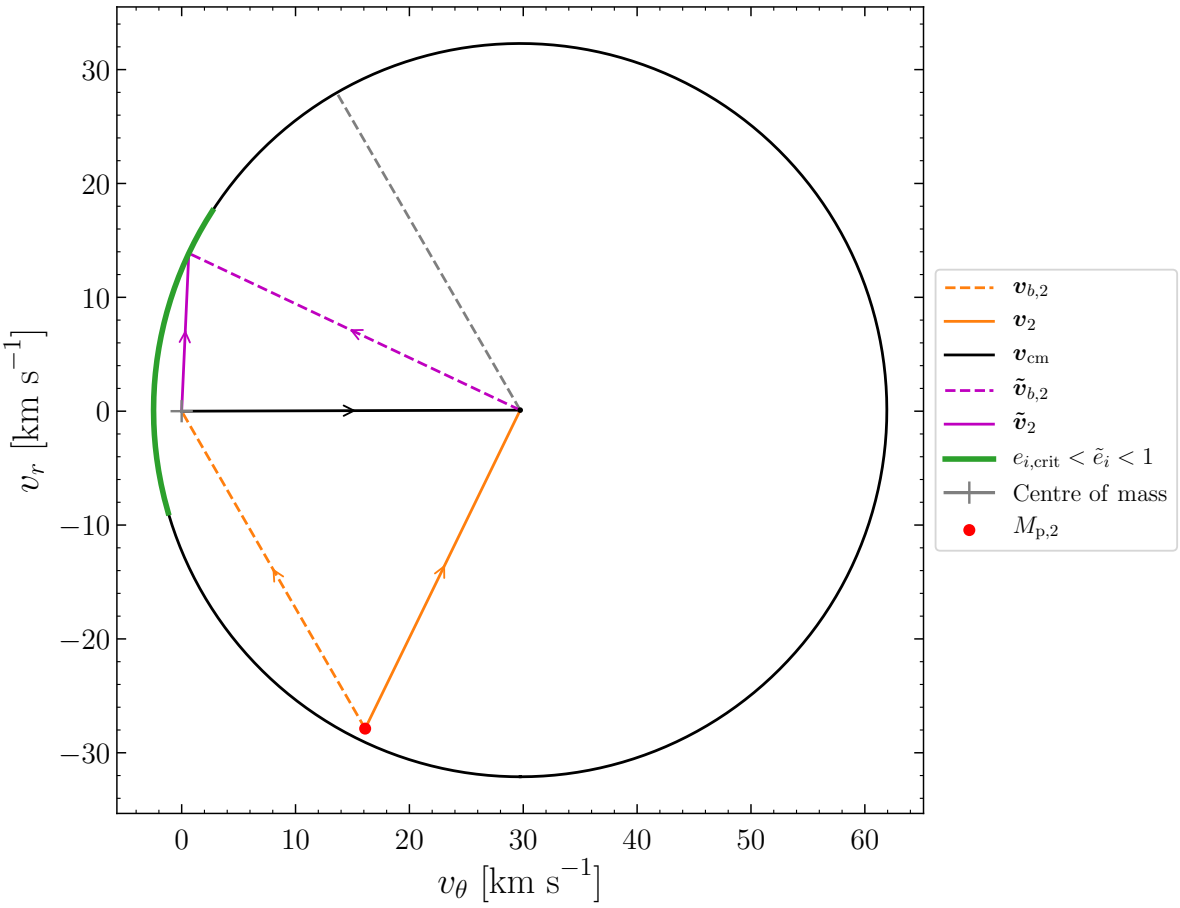

Figure 5.5: Visualisation of the vector circle corresponding to the change in velocities for an Earth-mass planet being deflected by a Jupiter-mass planet (see table 5.1). The black vector shows the centre-of-mass velocity. The yellow and yellow-dashed vectors represent the initial velocity and the velocity with respect to the centre of mass, while the purple vectors represent the corresponding velocities post-scattering. The green region of the circle indicates the range of deflection angles that yields a planet-consuming orbit.

require that it must be smaller than some constant γ, i.e.

$$\frac{\mathrm{d}\tilde{e}}{\mathrm{d}\beta} < \gamma. \tag{5.26}$$

4. If the gradient is larger than γ, I adjust my estimate of β and repeat from step 2. If not, or if $\beta = 1$, I let $b_{\max} = \beta R_{\rm Hill,m}$.

I found that a good initial estimate is $\beta_0 = 0.1$ and that adjustments of the estimate in steps of 0.01 was appropriate. Furthermore, a good value of γ proved to be 10^{-4}. The minimum

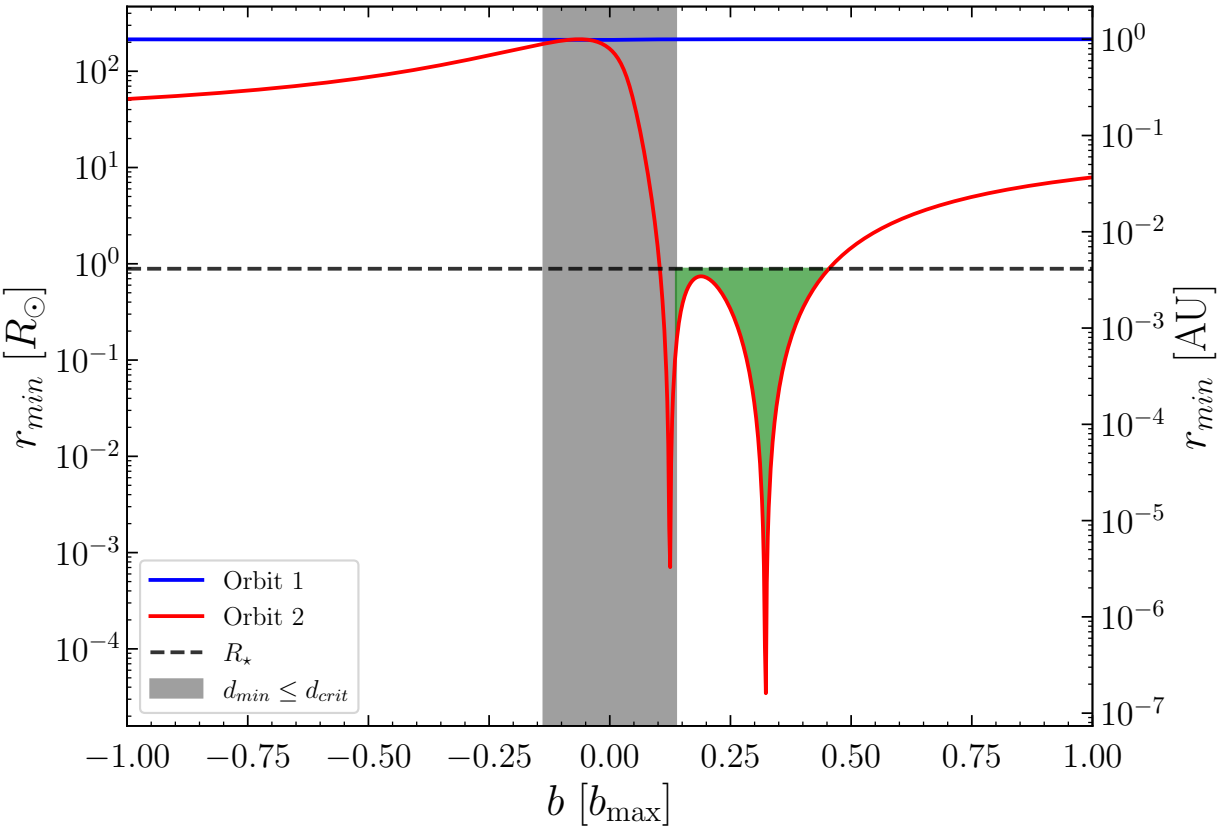

Figure 5.6: The minimum separation between the host star and the Earth-mass (red) and Jupiter-mass (blue) planets in the system described in table 5.1 given by $r_{\min} = \tilde{a}(1 - \tilde{e})$ as a function of b. Said encounters occur at crossing point A. The green region shows the range of impact parameters where the Earth-mass planet have been consumed, i.e. when $r_{\min} \leq R_\star$. Note that there are two minima, which indicates that the planet gets put on a retrograde orbit for $0.10 b_{\max} < b < 0.15 b_{\max}$.

separation between the planets and the host star as a function of b for the reference system in table 5.1 after scattering at crossing point A in figure 5.4, is shown in figure 5.6. I note again that there is a limited range for which the impact parameter will put the Earth-mass planet on a consuming orbit. Moreover, the reason why there are two minima for $r_{\min}$ is due to the fact that the high eccentricity will lead to a scattering event that becomes so violent that the Earth-mass planet is put on a retrograde orbit. Note that most of the values where the planet is put on a retrograde orbit are within the region where $d \leq d_{\text{crit}}$, which leads to a merger.

5.3 Requirements for orbit crossing

Typically, the crossing of orbits is not a common occurrence in planetary systems. As mentioned in chapter 4, orbits cross in short-term unstable systems where the initial orbital configuration leads to a chaotic evolution or in long-term unstable systems where there is a diffusive exchange of angular momentum that leads to significant radial excursions inwards or outwards in the system for one or more planets. Hence, the orbits of the planets that undergo close encounters should be more or less eccentric. This means that there has been a loss of angular momentum for one or both planets prior to the close encounter, leading to an increase in the AMD of the system, which is given by equation (4.3). For the purposes of this chapter, where the inclination is zero, the only difference is that the $\cos(i_k)$ factor simply vanishes. Thus, in the flat system scenario there are only two ways of increasing the AMD of an individual planet, which are by making its orbit more eccentric or by increasing its semi-major axis (assuming that the orbit is already eccentric).

In order to further illustrate which type of planet configuration with orbit crossing, I created a number of planetary systems where two planets are orbiting a Solar-mass star. The planets are again of masses $M_{\mathrm{p},1} = \mathrm{M_J}$ and $M_{\mathrm{p},2} = \mathrm{M}_\oplus$. The orbits of the planets were created in a Monte Carlo fashion, where the eccentricities, semi-major axes and ϕ angles are drawn from a uniform distribution. The eccentricities were between 0 and 1, the semi-major axes are between 0.1 and 20 AU and the ϕ angles are between 0° and 360°. I then used the functions `scatter.cross_check` and `scatter.get_isec` to check if the orbits are crossing for the created system. In total, 500 systems of 910 drawn proved to have crossing orbits. The AMDs of the resulting 500 systems have been plotted in figure 5.7. The colour of the dots indicate the angle ϕ and the diagonal lines show three cases where the eccentricities of the orbits have been kept static while the semi-major axes have been varied between 0.1 and 20 AU. From the figure, it is indeed clear that one or both of the planets need to have a significant AMD for the orbits to cross. Moreover, the angle ϕ does not seem to affect the crossing of orbits as there is a wide distribution of angles. Geometrically, this makes sense as the angle between the major axes should mainly affect the distance r_{cross} if both orbits are quite eccentric.

5.4 Which systems are planet-consuming?

The possible outcomes of scattering events in the 500 planetary systems of figure 5.7 does not necessarily include the consumption of a planet. Direct planet consumption from a single scatter appears to require high levels of total AMD in the system, as interpreted from figure 5.6 that again shows for which impact parameters the scattering will lead to planet consumption at crossing point A for the reference system in table 5.1. The Earth-planet orbit is already on a very eccentric orbit $e_2 = 0.9$ prior to the scattering event, yet a minority of the impact parameters considered lead to planet consumption. Given that the orbital parameters have been drawn from a uniform distribution without any bias, I expect that only a subset of all 500 systems in figure 5.7 are potentially planet-consuming.

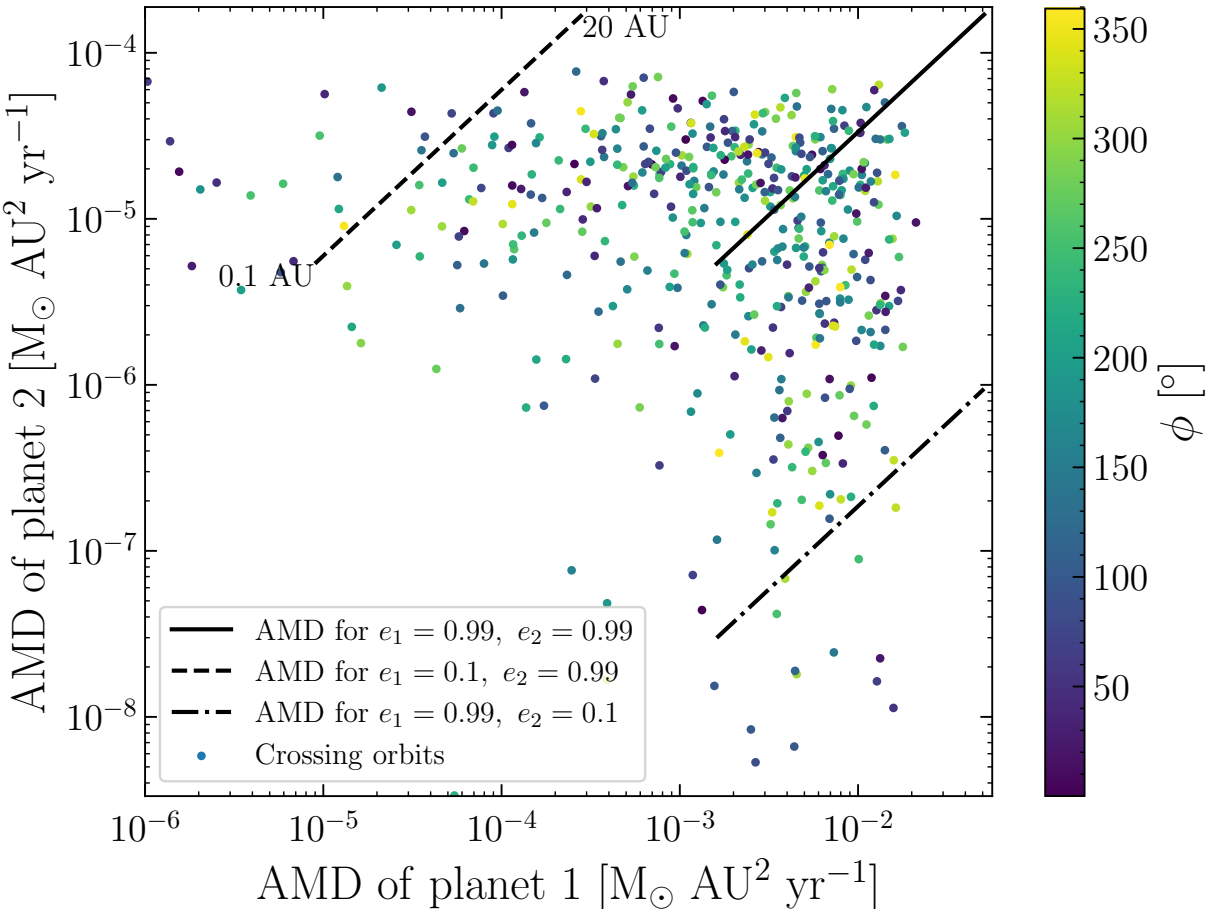

Figure 5.7: The distribution of the AMD for the Jupiter-type planet 1 and the Earth-type planet 2. The colour of the dots represents ϕ, which is the angle between the major axes of the two planetary orbits. The lines in the plot show the distribution of AMD values for the case where the two orbits have static eccentricities but the semi-major axes are varied between 0.1 and 20 AU. Observe that the crossing of orbits occurs if one or both of the planets have a high AMD.

In fact, I found that 118 out of the 500 crossing orbit systems and the 910 systems in total are planet-consuming. I have plotted the corresponding AMD distribution for the two planets in figure 5.8. Compared with all systems that are crossing but not consuming in figure 5.7 (now in grey), the planet-consuming systems mainly correspond to extreme cases of AMD combinations, i.e. where one or both planet have large AMDs. They are however difficult to distinguish from systems with extreme AMDs that are not consuming. In turn, it does not seem as if it is possible to formulate a criterion for planet consumption in terms of AMD from this simple analysis. Nevertheless, I still arrive at an important conclusion from the interpretation of the figure: it suffices that one of the planets has a large AMD for planet consumption to be possible.

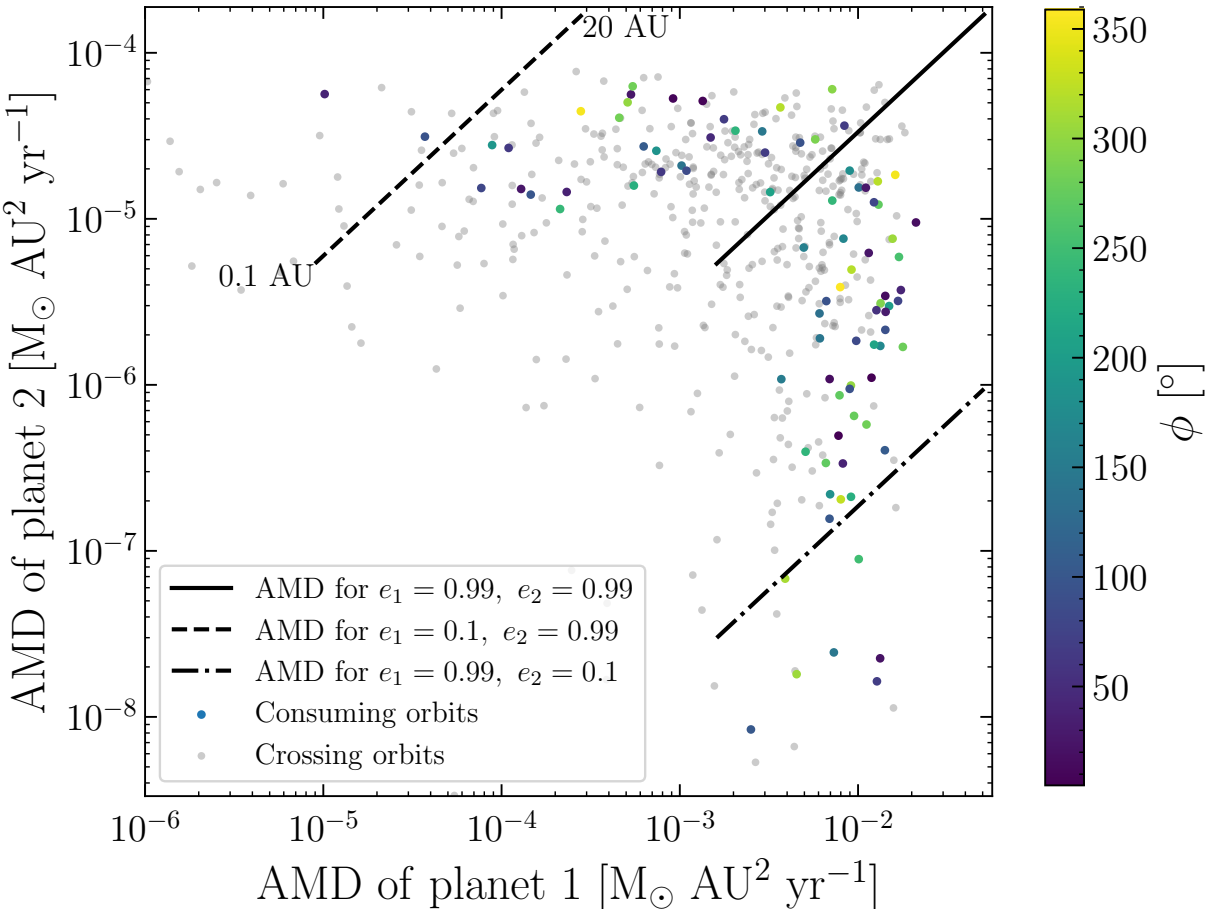

Figure 5.8: The same plot as in figure 5.7, but now highlighting the subset of systems that are planet-consuming. The grey data points represent the two-body systems that are not consuming.

To understand for which type of orbital configurations a system is more likely to be planet-consuming, I proceeded by investigating the impact of altering the various quantities that govern the outcomes of scattering events in this section.

5.4.1 Varying planetary mass ratios

The first quantity that I chose to investigate was the mass ratio between the planets in the system. From the analysis in section 5.1, I recall that there are implications that the mass ratio largely determines which outcomes are possible for scattering events within a system. This largely follows from the fact that the magnitudes of the velocities relative to the centre-of-mass, $\boldsymbol{v}_{1,b}$ and $\boldsymbol{v}_{2,b}$, regulate how large of a change is possible for the magnitudes of the velocities $\boldsymbol{v}_1$ and $\boldsymbol{v}_2$. Logically, if the planets are of equal mass i.e. $q_\mathrm{p} = 1$, it should be significantly more difficult to scatter one planet onto a consuming orbit than if one

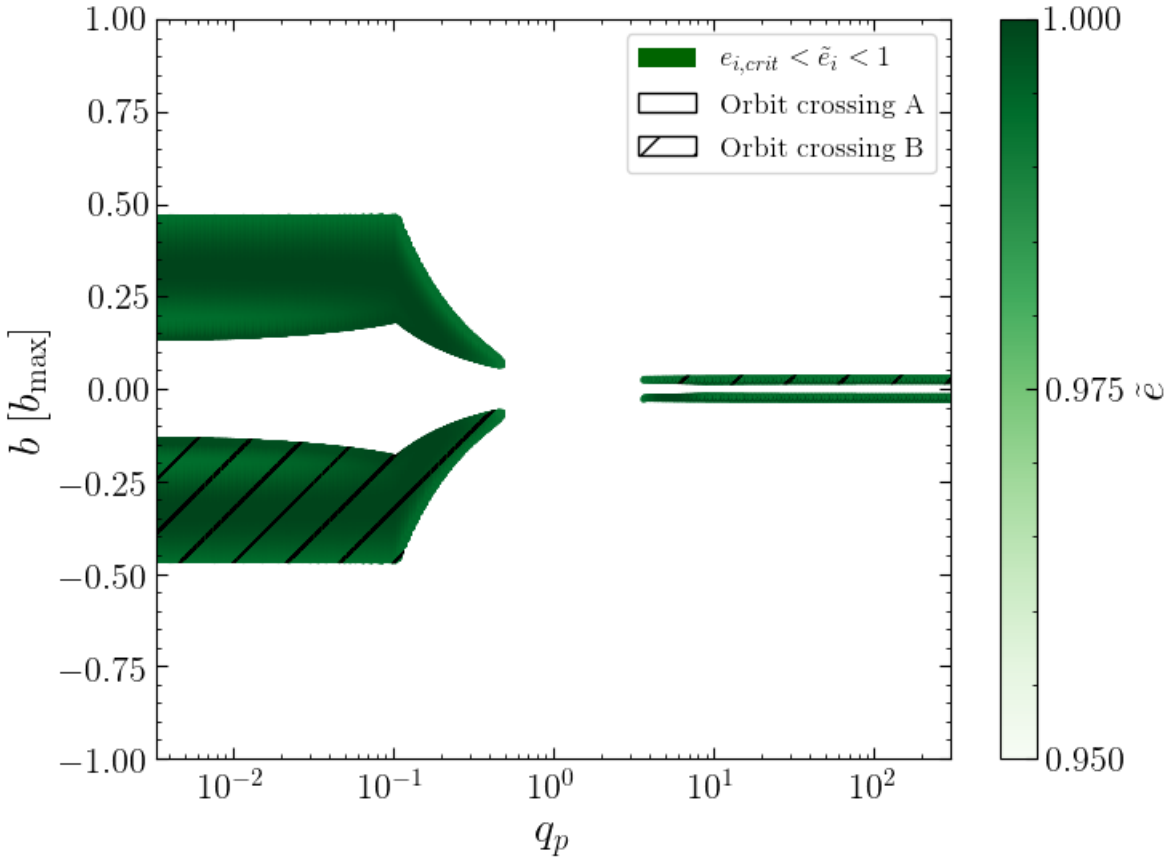

Figure 5.9: The combinations of mass fraction, q_p, and impact parameter that yield consuming scatterings. The total mass of the planets is fixed at 301 $M_\oplus$ meaning that the extreme cases correspond to an Earth-mass and a Jupiter-mass planet. The green non-hatched and hatched region represents the impact parameters that lead to planet consumption at crossing point A and B, respectively. The shade of green indicates the new eccentricity post-scattering.

planet is much more massive i.e. $q_\mathrm{p} \ll 1$ or $q_\mathrm{p} \gg 1$.

The impact of the mass ratio for the likelihood of having planet consumption in the system was found by taking the reference system in table 5.1 and altering the planetary masses, effectively changing the value of q_p. The masses were chosen such that the most extreme case is an Earth-mass and a Jupiter-mass planet. Since the mass ratio has been defined as $q_\mathrm{p} = M_{\mathrm{p},2}/M_{\mathrm{p},1}$, the values will be in the range $q_\mathrm{p} \in [0.0033, 300]$. For every single system, $b_{\max}$ was computed and then 10^4 impact parameters were again chosen by dividing the range $b \in [-b_{\max}, b_{\max}]$ using uniform steps in b. Here, I used a finer initial estimate and step size for `scatter.find_bmax` of $\beta_0 = 0.01$ and $\Delta b = 10^{-3}$ to increase the resolution. The results are shown in figure 5.9. In this plot, the green regions represent the range of impact parameters that lead to planet consumption. The non-hatched and hatched

regions represent the impact parameters that are consuming for orbit crossing A and B, respectively. The shade of green also shows the final eccentricity $\tilde{e}$ of the planet that is being consumed. It is unsurprising that the eccentricities all are close to unity for this case, as the critical eccentricity required to be directly consumed for a planet orbiting a Solar-type star at 1 AU is ~ 0.995.

There are three important features that I wish to emphasise in this plot. First, there is a regime below which the mass ratio does not directly affect the likelihood of planet consumption. At this critical $q_{\rm p}$ value, the secondary planet in the encounter will essentially be a test particle for the more massive planet. There is a slightly positive slope at the inner values when $q_{\rm p}$ decreases, which is only an effect of the planetary radius becoming smaller with decreasing mass, making merger between the planets less likely. The reason why this test particle regime exists can be found in the angular momentum of the less massive planet. The larger the mass difference is, the easier it is for the more massive planet to strip away a large fraction of angular momentum from the less massive planet. As can be seen in this plot, the primary planet removes practically all the angular momentum of the secondary planet for masses such that $q_{\rm p} \lesssim 10^{-1}$.

The second feature shows that for the reference system it is not possible for planets with equal mass to scatter each other into the host star. This also follows from the fact that the exchange of angular momentum will not be as extreme as for the low mass ratio cases. Additionally, the impact parameter range that potentially could cause a scattering to lead to planet consumption is narrowed due to $d_{\rm crit} = R_{\rm p,1} + R_{\rm p,2}$ becoming large and mergers becoming more likely. Hence, the initial eccentricity of the secondary planet must be larger than 0.9 for a planet to be consumed when $q_{\rm p} \sim 1$. This emphasises that the physical radii of the planets are important to consider in scattering events, as they limit the possible magnitude of the exchanged angular momentum and energy.

The third feature is that planet consumption is less likely if the planet on the eccentric orbit is much more massive than the other, i.e. for $q_p \gg 1$. Recalling once more that the possible change in orbital parameters is highly dependent on the position of the centre-of-mass, it is clear that it is not possible for an Earth-mass planet to scatter a Jupiter-mass planet onto an orbit with $\tilde{e} \sim 1$ such that it collides with the host star, no matter how close the planets get. Hence, the planet that gets consumed in the cases where $q_{\rm p}$ is large is still the less massive planet. Since the eccentricity of the planet has to be increased from $e_2 = 0$ to $\tilde{e}_2 \sim 1$, it is natural that only a few impact parameter values near $d_{\rm crit}$ will lead to a scattering that is strong enough.

5.4.2 Varying orbital elements

The next property of the system that I investigated was the orbital elements. Up to this point, I had found that a significant difference in mass facilitates planet consumption as an outcome and that there is a need for a large total AMD in the system. To understand more specifically what initial semi-major axes and eccentricities favour such an outcome,

Parameter	a_1 [AU]	e_1	$M_{\mathrm{p},1}$ [$\mathrm{M}_\oplus$]	a_2 [AU]	e_2	$M_{\mathrm{p},2}$ [$\mathrm{M}_\oplus$]	$M_\star$ [$\mathrm{M}_\odot$]
Value	0.3, 1, 3, 8	0	300	0.1 - 10	0.5 - 0.99	1 - 300	0.6 - 2

Table 5.2: The parameters considered for the planetary systems created to investigate the impact of altering orbital elements and masses.

I employ a more elaborate version of the analysis approach in the previous subsection. This is due to the fact that the parameter space is much larger for the orbital elements. Despite the flat system approximation, the semi-major axes and eccentricities of the orbits comprise four variables. If in addition I vary the masses, there are another two parameters to consider. Hence, to simplify the computations, I assumed that the properties of the primary orbit were static. I then varied the initial components of the secondary orbit in given ranges. The details can be found in table 5.2.

Before I go into the results of the analysis, I briefly discuss the governing principles using the Safronov number, which is given in equation (4.6) with a corresponding map for different masses and semi-major axes in figure 4.1. As explained in section 4.3.1, this number is simply the relative magnitude between the surface and planetary system escape velocities. Recall that a smaller semi-major axis will increase the likelihood for mergers whereas a larger semi-major axis will make ejections the more probable outcome. Since this essentially means that it is easier to deflect a planet that is further away from its host star, the impact parameter that leads to a specific absolute exchange of angular momentum increases with distance from the host star. This can also be motivated using the fact that the mutual Hill radius of a two-planet system increases with their semi-major axes. Intuitively, this would mean that planet consumption is more favoured for planets that are further out in the system, but there is an important trade-off that complicates matters. The further a planet is from its host star, the larger the critical eccentricity for planet consumption becomes. In order to determine which effect will dominate, it is necessary to evaluate a significant portion of the parameter space at hand.

The systems were set up by making a parameter grid for a_2 and e_2 using the ranges specified in table 5.2. For the semi-major axis, I chose to use 100 different values with logarithmic spacing and for the eccentricities I used 50 values with uniform steps of $\Delta e_2 = 0.01$. Furthermore, I employed 50 different masses for the secondary planet such that $q_\mathrm{p} \in [10^{-3}, 1]$ with logarithmic spacing. Additionally, I used 4 different semi-major axes for the circular orbit of the primary Jupiter-mass planet. All-in-all, 10^6 different systems were investigated, with 250 000 for each value of a_1. For each system, I carried out scatterings with 1000 different impact parameters within $b \in [-b_\mathrm{max}, b_\mathrm{max}]$, where b_max was estimated for each system using `scatter.find_bmax` with the fiducial settings. Given that there are two different crossing points, I obtained a total of 2000 scatterings. After the scattering I could obtain a fraction of impact parameters that are consuming which I chose to denote $f_\mathrm{consuming} = N_\mathrm{consuming}/N_\mathrm{scatter}$. By summing all of the values of $f_\mathrm{consuming}$ for each value of q_p, I obtained the plot in figure 5.10. There are four lines, one for each value of a_1 normalised

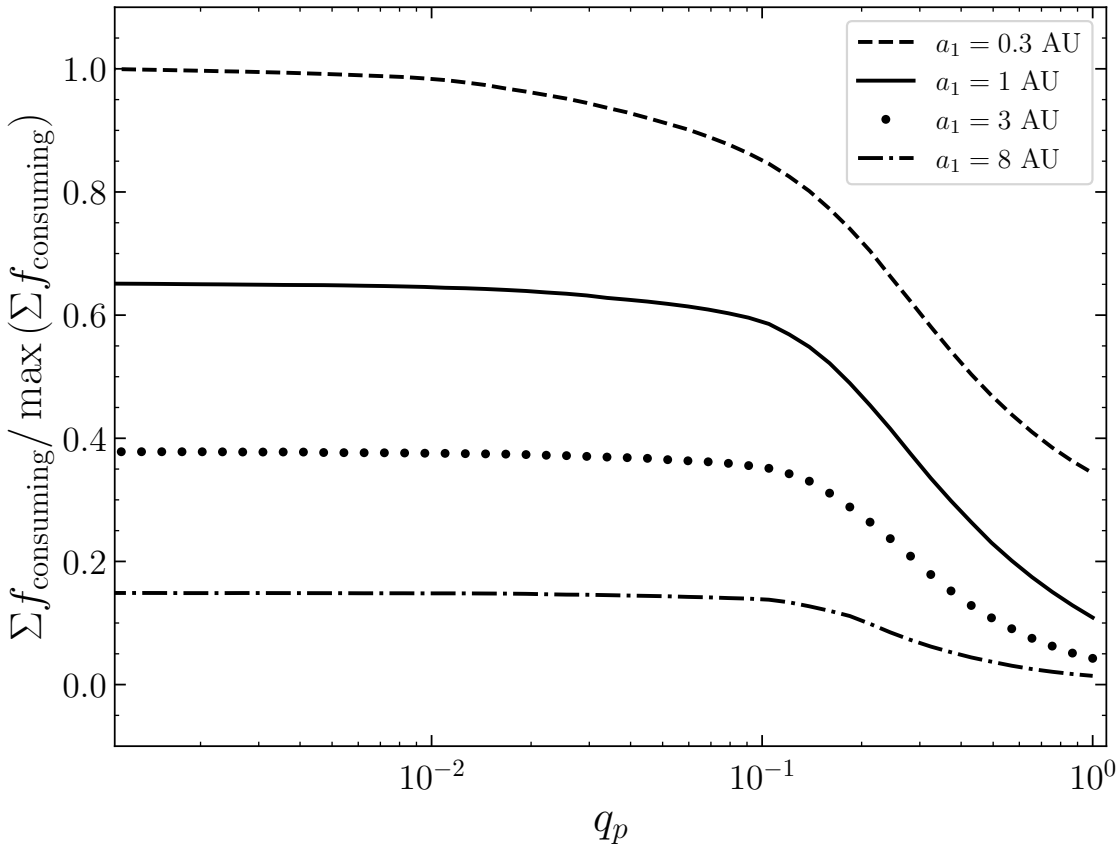

Figure 5.10: The relative fraction of systems that are potentially planet-consuming for the set of parameters considered, which are given in table 5.2. Each line represents a different static value of a_1 which is the semi-major axis of the circular orbit of a Jupiter-mass planet.

by the maximum value for each q_{p}, in this case given by $\sum f_{\text{consuming}}$ for $a_1 = 0.3$ AU. Hence, the plot mainly shows the relative difference between the number of consuming scatterings in the 250 000 systems for each specific value for a_1. From the figure, it is evident that the distance from the host star is more important than the increased likelihood of mergers rather than ejections. Looking at the critical eccentricities for the smallest and largest values of the primary planet's semi-major axis, I observe that $e_{\text{crit}}(a_1 = 0.3 \text{ AU}) = 0.9845$ and $e_{\text{crit}}(a_1 = 8 \text{ AU}) = 0.9994$, which explains the notable relative difference in consuming scatterings. Despite the angular momentum of the secondary planet being lower for $a_2 \sim 8$ AU, making it easier for the primary planet to eject, the difference in e_{crit} will dominate and make consumption more likely the closer in to the host star that the scattering takes place.

Another feature of figure 5.10 is the variation of the test particle limit with the distance from the host star. If the scattering occurs near the host star ~ 0.3 AU, the test particle limit is close to $q_{\text{p}} \sim 2 \times 10^{-3}$, while the test particle range begins at $q_{\text{p}} \sim 10^{-1}$ when the

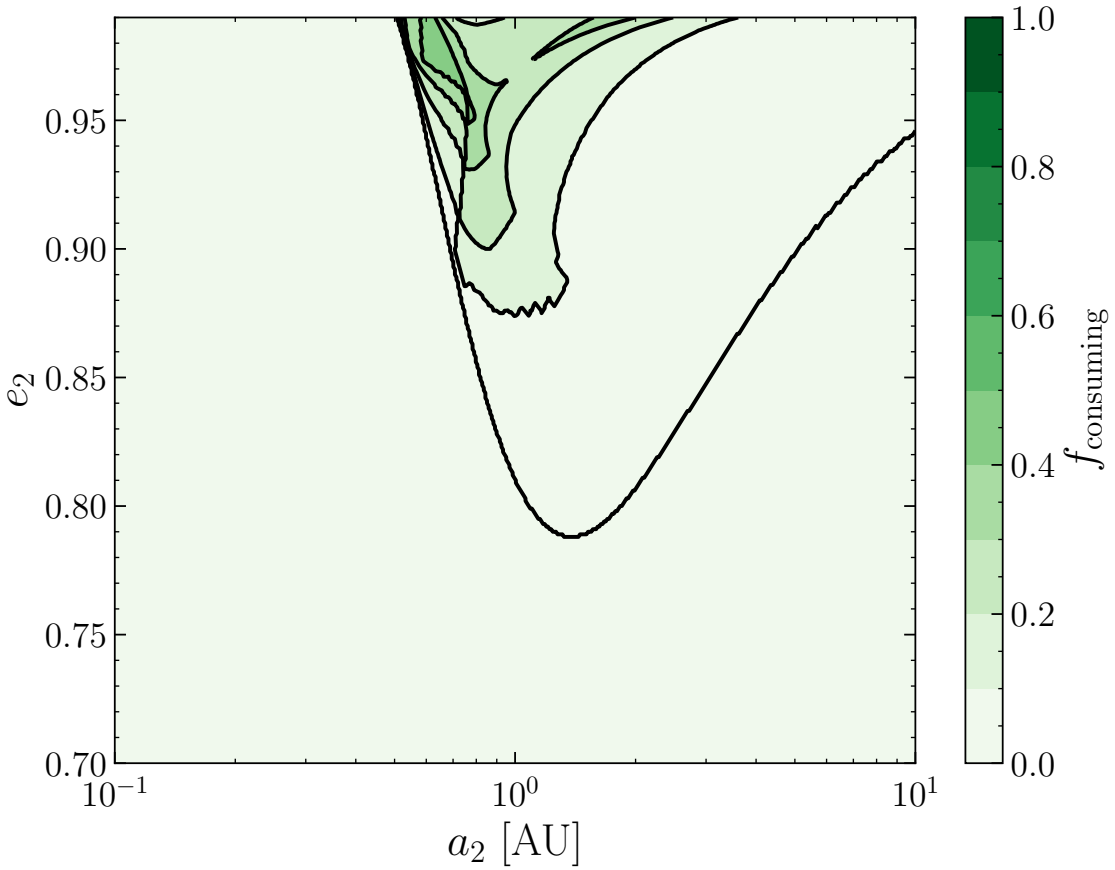

Figure 5.11: Contour plot of the fraction of consuming impact parameter values in the range $b \in [-b_{\max}, b_{\max}]$ for the parameter space of (a_2, e_2) given in table 5.2. The masses of the planets are kept static with $M_{\mathrm{p},1} = 300$ $\mathrm{M}_\oplus$ and $M_{\mathrm{p},2} = 1$ $\mathrm{M}_\oplus$ and the same goes for the circular orbit of the primary planet with $a_1 = 1$ AU.

scattering occurs at $a \sim 8$ AU. Said effect is again due to the increase in angular momentum with an increasing semi-major axis and the varying value of $b_{\max}$. The Jupiter-mass planet can get close enough to remove all of the angular momentum of a 30 $\mathrm{M}_\oplus$ planet at 8 AU, while a similar ΔJ scattering at 0.3 AU only can occur for scatterings where $d \leq d_{\mathrm{crit}}$ and the planets merge.

To show the importance of having a large initial eccentricity, I also show $f_{\mathrm{consuming}}$ for the parameter space (a_2, e_2) given a primary circular orbit with semi-major axis $a_1 = 1$ AU in figure 5.11. To improve resolution I have used $\Delta e_2 = 10^{-3}$. The plot evidently emphasises that more planetary systems are planet-consuming when the total AMD is above a given level and the semi-major axes of the two orbits are similar. Moreover, planet consumption is favoured when the secondary planet, in this case of Earth-mass, is closer to the host star than its more massive planetary companion. Another feature is that the fraction of consuming impact parameter values only reaches levels of ~ 0.5 despite having initial

eccentricities up to 0.99. In order to reach $f_{\text{consuming}}$ values ~ 1 the initial eccentricity at the time of scattering must be close to the critical eccentricity which is larger than 0.99 in all orbital configurations where the orbits are crossing for this primary orbit. Hence, I state the following hypothesis regarding two different planet consumption scenarios

1. **Strong planet consumption:** A few strong scatterings boost up the eccentricity of a planetary orbit, ultimately putting it on a consuming trajectory.
2. **Diffusive planet consumption:** A diffusive process where a planet undergoes a large number of weak scatterings, slowly increasing the eccentricity of its orbit until it is put on a consuming orbit.

I address this hypothesis further in section 5.6 where I investigate the effect of subsequent planet–planet scattering.

5.4.3 Varying the stellar mass

The last property of the system that I chose to vary is the stellar mass. This was done in a similar approach to that in section 5.4.1, but the mass of the secondary planet was kept at $M_{\text{p},2} = \text{M}_\oplus$. The stellar mass range was chosen to be $M_\star \in [0.6\ \text{M}_\odot, 2\ \text{M}_\odot]$, which includes a majority of the observed planetary hosts as seen in figure 3.5. The stellar mass mainly influences two physical properties of the scattering events. First, a lower mass will mean a larger Safronov number and in turn more ejections since the planets will have a smaller orbital velocity and less angular momentum, making them easier to eject. Hence, for larger masses mergers will become more likely and the minimum impact parameter value that is allowed for planet consumption increases. The second effect is directly related to the critical eccentricity needed for planet consumption, as the stellar radius will vary with the mass according to figure 3.5, effectively altering r_{crit}. Similarly to the case of the varying mass ratios, there is an ambiguity regarding which physical effect will dominate and facilitate planet consumption.

The results for the four different values of a_1 can be found in figure 5.12 which have been produced in the same manner as figure 5.10. Again, the systems where $a_1 = 0.3$ AU will have the most planet consumptions. The optimal mass for the host star is $M_\star \sim 1.3\ \text{M}_\odot$ and coincides with the second derivative global minimum of the ZAMS $R_\star(M_\star)$ relation presented in section 3.5. The relative physical radius per mass of the host star is evidently the dominating factor for all of these systems and this quantity is indeed maximal at $M_\star = 1.35\ \text{M}_\odot$. Looking at the value of $\sum f_{\text{consuming}}$, it decreases for $M_\star > 1.35\ \text{M}_\odot$ despite the increasing radius of the host star. Hence, the larger binding energy of the system and increased orbital velocity which leads to an overall decrease in the Safronov number still play a major role in making planet consumption less common. Given that $R_\star/M_\star = 0.98\ \text{R}_\odot/\text{M}_\odot$ for $M_\star = 1.35\ \text{M}_\odot$, I simply use the Sun as the fiducial star for the remaining analysis in this thesis.

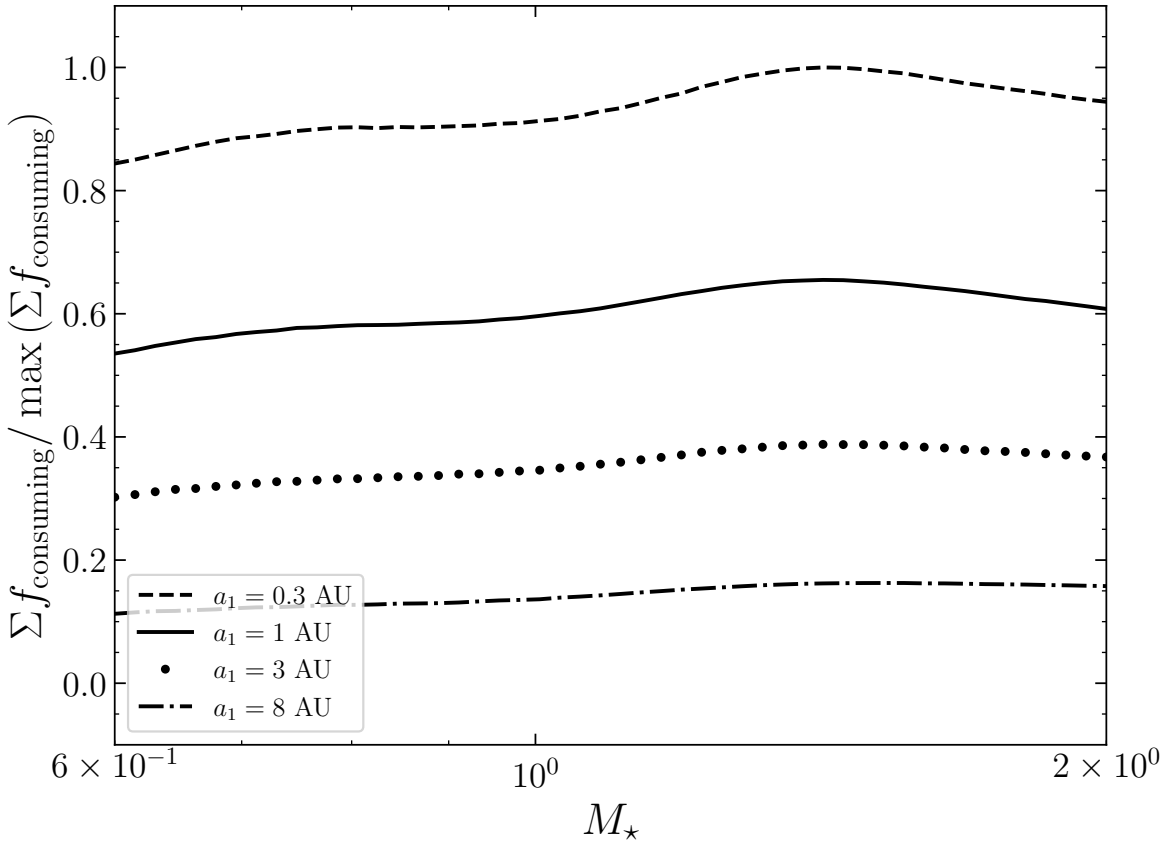

Figure 5.12: The relative fraction of systems produced with the parameter ranges given in table 5.2 that can have planet-consuming events for different stellar masses. The values have been normalised with respect to $\sum f_{\mathrm{consuming}}$ for the semi-major axis a_1 that yields most planet-consuming events.

5.5 Planet-consuming systems in 2D

Here I aim to summarise which orbital configurations are most likely to have planet consumptions in a flat system given the analysis in this chapter. The conclusions can then serve as an estimate for which type of orbital configurations will lead to planet consumption in a full three-dimensional analysis, which is done in chapter 6.

While the flat system parameter space $(a_1, e_1, M_{\mathrm{p},1}, a_2, e_2, M_{\mathrm{p},2}, M_\star)$ is large despite letting $i_1 = i_2 = 0°$, I managed to restrict it by inferring a few general trends where planet consumption is facilitated for certain orbital configurations. For reference, the following conclusions are mainly based on the information in figures 5.5 and 5.8 - 5.12.

Insights from the two-body analysis

1. The AMD in the two-planet subsystem needs to be above a given threshold for one or both planets in order for planet consumption through strong scattering to be possible.
2. While the AMD can be increased by having the scattering event be more distant from the host star, this increases the value of $e_{\rm crit} = 1 - r_{\rm crit}/a$, making consumption of a planet less likely. Hence, orbits with high initial eccentricities near the host star are more favourable than less eccentric orbits with large semi-major axes even if the AMD of these orbits is equal.
3. An extreme planetary mass ratio increases the strength of planet–planet scattering and thereby also the likelihood of a planet being consumed in a given system. However, below a limiting mass ratio related to the distance from the host star, the secondary planet can be considered a test particle and will always be consumed for impact parameters $d_{\rm crit} < b \leq \kappa b_{\rm max}$, where κ is a constant such that $0 < \kappa \leq 1$. The value of this constant depends on the orbital configuration $(a_1, e_1, a_2, e_2, M_\star)$.
4. It is preferable that the secondary, less massive planet is on an orbit within the primary planet orbit. Moreover, planet consumption is favoured when $e_1 < e_2$, where e_1 belongs to the most massive planet.
5. Planet consumption is more likely for stars with large values of $R_\star/M_\star$. For the $R_\star(M_\star)$ relation considered, this coincides with the case of $M_\star = 1.33$ $\mathrm{M}_\odot$. This again relates to the formula $e_{\rm crit} = 1 - r_{\rm crit}/a$. While it is more difficult to obtain large values of e for a more massive star due to the planets carrying more angular momentum, this is counteracted by the increasing value of $r_{\rm crit}$ if $R_\star/M_\star$ is large.

5.6 Subsequent planet–planet scattering

Up until this point, my method has been largely focused on investigating planet consumption through strong scattering. This corresponds to the first of two scenarios I formulated as a hypothesis in 5.4.2 where one of the planets within a system already has a high enough eccentricity to allow for planet consumption after one scattering event. In order to expand this analysis to include the second scenario where the two planets undergo a diffusive exchange of angular momentum and energy over a large number of subsequent scatterings before planet consumption, I have used a Monte Carlo simulation approach. In these cases, AMD is generated such that one planet ultimately ends up on a highly

eccentric planet-consuming orbit.

To perform these simulations, I wrote the function `mc_scatter` as a part of the `scattersim` class. The program takes the orbital configuration $(a_1, e_1, M_{\mathrm{p},1}, a_2, e_2, M_{\mathrm{p},2}, M_\star)$ as input and a number N_b, which corresponds to the number of impact parameters to consider. It will then operate according to the following algorithm:

1. An impact parameter is drawn from the uniform distribution $b \in [-b_{\max}, b_{\max}]$.
2. Scattering is carried out at either crossing point A or B of the system at random using `scatter.scatter`.
3. If any of the following statements are true regarding the outcome of the scattering, the current simulation will be terminated.
   - The orbits no longer cross.
   - One of the planets has collided with the host star.
   - One of the planets has been ejected from the system.
   - The two planets have collided and merged.
   - The system is unresolved after 10^4 scatterings.
4. If none of the above has occurred, the orbital parameters will be updated such that $a = \tilde{a}$ and $e = \tilde{e}$.
5. Repeat from step 2.

This process is then repeated N_b times for the given system.

The difficulty with this approach is to know which initial configurations to choose. While drawing eccentricities and semi-major axes at random until a crossing orbit is found as was done in section 5.3 is a possibility, such a method carries an important caveat. The fact that the orbital configuration with crossing orbits would be created at random also means that it could correspond to the configuration at any given time during the dynamical evolution. Hence, the two planets may already have undergone a series of subsequent scatterings to end up with the corresponding orbital elements. To remain as close to a real physical scenario as possible, it makes more sense to follow the subsequent scattering from the first close encounter after orbit crossing until the system has been resolved. Therefore, I chose to circumvent this issue by combining the Monte Carlo analysis with the results of the full three-dimensional numerical integrations in chapter 6. The resolution lies in the fact that both the initial configuration of the planets prior to orbit crossing and the orbital configuration of the two planets at the first scattering event are known.

The initial configuration for this study is the fiducial configuration from section 6.2, consisting of two inner Earth-mass (also referred to as X-type) planets and three outer Jupiter-mass (J-type) planets. I go into detail regarding the motivation behind this configuration in said section and the simulation setup is presented in section 6.1. For this analysis, it

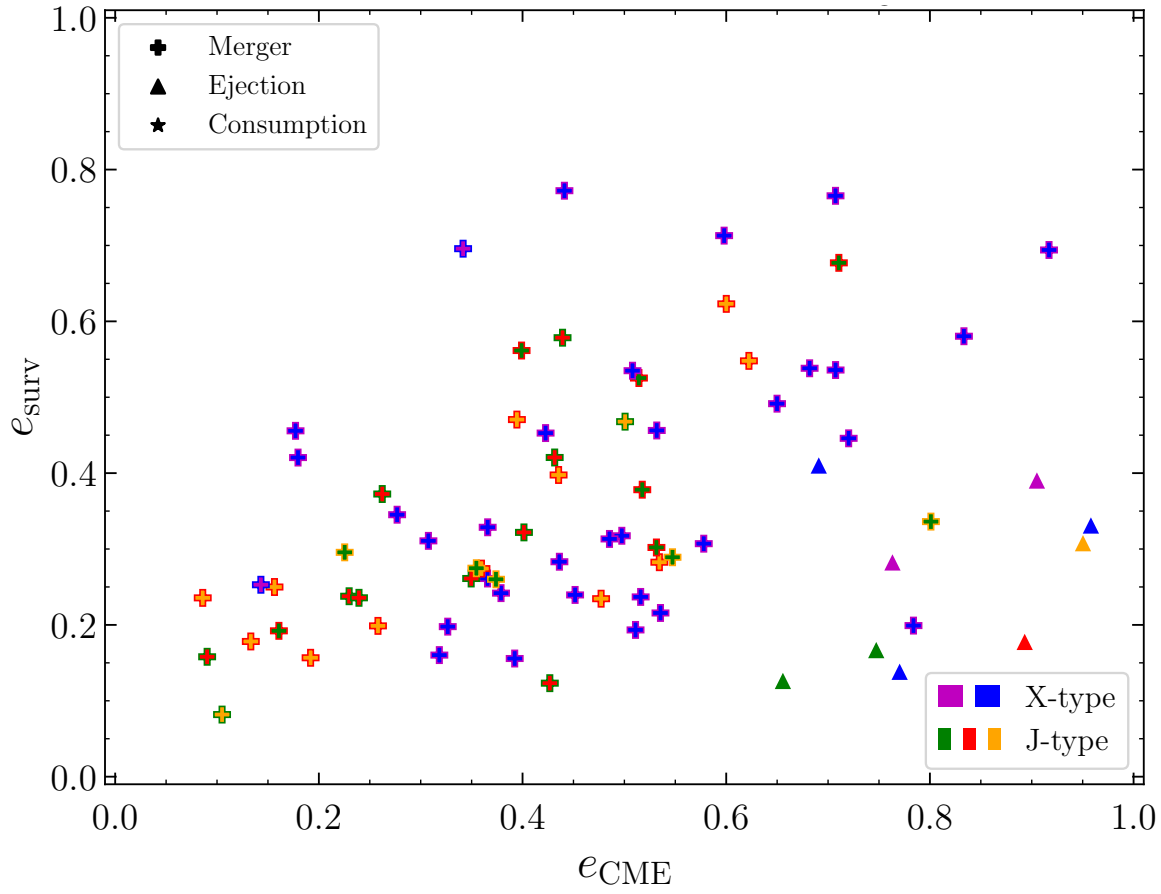

Figure 5.13: The eccentricities prior to the final scattering for the cases where one planets undergoes consumption, merger or ejection. For description of the markers, see text.

suffices to be familiar with their initial orbital semi-major axes, which can be found at the top of figure 6.1. The plots in this section follow the same colour scheme to pair a given planet with its outcome from the Monte Carlo simulation. In total, I used the first unique close encounter for each planet from 100 integrations and evolved them for a maximum of 10^4 scatterings.

In figure 5.13 I have plotted the eccentricities for the survivor e_{survivor} and the CME-type planet e_{CME} prior to the final scattering event. There are three different symbols, each representing a CME outcome

- ⋆ Indicates that the planet has been consumed by the host star.
- + Shows that the two planets considered have merged. The face and edge colours represents the CME and surviving planets, respectively.
- ▲ Indicates that the planet has been ejected.

From the results, the main issue with the flat system model becomes evident. Almost all

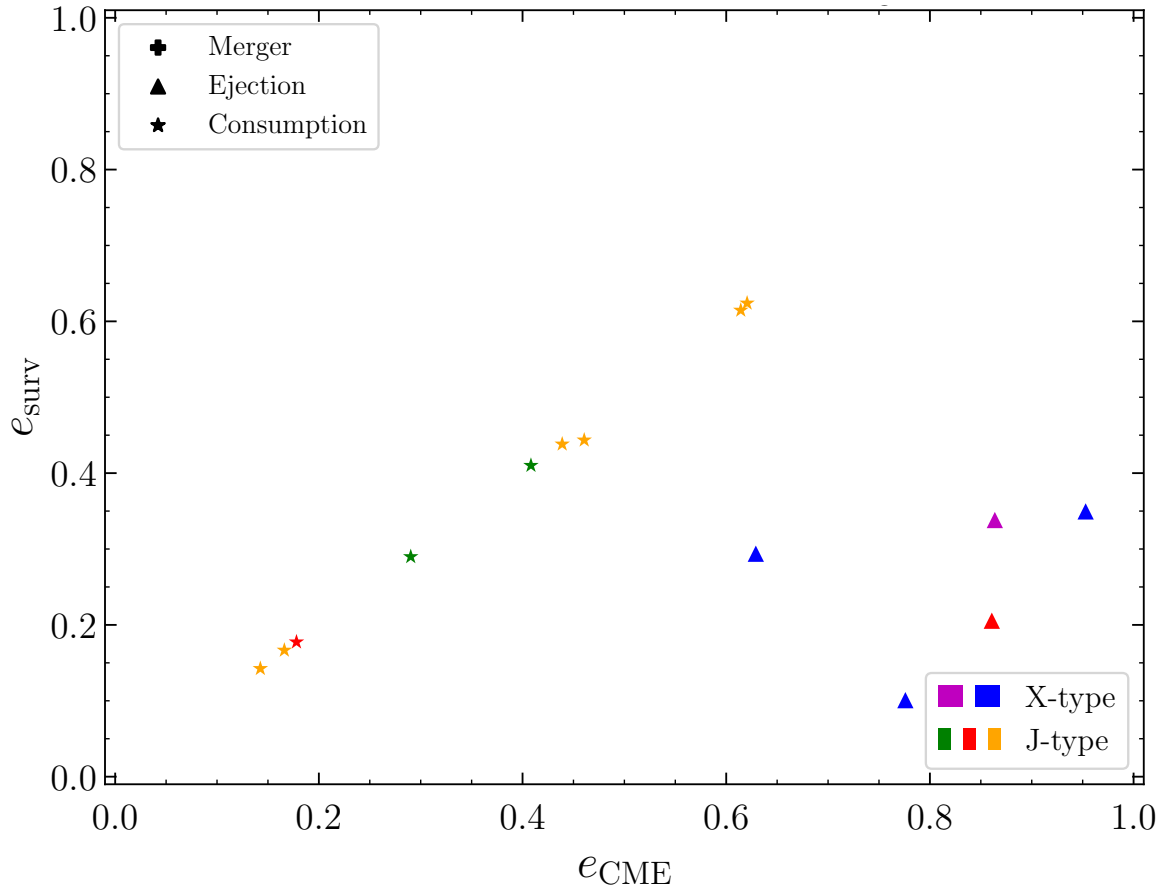

Figure 5.14: The same as in figure 5.13 but the planets are considered to be point-like particles with no physical radius.

CME outcomes are mergers, with the exception of nine ejections. The rest of the systems are either unresolved due to the orbits no longer crossing or the number of scatterings exceeding 10^4. For a more realistic case where $i_{\mathrm{p}} > 0$, the mergers would be much more rare as a mutual inclination of only a few degrees will cause the planets to pass each other without merging despite the scattering having a two-dimensional impact parameter such that $|b| \leq d_{\mathrm{min}}$. Nevertheless, the planets still end up with a rich distribution of eccentricities, many in which the eccentricities of the planets indicate AMD levels that are large enough for planet consumption to be possible. Moreover, when looking at the number of scatterings before a CME outcome, the planets only undergo between one and ten before merging. Therefore, it is plausible that the flat system approximation causes the systems to resolve too early and that they could potentially be planet-consuming in three dimensions.

In order to test this idea, I also performed a set of Monte Carlo simulations for the same systems while considering the planets as point-like particles, i.e. letting $R_{\mathrm{p}} = 0$, effectively removing mergers as a potential outcome. The corresponding eccentricity distribution

can be found in figure 5.14. While most systems are unresolved, there are a number of consumption events for this scenario. More specifically, there have been consumptions of Jupiter-mass planets after scattering against another Jupiter-mass planet between 50 and 1000 times. Simply by observing that the survivor and CME planet have similar eccentricities shows that this indeed has been a slow scattering process, where AMD is increased slowly over time. The values of their respective eccentricities prior to the final scattering do not coincide with the previous picture of planet-consuming scattering in this chapter. However, the reason why these cases still lead to planet consumption is due to the point-like particle assumption which allows the planets to have impact parameters $|b| \ll d_{\text{crit}}$ even close to zero, which would correspond to an extremely strong scattering that would not be physically possible in a real case scenario.

The other subset of outcomes correspond to ejections of Earth-mass planets and one Jupiter-mass planet. In this case, the surviving planets have low eccentricities prior to the final scattering event, while the CME-type planets have large eccentricities, indicating that these systems likely could have resolved in a planet consumption as well, given the AMD distributions for planet-consuming systems in figure 5.8. The number of scatterings for the ejection of the X-type planets are much lower than for the Jupiter, meaning that they have different dynamical histories. Unsurprisingly, the mass ratio in their scatterings is $q_{\text{p}} \sim 10^{-3}$ which again reinforces the theory that an extreme mass ratio facilitates consumption or ejection through a few strong subsequent scatterings.

I now summarise the findings of this section and come back to this topic in section 6.3 where I discuss said problem in a three-dimensional setting.

Subsequent scatterings with Monte Carlo

1. Due to the flat system approximation, most of the subsequent scatterings lead to mergers. This would most likely not be the case in a three-dimensional scenario.
2. The systems only undergo between one and ten scatterings before merging, indicating that they resolve too early and might be planet-consuming in a more physical scenario where $i_{\text{p}} > 0°$.
3. When treating the planets as point-like particles, the number of scatterings before resolution increases significantly. When $q_{\text{p}} = 1$ the consumed planets must scatter more than 50 times but when $q_{\text{p}} \sim 10^{-3}$ they only need a few scatterings to end up on planet-consuming orbits. Hence, a mass ratio near unity will favour diffusive consumption while an extreme mass ratio will favour strong consumption.

Chapter 6

Modelling the evolution of planet-consuming planetary systems

The results obtained from the study using the two-body analysis model lack real physical meaning for the true behaviour of multiple planet systems if it cannot be backed up with similar conclusions from a more realistic model. This is due to the fact that there are many limiting assumptions that make the model inherently unrealistic. However, it is not possible to find general analytical solutions for a system with three or more bodies. Hence, in order to truly understand when and how planet-consuming events occur, I have employed a numerical approach that can dynamically evolve planetary systems in three dimensions without the need to isolate separate scattering events from the other bodies in the system. This was achieved using N-body simulations with the software `MERCURY` (Chambers, 1999). In this chapter, I thus present the basic ideas of numerical N-body simulations and why they are the main tool for understanding planetary dynamics. I proceed by introducing the `MERCURY` code and the algorithm used to evolve planetary systems dynamically. Given that I have limited the phase-space of orbital configurations and formulated predictions for potentially planet-consuming systems using the two-body analysis in chapter 5, I can save a significant amount of computing time by using the results as a basis for the choice of initial configurations for the `MERCURY` runs. Hence, I compare the outcomes of the predictions from the two-body model and the N-body simulations, ultimately providing further insight into which types of systems allow for planet consumption.

6.1 Gravitational N-body simulations with `MERCURY`

As stated above, there is no general analytical solution for the dynamical evolution of a system with more than two bodies. Instead, one has to opt to use numerical methods to efficiently find approximate solutions to such a problem, which usually goes under the

name of 'the classical N-body problem', where $N > 2$. To find a solution, I consider a set of equations of motion that corresponds to the change in position and velocity over time in each dimension of our system. This type of relation is referred to as an Ordinary Differential Equation (ODE). They are integrated by considering the change in each parameter for a small time step over a finite period of time. The total force per unit mass acting on a specific particle with index k in set of N particles is given by the sum of its gravitational interactions

$$\ddot{\boldsymbol{r}}_k = -\sum_{k=1, n\neq k}^{N} \frac{GM_n(\boldsymbol{r}_k - \boldsymbol{r}_n)}{|\boldsymbol{r}_{k,n}|^3}. \tag{6.1}$$

The complete solution for the position $\boldsymbol{r}_k$ and velocity $\boldsymbol{v}_k$ at a given time t is given by $6N$ first order differential equations.

As integration can only be performed over a finite time, this hinders my ability to find a unique solution to the problem. Furthermore, numerical errors will arise during the integration due to the limitations of the instruments performing the calculation, since they have a limited precision as compared to analytical methods. This is commonly referred to as machine error. The numerical errors that arise can often be characterised by using conservation laws. For example, I expect the energy to be constant in a closed system and the change of energy can thus be used to quantify the success of the integration.

The energy loss in astronomical N-body simulations mainly comes from the fact that the choice of time steps for the integration generally do not provide the same detail in the movements of all objects in a system. To elaborate, errors tend to propagate in e.g. short-period orbits as a step in time affects the motion of such a particle more than for planet positioned further out in the system. Hence, if the time step is not adaptive or very small in order to account for such precision errors, they will quickly grow larger for a system with largely different semi-major axes, causing the integration to diverge from the true physically accurate behaviour. The simplest method for estimating the ODE solutions is given by Euler's method (Euler, 1768), which is based on the first order Taylor expansion

$$\dot{\boldsymbol{r}}_k(t) = \ddot{\boldsymbol{r}}_k \Delta t + \dot{\boldsymbol{r}}_k(t_0) \tag{6.2}$$

$$\boldsymbol{r}_k(t) = \frac{1}{2}\ddot{\boldsymbol{r}}_k \Delta t^2 + \dot{\boldsymbol{r}}_k(t_0)\Delta t + \boldsymbol{r}_k(t_0), \tag{6.3}$$

where $\Delta t = t - t_0$ and t_0 is the time for the previous position and velocity. This primitive method will quickly accumulate a large error if Δt is not kept small and also requires $\mathcal{O}(N^2)$ operations for each summation, making it computationally expensive. Such methods that do not introduce explicit approximations to compute the derivatives are referred to as 'direct methods'. While codes based on the direct method are much slower than other approaches, such as tree codes, mesh codes or fast multiple methods (see Aarseth, 2003,

for an extensive review), they nevertheless provide the highest accuracy, which is why it is the method of choice for this thesis.

In order to mitigate the time-consuming approach of the direct method, N-body simulation codes often employ *adaptive time steps*, where the size of the time step changes with the level of accuracy needed to find a good estimate for ODE solutions. Another way of reducing numerical errors when computing the solutions to the ODEs is to use various integration schemes that improves accuracy using higher order estimates of the derivatives. For example, one can opt for the commonly used explicit Runge-Kutta methods (Runge, 1895), which essentially are higher order versions of Euler's method with weighted derivatives from intermediate time steps in the range $[t_0, t]$.

The best choice for the integrator in this work is a highly accurate method with an adaptive time step to deal with extreme mass ratios, differences in orbital period and numerous close encounters. The well-tested and popular `MERCURY` code has several integrators to choose from and performs especially well for planetary systems with few bodies as shown in the comparison by Grimm & Stadel (2014), making it an appropriate code for this work. The integrator of choice is based on the Bulirsh-Stoer method (Bulirsch & Stoer, 1966), which I introduce in the next section.

6.1.1 The Bulirsch-Stoer method

Instead of using a static high order expansion of the derivatives to estimate a solution for the equation of motion (6.1), the Bulirsch-Stoer integrator is based on extrapolation. The main idea behind the method is the assumption that the answer to the numerical calculation over a single time step is in itself an analytic function, which is called 'Richardson's deferred approach to the limit'. Hence, by evaluating the derivative for a number of different time steps Δt that will not yield a high enough accuracy by themselves, the results can be fitted to said analytical function. A good approximation of the true value can then be obtained by evaluating the analytical function at $\Delta t = 0$ yr. This method is known as Richardson extrapolation (Press, 1992). The number of time steps needed for each analytical fit depends on the accuracy of the estimate. Hence if the errors for the extrapolation are deemed too large, the number of intermediate time steps will be increased along the proposed sequence from Stoer & Bulirsch (2013)

$$n = 2, 4, 6, 8, 12, 16, 24, 32, 48, 64, 96, \ldots \tag{6.4}$$

The fit to the assumed analytical function that solves the problem is carried out using Richardson extrapolation with either polynomials or rational functions. An elegant property of the Bulirsch-Stoer method is that it has an error series that is strictly even, i.e. consists of only even powers of Δt, which was found by William B. Gragg (Press, 1992). This result leads to the fact that the error can be evaluated in terms of Δt^2, increasing the

accuracy of the fit two orders at a time when combining all separate attempts for n steps within Δt.

While each fit can be a time-consuming process, since the value of n needed to obtain an adequate analytical fit varies, the key property of the Bulirsch-Stoer method is that the size of the time step depends on each separate problem, meaning that it is inherently using adaptive time steps. Given the fact that I expect a period of chaotic dynamical evolution, where a number of bodies are lost due to CME events that last between 10^3 and a few 10^6 yr, followed by a few $10^5 - 10^6$ yr of calm motion, the use of an adaptive time step is necessary to keep the elapsed real time reasonably low.

In order to govern the accuracy of the variable time step integration, `MERCURY` uses an accuracy parameter as input, which roughly determines how large error the integrator will tolerate for each time step. For a typical simulation of the dynamical evolution of a tightly packed planetary system with mass ratios between 10^{-3} and unity with an accuracy parameter of 10^{-11}, the relative energy error during the integration was always kept at less than 10^{-3}.

6.1.2 Initial setup in `MERCURY`

In order to investigate the evolution of potentially planet-consuming systems, I have used version 6.2 of `MERCURY` which was written by John Chambers in the programming language `Fortran77` (Chambers, 1999). For all integrations, I have used the Bulirsch-Stoer method with an accuracy parameter of 10^{-11} to have a low relative energy error for each time step. Due to the results in section 5.4.3, the choice of central body is a host star with $M_\star = \mathrm{M}_\odot$ and $R_\star = \mathrm{R}_\odot$. The coordinate system of choice is centred on the host star. This simple system facilitates the determination of the final position of the planets with respect to the host star after the conclusion of an integration. However, a potential issue with this approach is that a planet consumption event where the planet transfers a significant amount of energy will perturb the initial position of the host star relative to the system barycentre[1]. Hence, a barycentric coordinate system would allow for better estimates when comparing the final orbital elements of several planets. Nonetheless, since the main purposes of this work is to survey the separation between a given planet and the host star during the dynamical evolution, I chose to proceed with the central body coordinate system.

Each planet is initiated with a specific semi-major axis, average density and radius within which it will undergo close encounters. The average density is computed for a given mass by the joint mass-radius relation in equations (3.1) and (3.2) under the assumption that the planets are completely spherical. The number of mutual Hill radii needed to trigger a close encounter is kept at unity. The remaining orbital elements required to initiate the planetary orbits are drawn at random from a set of uniform distributions given in table 6.1.

[1] Usually the centre of mass for all bodies in the system.

Orbital element	e	i	θ	ω	Ω
Distribution range	$[0, 0.01]$	$[0, 5]^\circ$	$[0, 360]^\circ$	$[0, 360]^\circ$	$[0, 360]^\circ$

Table 6.1: Ranges for the initial orbital element values of each planet initialised in the `MERCURY` simulations.

The orbits are initially kept circular with low eccentricities $e < 0.01$, while they are given random inclinations between 0° and 5°. Such a distribution of inclinations leads to average mutual inclinations of $2^\circ - 3^\circ$, which is consistent with 'Kepler' satellite observations of planetary systems with multiple super-Earths (Johansen et al., 2012).

6.2 Potentially planet-consuming configurations

Given that I obtained a set of predictions from the two-body analysis (see section 5.5) as to which type of system will likely be planet-consuming, they were the motivation behind the choice of fiducial orbital configuration for the full three-dimensional analysis of planet-consuming systems. In this section, I go through them one by one and explain how the initial configuration of the planets abide by these theories.

First of all, the AMD within the two-planet subsystem that undergoes planet–planet scattering needs to be above a given threshold. Hence, since the initial orbits of my planetary systems of choice (see section 3.2) are quite circular, the AMD of the individual planets will not allow for orbital crossing. Therefore, there must be a clear pathway for that to occur during the evolution. To elaborate, the total AMD must be redistributed among the planets during the initial stages of the evolution such that there will be a surplus of AMD in at least one planet before there can be any close encounters. To ensure that the system will undergo a dynamical evolution with a significant change in AMD between the planets, it has to be initially unstable. While there can be various causes for the instability within the planetary system, as discussed in section 4.1.5, I simply assume that the system has been made unstable through one of the aforementioned mechanisms early on after the conclusion of the planetary formation phase. By then having a small initial spacing between two or more planets in the system, the planets are certain to exchange angular momentum at an early phase in the evolution, ensuring that planet–planet scattering will occur in just a few Myr. As shown by Malmberg, Davies, & Heggie (2011), the timescale for instability within a planetary system does not affect the duration of the scattering phase nor the general properties of the system post-evolution. Recalling from section 3.1, the presence of three gas giants within a planetary system can be related to the Kepler dichotomy (Johansen et al., 2012). Hence, placing three gas giants within a small distance of each other means that short timescale chaotic dynamical evolution will be highly probable. Additionally, previous studies have found that the highest eccentricities are produced by giant planets with equal mass during scattering experiments (Ford & Rasio, 2008; Carrera, Davies, & Johansen, 2016).

Furthermore, since planet consumption is more likely for planet–planet scattering events that occur at small semi-major axes, I opted to place the planets further in towards the host star. This also coincides with the distribution of orbital elements for observed exoplanets, as discussed in section 3.2. The third finding from the two-body analysis is that planet consumption is more likely to occur if there exists a large mass difference between planets in the system. Hence, I once more chose to include test-particle-like planets of Earth-mass, as well as Jupiter-mass planets in the fiducial configuration to increase the likelihood of getting planet–star collisions. A key part of the 'Kepler' dichotomy, where outer gas giants suppress the growth of inner planets, suggests that placing said terrestrial planets closer to the sun than the gas giants will be the most physically accurate scenario. From the two-body analysis, I also found that such a configuration will facilitate planet consumption.

Interestingly, the system of choice with two terrestrial planets interior to three outer giants is essentially a dynamically unstable and simplified version of Venus, Earth and the three outer giants Jupiter, Saturn and Uranus. I place the two Earth-mass planets at the same semi-major axes as Venus and Earth and the first Jupiter-mass orbit is placed at 5 AU. The separation between the three Jupiter-mass planets is set to $\Delta = 5.1$, which most often triggers instability in just a few Myr (Carrera, Davies, & Johansen, 2016). I refer to this system as 2E+3J. The system can be altered in a straightforward manner by either removing or increasing the masses of the inner planet to investigate how the fraction of planet-consuming outcomes changes. I refer to such systems as 3J and 2X+3J, respectively and each version of these are denoted with a given letter in alphabetical order, e.g 2X+3Ja, where $M_{\rm X} = 3\ {\rm M}_{\oplus}$. All initial orbital configurations used in this chapter can be found in figure 6.1, where the number in between each pair of planets corresponds to the separation between them in terms of Δ. Table 6.2 shows the specific properties of the planets for each configuration. There are a number of systems that I have not yet mentioned. As for 2E+2J, this configuration exists because I naturally wanted to understand how the evolution changes the number of Jupiter-mass planets outside the orbits of the terrestrial planets is reduced. For the different versions of 3J, I have altered the semi-major axis of the first orbit while keeping the separation in terms of Δ static. This was to confirm whether or not a smaller semi-major axis leads to a larger number of planet consumptions. There are also configurations with five Jupiter-like planets referred to as 5J, two systems with five planets of Saturn-mass called 5S and finally a single one with three Saturn-mass planets by the name of 3S. The reasoning behind the choice of simulating these initial orbital configurations will be laid out in section 6.4.1.

6.3 Post-evolution orbital configurations of planet-consuming systems

Before I go into the results of the numerical integrations, I will introduce the terminology used when referring to said simulations.

System	Planet 1	Planet 2	Planet 3	Planet 4	Planet 5
2E+3J	$M_{\rm X} = 1\ {\rm M}_\oplus$, $a_{\rm p} = 0.72$ AU	$M_{\rm X} = 1\ {\rm M}_\oplus$, $a_{\rm p} = 1.00$ AU	$M_{\rm p} = 300\ {\rm M}_\oplus$, $a_{\rm p} = 5.00$ AU	$M_{\rm p} = 300\ {\rm M}_\oplus$, $a_{\rm p} = 7.62$ AU	$M_{\rm p} = 300\ {\rm M}_\oplus$, $a_{\rm p} = 11.98$ AU
2X+3Ja	$M_{\rm X} = 3\ {\rm M}_\oplus$, $a_{\rm p} = 0.72$ AU	$M_{\rm X} = 3\ {\rm M}_\oplus$, $a_{\rm p} = 1.00$ AU	$M_{\rm p} = 300\ {\rm M}_\oplus$, $a_{\rm p} = 5.00$ AU	$M_{\rm p} = 300\ {\rm M}_\oplus$, $a_{\rm p} = 7.62$ AU	$M_{\rm p} = 300\ {\rm M}_\oplus$, $a_{\rm p} = 11.98$ AU
2X+3Jb	$M_{\rm X} = 10\ {\rm M}_\oplus$, $a_{\rm p} = 0.72$ AU	$M_{\rm X} = 10\ {\rm M}_\oplus$, $a_{\rm p} = 1.00$ AU	$M_{\rm p} = 300\ {\rm M}_\oplus$, $a_{\rm p} = 5.00$ AU	$M_{\rm p} = 300\ {\rm M}_\oplus$, $a_{\rm p} = 7.62$ AU	$M_{\rm p} = 300\ {\rm M}_\oplus$, $a_{\rm p} = 11.98$ AU
2X+3Jc	$M_{\rm X} = 30\ {\rm M}_\oplus$, $a_{\rm p} = 0.72$ AU	$M_{\rm X} = 30\ {\rm M}_\oplus$, $a_{\rm p} = 1.00$ AU	$M_{\rm p} = 300\ {\rm M}_\oplus$, $a_{\rm p} = 5.00$ AU	$M_{\rm p} = 300\ {\rm M}_\oplus$, $a_{\rm p} = 7.62$ AU	$M_{\rm p} = 300\ {\rm M}_\oplus$, $a_{\rm p} = 11.98$ AU
2X+3Jd	$M_{\rm X} = 100\ {\rm M}_\oplus$, $a_{\rm p} = 0.72$ AU	$M_{\rm X} = 100\ {\rm M}_\oplus$, $a_{\rm p} = 1.00$ AU	$M_{\rm p} = 300\ {\rm M}_\oplus$, $a_{\rm p} = 5.00$ AU	$M_{\rm p} = 300\ {\rm M}_\oplus$, $a_{\rm p} = 7.62$ AU	$M_{\rm p} = 300\ {\rm M}_\oplus$, $a_{\rm p} = 11.98$ AU
2X+3Je	$M_{\rm X} = 300\ {\rm M}_\oplus$, $a_{\rm p} = 0.72$ AU	$M_{\rm X} = 300\ {\rm M}_\oplus$, $a_{\rm p} = 1.00$ AU	$M_{\rm p} = 300\ {\rm M}_\oplus$, $a_{\rm p} = 5.00$ AU	$M_{\rm p} = 300\ {\rm M}_\oplus$, $a_{\rm p} = 7.62$ AU	$M_{\rm p} = 300\ {\rm M}_\oplus$, $a_{\rm p} = 11.98$ AU
5Ja	$M_{\rm X} = 300\ {\rm M}_\oplus$, $a_{\rm p} = 0.48$ AU	$M_{\rm X} = 300\ {\rm M}_\oplus$, $a_{\rm p} = 0.67$ AU	$M_{\rm p} = 300\ {\rm M}_\oplus$, $a_{\rm p} = 5.00$ AU	$M_{\rm p} = 300\ {\rm M}_\oplus$, $a_{\rm p} = 7.62$ AU	$M_{\rm p} = 300\ {\rm M}_\oplus$, $a_{\rm p} = 11.98$ AU
5Jb	$M_{\rm X} = 300\ {\rm M}_\oplus$, $a_{\rm p} = 0.303$ AU	$M_{\rm X} = 300\ {\rm M}_\oplus$, $a_{\rm p} = 0.423$ AU	$M_{\rm p} = 300\ {\rm M}_\oplus$, $a_{\rm p} = 5.00$ AU	$M_{\rm p} = 300\ {\rm M}_\oplus$, $a_{\rm p} = 7.62$ AU	$M_{\rm p} = 300\ {\rm M}_\oplus$, $a_{\rm p} = 11.98$ AU
5Jc	$M_{\rm X} = 300\ {\rm M}_\oplus$, $a_{\rm p} = 2.086$ AU	$M_{\rm X} = 300\ {\rm M}_\oplus$, $a_{\rm p} = 3.230$ AU	$M_{\rm p} = 300\ {\rm M}_\oplus$, $a_{\rm p} = 5.00$ AU	$M_{\rm p} = 300\ {\rm M}_\oplus$, $a_{\rm p} = 7.62$ AU	$M_{\rm p} = 300\ {\rm M}_\oplus$, $a_{\rm p} = 11.98$ AU
2E+2J	$M_{\rm X} = 1\ {\rm M}_\oplus$, $a_{\rm p} = 0.72$ AU	$M_{\rm X} = 1\ {\rm M}_\oplus$, $a_{\rm p} = 1.00$ AU	$M_{\rm p} = 300\ {\rm M}_\oplus$, $a_{\rm p} = 5.00$ AU	$M_{\rm p} = 300\ {\rm M}_\oplus$, $a_{\rm p} = 7.62$ AU	-
3Ja	-	-	$M_{\rm p} = 300\ {\rm M}_\oplus$, $a_{\rm p} = 0.30$ AU	$M_{\rm p} = 300\ {\rm M}_\oplus$, $a_{\rm p} = 0.46$ AU	$M_{\rm p} = 300\ {\rm M}_\oplus$, $a_{\rm p} = 0.72$ AU
3Jb	-	-	$M_{\rm p} = 300\ {\rm M}_\oplus$, $a_{\rm p} = 1.00$ AU	$M_{\rm p} = 300\ {\rm M}_\oplus$, $a_{\rm p} = 1.55$ AU	$M_{\rm p} = 300\ {\rm M}_\oplus$, $a_{\rm p} = 2.40$ AU
3Jc	-	-	$M_{\rm p} = 300\ {\rm M}_\oplus$, $a_{\rm p} = 5.00$ AU	$M_{\rm p} = 300\ {\rm M}_\oplus$, $a_{\rm p} = 7.62$ AU	$M_{\rm p} = 300\ {\rm M}_\oplus$, $a_{\rm p} = 11.98$ AU
3Jd	-	-	$M_{\rm p} = 300\ {\rm M}_\oplus$, $a_{\rm p} = 10.00$ AU	$M_{\rm p} = 300\ {\rm M}_\oplus$, $a_{\rm p} = 15.48$ AU	$M_{\rm p} = 300\ {\rm M}_\oplus$, $a_{\rm p} = 23.97$ AU
3Je	-	-	$M_{\rm p} = 300\ {\rm M}_\oplus$, $a_{\rm p} = 15.00$ AU	$M_{\rm p} = 300\ {\rm M}_\oplus$, $a_{\rm p} = 23.22$ AU	$M_{\rm p} = 300\ {\rm M}_\oplus$, $a_{\rm p} = 35.96$ AU
5Sa	$M_{\rm X} = 100\ {\rm M}_\oplus$, $a_{\rm p} = 0.72$ AU	$M_{\rm X} = 100\ {\rm M}_\oplus$, $a_{\rm p} = 1.00$ AU	$M_{\rm p} = 100\ {\rm M}_\oplus$, $a_{\rm p} = 5.00$ AU	$M_{\rm p} = 100\ {\rm M}_\oplus$, $a_{\rm p} = 6.33$ AU	$M_{\rm p} = 100\ {\rm M}_\oplus$, $a_{\rm p} = 8.00$ AU
5Sb	$M_{\rm X} = 100\ {\rm M}_\oplus$, $a_{\rm p} = 1.47$ AU	$M_{\rm X} = 100\ {\rm M}_\oplus$, $a_{\rm p} = 1.84$ AU	$M_{\rm p} = 100\ {\rm M}_\oplus$, $a_{\rm p} = 5.00$ AU	$M_{\rm p} = 100\ {\rm M}_\oplus$, $a_{\rm p} = 6.33$ AU	$M_{\rm p} = 100\ {\rm M}_\oplus$, $a_{\rm p} = 8.00$ AU
3S	-	-	$M_{\rm p} = 100\ {\rm M}_\oplus$, $a_{\rm p} = 5.00$ AU	$M_{\rm p} = 100\ {\rm M}_\oplus$, $a_{\rm p} = 6.33$ AU	$M_{\rm p} = 100\ {\rm M}_\oplus$, $a_{\rm p} = 8.00$ AU

Table 6.2: The mass and semi-major axis for each planet in the various configurations considered in this chapter. Each system has a number of sub-systems where a main parameter has been altered. The various outcomes in the different cases can then be compared and allow for conclusions behind the optimal orbital configuration of a planet-consuming progenitor system.

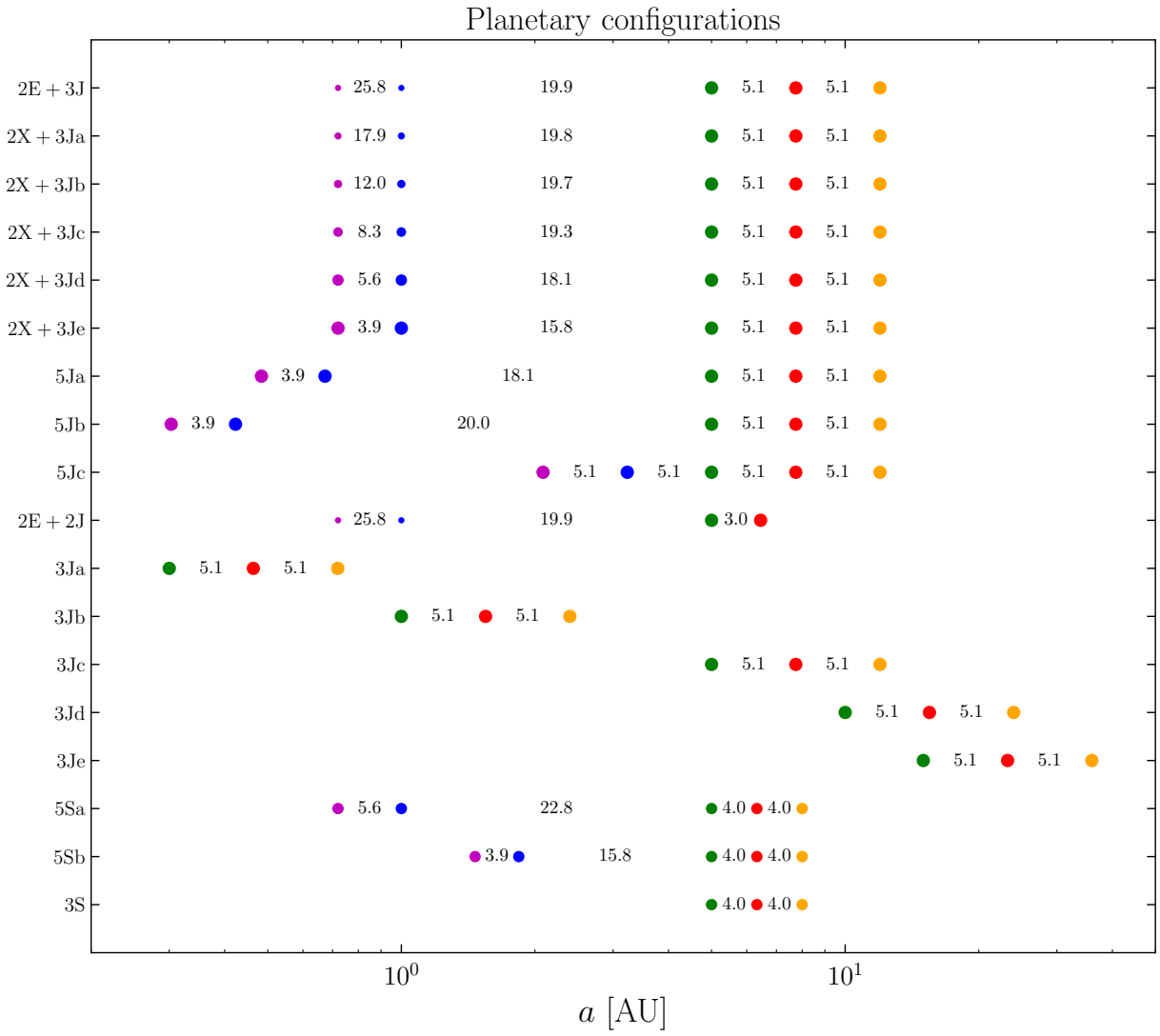

Figure 6.1: The orbital configurations of the systems I consider for the `MERCURY` simulations of this work. The planets are distributed in semi-major axis along the horizontal axis. The vertical axis shows the name of each system. The planet sizes are proportional to $M_{\rm p}^{1/3}$.

- ***planetary configuration*:** An initial setup of planets with predefined multiplicity, initial semi-major axes and masses orbiting a host star with a given mass.
- ***progenitor system*:** The initial phases of the planets in a planetary system at the onset of integration.
- ***planetary system*:** The final phases of a planetary configuration after $t_{\rm tot}$ yr of integration, where planets with static semi-major axes have been given randomised orbital elements from the distributions in table 6.1.

- ***realisation*:** A realisation is the integration over $t_{\rm tot}$ yr for a given progenitor system that in the end creates a planetary system.
- ***run*:** Refers to all N realisations for a given planetary configuration, creating N planetary systems.

Hence, the orbital configurations of planets in figure 6.1 are all planetary configurations because the planets have no specified phase except for their semi-major axis and mass. For each run N was set to be either 50 or 100 depending on the details needed for statistical purposes. The time of integration for the realisation was kept at a static $t_{\rm tot} = 10$ Myr, with output every yr. However, to save computation time during analysis and keep data files at a reasonable size, the minimum time between outputs for orbital elements was set to 10 days, which still yields a satisfactory level of detail for changes in the orbital elements of the planets during the dynamical evolution. While many previous studies on planet–planet scattering and their outcomes have employed a static radius for ejection, usually $r_{\rm eject} \sim 10^3$ AU (e.g. Ford & Rasio, 2008; Raymond, Armitage, & Gorelick, 2010; Carrera, Davies, & Johansen, 2016), this was shown by Carrera, Raymond, & Davies (2019) to preemptively remove planets at large semi-major axes with large eccentricities $e > 0.99$ that were still bound to the system. Prior to ejection, the semi-major axis of a high-eccentricity planet increases diffusively through scatterings with other planets, meaning that it still could obtain an eccentricity such that it collides with the host star before being ejected. Hence, I have employed their value of $r_{\rm eject} = 10^5$ AU.

6.3.1 The Carrera plot

In order to show the resulting distribution of semi-major axes and eccentricities for the surviving planets in the N planetary systems produced after 10 Myr of integration, I have adopted the plotting style from Carrera, Davies, & Johansen (see their figure 2) with a few modifications. The orbital configurations of the planetary systems from a $N = 50$ run of 2E+3J can be found in figure 6.2.

The initial orbital configuration of the five planets can be seen at the top of the plot with their semi-major axes indicated on the horizontal axis. The sizes of each planet's dot is proportional to $M_{\rm p}^{1/3}$. The eccentricity of the final orbits is shown by the error bars centred on each planet, representing the periastron and the apastron. Mergers are shown by a multi-coloured dot, where the outer and inner colours correspond to the primary and secondary planet in the merger, respectively. For each realisation, distinguished by its system index on the vertical axis, we can observe which planets have been consumed as they are plotted within of the physical radius of the host star, indicated by a black dashed line. All systems where a planet-consuming event has occurred are also marked with a green, translucent bar to the left of the star radius line. The translucency of the green bar indicates the varying amount of mass consumed by the host star in the given system, allowing us to see that there are five distinct groups of systems in terms of mass consumed. Furthermore, there is a red bar that shows the range of $r_{\rm min} = a(1 - e)$ and

$r_{\max} = a(1+e)$ values for the surviving planets over the course of the simulation, indicating radial incursions and radial excursions, respectively. The purple bars indicate the range of semi-major axis values over the simulation for the surviving planets. The systems have been ordered in terms of

1. The mass consumed by the host star.
2. The extent of radial incursions made by the surviving planets.

In this way I can observe the distribution of radial incursions for each type of planetary system that is shown in figure 6.2.

There are two additional vertical lines in the plot. The grey dashed line indicates the tidal disruption radius of the least dense planet remaining in the system, with a bulk density $\overline{\rho}_{\min}$. Said radius is given by the Roche radius

$$R_{\text{Roche}} = \left(\frac{9M_\star}{4\pi\overline{\rho}_{\min}} \right)^{1/3}. \tag{6.5}$$

As for the dotted line, it represents the semi-major axis corresponding to the binding energy of a planet on a circular orbit that has ejected two other Jupiter-mass planets, computed by

$$a_{\text{f}} = \left[\frac{1}{a_{\text{J1}}} + \frac{1}{a_{\text{J2}}} + \frac{1}{a_{\text{J3}}} \right]^{-1}. \tag{6.6}$$

For the planetary configuration 2E+3J, this value corresponds to $a_{\text{f}} = 2.41$ AU. While some of the absolute energy among the planets in the system has been lost with the consumed Earth-mass planets or transferred to a Jupiter-mass planet in the cases where a terrestrial planet has been ejected, their comparably low fractional energy will not affect the position of a_{f} in a notable manner.

I will now go through the five groups of systems one by one in terms of increasing consumed mass and point out noteworthy features of their orbital parameter distributions.

Systems 0-2: This is arguably the least interesting group of planetary systems from the integration, where no planet has been consumed. System 0 is still unresolved after 10 Myr of integration, indicating that the set of phases for the Jupiter-mass planets impedes exchange of angular momentum, keeping the system stable for a long time. In the remaining two systems, there has been a merger between two Jupiter-mass planets that appear to have occurred early on during the evolution given the lack of radial incursions and excursions for the planets. The remaining two giant planets are seemingly Hill stable, which indicates that any further evolution is unlikely.

Systems 3-9: Here, one of the terrestrial planets has been consumed after being scattered into the host star. There are signs of significant radial incursions for all these cases, but

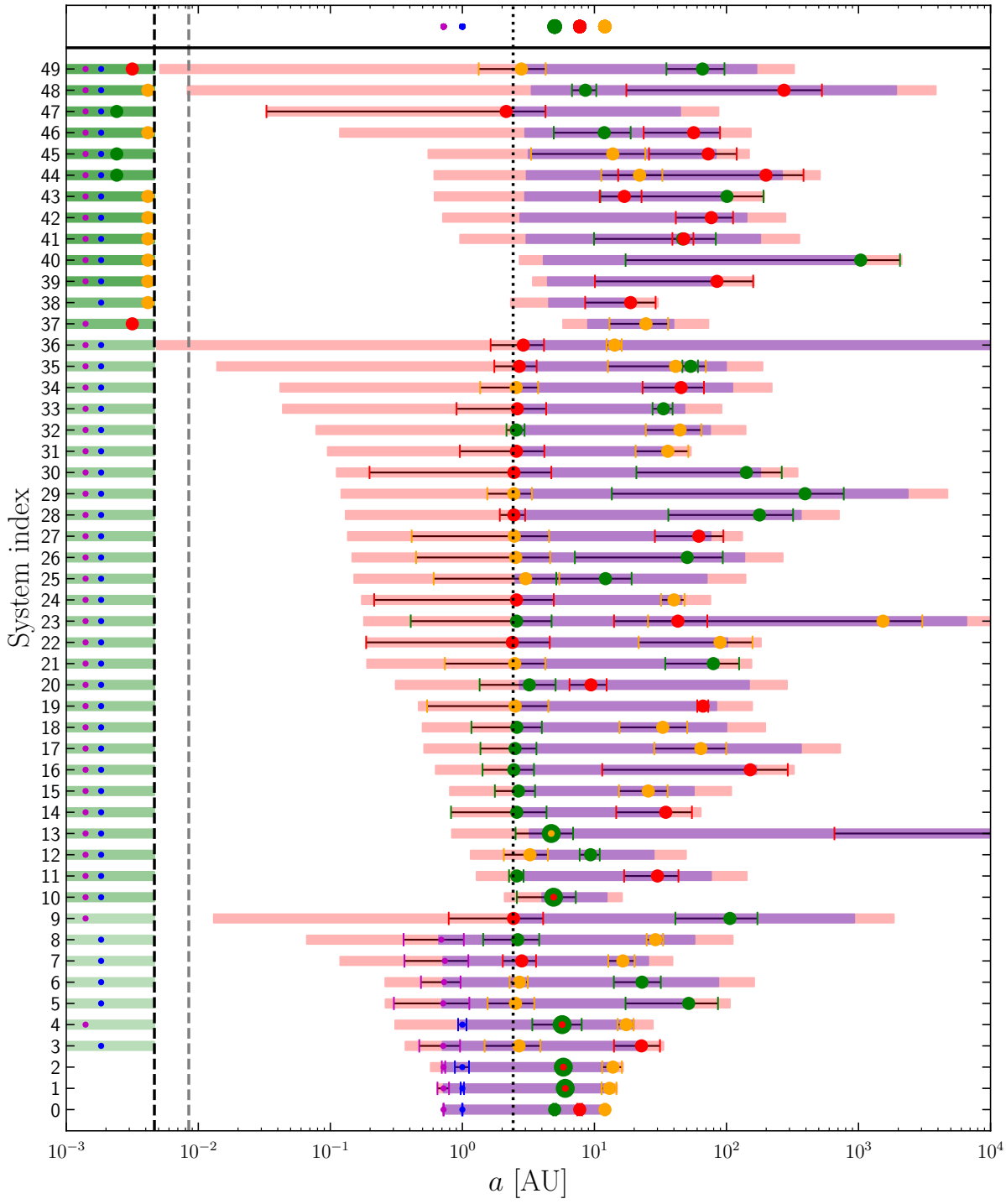

Figure 6.2: Examples of the final orbital configurations of the surviving planets in the 2E+3J configuration considered. For an explanation, see the text in section 6.3.1.

none of the planets are on highly eccentric orbits in the final configuration, as indicated by their error bars. In turn, it appears that one of the Jupiter-mass planets has been on a more eccentric orbit and then undergone planet–planet scattering with another Jupiter, ultimately leading to an ejection. Since ejection occurs for planets with small absolute orbital energy $|E| \sim 0$ J, said quantity must have been transferred to one of the remaining planets in the system. In all but one case, system 4, there is one Jupiter-mass planet with $a_\mathrm{p} \simeq a_\mathrm{f}$. The further out the second Jupiter-mass planet is, the closer the semi-major axis of the innermost Jupiter will be to a_f, indicating the importance of energy conservation to explain the final orbital configuration in these systems. Given the semi-major axis dependence of the binding energy, a planet at ~ 100 AU can practically be considered to have been ejected, which can be clearly seen for system 9. Furthermore, the radial incursion has been most considerable in said system. This is a clear case of *anti-scattering*, where a planet on an eccentric orbit is put on a less eccentric and wider orbit. Such an event often culminates with the other planet being ejected. In system 4, the Jupiter-mass planet that was on an eccentric orbit has, instead of anti-scattering, directly merged with another Jupiter-mass planet. A noteworthy feature of the final orbital configurations is the production of Jupiter-mass planets with large semi-major axes $a_\mathrm{p} > 40$ AU on both circular and eccentric orbits in some systems. The existence of such planets is difficult to explain in planet formation models due to early planet migration (e.g. Bitsch, Lambrechts, & Johansen, 2015; Wimarsson, Liu, & Ogihara, 2020). This result is consistent with Veras, Crepp, & Ford (2009), who predicted the existence of wide orbit giant planets due to planet–planet scattering that can survive for several tens of Myr before they are eventually ejected.

Systems 10-36: The dominant type of system is where two terrestrial planets have been consumed and two massive planets remain. There are three exceptions. In systems 23 and 35 there are three Jupiter-mass planets remaining, but the orbits of the two outer Jupiters are still crossing meaning that the dynamical evolution has not concluded. One of the planets will undoubtedly be ejected if the simulation was to be continued for another Myr. The other exception is system 10, where the radial incursion of the surviving planet has not been large enough to invade the orbits of the inner two planets and scatter them into the host star. Instead, looking at the detailed evolution of this system, this is one of the cases where the inner two planets have been made eccentric through Lidov–Kozai oscillation with either the $M_\mathrm{p} = 2$ M$_\mathrm{J}$ planet or the remaining Jupiter before it was ejected from the system. I will return to this new pathway to consumption in the next section. A majority of the remaining systems have all behaved similarly to system 9 in the previous group, where one Jupiter has been fully ejected and the other is on a large semi-major axis orbit. The distribution of eccentricities for the two planets differ notably between the two-Jupiter systems and seems to indicate that consumed planets remove different amounts of angular momentum from the surviving planets. However, recall that the AMD in this full three-dimensional scenario also is affected by the inclinations of the orbits (see equation (4.3)), which does not become clear from figure 6.2. Another outstanding feature is the radial incursion of the surviving planets in system 36, indicating that one of the

planets would have been fully consumed if I had opted for $r_{\rm crit}$ equal to the tidal disruption radius of a Jupiter-mass planet (grey dashed line). As a matter of fact, this is a case where the outermost planet, J1, is yet to be considered fully ejected by `MERCURY`, meaning that it has a semi-major axis of $10^4 < a_{\rm p} < 10^5$ AU and is thereby not visible in the plot. Given the extreme semi-major axis, it will have an immensely long period as $P^2 \propto a^3$ and will probably never get close enough to the host star for such an event to occur before being fully ejected. The final observation from this group is that the magnitudes of the radial incursions for the two cases where two Jupiter-mass planets have merged are at the lower end of the distribution. This coincides with the merger-type systems from the two previous groups as well, which again indicates that mergers tend to happen early on during the dynamical evolution, impeding the magnitudes of radial incursions within the system.

Systems 37 and 38: In these two systems, a single terrestrial planet and a Jupiter-mass planet has been consumed. After a more detailed analysis of the evolution of the orbital elements as a function of time, it is clear that the ejection of the other terrestrial planet is due to the invasion of a Jupiter-mass planet into the inner subsystem, which then weakly scatters the Earth-mass planet outwards where it is subsequently ejected by the other Jupiters. Recalling that ejection becomes more likely with larger distance from the host star from section 5.4.2, it is unsurprising that such an outcome is favoured when the terrestrial planets are moved outwards. A notable aspect of the single surviving planet is that it has a semi-major axis $a_{\rm p} > a_{\rm f}$. This comes from the fact there are scenarios where a large proportion of the energy will not be conserved among the planets if a massive planet gets consumed. Instead any excess energy stored within the consumed planet will be transferred to the host star. For these two systems, this has indeed been the case.

Systems 39-49: The main difference between the previous group and the final group is that both terrestrial planets have been consumed during the evolution. There are also systems that still retain two Jupiter-mass planets, but a majority of these still have crossing orbits and will likely resolve with another ejection if integrated for a longer time. Hence, there are only one or two systems where the two Jupiter-mass planets can exist in a stable orbital configuration. Moreover, system 49 shows the case of a strong anti-scattering event where a planet on an almost consuming orbit has significantly increased its angular momentum by ejecting another Jupiter-mass planet. As compared to system 36, the planet with the significant radial incursion could have been either tidally captured by the host star becoming a hot Jupiter or eventually tidally disrupted and consumed. Looking at systems 47 and 49, there is another distinct characteristic of systems where a Jupiter-mass planet has been consumed, namely that it is still possible for Jupiters within such systems to have $a_{\rm p} \sim a_{\rm f}$. This points to different pathways to consumption, as the consumed planet clearly carries less absolute orbital energy with it that is transferred to the host star in this scenario. I note here that the ejected planet can have a small positive energy at the point of ejection, but it generally is non-negligible (Ford, Havlickova, & Rasio, 2001). Hence, the consumed Jupiters in these two systems appear to have gone through diffusive consumption. In the remaining cases, the Jupiter has been consumed with a lower $a_{\rm p}$ value

and in turn a large (negative) energy, which indicates strong consumption through a few scatterings.

I now summarise the most important findings from this plot briefly.

Insights from dynamical evolution of 2E+3J

1. Both terrestrial planets have been consumed in the majority of the systems and a Jupiter-mass planet has been consumed in about a quarter of them.
2. Mergers appear to happen early on during the dynamical evolution.
3. If one Jupiter has been ejected, the other two planets will most probably have semi-major axes such that $a_1 = a_f$ and $a_2 > 30$ AU. This can potentially explain the formation of gas giants with wide circular orbits, consistent with the prediction of Veras, Crepp, & Ford (2009).
4. If a Jupiter has been consumed, the final semi-major axis of the surviving planet(s) depends on how much orbital energy the consumed planet has removed from the system.
5. The various configurations of the Jupiter-consuming systems reinforces the theory of the two planet consumption mechanisms introduced in section 5.4.2.
6. The consumption of terrestrial planets without any orbit crossing indicates the existence of a third pathway to planet consumption, namely Lidov–Kozai oscillations.

6.3.2 Pathways to planet consumption

In this section, I further investigate insights 5. and 6. based on the 2E+3J Carrera plot. Note that while the main analysis is based on the $N = 50$ systems in figure 6.2, I have confirmed the major findings using an extended set of $N = 100$ planetary systems. In order to infer whether there indeed exist different types of pathways to planet consumption for the planets in the 2E+3J configuration, it makes sense to look at the number of scatterings for each CME-type planet in the planetary systems. As previously discussed in section 5.4.2, there appear to exist diffusive and strong versions of the planet consumption process. Either the planet will undergo a few strong scatterings that directly puts the planet on a consuming orbit, or the orbital eccentricity will increase diffusively over time through a large number of scatterings. If I expand this theory to include the consumption through Lidov–Kozai oscillations, the planets that have been consumed through this mechanism should have undergone only a few to no close encounters at all throughout the dynamical evolution of the system. While simply looking at the number of scatterings for

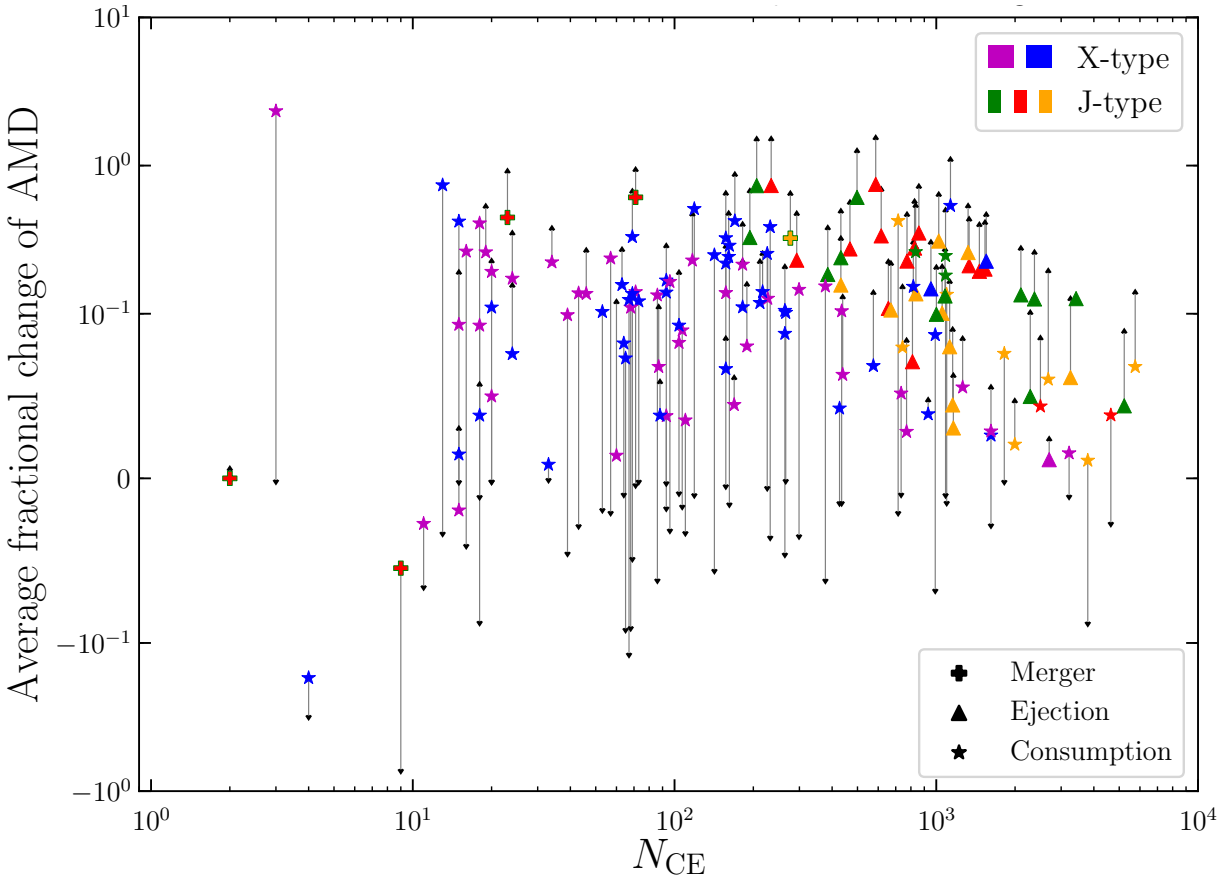

Figure 6.3: The average fractional change in AMD for each close encounter plotted against the number of close encounters for each CME-type planet in 100 2X+3J planetary systems. The star, plus and triangle symbols represent the fate of consumption, merger and ejection for a planet, respectively. The colour indicates the initial position of the planet in the 2E+3J configuration from figure 6.1. The arrow attached to every data point indicates the fractional change in AMD for the final encounter of the planet.

each CME-type planet will provide a lot of information, it would be well complemented by a quantitative measure of scattering strength. The most important quantity that governs the outcome of scattering events appears to be the AMD, given that it carries composite information of the distribution of orbital elements. Hence I provide a plot in figure 6.3 of the average fractional change in AMD per scattering of all CME-type planets across the previously discussed $N = 50$ realisations of 2E+3J as a function of the number of scatterings, N_{CE}.

In the plot, I have added an arrow for each data point that indicates the fractional change in AMD for the final registered closed encounter during the realisation. I will refer to this quantity as ξ_{f} in the text, while the average fractional change in AMD is $\overline{\xi}$. Given the nature of how `MERCURY` treats close encounters, there is no guarantee that the final

encounter for the CME-type planet occurred with the survivor that ultimately put it on a CME orbit, except for the mergers. Nevertheless, the information inferred from the final fractional change in AMD still hints at the dynamical history of all CME-type planets. I now go through each CME type one by one.

Mergers: While mergers generally are a rare outcome, the majority of them tend to happen at an early point during the evolution after a few to 100 close encounters. This aligns with the perception from the analysis of figure 6.2, where the surviving planets in an M-type system have not made any significant radial incursions. From the two-body analysis, it has become clear that mergers are favoured when there is little-to-no total deflection during the encounter. Given the importance of a large $\boldsymbol{v}_b$ velocity, deflection will be weak when either $q_\mathrm{p} \sim 1$ or if the relative velocity between the planets is low. Moreover, the relative velocity will be minimised for two planets with similar orbital elements. This statement can be reinforced by simply looking at the geometry of the orbits in figure 5.4 and considering that a larger difference in eccentricity and semi-major axis will induce a larger angle between the two initial velocities $\boldsymbol{v}_1$ and $\boldsymbol{v}_2$ at the crossing points. Considering that the orbits most likely will have similar semi-major axes, eccentricities and low mutual inclinations at the onset of the integration, it makes sense that mergers are favoured early on during the dynamical evolution. As for the strength of the scatterings leading up to the mergers, indicated by $\overline{\xi}$, there is a significant spread of values. Given that the final scattering strength represents the change for the primary planet prior to and after merging with another planet, the overall trend clearly depends on the dynamical history of the secondary planet as well. For the two leftmost examples, there is one case with $N_\mathrm{CE} = 1$ where the two planets merge without inducing a notable change in AMD for the primary planet. In the other with $N_\mathrm{CE} = 9$, the nature of the collision leads to an overall decrease in the AMD for the primary planet. Hence, there does not seem to be a typical scattering pathway that favours mergers, except for the fact that they occur early on during the evolution of the system. Nevertheless, I expect that the eccentricities and mutual inclinations should be kept small, meaning that the major change in AMD comes from semi-major axis variations. I proceed to verify this hypothesis later in this section.

Ejections: This outcome is evidently more of a diffusive process given it occurs for $N_\mathrm{CE} > 100$ in all cases. This makes sense, since an enormous radial distance of 10^5 AU is needed to fully eject a planet in the simulations, which also indicates that eccentricities of $e \sim 1$ are needed. It is also apparent that ejection is the dominating outcome for scattering cases where $q_\mathrm{p} = 1$. Again, ejection becomes more likely and consumption becomes less likely with increasing distance from the host star (see section 5.4.2). With this idea in mind, the explanation for the increased likelihood of ejection with N_CE can be found in the conservation of energy among the Jupiter-mass planets. If two Jupiter-mass planets undergo a number of scattering events, I expect that one will gain a surplus of the total energy between them. Hence, the semi-major axis of one planet will decrease while the other planet's semi-major axis increases over time. The more scatterings the planets undergo, the larger this difference in energy (and angular momentum) will become. The

insights from the two-body analysis have already hinted at the result that planets with $q_{\rm p} \sim 1$ will need a much larger number of scatterings for one planet to reach $e \sim 1$ and possibly be consumed. Hence, if two scattering Jupiter-mass planets do not merge early on, the difference in their orbital elements and AMD will keep growing until one of the planets is either consumed or ejected. Due to their distance from the host star in this planetary configuration, the favoured outcome for $q_{\rm p} \sim 1$ scattering is ejection. The strength of the scatterings varies, but will always be positive, which agrees with the need for a large initial AMD for ejection to be possible. Moreover, each ejection is concluded with a final scattering event that has one of the largest relative strengths during the dynamical history. There is also a clear trend where both $\overline{\xi}$ and $\xi_{\rm f}$ decrease with $N_{\rm CE}$. Hence, the fractional change in AMD is lower for planets that already are on highly eccentric and wide orbits.

Consumption: As for the average fractional change in AMD for the consumed planets, there are a variety of noteworthy features. First of all, there is a clear difference in the number of scatterings needed to consume an Earth-mass planet and a Jupiter-mass planet, where the minimum values for $N_{\rm CE}$ are 3 and ~ 750, respectively. Focusing on the consumption of Earth-mass planets, there is a wide range of $\overline{\xi}$ that can produce such events. There is an especially large discrepancy between the two leftmost cases, where the Earth at $N_{\rm CE} = 3$ has clearly undergone two very strong scatterings followed by a final weak one, probably by the other Earth-mass planet in the system. The next planet at $N_{\rm CE} = 4$ seems to have undergone four weak scatterings with the other Earth-mass planet, where it has lost AMD on average. This is evidently a case where scattering has not been the pathway to consumption. Instead this planet has gained AMD through Lidov–Kozai oscillations with a planet in the outer 3J subsystem. There are two other cases with $N_{\rm CE} < 20$ where $\overline{\xi}$ is negative and these planets are also likely to have been consumed through the Lidov–Kozai mechanism. The remaining cases all have a positive $\overline{\xi}$ value, which indicates that they have undergone strong or diffusive consumptions. To formulate a more robust definition for the three different pathways, I define them as follows

- **Lidov–Kozai consumption:** $\overline{\xi} < 0$
- **Diffusive consumption:** $0 < \overline{\xi} < 10^{-1}$ and $N_{\rm CE} > 20$
- **Strong consumption:** $\overline{\xi} > 10^{-1}$

Note that these definitions imply that there is a strict boundary between diffusive and strong scattering. However, judging from figure 6.3, these two regimes appear to be connected by a continuum of average scattering strengths, $\overline{\xi}$. In turn, diffusive and strong scattering merely represent two extreme pathways to planet consumption. Nevertheless, the two different cases provide an intuitive distinction between the qualitative difference of consumption by many weak scattering events and a few strong ones. Therefore, I still opted to use this terminology throughout this thesis to facilitate the discussion of planet consumption events.

While it would be intuitive to categorise these mechanisms in terms of number of scatterings, it is rather the nature of the scatterings that is of interest. To elaborate, an

Earth-mass planet can undergo a large number of weak $\overline{\xi} \sim 0$ scatterings with its Earth-mass companion that do not result in a significant change in AMD, which in turn will not bring it close to the critical AMD needed for planet consumption. Hence said scatterings have not affected the orbital elements of the primary Earth-mass planet in a significant manner. If it then undergoes a series of strong subsequent scattering events with a Jupiter-mass planet that boosts the value of $\overline{\xi}$, bringing the planet to its critical AMD, it makes most sense to categorise this C-type planet as a strong consumption candidate. Looking at the values of $\xi_{\rm f}$, there are two scenarios that each make up approximately half of the population: either $\xi_{\rm f} > \overline{\xi}$ or $\xi_{\rm f} \leq 0$. While the fact that there are so many cases where $\xi_{\rm f} \leq 0$ may seem surprising, since one would expect that the final scattering is the scattering that ultimately puts the planet on its consuming orbit, there is a logical explanation. When the planet travels along its planet-consuming orbit towards the host star, it can still undergo close encounters with other planets still present in the system. Said theory is supported by the fact that $\xi_{\rm f} > \overline{\xi}$ for all ejections. Given that ejections occur after a period of diffusive scattering followed by strong scattering, planets eligible for ejection will generally be on the orbit that is furthest away from the host star in the planetary system. Hence, the planet is unlikely to encounter any other planets on its trajectory away from the system. If this were to be the case, the relative strength of the scattering would still be large given the sizeable AMD of the E-type planet.

Inclinations and eccentricities of CME-type planets

To verify the hypothesis of mergers occurring early on for orbits with little-to-no eccentricities and mutual inclinations, I have plotted these respective traits prior to the final scattering of the CME-type planets for the 2E+3J system in figure 6.4. The mutual inclinations of the planets have been plotted against the minimum separation between the two scattering planets in terms of $d_{\rm crit} = R_{\rm p,1} + R_{\rm p,2}$. From the two plots, I observe that the M-type final scatterings have low mutual inclinations $i_{\rm m} < 9^\circ$ and low eccentricities $e < 0.5$ for both the survivor and CME-type planet. Hence, it is fair to conclude that mergers generally occur early on during the dynamical evolution when there is a small difference in AMD between the two scattering planets.

The plots also provide more evidence for the Lidov–Kozai consumption pathway. A majority of the Earth-mass CME-type planets has mutual inclinations with the surviving planet in their final close encounter within the active regime for Lidov–Kozai oscillations $39.20^\circ \leq i_{\rm m} \leq 140.77^\circ$ (Naoz, 2016). Moreover, there are eleven cases where the eccentricities of the scattering planet are within the low-eccentricity regime $e < 0.5$, which, judging from the two-body analysis, does not allow for direct consumption through scattering. Hence, Lidov–Kozai consumption may be more common than would be expected from figure 6.3 and could be an active mechanism even for $N_{\rm CE} > 20$.

Further, the diffusive nature of the ejection process is also revealed as a vast majority of the E-type planets have eccentricities ~ 1 at the onset of the final scattering event. There are some cases where $e > 1$, but this is due to the planets being able to undergo close

encounters post-ejection because of their sizeable Hill radii. Again, the planets will not be considered lost from the system by MERCURY until $r_{\rm p} \geq 10^5$ AU.

I once more note that the final encounters for the C-type planets may be with a planet that they pass on their path towards the host star given that around half the planets in figure 6.3 have negative $\xi_{\rm f}$. This could affect the distribution of the parameters for the surviving planet in these plots. Nevertheless, the two-body analysis in chapter 5 indicates that a large AMD in the CME-type planet is more influential than a large AMD in the survivor.

6.4 Planetary mass ratio in planet-consuming scatterings

At this point, it is clear that the mass ratio between the two planets undergoing a scattering event heavily affects the outcome. To delve deeper into the findings of section 5.4.1, where the mass ratio was investigated using the two-body model, I extended the study to the full three-dimensional case using MERCURY. The configurations used for this investigation are versions of the 2E+3J setup where the mass of the inner planets have been altered in logarithmic steps. I refer to these systems as 2X+3J. Including 2E+3J, the inner planets have masses of $M_{\rm X} = 1,\ 3,\ 10,\ 30,\ 100,\ 300\ {\rm M}_\odot$. The semi-major axes of all planets in the system are kept static, as can be seen in figure 6.1, while ensuring that the innermost subsystem is always Hill stable (i.e. $\Delta > 2\sqrt{3}$). To compare the results in the different configurations, I have plotted the average fractional outcome for the planets in a planetary system across $N = 100$ realisations in figure 6.5. The outcomes shown in the bar plots are consumption (green), ejection (orange), merger (grey) and survival (blue). Furthermore, each bar has a hatched region which represents the average fractional outcome for the inner 2X subsystem. From the plot, there is a strong indication that the fraction of consumed planets indeed goes down with increasing mass of the inner subsystem. Since the mass of the outer 3J planets is constant, the number of times a Jupiter-mass planet is consumed will remain roughly similar. Due to the number of consumptions per realisation being independent of the number of realisations, I can expect the error in the statistics to follow a Poisson distribution, i.e. $\sigma_{\rm outcome} = \sqrt{N_{\rm outcome}}$. Given that I am looking at the mean value for N realisations, the standard error will be $\sigma = \sqrt{\overline{N}_{\rm outcome}/N}$. The standard error for the fraction of consumed planets is indicated with a thin black bar in the diagram. With that in mind, it is difficult to judge whether or not the test particle limit lies inside or outside of $M_{\rm X} = 30\ {\rm M}_\oplus$. Nevertheless, the decrease in the average fraction of consumed X-planets between $M_{\rm X} = 30\ {\rm M}_\oplus$ and $M_{\rm X} = 100\ {\rm M}_\oplus$ cannot be explained by statistical errors alone and there is a clear decrease for $M_{\rm X} = 300\ {\rm M}_\oplus$ as well. Hence, the mass ratio test particle limit indeed seems to lie close to $q_{\rm p} \sim 10^{-1}$, which agrees with what was found in figure 5.10. Looking at the change of average fraction for the outer outcome as $q_{\rm p} \to 1$, the increased number of mergers and ejections for the 2X subsystem also lies in line with the previous analyses in the current and previous chapters. The more work a planet has

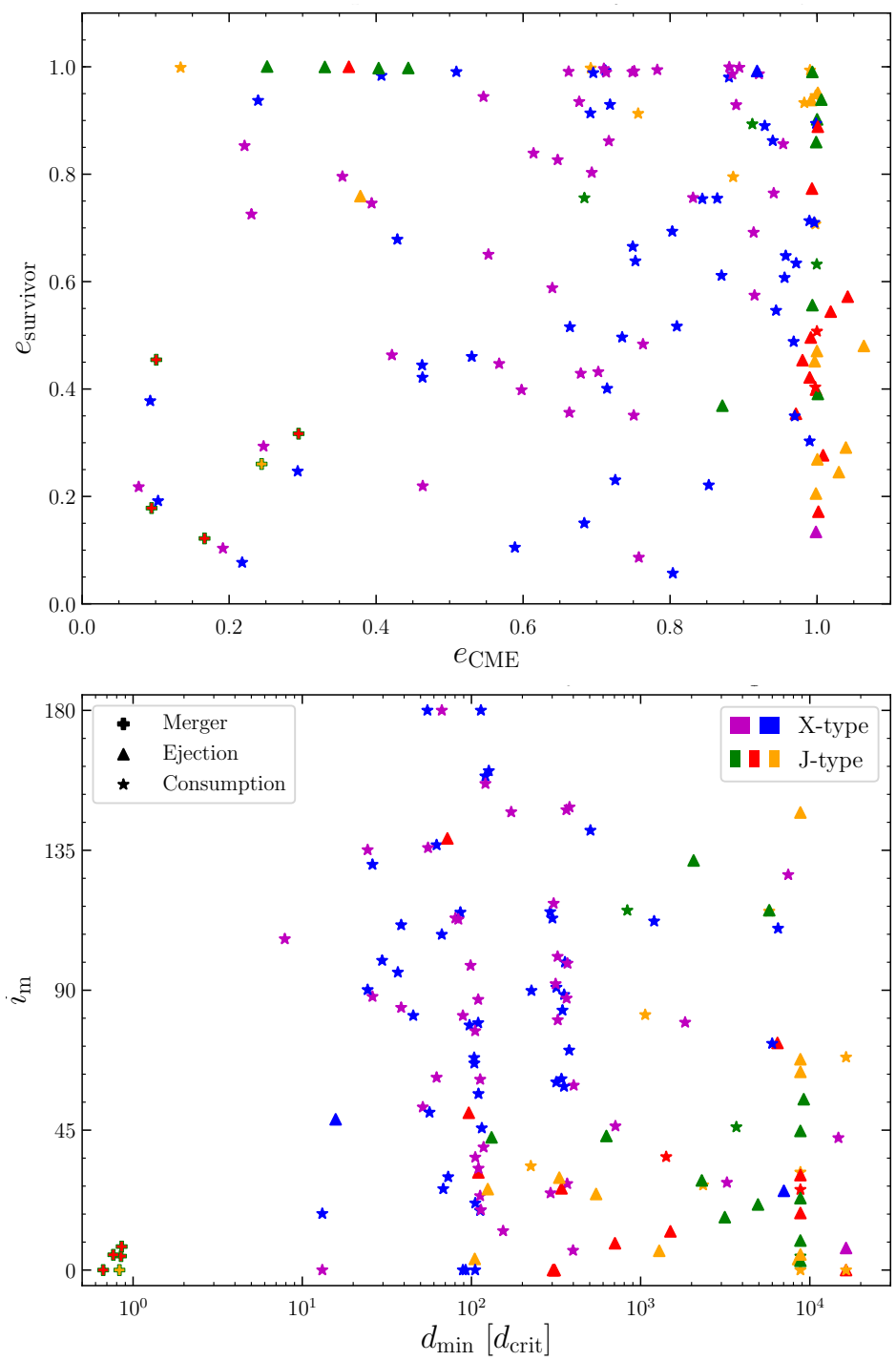

Figure 6.4: Top: The eccentricities of the survivor planet plotted against the eccentricity of the CME-type planet at the final close encounter. **Bottom:** The mutual inclination as a function of the minimum separation in terms of $d_{\mathrm{crit}} = R_{\mathrm{p},1} + R_{\mathrm{p},2}$ before the final close encounter. The colour and markers follows the same scheme as in figure 6.3.

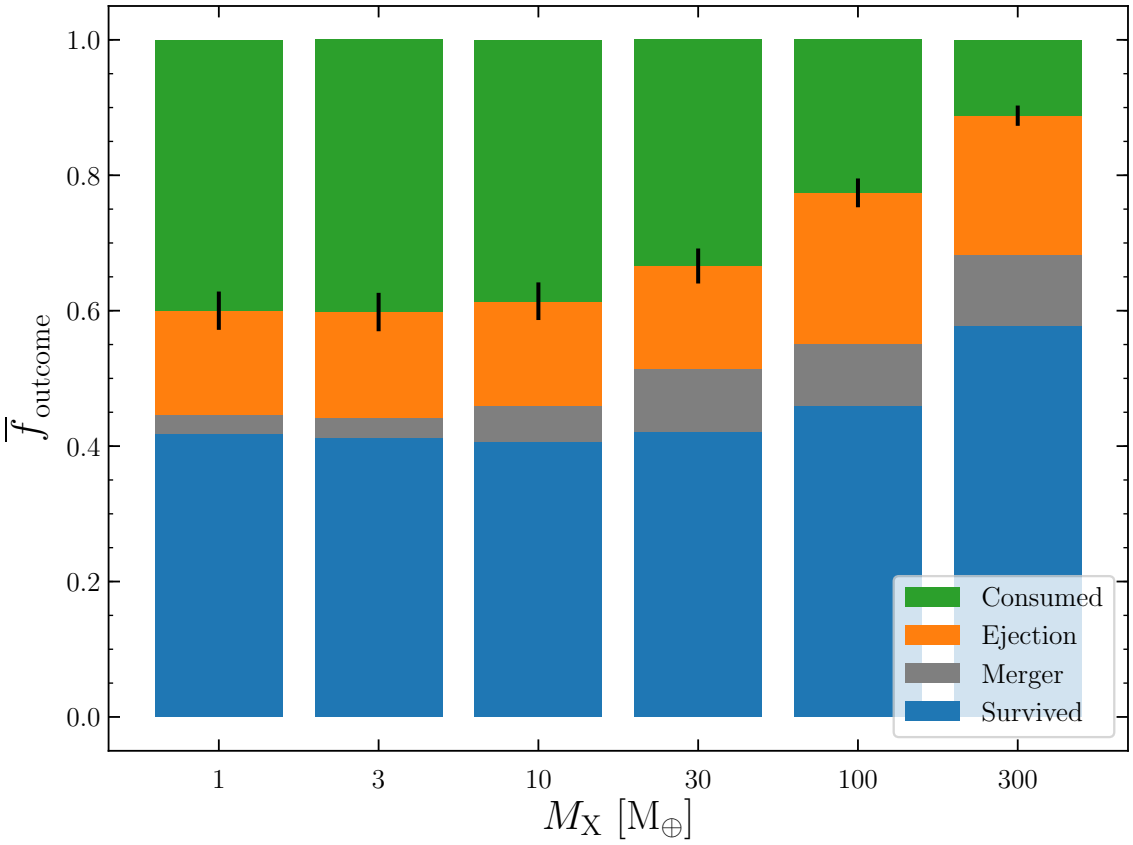

Figure 6.5: The mean fractions of outcomes per system across the 100 realisations I have carried out for the 2X+3J configurations with varying M_{X} values: 1, 3, 10, 30, 100 and 300 M$_\oplus$. The 1 M$_\oplus$ case corresponds to the 2E+3J configuration. The outcomes considered are survival (blue), consumption (green), merger (grey) and ejection (orange). Hatched regions represent the fractional outcomes for the inner 2X planetary subsystem. The black bar represents the standard error for the mean fraction of consumed planets. For example, if we consider an average planetary system for the leftmost configuration, 40% of planets are consumed. Further, it is more likely that said planet is an X-type since the consumption of an X-type planet corresponds to $\sim 35\%$ of the outcomes on average.

to do to change the trajectory of the other planet during a scattering event, the less likely planet consumption will be.

Another feature that needs to be addressed is the increased number of surviving X-planets for $M_{\text{X}} = 100$ M$_\oplus$ and $M_{\text{X}} = 300$ M$_\oplus$. While it is expected that it will be more difficult to consume planets as $q_{\text{p}} \to 1$, the dynamical evolution for systems based on these configurations should still resolve on a similar timescale to those with a lower M_{X} value. Looking at orbital elements of the planetary systems after 10^7 yr, there is a significant difference between the systems evolved from 2X+3Jd and 2X+3Je. In the former case there are three completely unresolved systems that have yet to reach instability, which is in line with the

cases of $M_X < 100$ $M_\oplus$ and can be explained by the random phase of the progenitor system not favouring early instability. However, for the case of five Jupiter-mass planets, there are 22 unresolved systems, which is counterintuitive given that there is much more AMD available for redistribution in the system that could trigger destabilisation. I dedicate the upcoming section to the investigation of this peculiar result.

6.4.1 The five Jupiter problem

The entire motivation behind the 2E+3J and 2X+3J configurations is to have the three outer Jupiter-mass planets become unstable on a short timescale, which will trigger chaotic dynamical evolution that leads to strong exchanges of AMD and ultimately CME-type outcomes. The prolonged stability timescale of 2X+3Je configuration directly led to thoughts of numerical errors. Given the significant increase in total mass of the system, the behaviour of the integrator used in `MERCURY` could potentially be affected. Nevertheless, there was no increase in the fractional energy error of the integrations, which systematically stayed below 10^{-4} for all realisations. Further, a thorough investigation of the initial orbital elements for each progenitor system showed that there was no indication of a systematic decrease in initial AMD for the planets, which could have been a potential explanation for the existence of such a large number of unresolved systems. In the absence of an obvious numerical explanation for this discrepancy, I formulated two possible scenarios that could suppress chaotic dynamical evolution in these 22 systems.

1. **AMD sink theory:** The inner planets are massive enough to absorb an early excess of AMD created in one of the outer planets, effectively acting as 'sinks' for the AMD and prolonging the timescale for stability in the planetary system.
2. **Altered potential theory:** The increased mass of the inner planets creates a mass quadrupole, which alters the gravitational potential acting on the outer 3J subsystem. This effect is an important barrier that can effectively suppress Lidov–Kozai oscillations (Mustill, Davies, & Johansen, 2017).

In order to determine if either of these theories are plausible explanations for the prolonged stability of the 5J configuration, I conducted a more in-depth study of the problem using the 5J, 5S and 3S configurations in figure 6.1. This can be found in appendix B. While a conclusion would require additional integrations and deeper analysis, the investigation points towards the second scenario being more likely. To summarise, the inner planets in the 2X+3Je realisations appear to be massive enough to create a significant quadrupole moment which alters the potential acting on the outer planets by breaking the symmetry of the otherwise spherical stellar potential. This causes precession of the outer planets, which can suppress oscillations of their orbital eccentricities. Moving the inner planets closer to the host star reduces the timescale of instability for the 5J systems, probably due to the potential becoming more symmetric.

6.5 Radial dependence of planet-consuming scattering events

With the mass dependence verified, I next restricted the parameter space for radial distance from the host star to find which regions of a planetary system favours planet consumption. Since I had already confirmed that there are systems where giant planets are consumed even when dealing with inner-outer planetary mass ratios of $q_{\rm p} \ll 1$, it was evident that the isolated 3J subsystem would be able to produce planet consumptions. Hence, I opted to not use the full 2X+3J configuration for these integrations. Instead I focused on altering the semi-major axis of the first planet in the isolated 3J configuration while keeping the Δ separation static at 5.1. The $a_{\rm J1}$ values of choice were 0.3, 1, 5, 10 and 15 AU, where the 5 AU configuration correspond to the position of the 3J subsystem in the 2E+3J configuration. The corresponding planetary configurations 3Ja-e can be found in figure 6.1. The main gain of only using the three Jupiter-mass planets is that the elapsed real time for the integration is significantly reduced when dealing with less planets that all have similar periods.

The outcome fractions for the corresponding $N = 100$ realisation runs for all 3J configurations are displayed in figure 6.6. From the results, I once more see indications that the fraction of consumed planets steadily drops with increased semi-major axis, which coincides with the findings in section 5.4.2. While there is unexpectedly a minimum at $a_{\rm J1} = 1$ AU instead of at the innermost value of 0.3 AU, this can be explained by the fact that the rate of mergers is significantly increased at such small distances from the host star. The escape velocity of the system will be much larger than the surface escape velocity of the Jupiter-mass planets at these small semi-major axes, which from the Safronov number indicates that planets are much more likely to merge than proceed to exchange large amounts of AMD. Furthermore, given that $d_{\rm crit}$ is large for planets of this mass and $b_{\rm max}$ decreases with the semi-major axis, the range of impact parameters that are planet-consuming will be a small fraction of the entire distribution of possible b-values. Hence, a planet–planet scattering with a small $q_{\rm p}$ would still be more likely to produce a planet consumption than a merger due to $d_{\rm crit}$ being a much smaller fraction of $b_{\rm max}$, since the latter is proportional to $(M_{\rm p,1} + M_{\rm p,2})^{1/3}$. Hence, these results are still in line with the conclusions from the two-body analysis.

One noteworthy feature remains to be addressed in figure 6.6. The number of unresolved systems appears to increase significantly with $a_{\rm J1}$. To investigate this further, I looked at the cumulative distribution for the timing of the first close encounter, $t_{\rm CE}$, which functions well as a measure for the level of instability for a given configuration (Chambers, Wetherill, & Boss, 1996). The corresponding distributions for the 3J configurations can be found in figure 6.7. There is a drastic decrease in $t_{\rm CE}$ for smaller values of $a_{\rm J1}$ despite the planets having a constant separation in Δ. The explanation lies in the initial orbital period for planets on different semi-major axes, since the orbital period is proportional to $a^{3/2}$ and will ensure that planets exchange angular momentum less frequently by action at

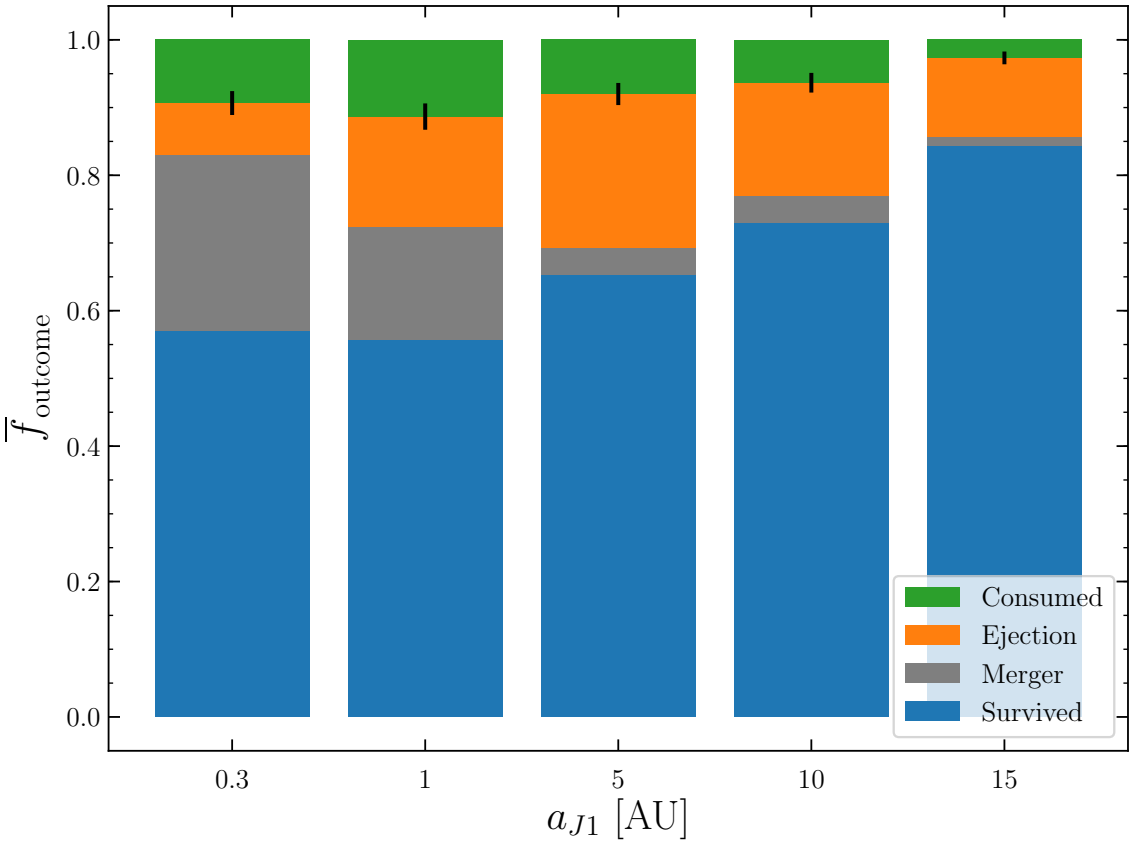

Figure 6.6: The mean fractional outcomes across the 100 simulations I have carried out for the 3J configuration with varying a_{J1} values: 0.1, 1, 5, 10 and 15 AU. The 5 AU case corresponds to the position of the 3J subsystem in the 2X+3J configurations. The outcomes considered are surivival (blue), consumption (green), merger (grey) and ejection (orange). The black bar represents the standard error for the mean fraction of consumed planets.

a distance, effectively increasing t_{CE}. Therefore, it will be much more difficult to induce a large fractional increase in AMD for one of the Jupiter-mass planets early on that could eventually lead to orbit crossing when the subsystem is far from the host star. Recall that there is not much exchange of energy before orbits have crossed. Instead, the dynamical instability timescale depends on the ability of the system to produce eccentric orbits, i.e. create a surplus of AMD in one of the orbits. Moreover, after the onset of instability it will take a longer time for the system to fully resolve since the close encounters will happen less frequently. This theory is reinforced by the fact that the number of close encounters needed to reach a CME outcome is not different from 3J systems that are situated further in, since I found the relationship between $\overline{\xi}$ and N_{CE} for these close encounters to be similar for all values of a_{J1}. This is due to the scale-invariance of planetary dynamics (Malmberg et al., 2011). Hence, each close encounter will lead to a large fractional change in energy

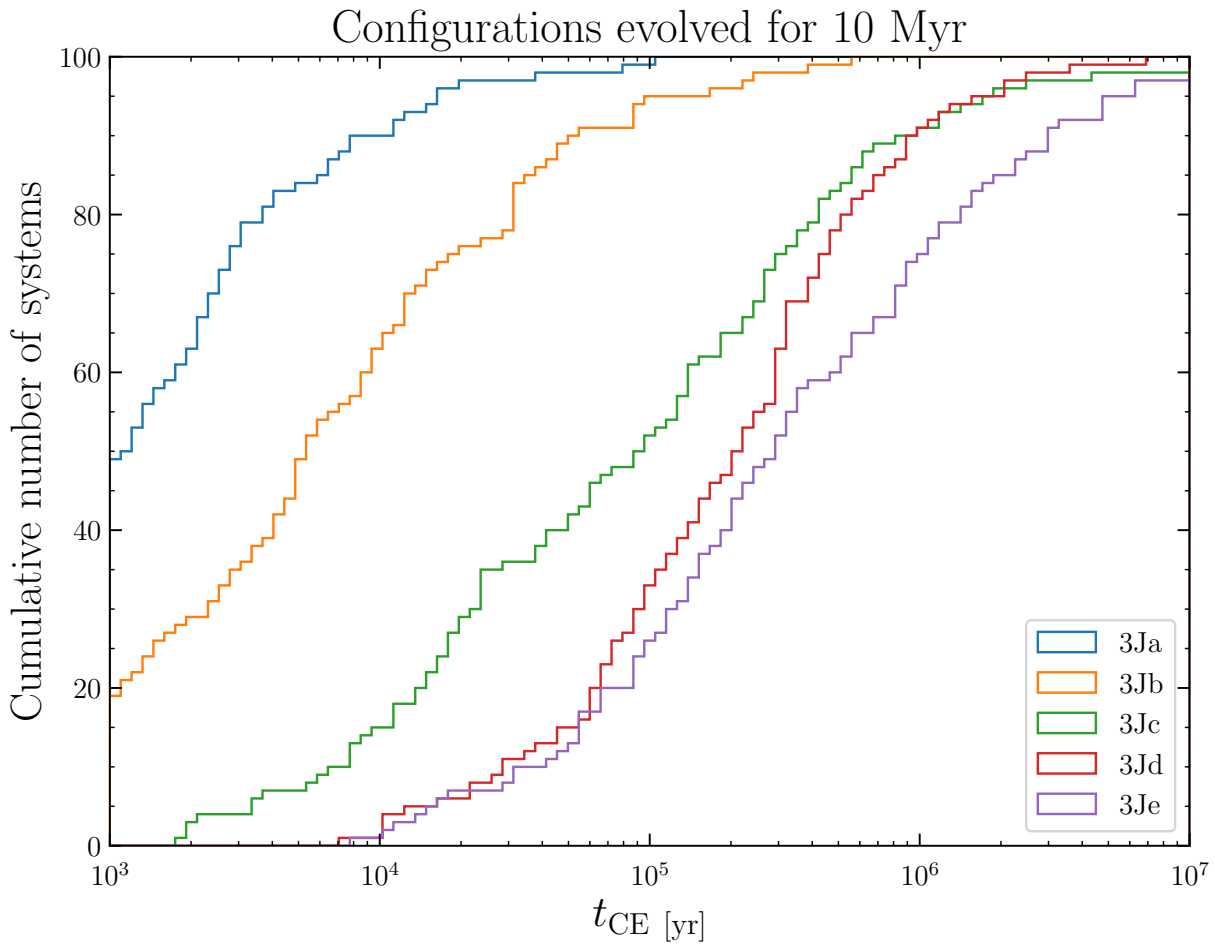

Figure 6.7: The cumulative number of systems as a function of the timing of first encounter t_{CE} in years for the different configurations used in the radial dependence investigation.

and thereby a large change in the semi-major axis, which in turn also alters the angular momentum of the orbit. Due to the long periods, around 20% of the systems are not yet fully resolved after 10 Myr for the cases of $a_{\mathrm{J1}} = 10$ AU and $a_{\mathrm{J1}} = 15$ AU, which should be kept in mind when interpreting the results of figure 6.6.

6.6 Multiplicity of giant planets in planet-consuming configurations

The behaviour of the giant planets within a planetary configuration is clearly the driving factor behind how much mass a host star of a given planetary system will consume. Up until now, I have always assumed that there are at least three Jupiter-mass planets in the configurations that all planetary systems are based on. As mentioned in section 3.1.1, it is

still not well understood how multiple giant planets are formed. Yet, if a planetary system is capable of producing one giant planet, there are indications that it will produce more than one (Wittenmyer et al., 2020), especially around high metallicity stars (Buchhave et al., 2018). But there will be scenarios where creating three giant planets around a Solar-type star will not be possible. Hence, I investigated the impact of reducing the number of giant planets in the fiducial 2E+3J configuration, creating a 2E+2J system. I opted not to integrate any configuration with a single giant planet as such a configuration would be completely stable unless the inner two Earth-mass planets would be Gladman unstable with $\Delta < 2\sqrt{3}$. Such a configuration would be unlikely to produce any planet-consuming events since the Safronov map in figure 4.1 indicates that mergers are highly favoured as an outcome for Earth-mass planets at $a \sim 1$ AU. There could be scenarios where the Jupiter-mass planet is situated much further in towards the inner subsystem producing a Gladman unstable configuration with the outermost Earth-mass planet. Here the Jupiter could drive up the eccentricity of the Earth-mass planet and ultimately put it on a planet-consuming orbit. The evolution of hierarchical two-planet systems has been investigated in Petrovich (2015), who found that the fraction of consumed terrestrial planets increases with $R_\star/a_\mathrm{p}$, which coincides with the findings in sections 5.4.2 and 6.5.

As seen in figure 6.1, the 2E+2J system has a giant planet separation of $\Delta = 3.0$ in order to ensure fast dynamical evolution. The resulting planetary systems from a $N = 50$ run can be found in figure 6.8. Firstly, there are a larger number of unresolved systems as compared to the 2E+3J case. Secondly, a majority of the innermost Jupiter-mass planets have semi-major axes smaller than a_f. This indicates that planet–planet scattering has been a more common pathway than Lidov–Kozai consumption for these systems. To elaborate, all of these surviving Jupiter-mass planets have made radial incursions into the inner subsystem, absorbing energy from the two Earth-mass planets. Nevertheless, the combined orbital energy of the two Earth-mass planets is not be large enough to put the survivors' semi-major axes inside of a_f. Instead, the ejected planet likely has carried a non-negligible amount of (positive) energy away from the system (Ford, Havlickova, & Rasio, 2001). Since two Jupiter-mass planets undergo a much less chaotic dynamical evolution than three Jupiter-mass planets, I also expect the orbital inclinations of the Jupiters to be kept small, which limits the possibility of having Lidov–Kozai oscillations between a Jupiter-mass and a Earth-mass planet without any scattering events between them after radial incursions by the Jupiter. The less chaotic dynamical evolution can also be inferred from the fact that there are only two cases of a Jupiter-mass planet being consumed for this configuration as compared to the 13 of the 2X+3J systems in figure 6.2. Interestingly, system 49 does not have a single surviving planet left. This curious result is due to a single scattering between two Jupiter-mass planets resulting in both an ejection and a planet consumption event. In order for this to occur, both planets must be on highly eccentric orbits $e > 0.8$ at the final encounter, leading to the ejected planet being scattered into an orbit with $e > 1$ while the consumed planet has an initially planet-consuming orbit with a large semi-major axis and an initial eccentricity of $e \lesssim 1$ and then gets anti-scattered onto a less eccentric orbit by the ejected planet.

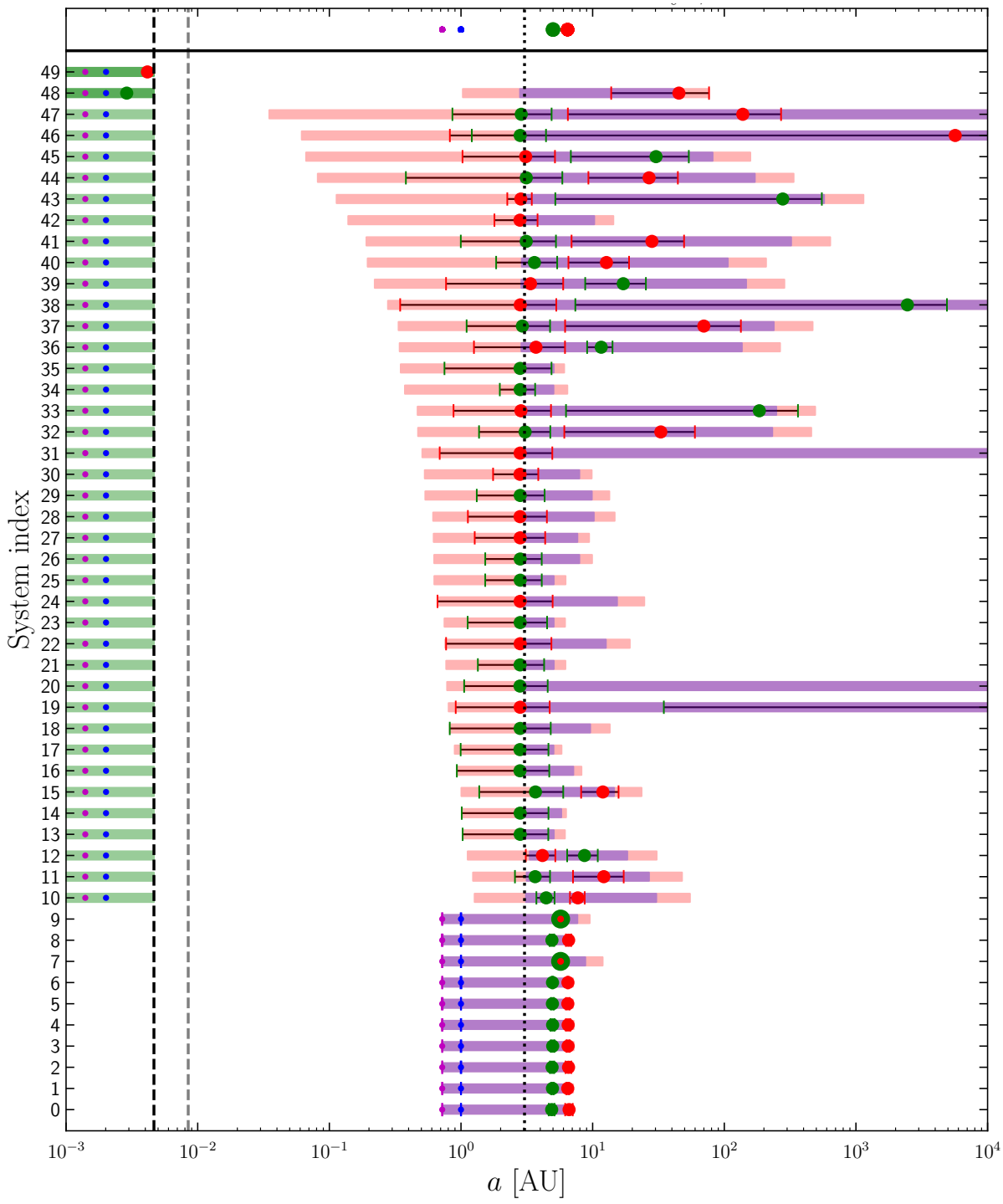

Figure 6.8: Examples of the final orbital configurations of the surviving planets in the 2E+2J configuration considered. For an explanation of the plot, see the text in section 6.3.1.

6.7 Planet-consuming systems in 3D

I now formulate a few statements regarding three-dimensional planet-consuming systems based on the findings in the analysis of this chapter, analogous to section 5.5, which I proceed to tie to observational consequences of planet consumption in the next chapter.

Insights from 3D analysis with MERCURY

1. Consumption of terrestrial planets up to a few ten $M_\oplus$ is very common for planetary systems with at least two unstable giant planets.
2. Consumption of giant planets with $M_\mathrm{p} > 100\ M_\oplus$ occurs in approximately 10% of my systems where there are at least three giant planets undergoing chaotic dynamical evolution.
3. There are three extreme pathways to planet consumption:
   - **Diffusive consumption:** A planet undergoes a large number of close encounters, slowly boosting up its eccentricity in a diffusive manner.
   - **Strong consumption:** A few strong subsequent scatterings rapidly drives up the eccentricity of a planet, putting it on a planet-consuming orbit.
   - **Lidov–Kozai consumption:** The eccentricity of a planetary orbit is increased due to Lidov–Kozai oscillations with a massive companion with high mutual inclination. Relevant for systems where there are mass ratios $q_\mathrm{p} \ll 1$ and more than two giant planets.
4. Planet consumption of terrestrial planets is more likely if they become strongly scattered at small distances from the host star $r \lesssim 1$ AU.
5. Planet consumption of giant planets is more likely if they are scattered at distances of $r \sim 1$ AU. For smaller distances merger will be the dominating outcome due to the large physical radii of Jupiter-mass planets, yielding a large d_crit. Nevertheless, a small separation from the host star is preferable to distances of $r > 5$ AU.
6. The final orbital configuration of surviving giant planets within a resolved planetary system depends on the system's initial energy, which is conserved in the system. However, if a giant planet has been consumed, a fraction of the total energy of the planets can be transferred to the host star. Hence, planet-consuming systems can produce single giant planets with wide orbits of $a_\mathrm{p} > 20$ AU.
   - The magnitude of transferred energy depends on the pathway to consumption. Strong consumption of a sufficiently massive planet will put the remaining innermost planet on an orbit with $a_\mathrm{p} \gg a_\mathrm{f}$, while diffusive consumption will transfer less energy to the host star.

Chapter 7

Observational consequences of planet consumption

From the analyses in chapters 5 and 6, planet consumption seems to be a common occurrence in young, unstable planetary systems with multiple giant planets. However, given the facts that the process of planet–planet scattering in such systems resolves over timescales much shorter than the lifetime of the system and that it is generally difficult to detect exoplanets, the probability of observing such an event directly is astonishingly small. Therefore, any occurrences of planet consumption events in the history of a planetary system have to be inferred using indirect methods. Luckily, there are a variety of possible observational consequences of planet consumption, not only for the host star, but also for the remaining planets in the system. The main signatures are caused by the transfer of angular momentum, energy and heavy elements to the host star. Hence, the signature caused by a specific consumption event is highly dependent on the intrinsic properties of the consumed planet, as well as the nature of the collision. The observational consequences of planet consumption are summed up in Stephan et al. (2020) as

- **Stellar spin-up:** A planet tidally interacts with the host star, transferring angular momentum, which leads to a decrease in the rotational period of the star and potentially reorientation of its spin.
- **Planet merger *transient*:** The transfer of energy from a planet to the host star over small timescales leads to signatures in the form of electromagnetic radiation and a temporary increase in luminosity.
- **Surface-grazing interactions:** A planet grazes the surface[1] of a star, leading to the ejection of stellar matter through gravitational disruption.
- **Stellar metallicity enhancements:** Disruption of a planet within the convective envelope of a star leads to pollution with heavy elements, altering its metallicity.

[1] With surface, I refer to the edge of the stellar photosphere.

In this chapter, I go through the main effects of planet consumption on the host star[2] listed above one by one and constrain the possible observable effects of such events based on the results from my N-body simulations. Furthermore, I discuss the effects that planet consumption can have on the observed configuration of surviving planets after the conclusion of chaotic dynamical evolution.

7.1 Tidal planet–star interactions

A low density, massive planet with $r_{\min} \sim R_\star$ undergoing a close encounter with its host star will be made subject to strong tidal forces. These forces can lead to the creation of hot Jupiters through tidal circularisation. The tidal forces acting on the planet dominate the exchange of angular momentum which circularises the orbit, while the tidal forces acting on the host star dominate the exchange of energy which reduces the orbital period (Davies et al., 2014). Short-period orbits that have periods longer than the rotational period of the host star will decay through tidal interaction with the host star such that the planet spirals in towards the star and ultimately gets tidally disrupted at $r \sim R_{\text{Roche}}$ (Metzger, Giannios, & Spiegel, 2012).

The time it takes for a giant planet to circularise to short-period orbits depends highly on the initial periastron of the orbit, tidal dissipation mechanics, as well as planetary properties and spans several orders of magnitude (Dawson & Johnson, 2018). Nevertheless, Nagasawa, Ida, & Bessho (2008) estimated that the circularisation timescale for a Jupiter-like planet with a periastron around 0.03 AU is $\sim 10^6$ yr. Hence, given that the initial period of a planet at 5 AU is ~ 11 yr, such a planet would need at least 10^5 orbits to circularise. Moreover, the authors determined that a planet with $r_{\min} < r_{\text{tide}}$ will not be circularised during the chaotic dynamical evolution phase of the system. This is due to the fact that the changes in orbital elements from planet–star tidal interactions occur on much longer timescales than the exchanges of angular momentum and energy between the unstable three Jupiter-mass planets. In order to circularise a giant planet during this stage, it would first have to be scattered onto an orbit such that it is isolated from close encounters with the other planets. This would also makes the system eligible for eccentricity increase by Lidov–Kozai oscillation.

Hence, since it is not certain that each planet becoming a hot Jupiter will ultimately be consumed by its host star, there might be an overestimation of the number of consumed Jupiter-mass planets in the results from chapter 6 because of the exclusion of tidal effects in my integrations. In order to get a rough estimate of how many hot Jupiters that would have been produced in the 2E+3J realisations, I compare the cumulative number of orbital periods spent in the region of tidal disruption and tidal decay, in terms of initial orbital period P_0. The region of tidal disruption corresponds to the distance from the host star where the planet fulfils $r_{\min} \leq R_{\text{Roche}}$. As for the region of tidal decay, this is where a

[2]Note that all the following analysis is for a Sun-like star prior to its turn-off towards the red giant branch.

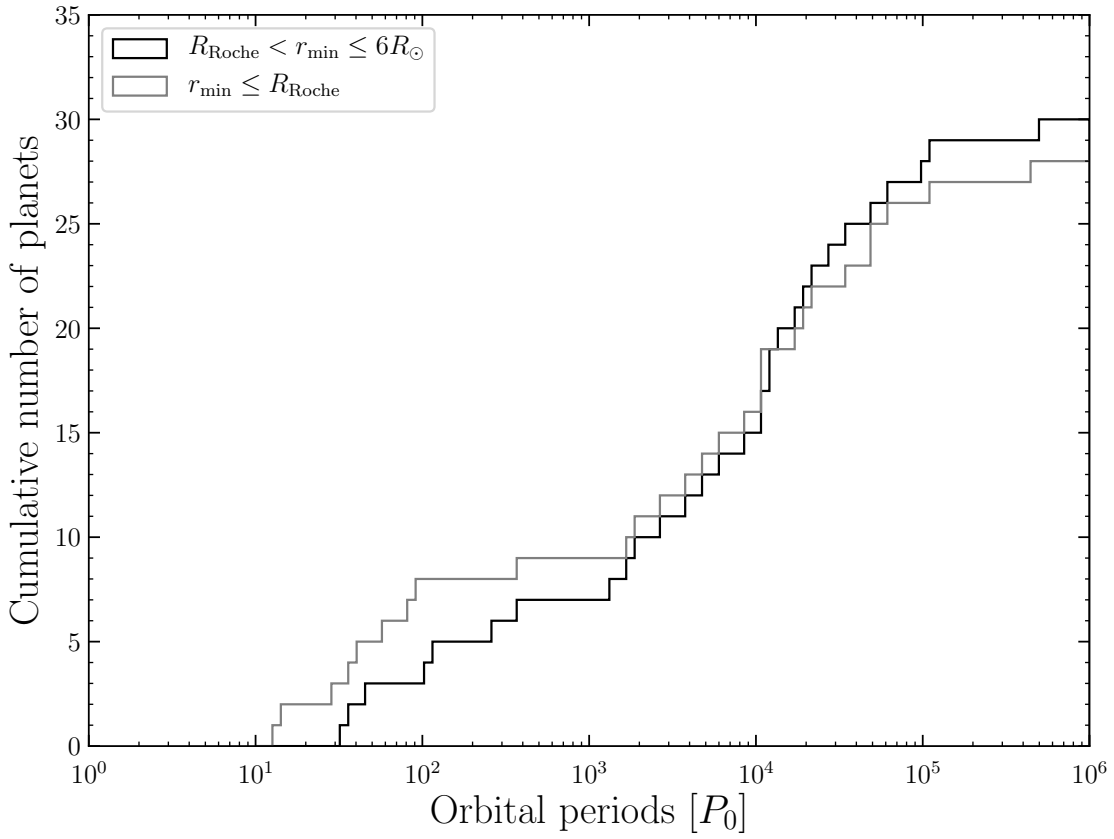

Figure 7.1: The cumulative number of consumed Jupiter-mass planets as a function of the number of periods spent in critical separations with the host star. $6R_\odot$ corresponds to the empirical limit for tidal circularisation determined for Sun-like stars by Beaugé & Nesvorný (2012), while $R_{\rm Roche}$ is the limit for tidal disruption.

tidal interaction with the host star leads to a significant exchange of angular momentum and energy and is given by $R_{\rm Roche} < r_{\rm min} \leq r_{\rm tide}$. For the critical tidal decay radius, I choose the empirically limited value for Sun-like stars from Beaugé & Nesvorný (2012) of 0.03 AU $\sim$ 6 $R_\odot$. The corresponding cumulative distributions can be found in figure 7.1. Given that a planet would need to spend around 10^5 orbits within the $R_{\rm Roche} < r_{\rm min} \leq 6\ R_\odot$ regime to circularise, the number of hot Jupiters produced during the 2E+3J run should approximately correspond to the difference between the two plotted distributions at 10^5 P_0 orbits or more. This difference of 3 to 4 planets is slightly lower than the results from Beaugé & Nesvorný, who estimated that 10% of planetary systems with three Jupiter-mass planets would produce a hot Jupiter, which I attribute to statistical fluctuation. Hence, the exclusion of tidal forces in my integrations does not cause any significant change in observed behaviour of the consumed Jupiter-mass planets. This is further reinforced by the fact that any hot Jupiters created most probably would end up being consumed by their host star due to rapid decay of their orbits. Teitler & Königl (2014) noted that there is a

dearth of observed hot Jupiters with orbital periods of $P_{\rm p} \lesssim 2-3$ days around host stars with rotational periods of $P_\star \lesssim 5-10$ days, which they attributed to this phenomenon. Rapid decay of a planet's orbit due to tidal interactions with its host star on timescales shorter than its period is referred to as *tidal plunging*. For a Sun-like MS star, the plunging radius is at approximately a tenth of the stellar radius below the stellar surface (Stephan et al., 2020).

7.1.1 Mass transfer before planet consumption

Whenever a giant planet passes its Roche limit near the host star, it is not certain that it will be completely disintegrated by the ensuing Roche lobe overflow. Instead, the mass transfer between the planet and the host star can be stable and take place over a few Gyr (Metzger, Giannios, & Spiegel, 2012), removing the gaseous envelope and leaving the planet with an exposed rocky core. Stable mass transfer would be more likely for low density planets with $\mathrm{R}_\odot < r_{\rm min} \leq R_{\rm Roche}$, which mainly targets short-period hot Jupiters. Said phenomenon could explain the existence of short-period super-Earths and hot Neptunes (Valsecchi, Rasio, & Steffen, 2014). There are three possible outcomes for the mass transferred due to Roche lobe overflow

1. Self-accretion by the planet.
2. Direct impact on the stellar surface.
3. Disk formation around the host star.

Dosopoulou, Naoz, & Kalogera (2017) employed numerical means to investigate the behaviour of the ejected mass particle due to mass transfer in the ballistic limit and found that scenarios 2. and 3. are only possible for low-eccentricity $e < 0.2$, prograde orbits. Said outcomes would therefore only be viable for circularised hot Jupiters or planets that have been put on short-period orbits through planet–planet scattering or disk migration. If that is the case, the only possible outcome for the planet–planet scattering cases in my integrations, where the planets have high eccentricities, would be self-accretion of the mass by the planet undergoing Roche lobe overflow. Hence, there would not be any mass transfer onto the host star before the planetary orbit decays, leading to direct impact on the stellar surface. In turn, I have assumed that planets will retain their mass until they break through the surface of their host star. This goes against the results in Guillochon, Ramirez-Ruiz, & Lin (2011), who argue that a majority of Jupiter-mass planets with $e \gtrsim 0.97$ within the tidal disruption radius would be ejected from the system in just a few orbits. However, their conclusion is largely based on the giant planet gaining a significant amount of energy due to asymmetrical mass transfer onto the host star during their close encounter, increasing its semi-major axis. Since I assumed that Jupiter-mass planets will retain their initial masses prior to their impact on the stellar surface, it follows that none of them will end up being ejected from the system.

7.1.2 Fates of planets due to stellar tides

Tidal interactions between a planet and its host star remain a hot topic for research (see review by Ogilvie, 2014) since different models can produce a large variation in results. This comes from the fact that they are highly dependent on the so-called tidal quality factor, $Q'_\star$, that can range several orders of magnitudes (see discussion in Popkov & Popov, 2019). The complexity of the problem is directly related to the many ways a planet can interact with its host star, given the star's strong magnetic field, energetic radiation and stellar winds (Vidotto, 2020). Hence, to fully understand what the outcome would be for each planet in my simulations it is clear that an extensive formal discussion would be needed with detailed modelling of the complex interior of both the host star and the planet, which is beyond the scope of this thesis.

Nevertheless, there are three main fates for a tidally interacting planet that can be derived from the outcomes of the Roche lobe overflow above. These outcomes are directly related to the bulk density ratio between the two bodies, which can highly affect the nature of the close encounter between them since it determines the Roche limit for tidal disruption. A low density planet, e.g. with Jupiter-mass, will get disrupted outside the stellar radius for a Sun-like star, while a rocky Earth-mass planet has a Roche limit beneath the stellar surface. This quantity will also determine the nature of mass transfer between the two bodies and in turn the properties of any transient events (Metzger, Giannios, & Spiegel, 2012). To a first approximation, the limits are defined as

- **Stable accretion** $\overline{\rho}_\mathrm{p}/\overline{\rho}_\star \lesssim 1$: The planet undergoes stable mass transfer with the host star.
- **Tidal disruption** $1 \lesssim \overline{\rho}_\mathrm{p}/\overline{\rho}_\star \lesssim 5$: The planet is disrupted close to, but outside the stellar radius.
- **Direct impact** $\overline{\rho}_\mathrm{p}/\overline{\rho}_\star \gtrsim 5$: The planet is disrupted below the stellar surface.

However, as previously mentioned, these conditions derived by Metzger, Giannios, & Spiegel appear to only remain true for planets that are already on circularised orbits with eccentricities $e \lesssim 0.2$ (Dosopoulou, Naoz, & Kalogera, 2017), which would only be the case for 3 to 4 of my planets. Hence, I have not taken any scenarios where the planet undergoes stable mass transfer or gets disrupted above the stellar surface, creating an accretion disk around the host star, into account. I have however assumed that any Jupiter-mass planets within the Roche radius will ultimately be consumed due to their strong tidal interactions with the host star.

7.2 Planet-consuming encounters

There are a few parameters that govern which observational effect will be strongest for a given planet. First of all, the properties of the orbit at collision will directly determine how much time a planet will spend within the convective envelope before reaching the plunging

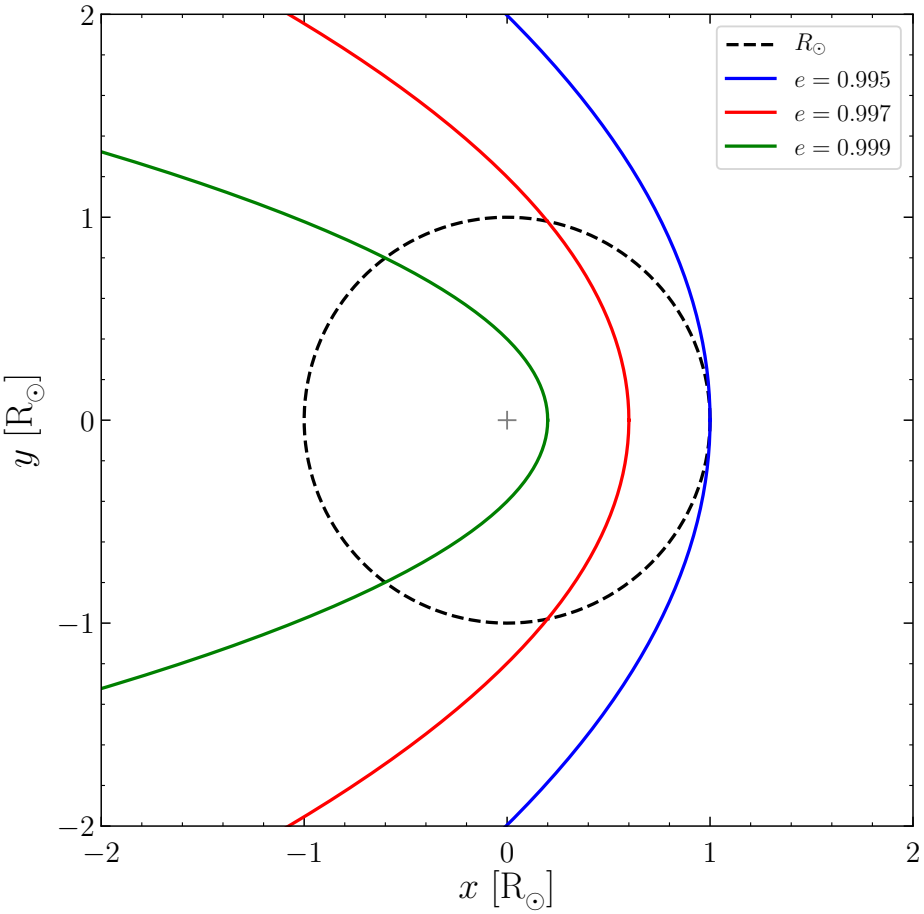

Figure 7.2: Three examples of consuming orbits for a Sun-like host star to show the difference in impact angle, which directly affects the time spent within the convective envelope of the host star. All the orbits have $a = 1$ AU.

radius. This becomes clear when looking at figure 7.2, where I have plotted three different cases of highly eccentric orbits with a semi-major axis of 1 AU. A change of merely 0.002 in eccentricity significantly alters the impact parameter and in turn the velocity of the planet relative to the surface. In the cases of $e = 0.997$ and $e = 0.999$, the planet will reach the plunging radius during its first entry. I refer to such a scenario as a *prompt collision*. The case where $e = 0.995$ and $r_{\rm min} \sim R_\star$ is a *grazing collision*. A useful quantity to determine whether or not the planet will plunge during its first passing within the host star is the fraction of the planets velocity that is radial at $r_{\rm p} = R_\star$, which is provided in Church,

Mustill, & Liu (2020) as

$$f_{\perp} = \sqrt{1 - \frac{a^2(1-e^2)}{R_{\star}(2a - R_{\star})}}. \tag{7.1}$$

For reference, from least eccentric to most eccentric orbit, they have $f_{\perp} \sim 0$, $f_{\perp} = 0.63$ and $f_{\perp} = 0.89$. For a planet to have a $r_{\mathrm{min}} = 0.9$ $\mathrm{R}_{\odot}$, the critical eccentricity for a 1 AU orbit yields $f_{\perp} = 0.40$. Hence, without taking energy loss through gas drag and tidal drag into account, a planet would need $f_{\perp} \gtrsim 0.40$ to be consumed directly on its first passage within the host star.

The second parameter is the the bulk density ratio between the planet and the host star, which as previously mentioned will determine the nature of the planet consumption. Nevertheless, this is mainly true for non-eccentric orbits (Dosopoulou, Naoz, & Kalogera, 2017). The final quantity is the inclination of the orbit, which can affect the exchange of angular momentum between the two planet and the host star. Assuming that the reference plane for Keplerian elements in the planetary system is perpendicular to the spin axis of the star, an inclined orbit will have an angular momentum vector that is misaligned with respect to the host star.

The most important quantities are summarised as follows:

- $a(1-e)$: The combined orbital elements (a, e) determine the impact angle for the planet and in turn the fractional radial velocity $f_{\perp}$. Hence, the periastron distance will decide when and where the planet will get disrupted by the host star.
- $\overline{\rho}_{\mathrm{p}}/\rho_{\star}$: The fraction between the density of the planet and the host star will determine the position of the Roche limit, at which the planet will be disrupted.
- i: The inclination is important when it comes to the reorientation of the spin axis due to exchange of angular momentum.

The distribution of the final registered orbits for consumed planets in 100 2E+3J `MERCURY` realisations is displayed in figure 7.3. Note the translucency of individual lines, which provides a visual measure of the orbit number density given by the colour strength of a line. The blue orbits represent Earth-mass planets and the red lines, which have been plotted on top of the blue lines, represent Jupiter-mass planets. Further, the stellar radius and Roche radius for the Jupiter-mass planet are shown with a black and grey dashed line, respectively. A vast majority of the orbits are directly grazing the stellar surface, which means that they will most probably survive the first passing beneath the surface of the host star. Only two of the planets have trajectories that will put them well within the plunging radius, meaning that they will spend much less time within the convective envelope. This was confirmed by computing $f_{\perp}$ for the orbits, which yielded only two orbits with $f_{\perp} \gtrsim 0.4$. Said result coincides well with the findings of Church, Mustill, & Liu (2020), which indicate that systems where the dynamical evolution is dominated by the

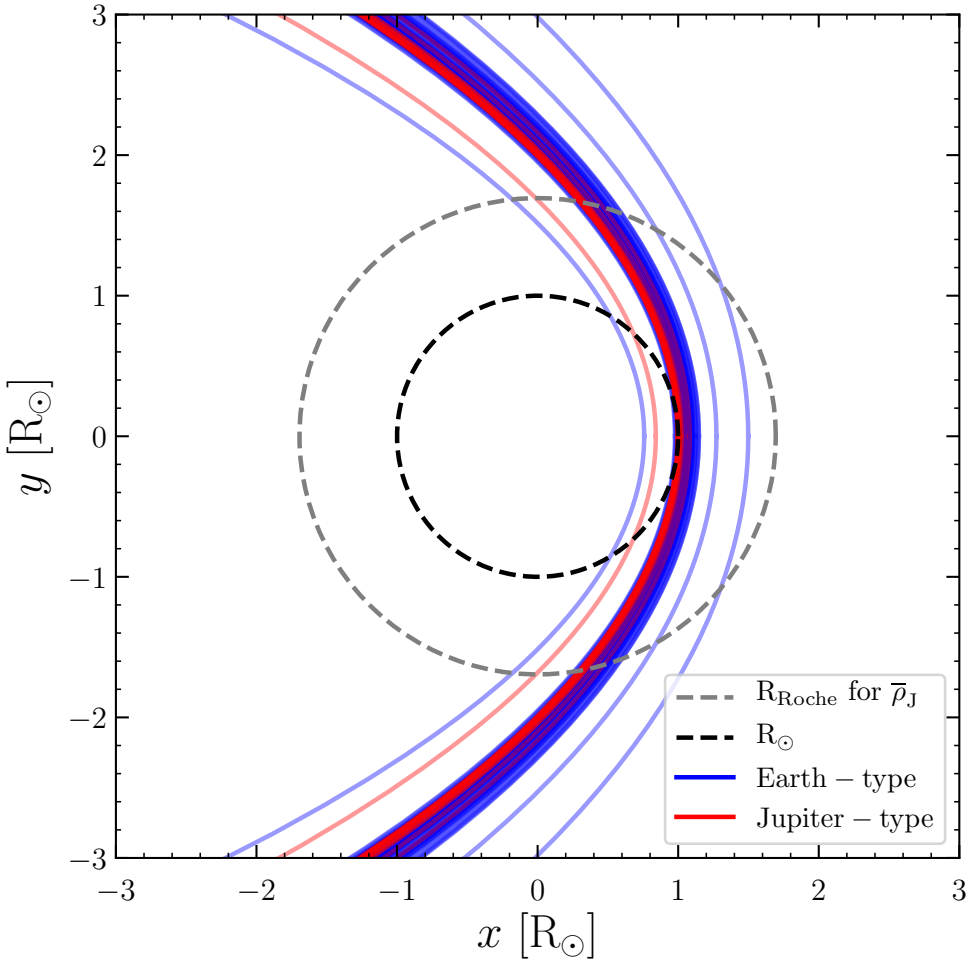

Figure 7.3: The final orbits of the consumed planets in $N = 100$ 2E+3J realisations. Blue orbits represent Earth-mass planets while the red orbits show the closest approach for Jupiter-mass planets. The grey dashed line represents the Roche radius for Jupiter-mass density for the MR-relation from section 3.4. The black dashed line is the radius of the host star. From the plot, it is clear that a majority of the orbits will be grazing at stellar impact.

Lidov–Kozai mechanism can produce a larger number of prompt collisions than systems that evolve through planet–planet scattering. I discuss the implications of this effect in section 7.6.

From figure 7.3, it is further evident that there is a significant number of orbits with $r_{\rm min} > {\rm R}_\odot$. This is due to a numerical caveat within `MERCURY`, where the final planetary phases at the time of consumption are not necessarily included in the output data due to poor resolution. To elaborate, planets that collide with the host star will be directly removed from the integration. Hence, if the consumption occurs during the period in

between two outputs $t = t_0$ and $t = t_0 + \Delta t$, at some time $t_{\rm CME}$, the final phase of the planet will be given by the orbital elements of the planet at $t = t_0$. Even though I chose a maximum period in between outputs of 10 days, it did not suffice for the detail needed in this analysis. Unfortunately, the nature of the numerical integration setup did not allow for changes in the resolution of the data prior to the conclusion of a realisation. Hence, I perform the analysis in this chapter with said issue in mind. The final few changes in AMD of the orbits in figure 7.3 must have a low ξ value since `MERCURY` logs the data of close encounters when they occur and not at the end of each time step. In turn, the final changes in AMD that bring the planet to an orbit with $r_{\rm min} \lesssim {\rm R}_\odot$ are caused by either Lidov–Kozai oscillations or other secular or resonant interactions. This means that any further increase in eccentricity will be diffusive, which allows me to assume that the final periastron distance for these planets will be equal to $R_\star$.

7.3 Stellar spin-up

A consequence of the interactions between a massive planet and its host star is that they can lead to changes in the stellar spin due to an increase of its angular momentum. The transfer of angular momentum to the host star can occur during two stages in the planet consumption phase. If the planet is outside or in the outer regions of the host star, exchange will mainly occur through the work done by tidal forces. If the planet instead breaks the stellar surface, gas drag will be the dominating mechanism for exchange of angular momentum (Metzger et al., 2012; Stephan et al., 2020). This holds under the assumption that the host star is still on the MS. The drag forces will not be as strong for e.g. a star on the Red Giant Branch (RGB), for which the stellar envelope has a lower density.

While the angular momentum of a terrestrial planet or super-Earth will not be large enough to induce a notable change in the rotational frequency of the host star, a Jupiter-mass planet can spin-up the host star by up to 70% with respect to its initial rotational frequency (Qureshi, Naoz, & Shkolnik, 2018). Given that the rotation of Sun-like stars slows down due to *magnetic braking*[3] effects (e.g. Parker, 1958), rapid rotation of a dwarf star deep into its MS lifetime serves as a possible indicator of past planet consumption events (e.g. Qureshi et al., 2018; Benbakoura et al., 2019; Stephan et al., 2020; Oetjens et al., 2020). Moreover, the transfer of angular momentum to the host star can also lead to reorientation of the stellar spin axis. Privitera et al. (2016) also found that a significant spin-up can cause an RGB star to develop an observable magnetic field at its surface.

The magnitude of spin-up and change in the stellar rotational orientation depend not only on the mass, but also on the inclination of the planet's orbit. A large inclination can lead to a large change in *stellar obliquity*, which is the angle between the rotational axis of the host star and the angular momentum vector of the orbital plane. There have been observations of hot Jupiters around MS stars with obliquities of $\sim 90°$. An example of

[3]The loss of angular momentum due to ejection of material caught in the magnetic field of the star.

such an observation, made by CHEOPS (Lendl et al., 2020), is WASP-189 b, which is a gas giant orbiting a 2 $M_\odot$ star with a stellar obliquity of $\sim 85°$.

7.3.1 Stellar spin-up for varying inclinations

In order to investigate the effects of stellar spin-up for the consumed Jupiter-mass planets in the 2E+3J systems, I employed a simple calculation to estimate the resulting angular momentum of the host star from Qureshi, Naoz, & Shkolnik (2018). Ignoring differential rotation within the host star, the angular momentum of a spinning star is well-approximated by the angular momentum of its envelope. Assuming that the envelope reaches down to the core, its moment of inertia is $I_{\star,\mathrm{env}} \sim 0.08 M_{\star,\mathrm{env}} R_\star^2$ (Stephan et al., 2020). This yields

$$J_\star \approx J_{\star,\mathrm{env}} \approx 0.08 M_{\star,\mathrm{env}} R_\star^2 \Omega_{\star,\mathrm{env}} \tag{7.2}$$

where $\Omega_{\star,\mathrm{env}}$ is the rotational frequency of the stellar envelope. Since angular momentum is conserved, the post-consumption angular momentum of the envelope is given by

$$\boldsymbol{J}_{\star,f} = \boldsymbol{J}_\star + \boldsymbol{J}_\mathrm{p} = 0.08 M_{\star,\mathrm{env}} R_\star^2 \boldsymbol{\Omega}_{\star,\mathrm{env,f}}. \tag{7.3}$$

Solving for the final rotational frequency, I obtain that

$$\boldsymbol{\Omega}_{\star,\mathrm{f}} = \boldsymbol{\Omega}_{\star,\mathrm{env}} + \frac{12.5}{M_{\star,\mathrm{env}} R_\star^2} \boldsymbol{J}_\mathrm{p}. \tag{7.4}$$

I now assume that the reference plane for the Keplerian coordinates is coplanar with the equatorial plane of the host star. Hence, I can obtain the final orbital frequency of the host star by adding the two vectors in equation (7.4). For the initial rotational frequency of the Sun-like star I obtained it from the average rotational period of the Sun, which is about 27 days (Stenflo, 1990).

To determine the mass of the Sun's envelope, I used the fact that its core has a radius of around 0.2 $R_\odot$. Employing modelled data for the Sun's interior obtained from the Yale Rotating Stellar Evolution Code (YREC: Demarque et al., 2008), the core makes up around 34% of the Sun's total mass, which yields $M_{\star,\mathrm{env}} = 0.66\ M_\odot$. Knowing said value, it was straightforward to compute the magnitude of $\boldsymbol{\Omega}_\mathrm{f}$, which in turn provided the new rotational period of the host star P_f. The negative fractional change in stellar rotational period as a function of the inclination of the consumed planet obtained from this simplified analysis is shown in figure 7.4. Note that only the orbits with $r_\mathrm{min} < R_\mathrm{Roche}$ have been included here. From the results, it is evident that Jupiter-mass planets can significantly spin-up the rotation of the host star, even for retrograde orbits where $i > 90°$, which aligns with results from Qureshi, Naoz, & Shkolnik and Stephan et al.. Due to the sizeable magnitude of the angular momentum for the Jupiter-mass planets, the resulting period will always

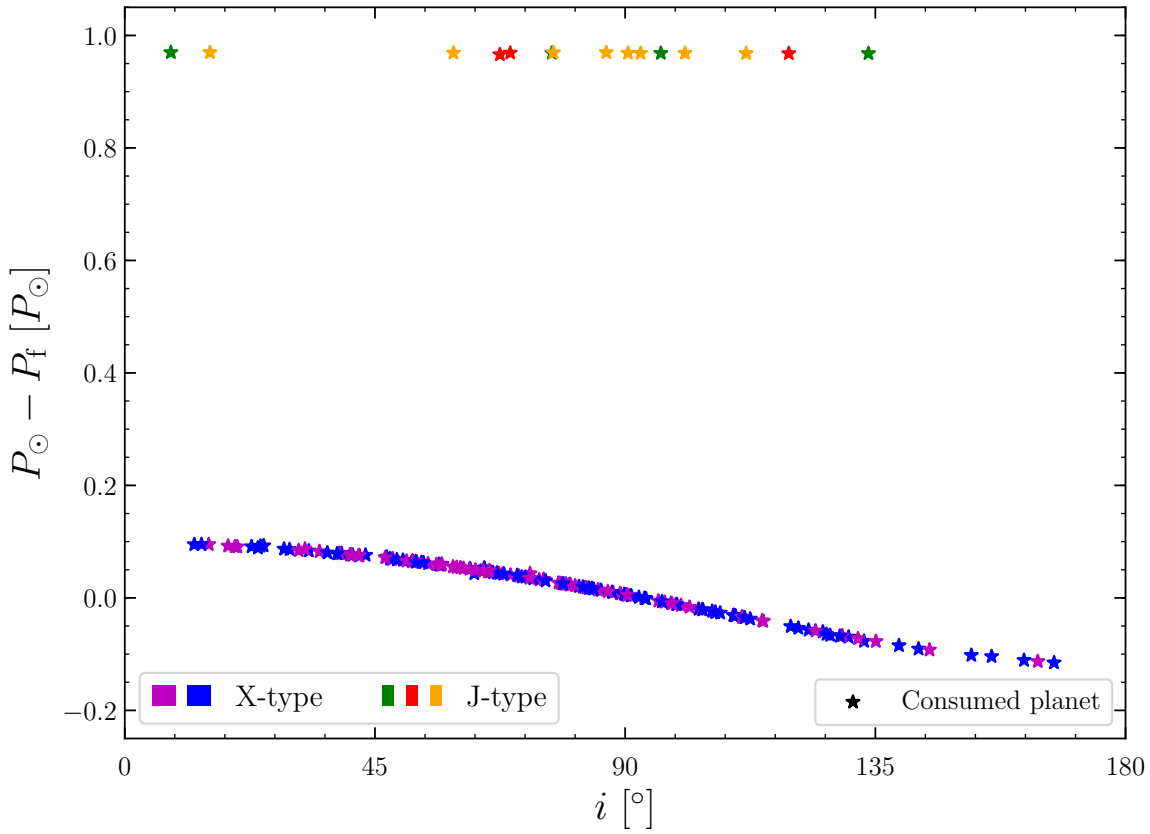

Figure 7.4: The negative fractional change in stellar rotational period after consumption of a planet. The colour and marker scheme follows the same prescription as in chapter 6. Note that any planets with $r_\mathrm{min} > R_\mathrm{Roche}$ for its final phase has been excluded.

lead to a decrease in the rotational period, even if the final orbit is retrograde. This result implies the importance of the pathway to planet consumption. Since the Jupiter-mass planets are more likely to undergo diffusive consumption, their eccentricities will slowly increase until $r_\mathrm{min} \sim \mathrm{R}_\odot$. In turn, they will retain a value of J_p that leads to new stellar rotational periods of $P_\mathrm{f} \sim P_\odot/40$. However, for the case of the Earth-mass planets, their angular momenta are too small to completely change the orientation of the rotation of the host star despite the fact that they mainly undergo grazing collisions and will as a result merely cause a small perturbation in the stellar spin period. From the simple analysis performed here, it appears that subsequent accretion of Earth-mass planets could cause an observable change in the stellar spin if the planets have i such that $\boldsymbol{J}_\mathrm{p}$ and $\boldsymbol{J}_\star$ are parallel or anti-parallel. However, due to likely overestimation of the orbital angular momentum of the planets due to poor resolution around t_CME and the lack of a proper stellar evolution model for the host star, I cannot draw such a conclusion. Nevertheless, I will continue this

discussion in chapter 8.

To a first approximation, if the host star gets spun up such that it has a period of

$$P_{\rm crit} = 2\pi\sqrt{\frac{R_\star^3}{GM_\star}}, \tag{7.5}$$

gravity will no longer be able to contain the stellar envelope since material would be launched into orbit (Stephan et al., 2020). However, for the case of the Sun, which is still on the MS, this period would correspond to an increase in rotational velocity by a factor ~ 200. Hence, the planet would need a larger angular momentum by being more massive. Another case where this effect could be more relevant is for post-MS RGB or Asymptotic Giant Branch (AGB) stars since they have large values of $R_\star/M_\star$. For example, a Jupiter-mass planet cannot spin up a Sun-like star beyond its critical rotational frequency in its MS phase, but it is entirely possible if the star is in its helium burning or AGB phases (Stephan et al., 2020).

7.3.2 Reorientation of stellar spin

Due to the angular momentum carried by the consumed Jupiters and their high inclinations, a merger with a host star and a Jupiter-mass planet can lead to reorientation of the stellar spin axis. For my simplified scenario, the star could obtain obliquities up to $\sim 90°$ when consuming a Jupiter-mass planet with an inclination of $\sim 90°$. While any quantitative evidence for this effect would need a more sophisticated investigation with a proper stellar model, the qualitative results align well with Matsakos & Königl (2015), who argue that early planet consumption of a short-period hot Jupiter can account for some of the observed misalignment patterns in planetary systems.

7.4 Surface-grazing interactions

When a planet grazes the stellar photosphere, it will gravitationally disturb matter at the stellar surface. In turn this can lead to ejections of gaseous stellar material in the form of 'gas bullets'. This is a plausible explanation of the periodic ejections of matter observed for the carbon star V Hya (Salas et al., 2019). Using a simple ballistic model from Dosopoulou, Naoz, & Kalogera (2017), the speed of the bullet can be estimated by the sum of the planet's velocity at its periastron passage and its surface escape velocity

$$v_{\rm bullet} \approx \sqrt{G(M_\star + M_{\rm p})\frac{1+e}{a(1-e)}} + \sqrt{\frac{2GM_{\rm p}}{R_{\rm p}}}. \tag{7.6}$$

By requiring that the bullet velocity must be larger than the stellar surface escape velocity,

$v_{\text{bullet}} \geq v_{\text{esc},\star}$, for ejection Stephan et al. (2020) formulated the following condition for bullet ejection

$$\frac{M_{\text{p}}}{R_{\text{p}}} \geq \frac{M_\star}{R_\star}\left(\frac{3}{2} + \frac{e}{2} - \sqrt{2(1+e)}\right) = \zeta(e). \tag{7.7}$$

Said relation only holds for the case of $M_\star \gg M_{\text{p}}$. The right-hand side of the expression will go to zero when $e \to 1$, which means that the probability for bullet ejection is largest for high density planets on highly eccentric orbits. On the other hand, note that an eccentricity larger than e_{crit} will produce prompt collisions with small impact parameters, which leads to little-to-no spin-up. I have plotted $M_{\text{p}}/R_{\text{p}}$ against the eccentricity of the C-type orbits from my `MERCURY` realisations of 2E+3J with $r_{\min} < R_{\text{Roche}}$ in figure 7.5. Due to the high eccentricities obtained from subsequent planet–planet scattering events, all the consumed planets would be able to eject gas bullets if they are on grazing orbits. It is noteworthy that the plotted values are for orbits with $r_{\min} \sim R_\star$, which is not the case for all the final orbits in figure 7.3. Hence, some of the eccentricities are not completely accurate. First and foremost, the ejection of bullets would not occur for planets with $r_{\min} < \text{R}_\odot$, since they would have too high a $f_\perp$ value and directly plunge towards the deep interiors of the star. Furthermore, I argue that the bullets ejected by an Earth-mass planet would prove difficult to detect due to their low mass. An additional issue with Earth-mass planets as an origin for the ejecta, is the fact that they are less likely to undergo diffusive planet consumption. As I showed in figure 6.3, Earth-mass planets are consumed earlier on during the dynamical evolution with fewer total scatterings. In turn, this means that they will make fewer passages close to the host star before they are consumed. Hence, the gas bullet ejections originating from grazing encounters by an Earth-mass planet would not be as numerous as for a Jupiter-mass planet. Moreover, the energy of the planet will slightly decrease after each ejection of surface material bullets, which reduces the impact velocity of the planet. Hence, subsequent bullet ejections become less likely the more grazing encounters a planet has undergone.

7.5 Planet merger transients

As determined in section 7.1.1, a planet with an eccentricity $e \lesssim 1$ will most probably not undergo stable mass transfer or get disrupted above the stellar surface. Hence, most planets from my simulations (ignoring potential hot Jupiters) will stay intact during tidal interactions with the host star and undergo grazing interactions with the stellar surface, leading to direct impact. For said reason, I will not discuss transients originating from tidal dissipation or stable accretion (for a discussion of said effects, see Metzger, Giannios, & Spiegel, 2012). Due to tidal decay of its orbit, the grazing planet will fully submerge in the convective envelope of the star after a few passages. Well within the stellar surface, the planet continuously sheds orbital energy and angular momentum due to turbulent gas drag, causing it to spiral in towards the centre of the star. Due to my assumption that

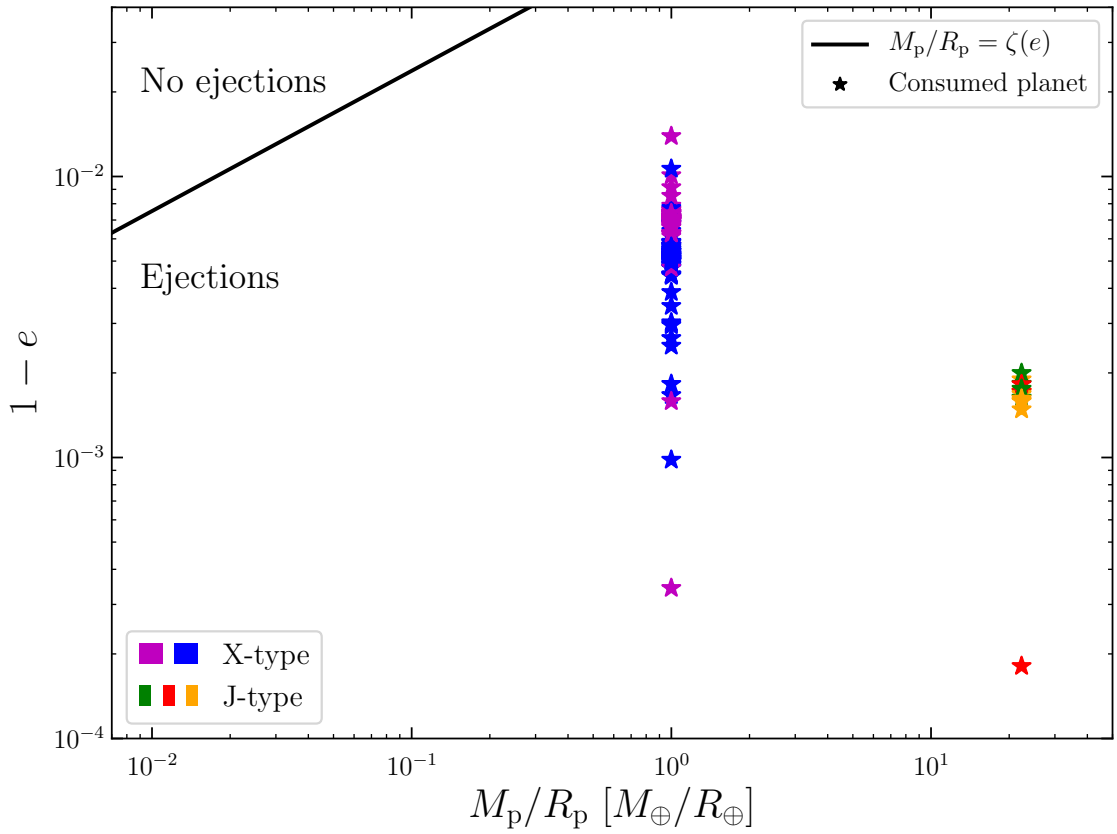

Figure 7.5: The mass-radius ratio for the consumed planets in 2E+3J plotted against their final registered value of $1-e$. The black line indicates the criteria for ejection of bullets made up of gaseous stellar material after a planet has grazed the surface of the host star. Planets on the right side of the line will eject bullets from the system. Valid for a Sun-like star with $M_\star \gg M_p$.

the planet will get fully disrupted beneath the stellar surface, the energy released during the disruption, given by $E_{grav} \sim GM_\star M_p/R_\star = 4 \times 10^{46}(M_p/\mathrm{M_J})$ erg, will heat up the matter in the convective envelope. With a hotter stellar interior, the stellar luminosity will initially increase, then decrease on the radiative cooling timescale. For the Sun, said cooling occurs on the order of $t_{cool} \sim 10^6$ yr at 0.5 $\mathrm{R_\odot}$, leading to an increase in luminosity of $L \sim E_{grav}/t_{cool} \gtrsim 10^{33}$ erg $\mathrm{s^{-1}}$, which is on the order of $\mathrm{L_\odot}$ (Metzger, Giannios, & Spiegel, 2012). While this is a notable change in behaviour of the star as compared to its natal luminosity, it would be difficult to detect using a transit survey that aims to detect variations in the luminosity of stars on much shorter timescales. Instead, the primary observational consequence of energy exchange between the planet and the host star is related to the production of a strong bow shock front as the planet breaks through the

stellar atmosphere with a velocity larger then the local sound speed. This shock front will produce electromagnetic radiation over timescales of weeks to a month that could potentially be detected by transient surveys (Metzger, Giannios, & Spiegel, 2012).

The temperature of the shock front can be estimated as

$$T_{\rm shock} = A\frac{\mu m_{\rm H}}{k_{\rm B}} v_{\rm coll}^2, \tag{7.8}$$

where A is a numerical factor depending on the nature of the gas, μ is the mean molecular gas of the mass, $m_{\rm H}$ is the mass of a hydrogen atom, $k_{\rm B}$ is the Boltzmann constant and $v_{\rm coll}$ is the velocity of the planet at collision with the stellar surface (Stephan et al., 2020). Assuming that the stellar envelope contains ideal, ionised gas, the numerical constants become $A = 3/16$ and $\mu = 0.62$. As for the velocity, I obtain it by solving equation (2.6) for θ at $r = R_\star$ and computing the radial and tangential velocities using equations (2.25) and (2.26). For the planets in figure 7.3 that have $r_{\rm min} > R_\star$, I assume that their semi-major axis will stay approximately constant and use the corresponding value of $e_{\rm crit}$ at $r_{\rm min} = R_\star$.

The resulting shock front temperature has been plotted against $1-e$ in figure 7.6. From the results, it is evident that a more eccentric orbit at collision causes a higher temperature in general. However, since the impact velocity is related to the periastron distance of the orbit, the bow shock temperature depends on the pathway to planet consumption. If the planet has undergone diffusive consumption, it will likely have a minimum distance $r_{\rm min} \sim R_\star$ and in turn a lower collisional velocity than a planet with $r_{\rm min} < R_\star$. As a result, the highest eccentricity orbit, corresponding to the J2 planet at $1 - e \sim 5 \times 10^{-4}$, will induce the same shock temperature as an Earth-mass planet on a much less eccentric orbit. The results in this plot does not tell the entire story however, since it does not provide information of how much gas is heated. A more massive planet has a larger radius and will in turn heat up a larger volume of gas, leading to a larger emitting area. Hence, the effective temperature of the radiation emitted from the volume is in reality less than $T_{\rm shock}$, especially for terrestrial planets.

As for the nature of the radiation, the problem gets quite complicated. For a hot Jupiter with a final eccentricity of $e \lesssim 10^{-3}$, Metzger, Giannios, & Spiegel argues that the bow shock will produce an Extreme Ultraviolet (EUV)/soft X-ray transient that lasts for several weeks. Furthermore, the collision is so strong that the luminosity produced by the bow shock will exceed the local Eddington limit, creating a stellar wind. The wind in turn induces an outflow of stellar material from the surface which can re-emit absorbed radiation from the EUV/X-ray radiation produced by the bow shock. Hence, the high energy transient will be followed by an Infrared Radiation (IR) transient that lasts for a few days. In contrast, Yamazaki, Hayasaki, & Loeb (2017) studied transients caused by planets on highly eccentric orbits. For such a scenario, they instead argue that the bow shock produces an expanding bubble of plasma with temperatures around $\sim 10^6 - 10^7$ K

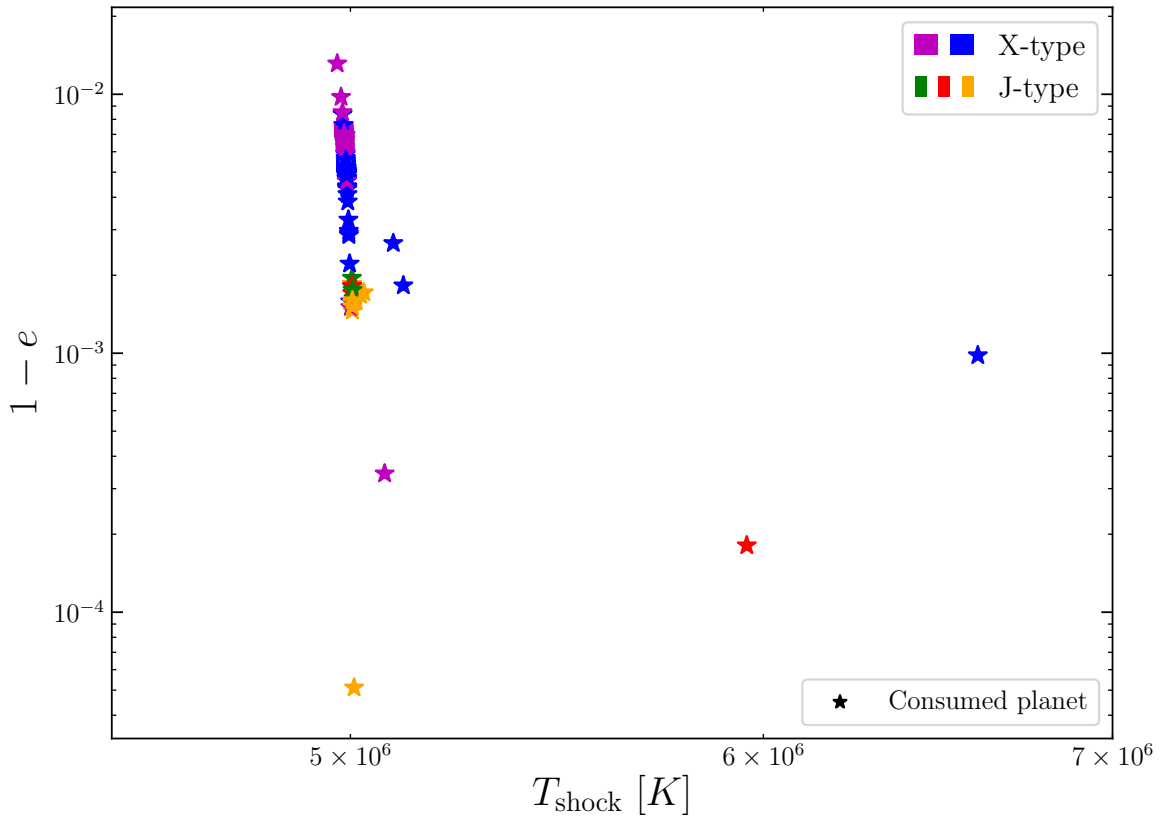

Figure 7.6: The temperature of the bow shock gas after collision with a planet plotted against $1-e$. Follows the same marker and colour scheme as the plots in chapter 6. Observe the significant increase in temperature for planets that have large eccentricities and undergo prompt collision. However, while a high eccentricity is important, a diffusive consumption at a large semi-major axis will still have a fairly low impact velocity, leading to a lower temperature. This is clearly seen for the high-eccentricity J2 planet with $e > 0.9999$ that only causes a temperature of $T_{\rm shock} \sim 5 \times 10^6$ K.

beneath the stellar surface. The bubble is created when a Jupiter-like planet spiralling in towards the deep layers of the stellar interior of a Sun-like star comes to a halt at a radius of ~ 0.9 $R_\odot$ prior to tidal disruption. This effect is due to energy loss by gas drag and also produces a bow shock. This shock transforms the dissipated energy into thermal energy, leading to the infusion of $E_{\rm th} \sim 1.8 \times 10^{45} (M_{\rm p}/{\rm M_J})$ erg into the stellar envelope. The surrounding gas in these external layers of the host star is optically thick, which leads to inefficient radiative cooling and ultimately the production of the expanding plasma bubble. The bubble will keep expanding, emitting radiation in the optical/IR wavebands over the course of $\sim$ 3700 s until it leaves the stellar photosphere. When it has reached the

atmosphere, the expansion will create a second shock, which accelerates free electrons in the vicinity. This produces an afterglow of radio synchrotron emission that can be seen for $10^3 - 10^4$ yr after the planet consumption event.

Given the complexity of the problem and the fact that only a few studies have focused on consumption of high-eccentricity planets, it is evident that there is a need for a more in-depth study with a dedicated tidal model for interaction with the host star during the N-body integration, followed by analysis using a hydrodynamical code for the post-impact behaviour. Moreover, since the results from Yamazaki, Hayasaki, & Loeb suggests that an Earth-mass planet on high-eccentricity can infuse $E_{\rm th} \sim 6 \times 10^{42}$ erg into the stellar photosphere from a prompt collision, such planet consumption events, which I predict to be common, could potentially create expanding plasma bubbles that produce observable transients and afterglow as well.

7.6 Stellar metallicity enhancements

After the planet has deposited a sizeable amount of its orbital energy into the outer layers of the host star, it can produce another form of detectable effect that could provide astronomers with a hint of a past planet consumption event for a planetary system host star. If a planet dissolves within the outer layers of the star, it can enrich the stellar surface abundances of heavy elements. This process was proposed as a possible origin of anomalously high metallicities in planet hosting stars early on after the detection of 51 Pegasi (Laughlin & Adams, 1997; Sandquist et al., 1998, 2002) and has lately been backed up with observations coupled to consumption of gas giants (Israelian et al., 2001; Li et al., 2008; Ramírez et al., 2015) and super-Earths (Meléndez et al., 2017; Church et al., 2020). One motivation for the consumption of planets with respect to metallicity enrichment is the observed correlation where the giant exoplanets are more likely to exist around high metallicity stars (see section 3.1.1). Furthermore, there is a connection between light metal enrichment and increased rotational velocities of stars (Carlberg et al., 2013). Detectable observational effects through the planet consumption mechanism has also been discussed in regard to post-MS stars on the RGB or AGB (MacLeod et al., 2018; Jimenez et al., 2020) and pollution of white dwarfs (Debes & Sigurdsson, 2002; Veras et al., 2013; Petrovich & Muñoz, 2017). I will however keep the analysis in this section to MS stars and briefly discuss planet consumption for post-MS stars in chapter 8.

When referring to metal enrichment by planet consumption, the main chemical compounds in mind are the two stable lithium isotopes ^{6}Li and ^{7}Li (Sandquist et al., 2002; Soares-Furtado et al., 2020), as well as heavy metals (Li, Lin, & Liu, 2008; Church, Mustill, & Liu, 2020). The lithium isotopes make for great tracers of planet consumption events due to the fact that the dominant ^{7}Li is destroyed through the chemical reaction

$$\mathrm{p} + {}^7\mathrm{Li} \rightarrow {}^4\mathrm{He} + {}^4\mathrm{He} \tag{7.9}$$

Configuration	2E+3J	2X+3Ja	2X+3Jb	2X+3Jc	2X+3Jd	2X+3Je
$M_{\rm X}$ [$M_\oplus$]	1	3	10	30	100	300
$f_{\rm cz}$	0.5	0.2	0.1	0	0	0

Table 7.1: The fraction of consumed mass that is deposited in the convective zone for a planet with a non-grazing consuming orbit a the time of collision with the host star.

at temperatures of $T \gtrsim 2.5 \times 10^6$ K (Bodenheimer, 1965). Hence, depletion of the initial lithium reserves in host stars onsets already during pre-MS, before the ignition of hydrogen. In stars between 1 $M_\odot$ and 2 $M_\odot$, the depletion of lithium will continue into the MS phase (Carlos et al., 2019). As a result, any enrichment through planet consumption can significantly alter the lithium content in MS stars, producing anomalously high abundances that can be detected through observations.

While the total metal mass in the star is guaranteed to increase for each planet consumption event, it is not certain that the chemical abundance enhancement will be detectable. Any signature of pollution in stellar spectra depends on both where and when the planet gets dissolved in the host star. The 'where' refers to the depth at which the planet gets dissolved. Given the low relative mass of the planet with respect to the host star, it is essential that any accreted rocky material is mixed into a small fraction of the star such that the abundance enrichment would lead to pollution in the stellar photosphere (Church, Mustill, & Liu, 2020). Further, if the planet is disrupted below the bottom of the stellar convective zone, any metallicity enhancement would not affect the observable surface abundances of elements. Therein lies the 'when', since the convective zone varies between stars of different masses in different phases of their evolution. Soares-Furtado et al. (2020) found that the convective zone is optimal for observations of lithium enrichment through planet consumption for F-type stars with masses of $1.4 - 1.6$ $M_\odot$ right before their MS turn-off, where they transition towards the subgiant branch. For such an environment, the lithium isotopes can survive between $10^8 - 10^9$ yr, while they would be completely depleted after merely 10 yr in a 1 $M_\odot$ post-MS star. As for heavy metals, Church, Mustill, & Liu concluded that consumption of a super-Earth of masses $M_{\rm p} \leq 30$ $M_\oplus$ could explain the average metal enhancement of 0.128 dex in the turn-off star M67 Y2235, which made it stand out with respect to other stars in the M67 cluster. This star appears to have a mass of 1.18 $M_\odot$, which is significantly less than the optimal mass for Lithium detection.

As discussed early on in this chapter, high-eccentricity planets are likely to have velocities such that they will retain their mass and undergo grazing collisions after dynamical evolution by planet–planet scattering or the Lidov–Kozai mechanism. Planets suffering such collisions will spend a few orbits beneath the stellar surface before ultimately getting disrupted or plunging down below the convective zone. Hence, it is necessary that the planets have $f_\perp \leq 0.4$, which serves as my limit between grazing collisions and prompt collisions, where the planets are fully consumed in one single orbit. To estimate the average consumed rocky mass deposited in the stellar convective zone, $\overline{M}_{\rm metals,CZ} = \sum M_{\rm metals} f_{\rm CZ}/N_{\rm sim}$, for

the planets in all realisations of the various 2X+3J configurations, I extrapolated the results from figure 7 in Church, Mustill, & Liu (2020). Said figure shows that rocky planets between 0.3 and 30 $M_\oplus$ will be fully disrupted within the convective zone of their 1.18 $M_\odot$ star if they have their critical value for grazing collisions, which in their case is $f_\perp \leq 0.42$. The fractional consumed mass for $f_\perp > 0.42$ will be around unity for $M_p < 0.4$ $M_\oplus$, but then quickly drops with increasing mass of the rocky planet. From 5 $M_\oplus$ and upwards, little-to-no mass will be deposited in the convective envelope if the planet has a velocity such that $f_\perp$ is larger than the critical value for grazing collision. Due to the limited time for this thesis and lack of a proper stellar model, I assumed that the Sun will have a fairly similar structure to M67 Y2235 at its turn-off age and used a simple estimation by eye of the fractional consumed mass within the convective zone from figure 7 in Church, Mustill, & Liu (2020). The corresponding values are found in table 7.1. If a planet of any mass has an orbit that leads to a grazing collision, I further assumed that it will be fully disrupted in the outer layers of the host star after just a few orbits. Moreover, if a planet has an orbit such that $r_{min} > R_\odot$, I again assumed that the planet will have a similar value of a_p at t_{CME} and assigned them an eccentricity such that $r_{min} = R_\odot$. I motivate this approach with the previous argument at the end of section 7.2, where I claim that these planets only undergo diffusive exchange of angular momentum through action at a distance in the time between the timestamp for the final registered orbital data and t_{CME}. I further assumed that the metal content of an exoplanet is limited to the mass of its core and used the corresponding values introduced in section 3.4.1.

The average consumed masses, $\overline{M}_{consumed}$, and corresponding average metal masses deposited in the convective envelope, $\overline{M}_{metals,CZ}$, in a realisation of each 2X+3J system are found in figure 7.7. Note again that the results only serve as a simple estimate and have to be backed up with dedicated numerical computations of collisions between a planet and its 1 $M_\odot$ MS host star. Nevertheless, there is a trend where $\overline{M}_{consumed}$ increases with M_X. The sole exception is the case of $M_X = 300$ $M_\oplus$ which has less consumed mass per run than $M_X = 100$ $M_\oplus$. Said behaviour can again be attributed to the large number of unresolved runs, discussed in appendix B. As for $\overline{M}_{metals,CZ}$, the values show that the average deposited metal mass will be $\sim 8 - 10$ $M_\oplus$ for all configurations with $M_X \leq 30$ $M_\oplus$. This result can be attributed to four coactive factors:

1. The fraction of consumed planets from the 3J subsystem is approximately constant for all configurations and they are almost exclusively on grazing collision orbits.
2. The fraction of consumed X-type planets decreases with increasing M_X.
3. The amount of metal within a planet is weakly dependent on the total mass and appears tied to the core mass, which is limited by planet formation (see section 3.4.1).
4. For planets with gaseous envelopes, i.e. $M_p \geq 30$ $M_\oplus$, that are on prompt collision orbits, no metals will be deposited in the convective zone of the host star.

The case with $M_X = 100$ $M_\oplus$, which displays the highest average consumed metal mass of

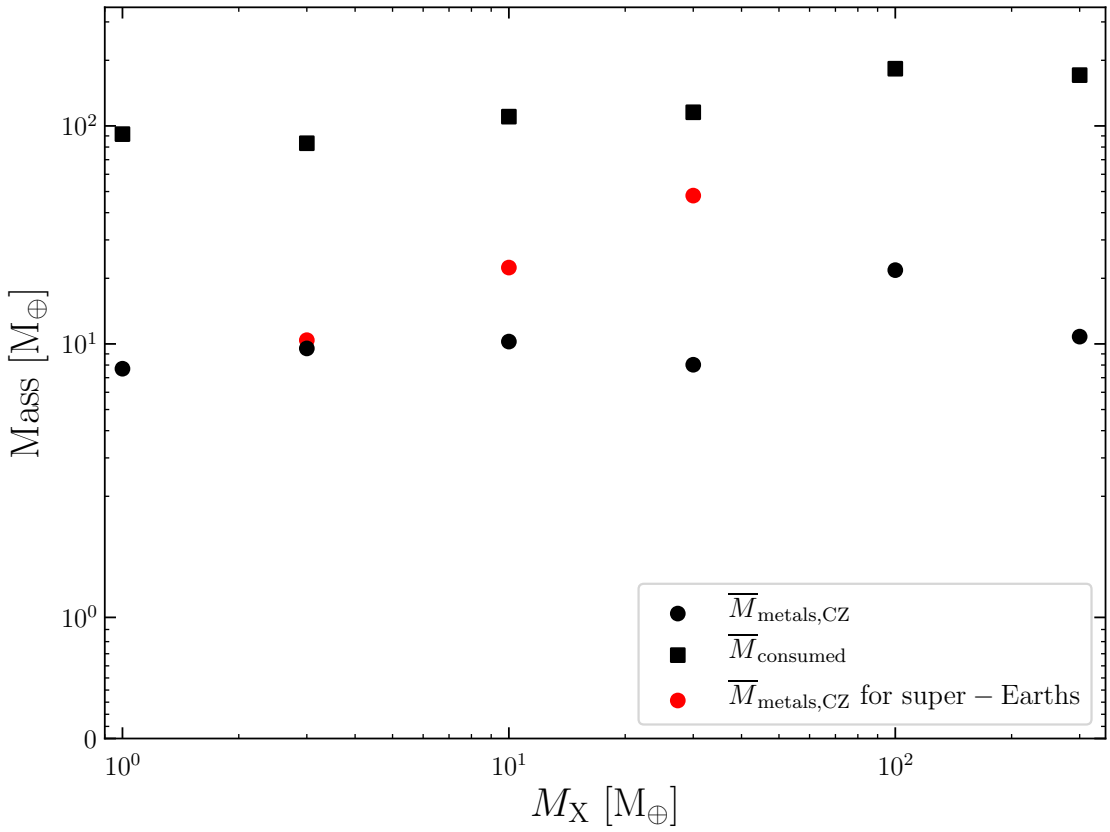

Figure 7.7: The average consumed mass (squares) and the corresponding estimated metal mass deposited within the convective zone of the host star (black circles) for all the 2X+3J configurations (see figure 6.1). The red circles represent how $\overline{M}_{\rm metals,cz}$ would change if the cases of $M_{\rm X} = 3, 10, 30$ were super-Earths. Note that there are many unresolved systems for $M_{\rm X} = 300$ M$_\oplus$ which skews the results.

all with its 20 M$_\oplus$, shows that if the total average planet mass of the system goes up, the dynamical evolution will be more chaotic. In turn each single planet consumption event will have a larger impact on the properties of the host star. Given that the core masses of the giant planets in my simulations are set to 20 M$_\oplus$, these type of systems will on average consume one giant planet. Again, this does not hold for the 2X+3Je configuration due to its prolonged phase of stability.

A critical caveat related to my choice of MR-relation is that it does not accurately depict the existence of super-Earths, since it is valid under the assumption that all planets above 2.62 M$_\oplus$ will have a gaseous envelope and cores with $M_{\rm core} < M_{\rm p}$. For the case of super-Earths, almost the entire planet will consist of rocky material, leading to a larger deposited metal mass. Hence I also include the values of $\overline{M}_{\rm metals,cz}$ for the case of $M_{\rm metals} = M_{\rm p}$ when

the X-type planets have masses of 3, 10 and 30 $M_\oplus$. As observed in the plot, these values are notably higher than for the fiducial composition cases, indicating that consumption of super-Earths may be the prime source of observable metallicity enhancement in planetary host stars.

While the Jupiter-mass planet consumptions seem to be rarer and generally require more than three massive giants present in the system at the onset of instability, they should yield far stronger detectable pollution signatures than for the case of the more common Earth-mass consumptions due to factor 1. above. Yet, if Earth-mass planets and rocky planetesimals prove to be numerous after the conclusion of the planetary formation phase in planetary systems, dynamical instability could lead to a large number of low-mass planet consumptions which would induce a strong observable metal enrichment in the photosphere, assuming that they would happen in rapid succession. Nonetheless, the 'when' and 'where' for disruption of Earth-mass planets will complicate matters, as consumptions of planets below the test particle limit for systems tend to occur early on during evolution, meaning that MS stars consuming Earth-mass planets in intrinsically unstable systems most probably will not obtain any detectable metal enrichment. Furthermore, it is more common for low-mass planets to end up on prompt collision orbits due to the fact that the primary pathways for consumption for these planets is Lidov–Kozai and strong scattering. Hence, for consumption of planets with masses below the test particle limit to produce a detectable signature, dynamical instability has to ensue at a later evolutionary stage of the host star by any of the mechanisms mentioned in section 4.1.5.

7.7 Orbital configurations of surviving planets

As found during the analysis of 50 2E+3J realisations in section 6.3.1, the final orbital configuration of the surviving planets in a planetary system can provide hints of prior planet consumption events. For cases where a Jupiter-mass planet is consumed by a host star, energy is not necessarily conserved among the planets, meaning that the semi-major axis of a sole surviving Jupiter can have semi-major axes that differ from a_f, which is the semi-major axis of a Jupiter-mass planet that has ejected two other planets. For several systems in figure 6.2, the single surviving Jupiter-mass planet will have $a_\mathrm{p} \gg a_\mathrm{f}$ with varying eccentricities and inclinations.

In order to infer if there are any significant giveaways for a past planet consumption event, I chose to investigate the final orbital element of the surviving 3J planet(s) in the 2X+3J configurations. In the cases where $M_\mathrm{X}/\mathrm{M_J} \ll 1$, the inner planets are not massive enough to carry a notable portion of the total orbital energy to the host star. Hence, it makes most sense to only investigate the distribution of the surviving 3J planets, which is the common feature of all six configurations. While the inner X-type planets are massive enough to remove energy from the J-type planets for 2X+3Jd and 2X+3Je effectively altering the value of a_f, the final orbital properties of the surviving 3J planets in these configurations serve as a comparison for how the orbital elements change when increasing the total initial

System	$a_{\rm p}$ [AU]	e	i [°]
2E+3J, $M_{\rm X} = 1$ M$_\oplus$	87.3[2.2-1039.3]	0.62[0.18-1.01]	20.1[1.1-175.8]
2X+3Jc, $M_{\rm X} = 30$ M$_\oplus$	67.2[5.0-1069.0]	0.54[0.10-0.96]	19.0[1.1-99.6]
2X+3Jd, $M_{\rm X} = 100$ M$_\oplus$	71.7[2.9-585.3]	0.58[0.09-0.96]	18.5[0.3-70.0]
2X+3Je, $M_{\rm X} = 300$ M$_\oplus$	108.0[5.1-1807.9]	0.52[0.11-0.99]	23.0[0.8-141.5]

Table 7.2: The distribution of semi-major axes, eccentricities and inclinations for the orbital configuration of surviving 3J planets in J-type planet-consuming systems. The leftmost value is the mean of the quantity over all surviving planets while the values within the bracket represents the minimum and maximum.

System	$a_{\rm p}$ [AU]	e	i [°]
2E+3J, $M_{\rm X} = 1$ M$_\oplus$	6735.0[2.2-93750.8]	0.49[0.01-0.99]	16.6[0.4-98.2]
2X+3Jc, $M_{\rm X} = 30$ M$_\oplus$	36.2[1.7-559.7]	0.47[0.02-0.97]	16.9[0.5-141.5]
2X+3Jd, $M_{\rm X} = 100$ M$_\oplus$	53.2[0.8-3323.2]	0.43[0.03-0.99]	17.0[0.4-164.5]
2X+3Je, $M_{\rm X} = 300$ M$_\oplus$	107.5[1.1-5393.1]	0.46[0.01-0.99]	14.3[0.2-48.6]

Table 7.3: Same as in 7.2 but for systems that had no J-type planet consumption.

mass of the system.

I show the final semi-major axes and eccentricities for surviving 3J planets in the 2E+3J and 2X+3Jc-e configuration systems where a Jupiter-type (J-type) planet has been consumed in the top plot of figure 7.8. Furthermore, I provide the corresponding distribution for the case of no J-type consumption in the bottom plot of said figure. The average values of the parameters for each configuration plotted in figure 7.8 along with the minima and maxima are provided in tables 7.2 and 7.3, for J-type and no J-type consumptions, respectively. I chose not to include the orbital elements of the 2X+3Ja-b 3J planets because of results in section 6.4, where I found that the test particle limit when there is a Jupiter-mass planet in the system seems to be around 10 M$_\oplus$. Hence, I expect these configurations to behave similarly to 2E+3J. There is one major difference between the top and bottom distributions given the lack of planets around $a_{\rm f}$ in the top panel (indicated by a dotted line). This can, as mentioned in section 6.3, be attributed to energy conservation since the consumed planet has transferred a significant portion of the total orbital energy to the host star. Another important observation is that close to all $M_{\rm X} = 1,\ 30$ M$_\oplus$ systems in the bottom plot have two or more surviving planets while a large fraction of the systems that have undergone J-type planet consumption have only retained one planet, as can be seen in figure 6.2. In turn, many J-type planet consumption systems also had an ejection of a Jupiter-mass planet. From the timestamps indicating $t_{\rm CME}$, I conclude that the ejections almost exclusively occur very shortly before the planet consumption. Hence, I can lay out a general timeline for the consumption of a J-type planet.

1. The system becomes dynamically unstable.

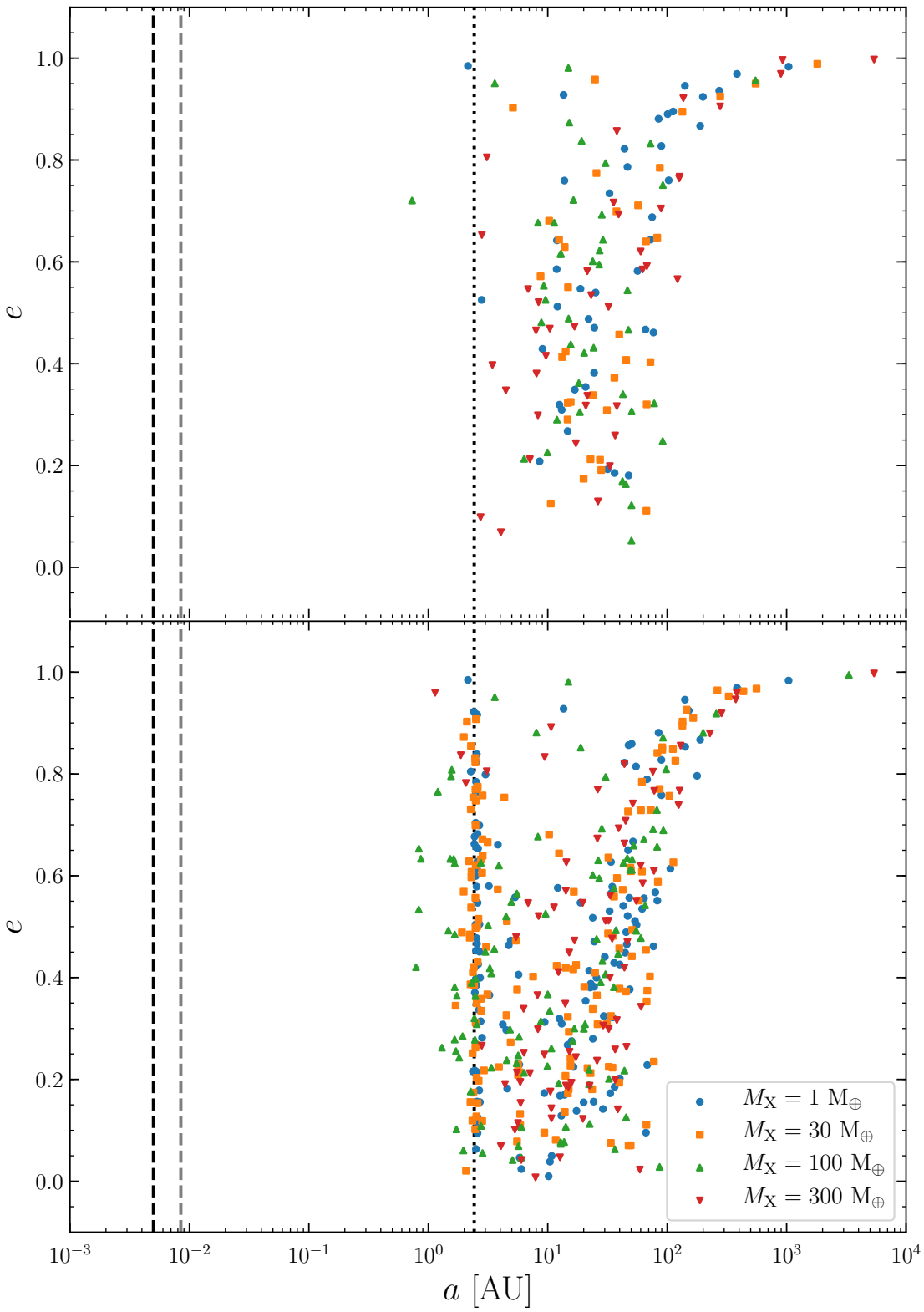

Figure 7.8: Distribution of semi-major axes and eccentricities for surviving 3J planets. **Top:** J-type planet-consuming systems. **Bottom:** Systems without J-type consumption.

2. The three planets in the 3J subsystem exchange AMD, which leads to the crossing of orbits.
3. AMD exchange grows larger, leading to a surplus of AMD in one J-type planet.
4. Perturbation of the inner X-type orbits leads to Earth-mass planet consumption through strong scattering with a J-type planet after radial incursion or through Lidov–Kozai oscillation.
5. The highly eccentric Jupiter-mass planet undergo close encounters with one or both of the other Jupiters.
6. The close encounters are resolved with a scattering and anti-scattering (the planet becomes less eccentric and more bound) event in close succession, where one planet is ejected shortly before the innermost planet is consumed.

As for the rest of systems 37 to 49 in figure 6.2 that have two remaining Jupiter-mass planets, the fact that a majority of them (systems 41, 43, 44 and 45) are unresolved due to crossing orbits indicates that the anti-scattered planet did not gain enough energy to be ejected. Instead it will proceed to undergo close encounters with the other remaining Jupiter, which likely will end with an ejection because of their large semi-major axes (as found in section 6.5). The lower number of scatterings for these planets explains the lower average eccentricities and inclinations when comparing tables 7.2 and 7.3. As for the few planets that are close to a_{f}, they have indeed had planet consumptions that are diffusive, meaning that the innermost planet never suffered any anti-scattering.

Another noteworthy feature is that many of the $M_{\mathrm{X}} = 100\ \mathrm{M}_{\oplus}$ planets have semi-major axes such that $a_{\mathrm{p}} < a_{\mathrm{f}}$. This is due to the increased total mass in the system, meaning that the X-type planets are massive enough to remove energy from an outer J-type planet, significantly decreasing the Jupiter's orbital separation with the host star. This should intuitively also be the case for the $M_{\mathrm{X}} = 300\ \mathrm{M}_{\oplus}$ systems, but they again remain largely unresolved. The fact that the remainder of the distribution for $a_{\mathrm{p}} > a_{\mathrm{f}}$ is similar is unsurprising since ejections and consumptions most often follow the same type of dynamical evolution where the eccentricity is diffusively increased over a large number of scattering events.

7.8 Conclusions regarding observational consequences of planet consumption

I now present the main ideas obtained from the literature study and toy–model computations employed in this chapter to review the various consequences of planet consumption for Sun-like MS host stars and the configuration of surviving planets in consuming planetary systems.

Observational consequences of planet consumption

1. The strength of observational consequences depends on both 'when' and 'where' the planet collides with the host star.
   - 'Where': The impact parameter is highly dependent on the eccentricity and semi-major axis of the planet at consumption. This leads to two different types of collisions.
     - **Grazing collision:** The planet grazes the surface and spirals in towards the center of the host star over a few orbits
     - **Prompt collision:** Planets plunge directly towards the deeper parts of the host star on its first orbit.
   - 'When': The evolutionary phase of the host star determines the detectability of an observational signature of planet consumption.
2. A large majority of the planets consumed in the `MERCURY` simulations will end up on grazing orbits. Planets undergoing strong scattering are more likely to end up on prompt collision orbits.
3. Planets on high-eccentricity orbits will largely stay intact prior to collision, meaning that tidal disruption most probably will occur below the stellar surface (Dosopoulou, Naoz, & Kalogera, 2017).
4. **Spin-up:** Transfer of angular momentum from the consumed planet to the host star can lead to spin-up of the star's rotation. Jupiter-mass planets on any grazing orbit will reduce the rotational period of the host star by a factor ~ 40.
5. **Grazing encounters:** Grazing collisions between a planet and its host star will lead to the ejection of stellar surface material in the form of 'gas bullets'. All consumed planets in the `MERCURY` simulations can eject material due to their high impact velocities but it is likely only the Jupiter-mass planets could produce periodic ejections that would be detectable.
6. **Planet merger transients:** Consumption of a high-eccentricity planet will lead to the creation of an expanding plasma bubble beneath the stellar surface, emitting in the optical/IR waveband for ~ 1 hr. The bubble will expand and accelerate electrons, creating radio synchrotron radiation that could be detectable for up to $10^3 - 10^4$ yr (Yamazaki, Hayasaki, & Loeb, 2017).
7. **Stellar metallicity enhancements:** The two isotopes ^{6}Li and ^{7}Li,

as well as heavy metals, make for great tracer elements for planet consumption. Relevant for post-MS FG stars at their turn-off point, when their convective zone is shallow. All planet consumptions for the 2X+3J configurations will deposit at least 8 $M_{\oplus}$ worth of metals on average, which is enough to produce a detectable metallicity enhancement (Church, Mustill, & Liu, 2020) for post-MS FG stars at their evolutionary turn-off towards the giant branch within stellar clusters.

8. **Configuration of surviving planets:** Due to conservation of energy and transfer of energy to the host star, the final semi-major axes of the surviving planets can hint at a previous giant planet consumption event. When a host star in a multiple giant planet system has consumed a Jupiter-mass planet carrying a fair share of the orbital energy in the system, the remaining planets will orbit the host star at wider orbits. In some cases, this will produce planetary systems with a single giant planet on a wide orbit.

Chapter 8

Discussion

In this chapter, I discuss the results from this thesis in a broader context. First, I lay out potential shortcomings of the methodological approach employed in this thesis. Second, I tie planet consumption to the current state of planet formation theory and properties of observed exoplanets. Third, I discuss the detectability of observational consequences induced by planet consumption. Finally, I lay out future work that can be done to expand on this study.

8.1 Shortcomings of theoretical models

Two separate theoretical models have been used to simulate planet–planet scattering events in this thesis. In chapter 5, I employed the isolated, two-dimensional two-body planet scattering scenario with the analytical solution derived in section 5.1. As mentioned in the beginning of said chapter, this simplified scenario only holds for a coplanar two-body planetary system where the separation between the two planets fulfils $R_{\mathrm{p},1} + R_{\mathrm{p},2} < d \ll 0.03 r_{\mathrm{p}}$. For the case of a Jupiter-mass planet undergoing a close encounter with an Earth-mass planet at 1 AU, the maximum impact parameter $b_{\max}$ for a close encounter would be ~ 0.02 AU, which still would yield a force between the two planets that has a magnitude of 3/2 times the magnitude of the force exerted on the Jupiter by the host star, i.e. $F_{\mathrm{pp}} = 2F_{\star\mathrm{p}}/3$. Hence, the isolation approximation would only be valid for the very smallest impact parameters in the collision. For the example system in table 5.1, the largest impact parameter that will put the Earth-mass planet on a consuming orbit is $b \sim 0.25 b_{\max}$, as seen in figure 5.6, which still means that $F_{\mathrm{pp}} = F_{\star\mathrm{p}}/6$. When it comes to the flatness approximation, it overestimates the total fraction of mergers in a given system. Looking at the impact parameter that yields a merger for the example Jupiter-Earth system $b = 0.057 b_{\max}$, the corresponding mutual inclination needed for the planets to miss each other would be $i_{\mathrm{m}} \sim 28°$. While this seems like a large mutual inclination, the Jupiter-Earth system in consideration must have already undergone substantial dynamical evolution to cross in the first place, meaning that they will likely have an even larger mutual inclination

than 28°, in line with the final mutual inclinations of CME-type planets in systems based on the 2E+3J configuration in figure 6.4. It is thus evident that my two-body model should not be used to estimate quantitative results in two-body scatterings. Nevertheless, from the results in chapter 6, I can conclude that it still replicates qualitative trends well. The ability to constrain the parameter space for planet-consuming orbits in an efficient way saved many hours of integration and allowed me to choose appropriate configurations for the `MERCURY` runs. It is unfortunate that the model did not function well for the Monte Carlo simulation attempted in section 5.6, as all planet–planet scatterings resolved in mergers before ejection or planet consumption was possible. However, this could potentially be circumvented by introducing an artificial inclination that will be altered after each individual scattering event during the Monte Carlo simulation, making the problem three-dimensional.

The second theoretical model I have employed to investigate the dynamical evolution of planet-consuming systems is the full three-dimensional N-body scenario from chapter 6. A potential error source for the consumption of Jupiter-mass planet within this model is related to the choice of coordinate system, which is centred on the host star (see section 6.1.2). While this reference system is optimal for tracking the position of planets relative to the host star, it does not account for changes in the position of the host star with respect to the barycentre of the system. If a high-mass planet undergoes a prompt collision with a high $f_{\perp}$, transfer of momentum will perturb the host star from its initial position within the planetary system. In turn, the total change in orbital elements for the planets might be skewed. In particular when it comes to the position of multiple planets relative each other. However, since the host star is not a rigid object, it is difficult to predict the magnitude of the perturbation for the host star position when the planetary orbit decays over the course of several orbits. Hence, it would be necessary to perform detailed simulations of the planet–star collision in question to fully understand how large of an error this model inaccuracy will produce. Nevertheless, it is not certain that this will be a significant problem given that host stars are more likely to consume lower-mass planets than Jupiter-mass planets for the hierarchical type of system that I have investigated. Consumption of a low-mass planet will induce a much weaker perturbation to the position of the star, meaning that the final positions of the Jupiter-mass planets in systems without J-type consumption in the Carrera plot (figure 6.2) will not be misrepresentative. It is also noteworthy that J-type planet consumption systems are likely to only have one single Jupiter-mass planet left in the system after the conclusion of the dynamical evolution which means that potential perturbations in the position of the host star will not be of importance.

8.1.1 The absence of a tidal model

As previously discussed, the main assumption for the numerical integrations in this thesis is that tidal forces have been ignored. This leads to two possible sources of errors in the results. First, the absence of tidal interactions between planets means that none of the planets undergoing close encounters can end up in a planet binary system after tidal capture (Podsiadlowski et al., 2010). This phenomenon would mainly be relevant for 3J systems

at a minimum distance of 0.3 AU from the host star and could occur in $\sim$ 10% of N-body integrations, a number independent of the semi-major axis of the innermost Jupiter (Ochiai, Nagasawa, & Ida, 2014). Moreover, Ochiai, Nagasawa, & Ida found that most of the tidal captures that led to the creation of a planet binary occurred when the separation during the encounter was around 1 to 2 $d_{\rm crit} = (R_1 + R_2)$. Therefore, this effect is highly related to the strong scattering pathway to planet consumption for Jupiter-mass planets. In turn, it is unsurprising that only a tenth of integrated 3J systems will produce such a binary given that the dominant pathway for planet consumption and ejection is driven by diffusive exchange of angular momentum over a large number of close encounters (see figure 6.3). Since few J-type consumptions have large average fractional changes in AMD for their scattering events, it is difficult to say whether or not the inclusion of tidal effects would affect the number of observed J-type planet consumptions in the 2X+3J configurations without dedicated numerical integrations with an implemented tidal model.

Second, the stellar tides play an important factor for the creation of hot Jupiters and the disruption of low-density planets outside the confines of the host star. While I extensively discussed this section 7.1 in regards to the creation of hot Jupiters, it is clear from the rest of chapter 7 that tidal interactions with the host star will largely affect the nature of mass transfer and in turn the collision between the host star and the planet. The nature of the collision will directly affect the strength of the various observational signatures of a consumption event. Hence, the implementation of a tidal model in the N-body integration model is necessary to fully draw conclusions regarding the ultimate fate of Jupiter-mass planets. When it comes to compact, rocky planets of lower mass such as terrestrial planets and super-Earths, the Roche limit is situated inside the MS host star, making the exclusion of a tidal model less critical for the analysis of the planet consumption event. Given that the rate of low-mass planet consumptions is significantly higher than the corresponding rate for giants and occurs earlier on during the dynamical evolution (see figures 6.3 and 6.5), the resulting outcomes for low-mass planets from the simulations should be largely unaffected by the exclusion of the tidal model.

8.1.2 Planet population and stellar properties

The evident importance of the low-planet mass regime highlights another modelling inaccuracy, as I opted to use the highly simplistic joint planet MR-relation in figure 3.4. Given that the impact parameter between the planets during a scattering event needs to be small to cause planet consumption, but not small enough to cause a planet–planet merger, the bimodality of the observed MR-relation for planets between 3 and 20 $M_\oplus$ affects the outcome of the dynamical evolution for these planets. The radii of the two planets will therefore effectively determine the likelihood of a planet undergoing strong consumption. This conclusion is in line with Ford & Rasio (2008), where the authors found that planet consumption events are highly sensitive to the physical size of the planets. Furthermore, looking at the difference in metal mass deposited in the convective zone of the host star for consumption of super-Earths, it is clear that different compositions of the planet will

lead to highly different signature strengths for metallicity enhancements. In turn, it will be of high importance for any future studies to properly account for the varying internal structure for planets of these masses, preferably by using a state-of-the-art population synthesis model based on statistically derived distributions of parameters coupled to 'Kepler' data (e.g. He et al., 2020) or on planet formation theory (e.g. Lambrechts et al., 2019; Bitsch et al., 2019). To ensure that systems drawn from the underlying population will be inherently stable, the model could be further extended to require AMD instability criteria from Laskar & Petit (2017) (see section 4.1.3).

As concluded in section 7.8, the 'when' of a planet consumption event will largely determine its outcome and the detectability of any observational consequences. For my simulations there is a strong assumption that the system will dynamically evolve on timescales $t_{\rm CE} \ll \tau$ while the host star remains on the MS, which may not be true. In reality, the ZAMS approximation (which assumes that all planetary systems will be made unstable shortly after the conclusion of the planetary formation phase) breaks down for systems where the host star enters its post-MS phases before onset of dynamical instability. As mentioned in section 4.1.5, there exists several external sources that can trigger dynamical instability at later times during the stellar evolution. Therefore, there is a lack of information regarding the post-MS planet consumptions in my model. For example, RGB stars have a large $R_\star/M_\star$, which enhances the likelihood of planet consumption (see section 5.4.3) and have been studied elsewhere (e.g. Carlberg et al., 2013; Privitera et al., 2016; Jimenez et al., 2020). White dwarfs are also likely targets for planet collisions, as the mass loss at the initiation of the white dwarf phase can destabilise systems (Debes & Sigurdsson, 2002; Voyatzis et al., 2013). The detectability of metal pollution in white dwarfs is also high given that most heavy elements are expected to have sunk deep into the stellar interior, meaning abnormally high surface abundances of metals most probably are due to consumption of asteroids or, in some cases, rocky planets (Zuckerman et al., 2003, 2010; Veras et al., 2013; Koester et al., 2014; Petrovich & Muñoz, 2017; Gänsicke et al., 2019).

To circumvent the problems related to the stellar age and arrive at more realistic conclusions regarding the observational consequences of planet consumptions in multiple planetary systems, it would be necessary to create systems with a host star of a given age and mass populated with planets drawn from a population synthesis model. The N-body integration of the dynamical evolution should further be combined with a stellar evolutionary model that determines the structure of the host star at a given timestamp. After the detection of a planet consumption event, the final orbital elements of the planet should be directly saved in order to avoid the issues with poor output resolution from section 7.2. Finally, the host planet–star collision should be simulated with a separate hydrodynamical code to properly understand which observational consequences that the planet-consuming event can give rise to. Only then will it be possible to arrive at a more complete picture of how detectable various types of observational consequences from planet consumption can be.

8.2 Tying planet consumption to planet formation theory

A key property of the planet-consuming configurations investigated in chapter 6 is the presence of multiple giant planets. In section 3.1, I explained that while observational data from 'Kepler' indicate that there is a surplus of single planet systems, both observational methods and inaccuracies in the 'Kepler' pipeline introduces strong biases that can skew the current understanding of multiplicity in exoplanetary systems. Moreover, if planets tend to form in high multiplicity, hierarchical and tightly-packed systems, dynamical evolution would most probably lead to disruptions of one or more orbits by CME events early on after the depletion of the protoplanetary disk. In turn, it is difficult to constrain from observations how often a hierarchical system with at least two giant planets is born. From planet formation models, it seems as if multiple cold Jupiter planets can be grown consistently from massive protoplanetary disks by conventional pebble accretion and migration (Bitsch et al., 2019) combined with mergers between planetary embryos (Wimarsson, Liu, & Ogihara, 2020). Wimarsson, Liu, & Ogihara showed that their fiducial model on average could produce six cold giants with masses $M_{\rm p} \geq 18$ $\rm M_{\oplus}$ and $\overline{M}_{\rm p} = 99$ $\rm M_{\oplus}$. Nevertheless, the models from literature that can consistently grow multiple distant giant planets are highly dependent on the properties of the protoplanetary disk and how it interacts with the growing, migrating planets. Such parameters remain poorly constrained due to the lack of high resolution observations of protoplanetary disks.

In any case, while the presence of distant giant planets possibly can be explained from such theoretical models on planet formation, they still struggle when it comes to producing very distant giant planets with semi-major axes of several tens to hundreds of AU. This can be attributed to both heavy inwards migration in the disk and poor mass growth in the outer regions of the disk (Johansen & Lambrechts, 2017). However, the creation of such orbits has been predicted to be a direct consequence of planet–planet scattering (Veras, Crepp, & Ford, 2009). As seen in figure 6.2, the dynamical evolution of three tightly-packed giants consistently puts one of these planets on a very distant orbit with varying eccentricity. The fact that several cases (e.g. system 19) show that scattering can produce wide, pseudo-circular orbits also provides insight into the importance of planet–planet scattering as a part of the formation of stable planetary systems. Intuitively, the observation of a wide low-eccentricity planet implies that the planet has not undergone any close encounters with other planets and formed in-situ during the planet-formation phase, where its eccentricity has been dampened by interaction with the protoplanetary disk. Again, such a scenario is not supported by current planet growth models.

Planet consumption adds another aspect to this phenomenon, since the transfer of energy that occurs when a Jupiter-mass planet collides with its host star can lead to the creation of a planetary system with a single low-eccentricity planet on a wide orbit. While the wide orbit single planet systems in figure 6.2 have moderate to high eccentricities, the unresolved system 41 will likely conclude its phase of instability by producing a pseudo-

circular single-planet system with a semi-major axis of $\sim$ 100 AU after the ejection of planet J1. While planet consumption can be a pathway to single, wide orbit gas giants, there have been detections of giant planets forming at wide orbits through gravitational instability (Wagner et al., 2020). Furthermore, these type of orbits can be created after capture of a planet from another planetary system in stellar clusters (Li, Mustill, & Davies, 2019, 2020). Nevertheless, the detection of a single planet on a wide orbit can suggest the occurrence of a past planet consumption event.

8.3 Detectability of planet consumption consequences

Assuming that the toy–model estimates for the observational consequences of planet consumption by a MS star in chapter 7 are accurate, I have yet to answer how detectable these effects would be. Since a majority of the consuming orbits will be grazing, I base the discussion on such a case. Note that the observational consequence of surface-grazing interactions, where the planet causes periodic ejections of stellar surface material, has already been confirmed to be detectable (Salas et al., 2019). I will thus not discuss said effect any further.

First, it is necessary to know how often these types of events will happen. While there has not been any dedicated study to derive a planet consumption rate for planet–planet scattering events, Metzger, Giannios, & Spiegel (2012) and Popkov & Popov (2019) derived such rates for tidal decay of short-period orbits. The latter study used a population synthesis model to expand on the study by the former, leading to a more detailed result. Popkov & Popov found that for MS stars, the planet–star collision rate for low-mass planets is $\sim 0.006 - 0.009$ yr^{-1} per galaxy and 0.003 yr^{-1} per galaxy for giant planets. For RGB stars, planet consumption is more common with a rate of 3 yr^{-1} per galaxy. Since the authors do not take direct consumption by planet–planet scattering events into account, I expect that these rates are underestimated given the discussion in the sections above.

8.3.1 Planet merger transients

Popkov & Popov further argue that these different planet consumption types would have highly different detectabilities. Recalling that direct impact events for narrow, tidally decayed orbits with low eccentricity will produce EUV/X-ray transients, it is uncertain how much of this radiation it would be possible to observe. If the host star is in its MS phase when the collision occurs, the increase in luminosity from the bow shock can as mentioned exceed the Eddington limit, leading to the creation of stellar winds. Said winds will be optically thick to the emitted radiation, blocking a large portion and re-emitting it isotropically in the optical/IR wavebands. The re-emitted radiation would in turn overlap with the stellar blackbody radiation. Hence, this type of transient event would only be detectable for a brief period of time on the order of $\sim$ weeks after the onset of the merger (Metzger et al., 2012). Moreover, extinction in the galactic plane of the Milky Way would further complicate detections of planet consumption events within the Galaxy,

meaning that surveys aiming to detect planet merger transients from low-eccentricity direct impacts have to focus on other galaxies such as M31 (Andromeda) or the Large Magellanic Cloud (LMC). An instrument that would be capable of performing such a search would for example be the Vera Rubin Observatory (VRO) that is currently under construction (Ivezić et al., 2019).

When it comes to high-eccentricity direct impacts, the behaviour of the transient appears to be different, as argued for by Yamazaki, Hayasaki, & Loeb (2017). Instead of EUV/X-ray radiation being the most promising feature for detection, the plasma bubble created by the high velocity impact will instead produce radio synchrotron afterglow by acceleration of electrons that could be detectable for $10^3 - 10^4$ yr after the planet consumption event. The authors argue that the main argument against detection is the similar radio signatures of supernovae remnants and classical novae. However, for the case of planet consumption afterglow, the radio surface brightness would be smaller with a source diameter that is distinguishable from that of novae. Yamazaki, Hayasaki, & Loeb believe that the main reason for the lack of such observations is due to their model predicting a low surface brightness similar to that of the detection limit for current instrumentation. Hence, such observations may only be possible with the next generation of radio telescopes such as the Square Kilometre Array (SKA), which will be the largest radio telescope ever constructed with a total collecting area of 1 km^2 (Dewdney et al., 2009).

Note that it is unknown how the signature of of these transient events will change when considering the energy-loss due to ejection of gas bullets during the grazing encounters of the planet pre-consumption. This would have to be further investigated in future work.

8.3.2 Stellar spin-up

The rotational frequency of a star can be directly inferred from broadening effects of the absorption lines in its spectrum (Gray, 1992). Hence, this parameter can be obtained with the use of stellar spectroscopy. The difficulty in detecting stellar spin-up is due to the effect of magnetic braking, which causes stars to spin-down over time. Hence, even though a star may have consumed a Jupiter-mass planet on a grazing orbit, substantially decreasing its rotational period, it may have spun-down to nominal rotational frequencies predicted by stellar evolution at the time of observation. Nevertheless, this effect also provides a strong argument for the occurrence of stellar spin-up by planet consumption. From observations of stellar clusters of varying ages, a distinct bifurcation feature has been observed related to the stellar periods. Stellar clusters with ages of $\geq$ 100 Myr show two distinct groups of fast and slow rotating stars. This bifurcation is not seen from observations of young clusters of a few Myr and very old clusters with an age of $\geq$ 400 Myr (Qureshi, Naoz, & Shkolnik, 2018). In turn, there is an indication that planet consumption occurs around some young stars after the depletion of the protoplanetary disk and destabilisation of the remaining planets, leading to a spin-up of the stellar rotation which then slows down over a few hundred Myr until it reaches nominal rotational periods again.

Hence, the presence of fast and slow rotating stars has already been established. Yet, planet consumption is still only one possible explanation for the bifurcation (Qureshi, Naoz, & Shkolnik, 2018), meaning that observations of rapidly rotating stars have to be coupled to observations of other consequences of planet consumption to confirm whether or not this hypothesis is true.

8.3.3 Stellar metallicity enhancements

When it comes to the enrichment of surface metal abundances by planet consumption, the 'when' and 'where' of the planet–star collision will determine the detectability of the enhancement. From my discussion in 7.6, the 'where' does not to seem to be an issue for planet consumption induced by planet–planet scattering, as they consistently will produce grazing collisions between the planet and the host star. The most important criteria is instead the 'when', given that the planet consumption event must occur during the early post-MS phase when the convective zone is shallow, before expansion of the stellar envelope on the RGB. Stars on the RGB and AGB will have deeper convective zones, meaning that no planet will contain enough heavy metals to produce a detectable signature of metal enrichment. Furthermore, the lifetimes of the ^{6}Li and ^{7}Li isotopes in RGB stars are too short for any enrichment by planet consumption to be detectable. In turn, any signatures of increased Li abundances in such stars must be due to other mechanisms (Soares-Furtado et al., 2020).

Hence, it is clear that the observational consequence of Li enrichment is most important for post-MS stars at their turn-off towards the subgiant branch in the mass region 1.4 $M_\odot \leq M_\star \leq$ 1.6 $M_\odot$, where depletion of Li is slower. For less massive stars post-MS stars, heavy metal pollution will produce detectable signatures. Given the different behaviour of these two detectable features of planet consumption, they can be used to locate planet-consuming host stars in different stellar environments. For metallicity enhancement by heavy metals, planet consumption surveys should mainly focus on stellar clusters. The intrinsic metallicity of a star is highly related to the environment it was born in, meaning that any deviations in metallicity must be detected through comparison with other stars originating from the same environment. Another benefit of surveying stellar clusters for planet consumption signatures is that the high number density of stars within such an environment facilitates stellar fly-by encounters, which can trigger dynamical instability (Malmberg et al., 2011). In turn, the issue where planet consumption of rocky planets in an intrinsically unstable system occur during the early MS phase of the host star (when the convective zone is too deep) can be circumvented.

When it comes to signatures caused by enrichment of Li, the location of the planet is less important. This comes from the fact that the depletion of Li in the host star is mainly related to its evolutionary phase and mass. In turn, when it comes to the detection of planet-consuming systems using Li abundances, it can be used for free-floating stars in less densely populated regions of the galaxy. Nonetheless, this assumes that the age of the host star can be determined to restrict its expected intrinsic Li abundances. Age estimation

is facilitated if the star is located within a cluster, given that an approximate age for the entire cluster can be inferred from the MS turn-off in its Hertzsprung-Russell diagram (Prialnik, 2000).

8.3.4 Detection of wide orbit planets

As predicted by Veras, Crepp, & Ford (2009), planet–planet scattering can produce giant planets on wide orbits with semi-major axes $10^2 \leq a_{\rm p} \leq 10^5$ AU. The authors argue that these planets are detectable over their lifetime, which is on the order of ~ 10 Myr, by direct imaging or microlensing methods. Since my analysis predicts that planet consumption of giant planets can produce single-planet systems with wide orbit giants, the presence of such a planet serves as an indicator of a past planet consumption event. Again, such planets can also be produced through gravitational instability (Wagner et al., 2020) or by the exchange of a planet in a close encounter between stars in a stellar cluster (Li, Mustill, & Davies, 2019, 2020). Hence, such a detection must be coupled with additional observable signatures to firmly conclude that it belongs to a planet-consuming system, especially if the star is a member of a stellar cluster. However, it still poses a challenge to detect these wide orbit planets given that the direct imaging and microlensing methods for detection of an exoplanet still are highly inefficient in comparison to the the more common methods (Wright & Gaudi, 2013). Nevertheless, the detection of wide orbit planets can still serve as a primary indicator for the consumption of a giant planet.

8.3.5 How to detect a planet-consuming system

While detectable outcomes of planet consumption produced by planet–planet scattering events are highly dependent on several parameters such as the mass, age and environment of the host star, as well as the impact parameter and intrinsic properties of the consumed planet, I can still formulate a rough recipe for which observational consequence will produce the most detectable signatures for a given planet type. Note that I only consider the stellar mass range inferred from figure 3.5 of $0.6\ {\rm M}_\odot \leq M_\star \leq 2\ {\rm M}_\odot$.

Detectability of planet consumption

1. **Terrestrial planets:** Consumption of a single Earth-like planet will not produce strong enough signals to indicate a past planet consumption event. However, the consumption of multiple Earth-like planets can most probably induce weak perturbations in stellar spin and stellar luminosity that can be detectable with the next generation of observational instruments. Said effects would likely only be detectable for MS stars on the lower end of the mass range.
2. **Super-Earths:** Consumption of a single super-Earth will primarily produce a detectable enhancement in a star's observed metallicity, both

in terms of heavy metals and Li. This type of event is highly likely to occur in hierarchical multiple giant planet systems, and probably more common than the rate of narrow, low-eccentricity orbit consumptions from Popkov & Popov (2019) of ~ 0.1 yr^{-1} per galaxy. In turn, I expect that consumption of super-Earths will occur one to a few times per year in the Milky Way. Most easily detectable for post-MS stars with 1 $M_\odot \leq M_\star \leq$ 1.6 $M_\odot$ at their MS turn-off point.

3. **Mini-Neptunes/Neptunes:** Since these planets have cores of roughly 2.5 $M_\oplus$, multiple consumptions would be required to induce a similar metallicity enrichment to that of super-Earths. Instead, the most promising detectable consequences would be perturbations in the stellar spin and radio afterglow caused by weak planet merger transients. Would mainly be relevant for low-mass MS stars.

4. **Giant planets:** While the consumption of giant planets is less likely than less massive exoplanets, they will induce the strongest detectable observational consequences. The consequence of choice when conducting a survey can be determined from the stellar types in consideration. Note that the detection of a single, wide orbit giant planet will be relevant for all of these mass ranges.

   - 0.6 $M_\odot \leq M_\star <$ 1 $M_\odot$: I expect that the main observational consequences for low-mass stars to be stellar spin-up and effects caused by a planet merger transient.

   - 1 $M_\odot \leq M_\star <$ 1.4 $M_\odot$: For a MS star, the planet consumption event can induce strong stellar spins, potentially threatening rotational break-up if the planet has a mass such that $M_\mathrm{p} > 10$ M_J. Furthermore, radio afterglow transients and gas bullet ejection will likely be detectable with future astronomical missions. Metallicity enhancements by heavy metal pollution in the convective zone of the host star will also be detectable, mainly for post-MS stars near its MS turn-off point. As for the RGB and AGB phases of the star, the most detectable effects will be periodic gas bullet ejections and stellar spin-up, which has a high possibility of ending with the star reaching break-up periods. For the white dwarf phase, the dominant consequence will likely be pollution of heavy metals.

   - 1.4 $M_\odot \leq M_\star \leq$ 1.6 $M_\odot$: For these stars, the dominant effect will likely be pollution of ^{6}Li and ^{7}Li when the planet is on its MS-phase. I expect the host star to behave similarly to those in the lower mass range during its remaining phases.

- $1.6\,M_\odot \leq M_\star \leq 2\,M_\odot$: Here, pollution is restricted by deeper convective zones and spin-up will be made difficult because of larger angular momenta. Hence, the most detectable effect will likely be planet merger transients during the MS phase and periodic ejections of gas bullets during the MS, RGB and AGB phases.

With this formulated recipe in mind, I can draw a final conclusion regarding which observational consequence is most reliable for detecting planet-consuming systems within 1. the Milky Way and 2. Other galaxies:

Most promising observational consequences

1. **the Milky Way:** Given the high consumption rate of super-Earths, observed metallicity enhancements of post-MS turn-off stars in stellar clusters within the mass range $1\,M_\odot \leq M_\star \leq 1.6\,M_\odot$ will provide a strong indication of a previous consumption-event. Said events could potentially also trigger weak radio afterglow events that should be detectable with mission such as SKA.
2. **Other galaxies:** The short but strong energy transients in optical/IR detected by e.g. VRO followed by the radio afterglow caused by the consumption of a Jupiter-mass planet detectable with SKA will strongly hint at a recent planet consumption event in a local galaxy such as M31 or LMC.

8.4 Future work

Below, I list a set of improvements based on the discussion above that can be applied to the methodology in this thesis to extend the study.

- Base the planetary systems investigated on a population synthesis model, e.g. based on statistics He et al. (2020) or planet formation theory Bitsch et al. (2019), and employ a more complete stability criterion in terms of AMD from Laskar & Petit (2017).
  - The population synthesis model should also include a proper stellar evolution model to properly understand the importance of stellar age on the detectability of observational consequences of planet consumption.
  - Varying properties should be stellar metallicity, age, mass and radius.
- Implement a tidal model in the N-body integrations for the treatment of both planetary and stellar tides to better understand the ratio between consumption of planets

on short-period orbits through tidal decay and planet consumption due to planet–planet scattering events. Furthermore, this would allow for a more physically accurate case with the creation of planet binaries.

- Ensure to increase the resolution when reaching low values of $r_{\min}$ to avoid having to extrapolate eccentricities to obtain $r_{\min} \sim R_\star$.
- Employ hydrodynamical simulations of a planet–star collisions to perform more in-depth studies on how the little-to-no mass loss during tidal decay of high-eccentricity orbits, predicted by Dosopoulou, Naoz, & Kalogera (2017), will affect the signature strength of observational consequences such as gas bullet ejection and planet merger transients.
- Improve the two-body model by including an inclination of the orbits.
- Further investigate the 5J problem, where the presence of two inner Jupiter-mass planets stabilises the system, to determine whether the effect originates from the 'AMD sink theory' or the 'altered potential theory' (see appendix B).

Chapter 9

Summary & conclusions

In this chapter, I briefly summarise the work done in this thesis before presenting the main conclusions from the analysis of planet-consuming events in multiple planetary systems.

9.1 Summary

In this thesis, I have investigated the phenomenon where planet–planet scattering in unstable, multiple planetary systems leads to the consumption of one or more planets by a single host star. Such a scenario has been proposed by previous theoretical studies on the outcome of planet–planet scattering and been tied to observational consequences of planet consumption, such as stellar spin-up, periodic ejection of stellar surface material, stellar metallicity enhancement and planetary merger transients. Using analytical and numerical analysis of planet–planet scattering events, I have been able to narrow down which type of systems are more likely to produce planet consumption events. Furthermore, I have employed toy–model estimates of planet–star collision outcomes based on the results of the numerical analysis, from which I have formulated a proposal for which kind of observational consequences that can be used to detect potential past planet consumption events in various planetary systems.

I began in chapter 5 by employing a simplified isolated, coplanar two-body model to investigate planet–planet scattering events after the crossing of two planetary orbits. This approach allowed me to narrow down the parameter space that governs the outcome of scattering events. Focusing on MS stars, I found that extreme mass ratios between the planets on hierarchical and short-period orbits, of which at least one is highly eccentric, around an F, G or K-type star with a low bulk density are optimal for consistently producing planet consumption events. The main conclusions from said chapter can be found in section 5.5. With a more constrained parameter space, I set up full three-dimensional numerical experiments in the N-body integrator `MERCURY` to in detail investigate the dy-

namical evolution of unstable hierarchical, multiple planetary systems in chapter 6. The fiducial system was a Solar System analogue consisting of two Earth-mass planets within three Jupiter-mass planets, referred to as 2E+3J. This choice was motivated by the results from the two-body analysis and architecture of planetary systems as predicted by observational data from 'Kepler' and planet formation theory (see section 6.2). I then altered properties such as mass, radial separation from the host star and multiplicity of this fiducial system to determine how they affect the system's ability to produce planet-consuming events. From the results of the numerical integrations, I found that the predictions from the two-body analysis are in line with the behaviour of the more complete model and serves well as a first approximation to single planet–planet scattering events. The main difference between the two-body and N-body analyses is that the former only can model the outcome of scattering events after substantial dynamical evolution since at least one of the orbits need to be on a high-eccentricity orbit. The current understanding of planet formation will favour initially circular and coplanar orbits, leading to a low initial AMD. Hence, I found that intrinsically unstable systems require a subsystem with at least two unstable giant planets to consistently trigger dynamical instability that leads to the crossing of orbits.

The properties of the system and the bodies involved in the scattering will furthermore determine the main pathway to planet consumption and the nature of the planet–star collision. From the analysis, I have concluded that there are three extreme pathways:

1. **Diffusive consumption:** A planet undergoes a large number of close encounters, slowly increasing its eccentricity in a diffusive manner. Common for scattering events with $q_{\rm p} \sim 1$, meaning that it is the main pathway for consumption of giant planets.
2. **Strong consumption:** A few strong subsequent scatterings rapidly drive up the eccentricity of a planet, putting it on a planet-consuming orbit. Mainly occurs for scattering events with $q_{\rm p} \ll 1$. Connected to diffusive consumption through a continuum of average scattering strengths.
3. **Lidov–Kozai consumption:** The eccentricity of a planetary orbit is increased due to Lidov–Kozai oscillations with a massive companion with high mutual inclination. Relevant for systems where there are mass ratios $q_{\rm p} \ll 1$ and more than two giant planets.

The pathway to consumption for giant planets is thus highly similar to the pathway to ejection. Furthermore, given that the Jupiter-mass planets in 2E+3J have been placed further out in the system, ejection frequently occurs for said Jupiter-mass planets and is their dominant CME-type outcome. As a result, consumption of low-mass planets occurs in a large majority of the integrated planetary systems, while consumption of Jupiter-mass planets only occurs in about 10% of them. The complete set of conclusions from chapter 6 are found in section 6.7.

In chapter 7, I carried out a literature study of observational consequences for planet-consuming events and performed simple calculations to predict dominant outcomes for the

systems created in my simulations. Firstly, I determined that there are two types of planet–star collisions when the consumed planet is on a highly eccentric orbit. For a Sun-like MS star, they can be distinguished by using the fractional radial velocity $f_\perp$ of the incoming planet (Church, Mustill, & Liu, 2020), which is a measure of the impact parameter of the collision.

1. **Grazing collision:** The planet undergoes close encounters with the host star, as its eccentricity grows diffusively such that $r_{\min} \to \mathrm{R}_\odot$. The planet ultimately reaches eccentricities such that $r_{\min} = \mathrm{R}_\odot$, where headwind from stellar gas, as well as tidal decay of the orbit, will cause the planet to spiral inwards over the course of several orbits. Holds for $f_\perp < 0.4$.
2. **Prompt collision:** The planet obtains a high-eccentricity orbit such that $r_{\min} < R_\star$. In turn, the planet will be directly consumed during its first orbit beneath the surface of the host star. Holds for $f_\perp \geq 0.4$.

From the results of the numerical integrations of 2E+3J and its derivative configurations, it stands clear that grazing encounters will dominate for consumption of Earth-mass and Jupiter-mass planets, especially for the latter which undergo diffusive consumption. Together with the toy–model computations based on literature studies of planet-consuming events, I could estimate which observational effects that will dominate for my simulations. The conclusions of the analysis in chapter 7, found in section 7.8, show that the outcome is dependent of many parameters such as the metallicity, age, mass and radius of the host star, as well as composition, mass and radius of the consumed planet. However, given the rate of planet consumptions within the dynamically evolved systems based on 2E+3J and discussion of the detectability of different observational consequences summarised in section 8.3.5, I could draw two main conclusions. For planetary systems within the Milky Way, it seems that metallicity enhancement by consumption of a massive or several less massive super-Earth(s) will consistently produce a detectable signal for Sun-like MS stars within stellar clusters, in line with the findings of (Church, Mustill, & Liu, 2020). Nonetheless, primary indications of planet consumption should be followed up with observations of secondary signatures. In this case, a good choice would be detection of radio afterglow caused by a planet merger transient (Yamazaki, Hayasaki, & Loeb, 2017) or perturbations in the period of the stellar spin (Qureshi, Naoz, & Shkolnik, 2018). For extragalactic planet-consumption events, consumptions of giant planets will induce a detectable optical/IR transient followed by radio synchrotron radiation afterglow, suggesting that such events make good candidates for multi-waveband astronomy with future observational missions such as VRO and SKA.

9.2 Conclusions

The main conclusions for the work done in this thesis based on the discussion above and the conclusions from sections 5.5, 6.7, 7.8 and 8.3.5 are as follows:

Major conclusions from this thesis

1. Planet consumption induced by planet–planet scattering is likely to occur when
   - the planetary mass ratio $q_{\rm p} = M_{\rm p,1}/M_{\rm p,2}$ is small:
   - the planets are orbiting a host star with low density:
   - one orbit is highly eccentric, preferably for hierarchical configurations where the eccentricity of the lower-mass planet is the highest:
   - the scattering event occurs for planets on short-period orbits near the host star.
2. Consumption of low-mass planets below $\sim$ 30 $\mathrm{M}_{\oplus}$ will consistently occur for hierarchical planetary systems with at least two giant planets.
3. Consumption of giant planets will occur in around 10% of my systems when the initial configuration contains three giant planets. Such an event can produce a unique observational consequence where a single giant planet is left on a wide orbit with arbitrary eccentricity.
4. There are three extreme pathways to planet consumption: diffusive, strong and Lidov–Kozai consumption (see description above).
5. Grazing collisions between the host star and the planet will dominate, no matter which pathway for consumption the planet follows.
6. The dominant observational consequence depends on
   - Stellar age, mass, metallicity and radius.
   - Planetary mass, radius, composition and impact parameter.
7. Detections of observational signatures that are likely to depend on planet consumption ought to be followed up with a secondary detection method, making planet consumption a good candidate for future multi-waveband astronomy missions.
8. From numerical integrations of a planetary configuration motivated from observations of planetary systems by 'Kepler' and planet formation theory, the dominant observational consequence from planet consumption in the Milky Way will be metallicity enhancement by consumption of super-Earths. Outside the galaxy, the dominant observational consequence will be planet merger transients caused by the consumption of a Jupiter-mass planet.

Bibliography

Aarseth, S. J. 2003, Gravitational N-body simulations : (Cambridge :: Cambridge University Press,)

Akeson, R. L., Chen, X., Ciardi, D., et al. 2013, , 125, 989

Bashi, D., Helled, R., Zucker, S., & Mordasini, C. 2017, A&A, 604, A83

Beaugé, C. & Nesvorný, D. 2012, ApJ, 751, 119

Benbakoura, M., Réville, V., Brun, A. S., Le Poncin-Lafitte, C., & Mathis, S. 2019, A&A, 621, A124

Benz, W., Broeg, C., Fortier, A., et al. 2020, arXiv e-prints, arXiv:2009.11633

Bitsch, B., Izidoro, A., Johansen, A., et al. 2019, A&A, 623, A88

Bitsch, B., Lambrechts, M., & Johansen, A. 2015, A&A, 582, A112

Bitsch, B., Trifonov, T., & Izidoro, A. 2020, arXiv e-prints, arXiv:2009.11725

Bodenheimer, P. 1965, ApJ, 142, 451

Borucki, W. J., Koch, D., Basri, G., et al. 2010, Science, 327, 977

Bryan, M. L., Knutson, H. A., Lee, E. J., et al. 2019, AJ, 157, 52

Buchhave, L. A., Bitsch, B., Johansen, A., et al. 2018, ApJ, 856, 37

Bulirsch, R. & Stoer, J. 1966, Numerische Mathematik, 8, 1

Carlberg, J. K., Cunha, K., Smith, V. V., & Majewski, S. R. 2013, Astronomische Nachrichten, 334, 120

Carlos, M., Meléndez, J., Spina, L., et al. 2019, MNRAS, 485, 4052

Carrera, D., Davies, M. B., & Johansen, A. 2016, MNRAS, 463, 3226

Carrera, D., Raymond, S. N., & Davies, M. B. 2019, A&A, 629, L7

Chambers, J. E. 1999, MNRAS, 304, 793

Chambers, J. E., Wetherill, G. W., & Boss, A. P. 1996, Icarus, 119, 261

Chatterjee, S., Ford, E. B., Matsumura, S., & Rasio, F. A. 2008, ApJ, 686, 580

Church, R. P., Mustill, A. J., & Liu, F. 2020, MNRAS, 491, 2391

Cumming, A., Butler, R. P., Marcy, G. W., et al. 2008, , 120, 531

Davies, M. B., Adams, F. C., Armitage, P., et al. 2014, in Protostars and Planets VI, ed. H. Beuther, R. S. Klessen, C. P. Dullemond, & T. Henning, 787

Dawson, R. I. & Johnson, J. A. 2018, ARA&A, 56, 175

De Pater, I. & Lissauer, J. J. 2015, Planetary sciences /, updated second edition edn. (Cambridge :: Cambridge University Press,)

Debes, J. H. & Sigurdsson, S. 2002, ApJ, 572, 556

Demarque, P., Guenther, D. B., Li, L. H., Mazumdar, A., & Straka, C. W. 2008, , 316, 31

Dewdney, P. E., Hall, P. J., Schilizzi, R. T., & Lazio, T. J. L. W. 2009, IEEE Proceedings, 97, 1482

Dosopoulou, F., Naoz, S., & Kalogera, V. 2017, ApJ, 844, 12

Dziewonski, A. M. & Anderson, D. L. 1981, Physics of the Earth and Planetary Interiors, 25, 297

Euler, L. 1768, Institutionum calculi integralis, Institutionum calculi integralis No. v. 1 (imp. Acad. imp. Saènt.)

Fernandes, R. B., Mulders, G. D., Pascucci, I., Mordasini, C., & Emsenhuber, A. 2019, ApJ, 874, 81

Ford, E. B., Havlickova, M., & Rasio, F. A. 2001, Icarus, 150, 303

Ford, E. B. & Rasio, F. A. 2008, ApJ, 686, 621

Gänsicke, B. T., Schreiber, M. R., Toloza, O., et al. 2019, Nature, 576, 61

Gilbert, G. J. & Fabrycky, D. C. 2020, AJ, 159, 281

Ginzburg, S. & Chiang, E. 2020, MNRAS, 498, 680

Gladman, B. 1993, Icarus, 106, 247

Gray, D. F. 1992, The observation and analysis of stellar photospheres., Vol. 20

Grimm, S. L. & Stadel, J. G. 2014, ApJ, 796, 23

Guillochon, J., Ramirez-Ruiz, E., & Lin, D. 2011, ApJ, 732, 74

He, M. Y., Ford, E. B., & Ragozzine, D. 2019, MNRAS, 490, 4575

He, M. Y., Ford, E. B., Ragozzine, D., & Carrera, D. 2020, arXiv e-prints, arXiv:2007.14473

Henry, T. J. & McCarthy, Donald W., J. 1993, AJ, 106, 773

Hodges, J. 1958, Arkiv för Matematik, 3, 469

Høg, E., Fabricius, C., Makarov, V. V., et al. 2000, A&A, 355, L27

Israelian, G., Santos, N. C., Mayor, M., & Rebolo, R. 2001, Nature, 411, 163

Ito, T. & Ohtsuka, K. 2019, Monographs on Environment, Earth and Planets, 7, 1

Ivezić, Ž., Kahn, S. M., Tyson, J. A., et al. 2019, ApJ, 873, 111

Jimenez, R., Grae Jorgensen, U., & Verde, L. 2020, arXiv e-prints, arXiv:2003.11499

Johansen, A., Davies, M. B., Church, R. P., & Holmelin, V. 2012, ApJ, 758, 39

Johansen, A. & Lambrechts, M. 2017, Annual Review of Earth and Planetary Sciences, 45, 359

Johnson, J. A., Aller, K. M., Howard, A. W., & Crepp, J. R. 2010, , 122, 905

Jontof-Hutter, D. 2019, Annual Review of Earth and Planetary Sciences, 47, 141

Jurić, M. & Tremaine, S. 2008, ApJ, 686, 603

Kipping, D. M. & Sandford, E. 2016, MNRAS, 463, 1323

Koester, D., Gänsicke, B. T., & Farihi, J. 2014, A&A, 566, A34

Kokaia, G. & Davies, M. B. 2019, MNRAS, 489, 5165

Kozai, Y. 1962, AJ, 67, 591

Lambrechts, M., Johansen, A., & Morbidelli, A. 2014, A&A, 572, A35

Lambrechts, M., Morbidelli, A., Jacobson, S. A., et al. 2019, A&A, 627, A83

Laskar, J. 1997, A&A, 317, L75

Laskar, J. 2000, , 84, 3240

Laskar, J. & Petit, A. C. 2017, A&A, 605, A72

Laughlin, G. & Adams, F. C. 1997, ApJ, 491, L51

Lendl, M., Csizmadia, S., Deline, A., et al. 2020, arXiv e-prints, arXiv:2009.13403

Li, D., Mustill, A. J., & Davies, M. B. 2019, MNRAS, 488, 1366

Li, D., Mustill, A. J., & Davies, M. B. 2020, MNRAS, 496, 1149

Li, S. L., Lin, D. N. C., & Liu, X. W. 2008, ApJ, 685, 1210

Lidov, M. L. 1962, , 9, 719

MacLeod, M., Cantiello, M., & Soares-Furtado, M. 2018, ApJ, 853, L1

Malmberg, D., Davies, M. B., & Heggie, D. C. 2011, MNRAS, 411, 859

Matsakos, T. & Königl, A. 2015, ApJ, 809, L20

Mayor, M., Marmier, M., Lovis, C., et al. 2011, arXiv e-prints, arXiv:1109.2497

Mayor, M. & Queloz, D. 1995, Nature, 378, 355

Meléndez, J., Bedell, M., Bean, J. L., et al. 2017, A&A, 597, A34

Metzger, B. D., Giannios, D., & Spiegel, D. S. 2012, MNRAS, 425, 2778

Millholland, S., Wang, S., & Laughlin, G. 2017, ApJ, 849, L33

Morbidelli, A., Levison, H. F., Tsiganis, K., & Gomes, R. 2005, Nature, 435, 462

Murchikova, L. & Tremaine, S. 2020, AJ, 160, 160

Mustill, A. J., Davies, M. B., & Johansen, A. 2017, MNRAS, 468, 3000

Muterspaugh, M. W., Lane, B. F., Konacki, M., et al. 2006, A&A, 446, 723

Nagasawa, M., Ida, S., & Bessho, T. 2008, ApJ, 678, 498

Naoz, S. 2016, Annual Review of Astronomy and Astrophysics, 54

NASA Exoplanet Archive. 2020, Confirmed Planets Table

Neil, A. R. & Rogers, L. A. 2020, ApJ, 891, 12

Nelson, R. P., Papaloizou, J. C. B., Masset, F., & Kley, W. 2000, MNRAS, 318, 18

Ochiai, H., Nagasawa, M., & Ida, S. 2014, ApJ, 790, 92

Oetjens, A., Carone, L., Bergemann, M., & Serenelli, A. 2020, arXiv e-prints, arXiv:2009.03624

Ogilvie, G. I. 2014, ARA&A, 52, 171

Otegi, J. F., Bouchy, F., & Helled, R. 2020, A&A, 634, A43

Parker, E. N. 1958, ApJ, 128, 664

Petrovich, C. 2015, ApJ, 808, 120

Petrovich, C. & Muñoz, D. J. 2017, ApJ, 834, 116

Podsiadlowski, P., Rappaport, S., Fregeau, J. M., & Mardling, R. A. 2010, arXiv e-prints, arXiv:1007.1418

Popkov, A. V. & Popov, S. B. 2019, MNRAS, 490, 2390

Press, W. H. 1992, Numerical recipes in FORTRAN :, 2nd edn. (Cambridge :: Cambridge Univ. Press,), föreg. uppl. med titeln: Numerical recipes

Prialnik, D. 2000, An introduction to the theory of stellar structure and evolution (Cambridge University Press)

Privitera, G., Meynet, G., Eggenberger, P., et al. 2016, A&A, 593, L15

Pu, B. & Wu, Y. 2015, ApJ, 807, 44

Qureshi, A., Naoz, S., & Shkolnik, E. L. 2018, ApJ, 864, 65

Ramírez, I., Khanal, S., Aleo, P., et al. 2015, ApJ, 808, 13

Raymond, S. N., Armitage, P. J., & Gorelick, N. 2010, ApJ, 711, 772

Raymond, S. N., Armitage, P. J., Moro-Martín, A., et al. 2011, A&A, 530, A62

Ricker, G. R., Winn, J. N., Vanderspek, R., et al. 2015, Journal of Astronomical Telescopes, Instruments, and Systems, 1, 014003

Runge, C. 1895, Mathematische Annalen, 46, 167

Salas, J. M., Naoz, S., Morris, M. R., & Stephan, A. P. 2019, MNRAS, 487, 3029

Sandford, E., Kipping, D., & Collins, M. 2019, MNRAS, 489, 3162

Sandquist, E., Taam, R. E., Lin, D. N. C., & Burkert, A. 1998, ApJ, 506, L65

Sandquist, E. L., Dokter, J. J., Lin, D. N. C., & Mardling, R. A. 2002, ApJ, 572, 1012

Soares-Furtado, M., Cantiello, M., MacLeod, M., & Ness, M. K. 2020, arXiv e-prints, arXiv:2002.05275

Sousa, S. G., Santos, N. C., Israelian, G., Mayor, M., & Udry, S. 2011, A&A, 533, A141

Spitzer, L. 1987, Dynamical evolution of globular clusters

Stenflo, J. O. 1990, A&A, 233, 220

Stephan, A. P., Naoz, S., Gaudi, B. S., & Salas, J. M. 2020, ApJ, 889, 45

Stoer, J. & Bulirsch, R. 2013, Introduction to numerical analysis, Vol. 12 (Springer Science & Business Media)

Szebehely, V. G. 1989, Adventures in celestial mechanics :, 1st edn. (Austin :: University of Texas Press,)

Teitler, S. & Königl, A. 2014, ApJ, 786, 139

Thorngren, D. P., Fortney, J. J., Murray-Clay, R. A., & Lopez, E. D. 2016, ApJ, 831, 64

Tout, C. A., Pols, O. R., Eggleton, P. P., & Han, Z. 1996, MNRAS, 281, 257

Tremaine, S. & Dong, S. 2012, AJ, 143, 94

Tsiganis, K., Gomes, R., Morbidelli, A., & Levison, H. F. 2005, Nature, 435, 459

Valsecchi, F., Rasio, F. A., & Steffen, J. H. 2014, ApJ, 793, L3

Veras, D., Crepp, J. R., & Ford, E. B. 2009, ApJ, 696, 1600

Veras, D., Mustill, A. J., Bonsor, A., & Wyatt, M. C. 2013, MNRAS, 431, 1686

Vidotto, A. A. 2020, IAU Symposium, 354, 259

von Zeipel, H. 1910, Astronomische Nachrichten, 183, 345

Voyatzis, G., Hadjidemetriou, J. D., Veras, D., & Varvoglis, H. 2013, MNRAS, 430, 3383

Wagner, K., Apai, D., Kasper, M., et al. 2020, arXiv e-prints, arXiv:2009.08537

Weiss, L. M., Marcy, G. W., Petigura, E. A., et al. 2018, AJ, 155, 48

Weiss, L. M. & Petigura, E. A. 2020, ApJ, 893, L1

Weisstein, E. W. 2020, Kepler's Equation – from Wolfram MathWorld

Williams, D. R. 2019, NASA Planetary Fact Sheet

Wimarsson, J., Liu, B., & Ogihara, M. 2020, MNRAS, 496, 3314

Winn, J. N. & Fabrycky, D. C. 2015, ARA&A, 53, 409

Wittenmyer, R. A., Wang, S., Horner, J., et al. 2020, MNRAS, 492, 377

Wright, J. T. & Gaudi, B. S. 2013, Exoplanet Detection Methods, ed. T. D. Oswalt, L. M. French, & P. Kalas, 489

Wright, J. T., Upadhyay, S., Marcy, G. W., et al. 2009, ApJ, 693, 1084

Yamazaki, R., Hayasaki, K., & Loeb, A. 2017, MNRAS, 466, 1421

Zeng, L., Sasselov, D. D., & Jacobsen, S. B. 2016, ApJ, 819, 127

Zhu, W. 2020, AJ, 159, 188

Zhu, W. & Wu, Y. 2018, AJ, 156, 92

Zink, J. K., Christiansen, J. L., & Hansen, B. M. S. 2019, MNRAS, 483, 4479

Zuckerman, B., Koester, D., Reid, I. N., & Hünsch, M. 2003, ApJ, 596, 477

Zuckerman, B., Melis, C., Klein, B., Koester, D., & Jura, M. 2010, ApJ, 722, 725

List of Symbols

α	Angle between radius and velocity vectors
β	Numerical factor for $b_{\max}$
Δ	Separation in Hill radii
δ	Deflection angle [°]
ℓ	Semi-latus rectum [m]
ϵ	Specific orbital energy [J kg^{-1}]
μ_r	Reduced mass [kg]
Ω	Longitude of the ascending node [°]
ω	Argument of the periastron [°]
$\Omega_\star$	Rotational frequency of host star [s^{-1}]
ϕ	Angle between semi-major axes of two orbits [°]
ψ	Angle between orbits at infinite separation [°]
ρ	Density [kg m^{-3}]
$\sigma_{\rm SB}$	Stefan-Boltzmann constant [W m^{-2} K^{-4}]
τ	Lifetime of a planetary system [s]
Θ	Safronov number
θ	True anomaly [°]
$\theta_{\rm cross}$	True anomaly at orbital crossing [°]
ε	Eccentric anomaly [°]
φ	Angle from point of closest separation during deflection [°]
ξ	Fractional change in AMD
$a, a_{\rm p}$	Semi-major axis [m]

a_{f}	Semi-major axis of a planet that has ejected two Jupiter-mass planets [m]
b	Planet–planet scattering impact parameter [m]
b_{max}	Limiting value of b during planet–planet scattering [m]
C	Centre of orbital ellipse
c	Position of the host star [m]
d	Distance between planets during planet–planet scattering [m]
d_{min}	Minimum distance between planets during planet–planet scattering [m]
E	Energy [J]
e	Eccentricity
$f_{\perp}$	Fraction of the velocity that is radial
$f_{\mathrm{consuming}}$	Fraction of consuming orbits in a set of systems
G	Gravitational constant [$\mathrm{m}^3\ \mathrm{kg}^{-1} s^{-2}$]
h	Specific angular momentum [$\mathrm{m}^2\ \mathrm{s}^{-2}$]
i	Orbital inclination [$^\circ$]
i_{mut}	Mutual inclination [$^\circ$]
J	Orbital angular momentum [$\mathrm{m}^2\ \mathrm{kg}\ \mathrm{s}^{-2}$]
k_{B}	Boltzmann constant [$\mathrm{J}\ \mathrm{K}^{-1}$]
$L_{\star}$	Luminosity of host star [$\mathrm{J}\ \mathrm{s}^{-1}$]
M	Mass [kg]
N_{CE}	Number of close encounters
P	Orbital period [s]
$P_{\star}$	Rotational period of host star [s]
q_{p}	Mass ratio of planets in a planet–planet scattering
$q_{\star}$	Mass ratio of planet and host star
R	Radius [m]
r	Radial distance from star [m]
r_{apa}	Apastron distance [m]
r_{crit}	The critical radial distance for planet consumption [m]
r_{cross}	Radial distance to orbit crossing [m]

$R_{\mathrm{Hill,m}}$	Mutual Hill radius [m]
$r_{\max}$	Maximum distance from host star [m]
$r_{\min}$	Minimum distance from host star [m]
r_{peri}	Periastron distance [m]
r_{p}	Radial distance between planet and star [m]
R_{Roche}	Roche radius of host star [m]
r_{tide}	Tidal circularisation radius [m]
T	Temperature [K]
t	Time [s]
t_{CE}	Time until first close encounter [s]
t_{CME}	Time at the onset of a CME-event [s]
t_{tot}	Total integration time [s]
v, v_{p}	Planet velocity [m s^{-1}]
v_{∞}	Velocity at infinite separation [m s^{-1}]
v_{cm}	Centre-of-mass velocity [m s^{-1}]
v_{esc}	Escape velocity [m s^{-1}]
v_{rel}	Relative velocity [m s^{-1}]
v_{r}	Radial velocity [m s^{-1}]
v_{θ}	Tangential velocity [m s^{-1}]
$v_{\mathrm{p},b}$	Velocity relative to the centre-of-mass [m s^{-1}]
Z	Metallicity
$\mathrm{M_J}$	Mass of Jupiter [kg]
$\mathrm{M_{Nep}}$	Mass of Neptune [kg]
$\mathrm{M}_{\odot}$	Mass of the Sun [kg]
$\mathrm{M}_{\oplus}$	Mass of Earth [kg]
$\mathrm{R_J}$	Radius of Jupiter [m]
$\mathrm{R}_{\odot}$	Radius of the Sun [m]
$\mathrm{R}_{\oplus}$	Radius of Earth [m]

Acronyms

AGB Asymptotic Giant Branch. 113

AMD Angular Momentum Deficit. 35

CME Consumed, Merged or Ejected. 53

CMF Core Mass Fraction. 27

EUV Extreme Ultraviolet. 116

IR Infrared Radiation. 116

LMC Large Magellanic Cloud. 134

MMR Mean-Motion Resonance. 35

MR-relation Mass-Radius relation. 27, 40

MS Main Sequence. 7, 105

ODE Ordinary Differential Equation. 74, 75

RGB Red Giant Branch. 110

SKA Square Kilometre Array. 134

VRO Vera Rubin Observatory. 134

ZAMS Zero Age Main Sequence. 30

Glossary

'Kepler' dichotomy The apparent existence of two populations within the sample of planets observed with the *Kepler Space Telescope*. One of the populations consists of multiple planet systems with low mutual inclinations, while the other consists of single planet systems or systems with high mutual inclinations. 22, 25, 78

action at a distance Interactions between two planets with low separations where they exchange angular momentum without the crossing of orbits. 36, 95, 120

adaptive time step A variable step size in time for integrators that depends on the level of accuracy needed to provide a good estimate of the solution to the problem at hand. 75

anti-scattering When a planet on an eccentric orbit is put on a less eccentric and wider orbit after planet–planet scattering. 84

close encounter When two planets which have crossing orbits are within one mutual Hill radius of each other (see equation (4.1)). 34, 43, 156

cold Jupiter A giant planet with a minimum mass of 0.3 M_J orbiting its host star at distances of $a_p > 1$ AU. 22

deflection The alteration of a planet's trajectory and in turn its orbital parameters during a scattering event. 43

ejection An outcome of a planet–planet scattering event where a planetary orbit becomes so eccentric that the planet becomes unbound from the planetary system. 7, 38

flat system A planetary system where the orbits have little to no mutual inclination, meaning that they will all be coplanar. 42, 67, 70

gravitational focusing A deflection where the gravitational force between the two objects enhances the likelihood of them colliding and merging. 44

grazing collision The planet impacts its host star with an eccentricity $e \sim e_{\rm crit}$ such that it spirals in towards the tidal plunging radius over the course of several orbits. 107

Hill stable When two orbits are sure to never cross due to exchanges of angular momentum and energy during their mutual long-term gravitational interactions. 34

hot Jupiter A giant planet with a minimum mass of 0.25 $\mathrm{M_J} \lesssim M_{\rm p} \sin(i) \lesssim 20\ \mathrm{M_J}$, orbiting its host star with a period of 10 days or shorter ($a_{\rm p} \lesssim 0.1$ AU). 7, 30, 103, 130

impact parameter The distance between two planets during a close encounter on their unperturbed orbits. 43

Lidov–Kozai A mechanism where a highly inclined companion perturbs a planetary orbit inducing large periodic changes in orbital eccentricity and inclination (see section 4.2). 37

magnetic braking The loss of angular momentum for a star due to ejection of material getting caught in the star's magnetic field. Effectively causes the star to spin-down over time. 110, 134

mutual inclination The angle between the angular momentum vectors of two orbits. 14

planet consumption An outcome of a planet–planet scattering event where one planet physically collides with the host star of the planetary system. 4, 8, 38

planet–planet merger The outcome of a scattering event where the impact parameter is smaller than the combined physical radii of the two planets, resulting in a physical collision. Also referred to as *merger*. 7, 38

planet–planet scattering An event where two planets with crossing orbits are close enough to each other to exchange a significant amount of angular momentum and energy to alter the orbital elements of one or both of the orbits. 7, 34, 43, 155, 156

planet-consuming orbit An orbit where the planet is heading directly towards the host star and will be consumed. 39

planetary configuration An initial setup of planets with predefined multiplicity, initial semi-major axes and masses orbiting a host star with a given mass. All planetary systems are subsets of planetary configurations. Also referred to as *orbital configuration*. 80, 81, 156, 157

planetary system Part of a subset of a given planetary configuration where planets with static semi-major axes have been given randomised orbital elements. 80, 81, 156, 157

progenitor system The initial phase of a planetary system at $t = 0$ yr. 80, 81, 157

prompt collision The planet impacts its host star with an eccentricity $e > e_{\rm crit}$ such that it undergoes tidal plunging after only one orbit. 107

radial excursion Refers to the excursion made by a planet outwards in the planetary system, away from the host star. Corresponds to the apastron distance of $r_{\rm max} = a(1 + e)$. 34, 82

radial incursion Refers to the incursion made by a planet inwards within the planetary system, towards the host star. Corresponds to the periastron distance of $r_{\rm min} = a(1 - e)$. 34, 82

realisation A realisation is the integration over 10 Myr for a given progenitor system that in the end creates a planetary system. 81, 157

run A run refers to all N realisations for a given planetary configuration, creating N planetary systems. 81

secular theory The long-term change in the orbital elements of a Keplerian orbit over time. 35

short-period orbit A short-period orbit has a small semi-major axis, meaning the planet will have a small separation with its host star. 21

stellar obliquity The angle between the stellar spin axis and the angular momentum axis of a planetary orbit. 110

tidal circularisation A planet on an eccentric orbit obtains angular momentum from the host star, effectively decreasing its eccentricity, putting it on a more circular and shorter period orbit. This is a potential formation channel for hot Jupiters. 24, 31, 103

tidal plunging The decay of a short-period orbit caused by tidal interactions with the host star, which ultimately leads to disruption of the planet. 105

transient Short for 'transient astronomical event' which refers to an observable astronomical event that occurs on very short timescales that can last between a few seconds and several years. In this thesis, the word indicates luminous transients, where the radiative activity of a star is increased for a short period of time. 102

wide orbit A wide orbit has a large semi-major axis, meaning the planet will have a large separation with its host star. 21

Appendix A

Impact parameter distribution

I have until now not addressed the assumption that the impact parameter will be uniformly distributed for a given planetary system. Which impact parameter a given scattering will have in a two-planet system depends on the relative values of the initial true anomaly θ_0 for the planets. Hence, where the planets will have their closest approach during a period of their orbits is entirely a question of timing. In order to test the assumption, I have used a simple numerical approach where I estimate orbital motion using Kepler's equation. The details can be found in the function `scatter.test_bvals`.

First, I compute the periods of both planets using Kepler's third law of planetary motion

$$P^2 = \frac{a^3}{M_{\rm tot}}, \tag{A.1}$$

where $M_{\rm tot}$ is the total mass in Solar masses and P is the period in yr. The total computation time is then given by $t_{\rm tot} = \max(P_1, P_2)$. To setup the test, I produced 500 initial angles for the true anomaly of the secondary orbit $\theta_{0,2}$ with uniform steps while the true anomaly of the primary orbit is kept static $\theta_{0,1} = 0°$. Each combination of $\theta_{0,1}$ and $\theta_{0,2}$ in turn yields a given separation at closest approach $\min(d)$ which will be equal to the impact parameter. Hence, by computing all these different variations of the orbital motions for $t_{\rm tot}$ yr, I obtained a set of separations that corresponds to the closest approach between the two planets at every single time t. Kepler's equation is given by

$$\theta = \varepsilon - e\sin(\varepsilon), \tag{A.2}$$

where ε is the eccentric anomaly of the orbit. The iterative scheme used to solve this

equation is based on Newton's method (Weisstein, 2020)

$$\varepsilon_{n+1} = \varepsilon_n - \frac{\varepsilon_n - e\sin(\varepsilon_n) - \theta(t)}{1 - e\cos(\varepsilon_n)}. \tag{A.3}$$

The initial guess is $\varepsilon_0 = \theta_0$ for $e < 0.8$ and for large eccentricities $e \geq 0.8$, an appropriate guess was found to be $\varepsilon_0 = \pi$. For each time step, Δt, the Cartesian coordinates are computed with the following coordinate transformations

$$x = a(\cos(\varepsilon) - e) \tag{A.4}$$

$$y = a\sqrt{1 - e^2}\sin(\varepsilon). \tag{A.5}$$

The separation for each value of $\theta_{0,2}$ at a time t is then given by

$$d = \sqrt{(x_1 - x_2)^2 + (y_1 - y_2)^2}. \tag{A.6}$$

Note that the separation d is unaffected by gravitational focusing in this model. Nevertheless, since the sole purpose of this analysis was to find the distribution of impact parameters between the two planets this posed no problem. The impact parameter for each value of θ_0 will naturally correspond to $b = \min(d(t))$. All-in-all, I performed two sets of computations. The first set was coarse with only 250 different time steps. For each step I iterated equation (A.3) 100 times to guarantee convergence. By then finding the sign change in the difference between each adjacent value of b I could detect the two minima for each initial angle θ_0, which correspond to the closest initial separation within a circle of radius $R_{\mathrm{Hill,m}}$ centred on the two orbit crossing points, i.e. $\theta_{\mathrm{cross},2}$. Here, I performed the second set of computations where I only estimated the orbital motion in the range $\theta_{0,2} \in [\theta_{\mathrm{cross},2} - 5°, \theta_{\mathrm{cross},2} + 5°]$ to obtain a finer distribution of impact parameters using 10^4 time steps.

After again finding the minima for the finer distribution, I could test the hypothesis of a uniform distribution of impact parameters by making four first order polynomial fits to the distribution of impact parameters left and right of the minima. If these linear fits proved to be good approximations with similar absolute values of their first order constant, I could conclude that the assumption of a uniform distribution for b is indeed fair. After testing several different combinations of orbital elements for the two orbits with different values of ϕ, I found that this was indeed the case.

Appendix B

5J stability investigation

In order to conduct a study of the instability timescales for the configurations mentioned in section 6.4.1, it was necessary to define a metric that will quantify said timescale. A conventional way of measuring this timescale is to look at the timing of the first close encounter between two planets in a planetary system, which I have chosen to denote t_{CE}. While said timescale depends on the initial phase of the system, the overall distribution of t_{CE} for a given configuration will give insight an into how unstable it is. Hence, comparing the distributions of t_{CE} for different configurations can provide a good general understanding of how they differ. As for the two hypotheses for the 5J stability problem, I began by investigating the AMD sink idea.

To begin, I noted that there are two main distinctions between the 2X+3Jd and 2X+3Je configurations in figure 6.1. Firstly, the masses of the planets in the inner subsystem are equal to the masses of the planets in the outer subsystem. Secondly, there is a significant difference in Δ separation between the inner and outer subsystem since 2X+3Jd has $\Delta_{23} = 18.1$ and 2X+3Je has $\Delta_{23} = 15.8$. If the hypothesis is correct, replicating these key features in another system should produce similar results. Hence, I created the 5S and 3S configuration. The first distinction between 2X+3Jd and 2X+3Je can be reproduced by creating another configuration where all planets have equal masses, in a 2X+3J-type manner. I chose to use planets that are approximately of Saturn-mass, i.e. $M_{\mathrm{p}} = 100\ \mathrm{M}_{\oplus}$ and denoted this configuration 5Sa. The second distinction can be reproduced by using the same Δ_{23} separation as for 2X+3Je, which gave birth to the 5Sb system. Since the instability timescale does not only depend on separation, but also on mass (Chambers, Wetherill, & Boss, 1996), the Δ separation between the outer subsystem planets was set to 4.0 instead of 5.1 to hasten the elapsed real time of the integrations. This should only offset the instability timescales between the 2X+3J-type and 5S-type systems. The two configurations were both integrated for 10 Myr in sets of 50 realisations. Lastly, I performed a run with 50 realisations for a system only consisting of the outer subsystem, which served as a reference to determine how the position of the inner planets affected the t_{CE} distribution of 5Sa and 5Sb. The cumulative distribution of t_{CE} for all systems

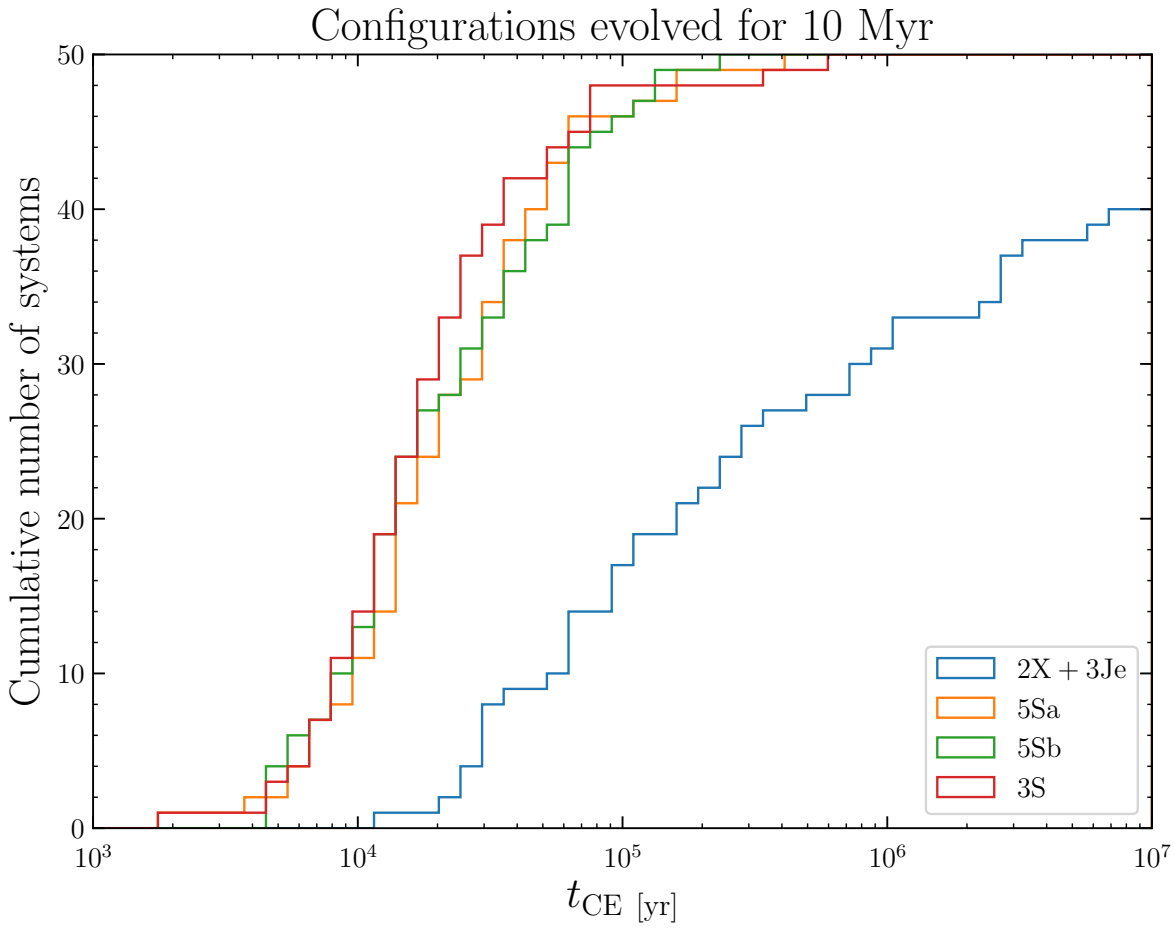

Figure B.1: The cumulative number of systems as a function of the timing of first encounter t_{CE} for the different configurations used in the investigation of the AMD sink theory.

in the three configurations can be found in B.1. I have also included the corresponding distribution for 2X+3Je. While it is not possible to directly compare said distribution with the other three due to the difference in Δ between the outer planets, it still provides a reference for the varying behaviour between the planetary systems in the 5S-type and 5J-type configurations. Nevertheless, it is clear that the presence of the inner subsystem does not affect the instability timescale in a notable manner. To verify the similarity between the cumulative distributions for these three configurations, I employed a two-sample Kolmogorov–Smirnov (KS) test based on the method laid out in Hodges (1958). The KS statistic of relevance is given by

$$D_{n,m} = \sup |F_{1,n}(x) - F_{2,m}|, \tag{B.1}$$

	5Sa & 5Sb	5Sa & 3S	5Sb & 3S
$D_{n,m}$	0.16	0.10	0.16
p-value	0.549	0.967	0.549

Table B.1: The KS-test statistics and p-values for the three S-type configurations investigated for the AMD sink theory.

	2X+3Je & 5Ja	2X+3Je & 5Jb	5Ja & 5Jb
$D_{n,m}$	0.08	0.21	0.22
p-value	0.981	0.101	0.179

Table B.2: The KS-test statistics and p-values for the three J-type configurations of interest investigated for the five Jupiter problem.

where sup is the supremum function while $F_{1,n}(x)$ and $F_{2,m}(x)$ are the cumulative distribution functions of the two samples that are tested. The null hypothesis is that the two samples belong to the same underlying distribution. The results of the tests can be found in table B.1. Judging from the KS statistic, the 5Sa and 3S systems have evolved very similarly while the 5Sb system appears to differ slightly from both of them. Hence, while the separation between inner and outer planets seems to have some effect on the instability timescale, it does not prove the theory. In turn, it was still difficult to say whether or not there is a correlation between having equal mass planets and a more stable outer subsystem. I could nevertheless conclude that a separation of $\Delta_{23} = 15.8$ is small enough for some AMD to be transferred to the inner subsystem, thus prolonging stability.

To investigate further, I then turned to systems consisting of five Jupiters. I made use of five different configurations except for 2X+3Je. The first system was 5Ja, where I increased Δ_{23} to 18.1, which is the separation between the inner and outer subsystems in 2X+3Jd. I included a case where the separation is even larger as well, putting the inner subsystem inside 0.5 AU, closer to the host star. As a sanity check, I also carried out a run where the separation between all planets in terms of Δ was 5.1. This configuration should intuitively evolve significantly quicker and more chaotically than any other configurations considered in the `MERCURY` study since the AMD can easily be redistributed among the planets. If it did not, then there was some underlying effect in the treatment of large total planetary masses in `MERCURY` that yielded faulty results. The final configuration was a reference system with only the outer 3J subsystem, referred to as 3Jc.

All cumulative distributions for t_{CE} of these configurations can be found in figure B.2. As expected, the fastest evolving system by far was 5Jc, which indicates that the explanation is unlikely to lie in the behaviour of `MERCURY`. Moreover, the t_{CE} distributions for 2E+3J and 3J are very similar. This is consistent with the findings up to this point, where the inner planets will not affect the chaotic evolution of the outer subsystem for a small mass ratio $q_{\mathrm{p}} \ll 1$. The most noteworthy difference lies between the 2X+3Je, 5Ja and 5Jb

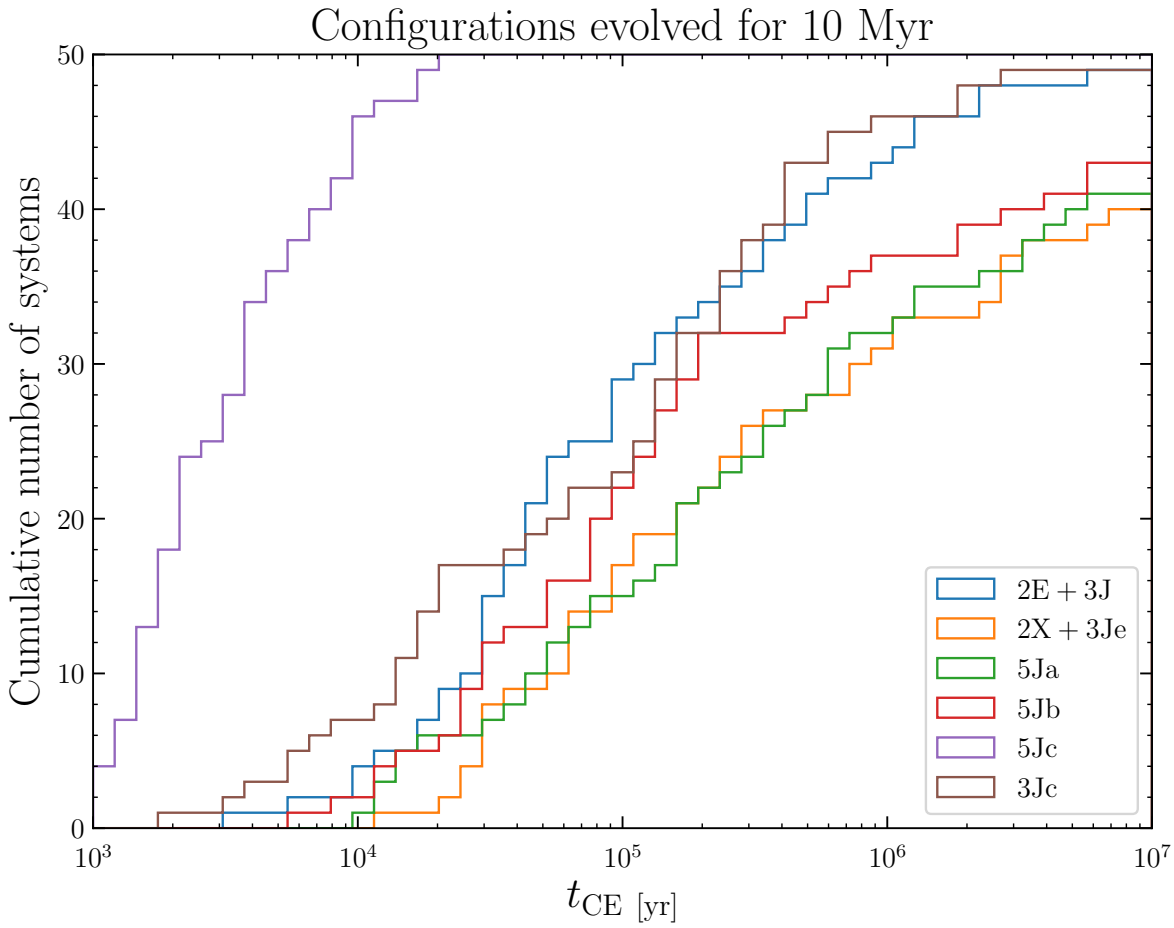

Figure B.2: The cumulative number of systems as a function of the timing of the first encounter t_{CE} for the different configurations used in the investigation of the altered potential theory.

cases. Again, there is a discrepancy between the 2X+3Je and the larger separation in 5Jb. However, 2X+3Je and 5Ja are practically identical, as can be inferred from the table of KS-test values for these three systems in table B.2. Intuitively, if the AMD sink theory is correct, then it should be more difficult to transfer AMD for $\Delta_{23} = 18.1$ than for the case of $\Delta_{23} = 15.8$. Furthermore, the next step in terms of Δ_{23} between 5Ja and 5Jb is even smaller, yet the two configurations seem to evolve on slightly different, albeit statistically indistinguishable, timescales. Therefore, it appears that the most likely explanation for the prolonged stability of 2X+3Je does not lie in AMD transfer.

Instead, the altered potential theory could provide the answer. A key idea is that the increase in separation between the two subsystems also moves the inner subsystem closer to the host star for these cases. Given the large total mass of two M_J for the inner two planets, they produce a large quadrupole term that will alter the potential experienced of

the outer planets. This induces precession, which stabilises the outer subsystem (Mustill, Davies, & Johansen, 2017). If a planet is closer to the host star, the potential will be less asymmetric, making precession weaker. Hence the large difference between t_{CE} for 5Ja and 5Jb.

While there is not enough evidence in this study to draw any firm conclusion regarding the origin of the prolonged stability for 2X+3Je, it can be expanded upon in future work by comparing the instability timescale for additional configurations with both intermediate and larger Δ_{23} values. Furthermore, it would be useful to employ a different integrator that is not based on the Bulirsch-Stoer method to confirm the behaviour.